

**Hydrothermal flow paths in the upper oceanic crust: magnitude  
and distribution of porosity and permeability in altered, fractured  
lavas, Oman ophiolite**

Inauguraldissertation  
der Philosophisch-naturwissenschaftlichen Fakultät der Universität Bern

vorgelegt von  
**Alannah C. Brett**  
von Australia & United Kingdom

Leiter der Arbeit:  
Prof. Dr. L. W. Diamond  
Institut für Geologie



**Hydrothermal flow paths in the upper oceanic crust: magnitude  
and distribution of porosity and permeability in altered, fractured  
lavas, Oman ophiolite**

Inauguraldissertation  
der Philosophisch-naturwissenschaftlichen Fakultät der Universität Bern

vorgelegt von  
**Alannah C. Brett**  
von Australia & United Kingdom

Leiter der Arbeit:  
Prof. Dr. L. W. Diamond  
Institut für Geologie

Von der Philosophisch-naturwissenschaftlichen Fakultät angenommen.

Bern, 30 April 2021

Der Dekan Prof. Dr. Zoltan Balogh





*In loving memory of Michael R. Mayson*

*Who inspired me to be a scientist at heart*

*Question the vast cosmos*

*And the rocks upon which we float*



## Acknowledgements

The spontaneous evolution of this thesis project from the wide-open ophiolite air, to the high tech experimental lab and into the world of fracture modelling, was superbly guided by my supervisor and mentor Prof. Larryn Diamond. Larryn, for your diverse geological and research talents, adaptable logic, creativity and impeccable editing, I am forever grateful and filled with respect. Thank you for teaching me about science, academia and German with openness and humour. “*Habe Geduld, junge Heuschrecke*” (have patience young grasshopper) you said, as I rushed eagerly into my first basaltic field campaign in a pair of running shoes. I and also, I believe, my future students, are incredibly grateful for your wise, understanding, reflective and humorous approach to supervision.

To the Swiss National Science Foundation, thank you for funding the Oman project; a fascinating start to my scientific career. Thank you to the Rock-Water Interaction Group and University of Bern for making my attendance to many conferences and incredible field trips around the world possible. To the Rock Physics and Mechanics Laboratory, ETH Zurich, thanks for sharing your well-oiled lab and amazing team.

This thesis was possible through many scientific and enriching discussions with my supervisor and collaborators. Many thanks to Claudio Petrini and Claudio Madonna for introducing me to the thousand-step workflows required for permeability experiments, for many hours answering my questions in basement conditions and for switching off the lights of the Patty so I could rush off for the long train-ride home. Thank you also for making my measurements go so smoothly and efficiently. Thank you to Peter Alt-Epping, Jeffrey Hyman and Matt Sweeney for your guidance of my flow simulations and fracture modelling, and for rapidly creating new solutions to my unpredictable code and fracture challenges (some self-induced!). Also, thanks to Sämi Weber for your patient modelling and assistance. Thank you to the Institute of Geological Science's, UNIBE laboratory experts, you have all been immensely helpful and efficient over the years with my seemingly endless, unvarying, and hopelessly fine-grained samples. I would also like to thank Prof. Stanislas Sizaret for acting as external reviewer for this thesis and Prof. Marco Herwegh as examination Chair (sorry for the long read ahead, but hope you enjoy my fast-action wrap-up defence).

A huge thanks to the epic Oman team, Larryn Diamond, Tom Belgrano, Lisa Richter and Sämi Weber, who've mapped alongside me for four or more years and to those new members Robin Wolf, Sam Pierre, Ludwik de Doliwa Zielinski and Raphael Kuhn. Also, for those that taught me the Oman-field-ropes and in part inspired the start of my thesis Nevena Grkovic (née Novakovic) and Sam Gilgen, thanks! Together your company has made our four-week-long field campaigns scientifically fantastic and provided laughter through the challenges, as we lived under the same dusty roof, with plenty of canned tuna, endless burning curry, the occasional goat, snake, scorpion and piles of rock samples! Exploring and mapping the truly glorious Semail ophiolite with you all was the biggest pleasure and privilege of my time as a student.

Also, to our Omani colleagues, thank you for your warm welcomes and solving our many car and accommodation challenges over the years, which made for smooth sailing fieldwork.

To my friends and colleagues at the Institute of Geological Sciences thank you for your company, interesting discussions and geo-football games. Those at Ore Deposits Hub, especially Aaron Hantsche, Tom Belgrano, Marion Grosjean and Wren Bruce, you became my virtual family last year. I am so grateful for your warm smiles, diverse discussions and enthusiasm to spontaneously and slightly too instantaneously at times, create a global digital science platform. In that light, thanks again to my supervisor Larryn for putting up with but also encouraging my many non-thesis activities.

I would also like to acknowledge the many hours of help from my therapist, your contribution to my mental health has given me the tools to take on personal challenges, ones that are too often swept away but that form the basis of our lives and careers.

Dear Mum, thank you for the last 28 years of unconditional love and support. Your creative guidance inspired my love of learning. Michael was so proud of us both. Richard, thanks for the adventurous visits, and your welcoming home away from home. And to all my other family, the Jennisons, the Maysons, and the Adams' + Puteran's + Sorochanov's, as well as friends around the world, thank you all too.

Finally, and most of all, my deepest and heartfelt thanks to Arthur. For every step I have fallen, you have helped me up at least twice more, and for every tear I have shed you have given me months full of laughter. I eternally cherish your love, support, humour and understanding that make my life uniquely exceptional.





## Abstract

Convection of seawater and consequent fluid–rock interaction in the basaltic upper crust is responsible for numerous important processes, including the formation of valuable ore deposits at the seafloor, the buffering of composition of the oceans, and the cooling of the oceanic lithosphere. Circulation of hydrothermal fluid is facilitated by the porosity and permeability of the sheeted dyke complexes and submarine lavas that make up the upper crust. Previous studies have assessed the porosity and permeability of fresh basalts and basalts altered at low temperatures to clay and zeolite assemblages, but little is known about the hydraulic properties of the rocks deeper in the crust, where greenschist-facies dominate. Knowledge of these properties is a key prerequisite to performing realistic numerical simulations of the coupled processes caused by hydrothermal circulation. This Thesis provides new perspectives on the porosity and permeability architecture of the upper oceanic crust where it is altered pervasively to greenschist-facies assemblages, by investigating the MORB-type axial lavas and underlying sheeted dyke complex of the Semail ophiolite, Oman. The exceptional outcrop exposures of largely undeformed oceanic lithosphere in Oman provide a well-characterized context for observations and mapping of petrophysical properties at centimetre- to 100-meter scales. Sampling and mapping distinguished rocks altered by downwelling hydrothermal fluids (chl+alb+act-bearing spilites) from those formed by upwelling fluids (epi+qz-bearing epidiosites). These observations can be upscaled numerically to construct a model of rock-matrix and fracture-network flow paths that represents the upper crust at the km-scale. Development and interpretation of this model by integrating new measurements of rock-matrix porosity and permeability, fracture maps, high  $P$ – $T$  experiments and flow simulations are the principle goals of this Thesis.

The first part of this Thesis assesses whether standard permeability measurements of spilites and epidiosites at room conditions represent *in-situ* permeabilities at the effective  $P$  (5–55 MPa) and  $T$  (25–450 °C) of hydrothermal alteration. Our experiments in a Paterson permeameter at 50 MPa show that heating from 25 to 450 °C reduces permeability by ~40–50% and increasing pressure at 25 °C from 5 to 55 MPa reduces permeability by ~70–80%. Based on these results we provide quantitative correlations to adjust results of standard measurements to their *in-situ*, high  $P$ – $T$  values. However, duplicate measurements demonstrate that hand-sample heterogeneity spans up to three orders of magnitude in permeability, outweighing the  $P$ – $T$  effects and rendering corrections unnecessary for large natural datasets. Consequently, we performed all further permeability measurements reported in this Thesis at high  $P$  without adjustment for elevated temperature.

The second study in the Thesis examines how rock-matrix porosity and permeability of spilites and epidiosites depends on volcanic rock type and on the extent of the spilite-to-epidosite alteration reaction. Our results demonstrate that the porosity and permeability of spilites increase in the order dykes < massive lava flows < pillow lava rims < pillow lava cores < interpillow hyaloclastites. These findings are consistent with field observations showing how epidiosite alteration progresses through the different lava types. Additionally, combination of our data on pillow cores, rims and interpillow hyaloclastites reveals that spilite pillow stacks have permeabilities up to  $\sim 2 \times 10^{-16} \text{ m}^2$ . This relatively high value is an important step towards reconciling the large differences between the low rock-matrix permeabilities determined in laboratory measurements and those required by numerical models constrained to reproduce observations of heat and fluid discharge from the crust.

As part of this study we take a more in-depth examination of epidiosites. Although epidiosites are thought to form mainly at the base of the sheeted dyke complex, numerous occurrences up to  $\sim 1 \text{ km}^2$  in outcrop have been

documented in the Semail lavas. It is known that extreme fluid–rock ratios are required to convert the precursor spilites to endmember epidiosites, but mechanism by which the hot (230–450 °C) fluids become so focused during upflow, apparently independently of any fracture networks, is still unclear. Previous studies have suggested epidiotising fluids may create their own porosity and permeability, enabling self-propagation without fracture permeability. We quantified this process by directly comparing the porosity, permeability and mineralogy of pairs of spatially adjacent spilite and epidosite samples, and we integrated these results in reactive-transport simulations, showing that the spilite-to-epidosite reaction creates 9–14 vol.% porosity and up to 4.5 order of magnitude ( $\sim 10^{-15}$  m<sup>2</sup>) permeability. This results in a highly porous (13–26 vol.%) and permeable ( $\sim 10^{-15}$  m<sup>2</sup>) epidosite rock-matrix, which focuses hydrothermal upflow in the absence of significant fracture networks.

In the third study, we bring together upscaled rock-matrix properties for lava stacks with fracture distribution maps, to create 100-meter-scale, dual-porosity, dual-permeability models in order to estimate the bulk permeability of the volcanic layer of the upper crust. The current view is that regional fluid flow in the lavas is characterised by fractured aquifer properties, dominated by fracture networks and extensional faults. However, between kilometre-scale faults and their localised damage zones, termed ‘distal zones’, the distribution and connectivity of fracture networks are not quantified. Moreover, the results from our rock-matrix study and the pervasive alteration of the rock-matrix in ophiolites demonstrates that rock-matrix pathways cannot be ignored at a regional scale. Combining rock-matrix porosities and permeabilities at outcrop scale (weighted for pillow core, pillow rim and interpillow hyaloclastite averages from our previous study) yields porosities of  $\sim 10$ – $12$  vol.% and permeabilities of  $\sim 2.5 \times 10^{-16}$  m<sup>2</sup> for spilite pillow stacks. In distal zones, the fractures (mapped as hydrothermal veins) are sparse and discrete, with fracture intensities of only  $\sim 0.005$  m of fracture per m<sup>2</sup> of outcrop, yet an order of magnitude higher intensity is present in damage zones ( $\sim 0.063$ ). Using *dfnWorks* software, simulations of coupled fracture- and matrix-flow through upscaled discrete fracture matrix models integrate these properties and confirm that damage zones are indeed fracture-controlled fluid channels with permeabilities of  $\sim 10^{-11}$  m<sup>2</sup>. This contrasts with the permeabilities of  $\sim 5 \times 10^{-16}$  m<sup>2</sup> found for sparsely fractured distal zones, in which flow is controlled by the rock-matrix and in which fractures contribute only  $\sim 0.25$  of an order of magnitude to the bulk permeability. This supports the idea that spilitising and epidiotising fluids largely migrate through the rock-matrix in distal zones of the upper oceanic crust.

The results of this Thesis constitute a new perspective on hydrothermal flow paths in the upper oceanic crust. The new datasets of spilite and epidosite rock-matrix petrophysical properties, accounting for *in-situ* pressure and temperature, fill gaps in previous understanding and complement available data on fresh and low-temperature altered basalts. The changes in porosity and permeability during the spilite-to-epidosite reaction reveals how hydrothermal upflow becomes self-focused and attain extreme water–rock ratios. While we confirmed that fault zones spaced at 0.5–1 km distances act as major conduits, a new insight is that the large blocks of crust between such faults behave as permeable rock-matrix aquifers, which facilitate the pore-scale fluid–rock interactions necessary to extract metals and heat for formation of VMS deposits and other chemical elements and isotopes that buffer the composition of the oceans. The next generation of numerical thermal–hydraulic–chemical models will be able to incorporate the km-scale permeability architecture provided by our analysis of hydrothermally altered distal zones and fault-damage zones, to better describe the water–rock interactions in the upper crust.







# Table of Contents

## Acknowledgements

## Abstract

## Table of Contents

<b>1. Introduction.....</b>	<b>1</b>
1.1. Thesis motivation.....	1
1.1.1. Understanding hydrothermal processes in oceanic crust .....	1
1.1.2. Research context regarding genesis of massive-sulphide deposits in Oman .....	2
1.2. Thesis Outline and Aims.....	3
1.3. Geological Setting and Study Site .....	5
References.....	10
<b>2. Influence of in-situ temperatures and pressures on the permeability of hydrothermally altered basalts in the oceanic crust.....</b>	<b>17</b>
Abstract.....	17
2.1. Introduction.....	18
2.2. Materials and Methods.....	19
2.2.1. Geological setting of sampled spilites and epidiosites.....	19
2.2.2. Sample material and selection.....	20
2.2.3. Preliminary sample measurements for sample selection.....	21
2.2.4. Selection of experimental conditions .....	22
2.2.5. Permeability measurements at room temperature and elevated pressure.....	23
2.2.6. Permeability measurements at elevated pressure and temperature .....	23
2.3. Results.....	26
2.3.1. Effect of elevated pressure on the permeability of spilites and epidiosites.....	26
2.3.2. Experiments at elevated temperatures.....	28
2.3.3. Behaviour and uncertainty of permeability over multiple cooling and heating cycles .....	29
2.3.4. Temperature–permeability correlations .....	29
2.4. Discussion .....	31
2.4.1. Effects of pressure on permeability .....	31
2.4.2. Effects of temperature on permeability.....	31
2.4.3. Significance of measured changes in permeability .....	36
2.4.4. Temperature–permeability correlations .....	36

2.4.5. Influence of pressure on the temperature–permeability effect.....	37
2.5. Summary and conclusions .....	37
Acknowledgements.....	38
References.....	38
<b>3. Rock-matrix porosity and permeability in the hydrothermally altered, upper oceanic crust, Oman ophiolite.....</b>	<b>45</b>
Abstract.....	45
3.1. Introduction.....	46
3.2. Geological Setting and Hydrothermal Alteration .....	48
3.3. Approach.....	50
3.3.1. Samples .....	51
3.4. Analytical and Simulation Methods.....	55
3.4.1. Bulk-rock geochemistry, mineralogy and petrography.....	55
3.4.2. Porosity .....	55
3.4.3. Simulation of Spilite-to-Epidosite alteration .....	56
3.4.4. Permeability .....	56
3.4.5. Simulations of hyaloclastite permeability.....	56
3.5. Results.....	57
3.5.1. Petrography of pillow lavas and hyaloclastites.....	57
3.5.2. Rock-matrix porosity and permeability .....	62
3.5.3. Epidotisation: reaction porosity and permeability .....	65
3.6. Discussion.....	66
3.6.1. Reliability of results.....	66
3.6.2. Porosities and permeabilities representative of in-situ hydrothermal conditions.....	67
3.6.3. Controls on porosity and permeability of different rock types and their consequences for progressive epidosite alteration.....	67
3.6.4. Porosity–permeability correlations .....	68
3.6.5. Implications for permeability of the upper crust.....	69
3.7. Summary and Conclusions.....	74
Acknowledgements.....	75
References.....	76
<b>4. Permeability of hydrothermally altered and fractured lavas in the oceanic crust at centimetre to kilometre scales, Oman ophiolite: from field mapping to flow simulations .....</b>	<b>83</b>
Abstract.....	83
4.1. Introduction.....	84

4.2. Geological setting .....	85
4.3. Approach.....	87
4.4. Methods.....	90
4.4.1. Rock-matrix porosity and permeability upscaling .....	90
4.4.2. Fracture mapping .....	92
4.4.3. Fracture distribution analysis .....	93
4.4.4. dfnWorks workflow: DFN, domain build and flow simulation .....	95
4.5. Results.....	96
4.5.1. Bulk rock-matrix porosity and permeability .....	96
4.5.2. Syn-volcanic fault structures.....	96
4.5.3. Fracture distributions .....	100
4.5.4. Distal zone UDFM models and bulk permeability .....	108
4.5.5. Damage zone DFN models and bulk permeability .....	113
4.6. Discussion .....	114
4.6.1. Accuracy of upscaling from field observations to flow models.....	114
4.6.2. Implications of rock-matrix, fracture and bulk permeabilities for the hydrothermal circulation in the oceanic crust.....	120
4.7. Conclusions.....	127
Acknowledgements.....	129
References.....	129
<b>5. General Conclusions and Implications .....</b>	<b>137</b>
References.....	139
<b>Appendix.....</b>	<b>141</b>
<b>Declaration of consent.....</b>	<b>157</b>
<b>Curriculum Vitae .....</b>	<b>159</b>



# 1. Introduction

## 1.1. Thesis motivation

### 1.1.1. Understanding hydrothermal processes in oceanic crust

Hydrothermal circulation and rock–water interaction in the hot basaltic oceanic crust is widely known to be responsible for a range of important geochemical phenomena, including: hydration and mineralogical alteration of the entire upper crust, which has consequences for element cycling where the crust is later consumed in subduction zones; chemical buffering of the world's oceans throughout geological time; formation of valuable Cu–Zn–Au massive-sulphide ore deposits via black-smoker activity at seafloor vents, formation of valuable stratiform Mn-oxide deposit at distal sites from hydrothermal vents; and creation of an environment around seafloor vents in which specialised biological organisms have evolved and in which life on earth may have begun (e.g. , 2014; Humphris & Klein, 2018).

All the above processes are extremely complex, involving thermal–hydraulic–chemical coupling and feedbacks that are difficult to quantify and evaluate. Observations and measurements of seafloor hydrothermal processes are possible along modern mid-ocean ridges (MOR), and insight into the subsurface is gained by drilling, by geophysical surveys, by examining the geological record exposed in ophiolites and by conducting experiments at hydrothermal conditions. However, the only tool available so far to assess the physicochemical coupling is numerical simulation (e.g., Lowell et al. (2008), which relies on realistic crustal-scale parameters for calibration.

A particularly important calibration parameter for numerical simulations is *permeability*, which via Darcy's Law controls the paths and rates of hydrothermal circulation through the oceanic crust (e.g., Alt-Epping & Diamond, 2008 and references therein). In 3D form, Darcy's Law can be written as:

$$q = \frac{-k}{\mu} \nabla(P - pgz) \quad (1)$$

where  $q$  is the volumetric fluid flow rate ( $\text{m}^3/\text{s}/\text{m}^2 = \text{m/s}$ ),  $\nabla P$  (Pa/m) is the gradient in pressure along the spatial axes  $x$ ,  $y$  and  $z$ ,  $\mu$  is the dynamic viscosity ( $\text{Pa}\cdot\text{s}$ ),  $k$  is the intrinsic permeability tensor ( $\text{m}^2$ ),  $p$  is the fluid density ( $\text{kg}\cdot\text{m}^{-3}$ ),  $g$  is the gravity vector ( $\text{m}\cdot\text{s}^{-2}$ ) and  $z$  is vertical depth (m). Permeability thus expresses the ease with which a fluid can pass through a porous and/or fractured rock medium, and Darcy's Law serves as its definition. Although permeability is often treated as a constant, in fact it evolves in response to changes in mineralogy and pore connectivity induced by hydrothermal reactions, and to changes in fracture apertures induced by deformation or heating/cooling or mineral precipitation or dissolution. Equation (1) shows that permeability is the only term in Darcy's Law which depends on the properties of the rock medium, underscoring the importance of having reliable estimates for numerical simulations. The research reported in this thesis focuses on improving our understanding of permeability in the hydrothermally altered, basaltic oceanic crust.

Available permeability values for the upper crust show large ranges at different scales: *in-situ* hydraulic tests have measured permeabilities of  $\sim 10^{-18}$  to  $10^{-13}$  m<sup>2</sup> (Anderson et al., 1985; Becker, 1989; Becker & Fisher, 2000; Fisher, 1998), rock-matrix values are generally lower  $\sim 10^{-21}$  to  $10^{-14}$  m<sup>2</sup> (Christensen and Ramanantoandro, 1988; Einaudi et al., 2000; Gilbert and Bona, 2016; Gilbert and Salisbury, 2011; Gillis and Sapp, 1997; Hamano, 1980; Jarrard et al., 2003; Johnson, 1980a; Pezard, 1990) and models of fracture permeability are higher  $\sim 10^{-12}$  to  $10^{-6}$  m<sup>2</sup> (Nehlig, 1994; van Everdingen, 1995; Johnson, 1980b). Moreover, upper crustal porosity and permeability are consistently viewed as heterogenous at all scales and therefore complex to understand and constrain. This complexity evokes many questions: Which methodology can yield robust porosity and permeability estimates for both outcrop and crustal scales? Is the permeability of extrusive lavas influenced by *in-situ* temperatures and pressures? What controls upper crustal permeability, e.g., lava types and/or intensity of alteration? How is permeability distributed between the rock-matrix and fractures? How is permeability distributed at a regional scale? Does the real bulk permeability coincide with the  $10^{-16}$  to  $10^{-11}$  m<sup>2</sup> range that previous numerical models (Fisher, 1998 and references therein; Hasenclever et al., 2014) require to reproduce measured fluid and heat discharge from the seafloor? Therein lies the motivation and significance of this thesis: to provide answers to the above questions to clarify and improve our understanding of porosity and permeability and their role in fluid circulation through the upper oceanic crust.

### *1.1.2. Research context regarding genesis of massive-sulphide deposits in Oman*

In 2010 Professor Larry Diamond launched a research project at the Institute of Geological Sciences, University of Bern, entitled "Genesis of massive-sulphide deposits in Oman". Funded by the Swiss National Science Foundation, it aims to expand the current understanding of how volcanogenic massive sulphide (VMS) deposits form on the seafloor and how this understanding can be applied to aid exploration for such deposits. Field work was focused on the Semail ophiolite (Oman–UAE), owing to its well-preserved exposures of mafic oceanic crust. Within this context four PhD thesis projects (Belgrano, 2019; Gilgen, 2016; Richter 2020; Weber, 2020) and numerous Master projects have investigated the geological setting and large-scale rock–water interaction that has generated more than 20 major VMS deposits in the ophiolite.

The PhD project of Gilgen (2016) commenced this research by investigation of VMS metal affinities associated with axial and post-axial volcanic units in the Semail ophiolite, and the temporal and spatial relationship between high temperature *epidosite* alteration (rocks metasomatised to epidote + quartz + Fe-Ti-oxides) and VMS formation in the upper crust. As epidiosites are viewed as markers of upwelling hydrothermal fluids and potential sources of VMS metals (Richardson, 1987; Jowitt et al., 2012; Patten et al., 2016), syntheses of alteration of the crust (e.g. Alt, 1995) imply that every VMS deposit should be underlain by a zone of epidiosite in its deep footwall. Whether this relationship exists and whether it could be useful in VMS exploration was the motivation for the second part of Gilgen's project. In this context Gilgen (2016) found an intriguing result based on bulk rock analyses and



stoichiometric calculations: the metasomatic transformation of *spilite* (chlorite-albite altered basalts) to epidosite by  $\text{Ca}^+$ -rich hydrothermal fluids, increases lava porosity by ~10 vol.%. Given that porosity and permeability are usually correlated, this suggested that the spilite-to-epidosite reaction may enhance permeability, promoting self-propagation of porous medium-type hydrothermal flow through the lava matrix. These results corroborated previous work by Harper (1988), who had theorised a ~10 vol.% porosity increase, and by Cann et al., (2014), who had proposed self-propagating fluid pathways based on thin-section observations. The present thesis project was first inspired by these findings and it set out to quantify and expand our understanding of the extreme enhancement of porosity and permeability caused by the spilite-to-epidosite reaction (Chapter 3).

This thesis complements and builds on other aspects of epidosite alteration from previous PhD research within the “Genesis of massive-sulphide deposits in Oman” project. In addition to the research of Gilgen (2016), two other projects investigated epidosites and their formation fluids from the following perspectives: (1) the geochemical evolution of epidosites along fluid upwelling paths based on numerical reactive-transport simulations (Weber, 2020), and (2) the fluid chemistry, metal leaching and metal transport of epidotising fluids based on fluid inclusion analyses (Richter, 2020). The study by Richter (2020) showed that epidotising fluids contain low metal concentrations and do not match seafloor vent-fluids that form VMS deposits. Instead, the chloritising and albitising spilite fluids are much better VMS forming candidates. Despite this deviation from the prevailing model that links epidosites to VMS deposits (e.g. Richardson et al., 1987; Jowitt et al., 2012; Patten et al., 2016), the numerous epidosites throughout the Semail ophiolite upper crust are still undoubtedly anomalous kilometre-scale alteration zones (Gilgen et al., 2016) and markers of extreme water–rock ratios induced by upwelling fluids (Weber, 2020), for which the significance to hydrothermal circulation in the upper crust remains unclear. This thesis built on the project of Gilgen (2020) by addressing the mechanism for pervasive epidosite formation and extensive rock-matrix alteration by examining the reaction-enhanced permeability. Also, it provided pairs of spilite and epidosite samples and their associated porosities and permeabilities, to calibrate the reactive-transport simulations for the project of Weber (2020). With a basis in the investigation of spilite and epidosite porosities and permeabilities, this project evolved to address some of the long-standing questions regarding the complexities of porosity and permeability in the upper oceanic crust, from the thin-section to regional scale.

## **1.2. Thesis Outline and Aims**

The thesis is composed of five chapters that address the gaps in how we understand and quantify the permeability architecture of the upper oceanic crust. Following this Introduction, Chapters 2–4 present three journal articles in preparation or under revision for re-submission, the aims of which are summarised below. Chapter 5 ties together the main conclusions and consequences of this thesis for understanding hydrothermal processes in the oceanic crust.

In Chapter 2 we deal with the question of whether permeabilities measured at room conditions are valid for the *in-situ* pressures and temperatures at which hydrothermal alteration occurs. We report the results of experiments using a Paterson permeability apparatus in which spilites and epidiosites were subjected to temperatures of 25–450 °C at effective pressures of 50 MPa. We also report room temperature measurements of permeability over the pressure range of 5–55 MPa. The resulting temperature-permeability and pressure-permeability relationships can be used to correct routine room-temperature measurements to the required *in-situ*  $P$ – $T$  conditions.

Chapter 3 provides a comprehensive dataset of rock-matrix porosities and permeabilities of spilites and epidiosites. This includes measurements of the different components of a pillow lava stack (i.e. pillow rims, pillow cores and interpillow hyaloclastites), as well samples of massive lava flows and dykes. Additionally, we use this dataset to help explain outcrop alteration patterns and the difference between rock-matrix permeabilities and those from *in-situ* hydraulic tests in modern oceanic crust. Moreover, we quantify the reaction permeability produced during epidosite alteration and consequently discover how epidotising fluids infiltrate the rock-matrix with high water–rock ratios and form km<sup>3</sup>-size epidosite bodies in the absence of significant fracture permeability.

Finally, in Chapter 4 we quantify the field-scale magnitudes and distribution of rock-matrix and fracture permeability in lava sequences altered to spilitic and epidosite. In the literature the extrusive volcanic crust is broadly treated as a fractured aquifer but the contributions from rock-matrix permeability and fracture permeability to the bulk permeability of this crustal layer remain ambiguous. We therefore mapped two types of field situation in the Semail ophiolite: firstly, the kilometre wide “*distal*” zones of lavas that lie between extensional faults, and secondly the damage zones around the extensional faults. Based on the results we have upscaled and combined rock-matrix and fracture distributions to estimate a value of bulk permeability in distal and damage zones using flow simulations with the computer code *dfnWorks*. These simulations reveal whether distal lava zones are controlled by rock-matrix or fracture-network permeability and they provide a model and value for bulk permeability (combining rock-matrix and fracture permeabilities) that can be used to calibrate crustal-scale numerical simulations.

### 1.3. Geological Setting and Study Site

Three months of field mapping and sampling for this project were conducted over 4 field seasons in the Semail ophiolite, Oman. In addition, a one-week visit was made to the epidiosites in the Troodos Ophiolite, Cyprus, to compare and contrast its outcrops and literature with the Semail case.

The Semail ophiolite is a complete slice of oceanic lithosphere from mantle to seafloor sediments that formed in a proto-arc, supra-subduction zone setting at 97–93 Ma (Belgrano & Diamond, 2019; Guilmette et al., 2018; MacLeod et al., 2013; Pearce et al., 1984). Magmatism associated with fast spreading axial ridge above the nascent subduction zone formed the MORB-like sheeted dyke complex (SDC) and the comagmatic basaltic Geotimes lava unit (also known as V1; Fig. 1.1). These axial units were overlain by primitive, off-axis Lasail lavas and in turn buried by post-spreading lavas of the Tholeiitic Alley and Boninitic Alley units, which show an increasing signature of fluid input from the subduction zone (these units are also known collectively as V2; Fig. 1.1; Belgrano & Diamond, 2019). The trace-element and water contents of the axial units demonstrate their supra-subduction zone setting (Belgrano & Diamond, 2019 and references therein; Guilmette et al., 2018; MacLeod et al., 2013), hence they differ in these respects from typical MORB formed at mid-oceanic ridges far from the influence of subduction zones. However, in other essential respects, including structural, igneous and hydrothermal features, the Semail axial sequence is a well-recognised analogue of modern, fast-spreading mid-oceanic ridges. Thus, the insights it provides into the permeability architecture of the upper oceanic crust are likely to be directly applicable to modern MOR crust (e.g., Einaudi et al., 2000; Nehlig, 1995).

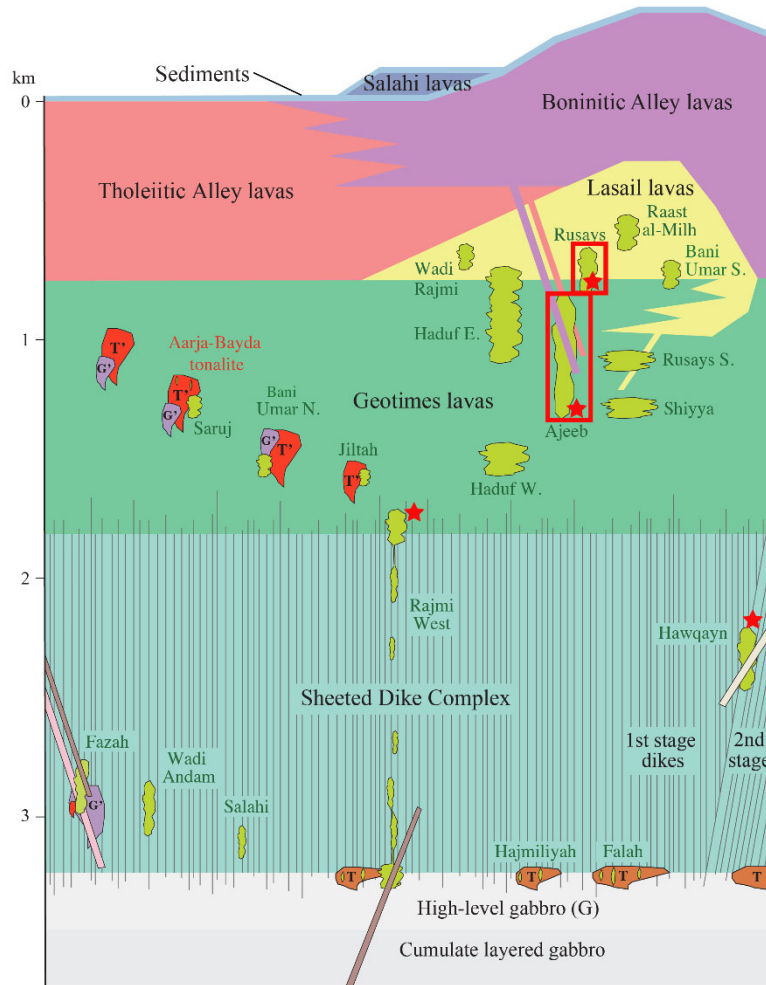


**Figure 1.1.** Stratigraphy of the upper crust of the Semail ophiolite, modified after Gilgen et al. (2016) and Belgrano et al. (2019). Epidosites identified by Gilgen et al. (2016) are highlighted in green with labelled locations. Key epidosite sampling locations for Chapter 3 are indicated with red stars and mapping areas to characterise fracture networks for Chapter 4 are shown in red boxes. Field work focused on the Sheeted Dyke Complex and the comagmatic axial Geotimes lavas, but at the Rusays epidosite, fracture-mapping overlapped into the Lasail lavas as discussed in Chapter 4. T' = High level tonalite, G' = High level gabbro, T = tonalite. Volcanic unit colours correspond to legend in Fig. 1.2.

The stunningly well exposed, ~500 km long section of obliquely dipping (~30°) upper crust is excellently preserved and easily accessible (Fig. 1.2). This makes it an ideal location to study lava morphologies, syn-magmatic structures, hydrothermal alteration patterns and Cyprus-type VMS deposits, all typical of the Cretaceous and Archean ophiolites and often seen at mid-oceanic ridges, such as the East Pacific Rise (Kusano et al., 2014; Nicolas et al., 2000). Obduction-related overprinting of syn-magmatic features is relatively rare, with the exception of the regional thrusts and normal faults that segmented the ophiolite into 10 main massifs along its length (MacLeod and Rothery, 1992; Nicolas et al., 2000; Searle and Cox, 1999). Although this process may have reactivated syn-magmatic faults, it caused minimal deformation within blocks, manifested by easily recognised block-faulting. In some areas quartz–hematite–pyrite veins and later calcite veins overprint and crosscut the magmatic rocks

and their main pervasive hydrothermal alteration. These features have been attributed to post-volcanic, presumably syn-obduction processes (Gilgen et al., 2014; Richter & Diamond, submitted).

Regionally, the SDC and all lava units are pervasively hydrothermally altered to three main assemblages from sub- to greenschist-facies conditions (~200–450 °C; Alabaster & Pearce, 1985). The SDC at depth is composed of basaltic dykes variably altered to "spilite"-type actinolite–chlorite–albite assemblages that grade upwards into intense chlorite–albite spilites in the Geotimes and Lasail lavas, and into low temperature, zeolite–celadonite–smectite ± chlorite–albite alteration in the overlying Tholeiitic Alley and Boninitic Alley lavas (Alabaster et al., 1982; Alabaster & Pearce, 1985; Cann, 1969). Spilite and low temperature alteration formed by downwelling of seawater that enriched the basalts in Mg and Na, while removing Ca (e.g., Alt, 1995). The third main type of alteration, "epidosite", occurred in more localised zones by upwelling of 230–420 °C, Ca-rich fluids, that metasomatically replaced spilites with an assemblage of epidote + quartz + titanite + Fe-Ti-oxide (Richardson et al., 1987; Schiffman and Smith, 1988; Coelho et al., 2015; Richter & Diamond, 2019; Seyfried et al., 1988; Weber et al., submitted). Spilites are common in Archean to Cretaceous ophiolites and in the sheeted dyke complexes of *in-situ* oceanic crust, but lower temperature alteration (clay–zeolite) dominates *in-situ* MOR lavas (Alabaster & Pearce, 1985; Staudigel, 2014). Epidosites have been rarely found in *in-situ* oceanic crust (Quon & Ehlers, 1963; Banerjee et al., 2000) but they are common in ophiolites (Coelho et al., 2015; Galley et al., 1993; Gilgen et al., 2014; Gillis & Banerjee, 2000; Hannington et al., 2003). Epidosites have been suggested as the source rocks for VMS deposits (e.g., Richardson et al., 1987; Hannington, 2014; Jowitt et al., 2012; Patten et al., 2016) and are evidence of extreme water–rock ratios (e.g., Mottl & Wheat, 1994; Bach et al., 2003; Weber et al., submitted). However, recent work by Richter & Diamond (submitted) has updated this model to show that spilite alteration and the resulting fluid is richer in metals and a better candidate to form VMS deposits than the fluids that generate epidosites.

In addition to the extensive literature on hydrothermal alteration in the Semail ophiolite, some previous studies have described rock-matrix porosity of the pillow lavas (Christensen & Smewing, 1981; Einaudi et al., 2000) and fracture permeability in the SDC (Nehlig, 1994). Einaudi et al. (2000) found that rock-matrix porosities of low temperature altered pillows from a 270 m transect through Wadi Shaffan vary from 0.5–10.8 vol.%, the lower values being due to high quartz content in the deeper part of the section. Using P-wave velocity measurements, Christensen & Smewing (1981) found porosities of ~3–7 vol.% in low temperature and spilitised pillows and ~1–4 vol.% in dykes. Fracture permeabilities were studied by Nehlig (1994) at five locations, Bayda-Arja, Hayl, Mahab, Haymiliyah, and Daris, focusing on the gabbros and SDC. They found that fracture densities of quartz–epidote–sulphide veins increased from 0.01 m<sup>-1</sup> in the gabbros to 0.5 m<sup>-1</sup> in the SDC, and based on mapped fracture spacing and apertures they calculated fracture permeabilities between 10<sup>-12</sup> and 10<sup>-11</sup> m<sup>2</sup>. These studies provide initial observations of porosity and permeability in the upper crust but the systematics and controlling factors for rock-matrix values in dykes, massive lava flows, pillow cores, pillow rims

and interpillow hyaloclastites are lacking, and fracture distributions and fracture permeability in the extrusive lavas have not yet been addressed. The hydrothermal alteration and permeable pathways preserved in the Semail ophiolite that are critical for VMS formation and heat and chemical cycling, make this an excellent site to document the complexities and variations in rock-matrix permeability and fracture permeability. Some of the important sampled and mapped areas in the axial SDC and Geotimes lavas are shown in Figures 1.1 and 1.2.

---

9

## References

- Aksyuk, A.M., Vitovtova, V.M., Pustovoy, A.A., Kharin, G.S., Shmonov, V.M., 1992. The permeability of oceanic basalts and some questions of the formation of hydrothermal springs in the rift zone of the Atlantic Ocean. *Oceanol. Engl. Transl.* 32, 1115–1122.
- Alabaster, T., Pearce, J.A., & Malpas, J., 1982. The volcanic stratigraphy and petrogenesis of the Oman ophiolite complex. *Contrib. Mineral. Petr.* 81, 168–183.  
<https://doi.org/10.1007/BF00371294>.
- Alabaster, T., Pearce, J., 1985. The Interrelationship between Magmatic and Ore-Forming Hydrothermal Processes in the Oman Ophiolite. *Econ. Geol.* 80, 1–16.  
<https://doi.org/10.2113/gsecongeo.80.1.1>.
- Alt, J.C., 1995. Subseafloor processes in mid-ocean ridge hydrothermal systems. *Geophysical Monograph* 91, 85–114. <https://doi.org/10.1029/GM091p0085>.
- Alt-Epping, P., Diamond, L.W., 2008. Reactive transport and numerical modeling of seafloor hydrothermal systems: a review. In: Lowell, R.P., Seewald, J.S., Metaxas, A., Perfit, M.R. (Eds.), *Magma to Microbe: Modeling Hydrothermal Processes at Oceanic Spreading Centers*. American Geophysical Union, Washington, D.C., pp. 167–192.
- Anderson, R.N., Zoback, D.M., Hickman, S.H., Newmark, R.L., 1985. Permeability Versus Depth in the Upper Oceanic Crust: In Situ Measurements in DSDP Hole 504B, Eastern Equatorial Pacific. *J. Geophys. Res.* 90, 3659–3669. <https://doi.org/10.1029/JB090iB05p03659>.
- Bach, W., Peucker-Ehrenbrink, B., Hart, S.R., Blusztajn, J.S., 2003. Geochemistry of hydrothermally altered oceanic crust: DSDP/ODP Hole 504B - Implications for seawater-crust exchange budgets and Sr- and Pb-isotopic evolution of the mantle. *Geochem. Geophys. Geosyst.* 4, 1–29.  
<https://doi.org/10.1007/s00269-010-0415-y>.
- Becker, K., 1989. Measurements of the permeability of the sheeted dikes in Hole 504B, ODP Leg 111. *Proc. ODP, Sci. Results* 111, 317–325. <https://doi.org/10.2973/odp.proc.sr.111.156.1989>.
- Becker, K., Fisher, A.T., 2000. Permeability of upper oceanic basement on the eastern flank of the Endeavor Ridge determined with drill-string packer experiments. *J. Geophys. Res.* 105, 897–912. <https://doi.org/10.1029/1999JB900250>.
- Banerjee, N.R., Gillis, K.M., Muehlenbachs, K., 2000. Discovery of epidiosites in a modern oceanic setting, the Tonga forearc. *Geology* 28, 151–154.
- Belgrano, T.M., 2019. Map distribution, tectonic setting and hydrothermal alteration of the volcanic sequence of the northern Semail ophiolite, Oman. PhD Thesis, Bern, Switzerland.



- Belgrano, T.M., Diamond L.W., 2019. Subduction-zone contributions to axial volcanism in the Oman-U.A.E. ophiolite. *Lithosphere* 11, 399–411. <https://doi.org/10.1130/L1045.1>.
- Cann, J.R., 1969. Spilites from the Carlsberg Ridge, Indian Ocean. *J. Petrol.* 10, 1–19. <https://doi.org/10.1093/petrology/10.1.1>.
- Cann, J.R. McCaig, A.M., Yardley, B.W.D., 2014. Rapid generation of reaction permeability in the roots of black smoker systems, Troodos ophiolite, Cyprus. *Geofluids* 15, 179–192. <https://doi.org/10.1111/gfl.12117>.
- Christensen, N.I., Smewing, J.D., 1981. Geology and seismic structure of the northern section of the Oman ophiolite. *J. Geophys. Res. Solid Earth* 86, 2545–2555. <https://doi.org/10.1029/JB086iB04p02545>.
- Christensen, N.I., Ramananantoandro, R., 1988. Permeability of the oceanic crust based on experimental studies of basalt permeability at elevated pressures. *Tectonophysics* 149, 181–186. [https://doi.org/10.1016/0040-1951\(88\)90126-6](https://doi.org/10.1016/0040-1951(88)90126-6).
- Coelho, G., Branquet, Y., Sizaret, S., Arbaret, L., Champallier, R., Rozenbaum, O., 2015. Permeability of sheeted dykes beneath oceanic ridges: Strain experiments coupled with 3D numerical modeling of the Troodos Ophiolite, Cyprus. *Tectonophysics* 644, 138–150. <https://doi.org/10.1016/j.tecto.2015.01.004>.
- Einaudi, F., Pezard, P. A., Cochemé, J.-J., Coulon, C., Laverne, C., Godard, M., 2000. Petrography, geochemistry and physical properties of a continuous extrusive section from the Sarami Massif, Semail ophiolite. *Mar. Geophys. Res.* 21, 387–407.
- Fisher, A.T., 1998. Permeability within basaltic ocean crust. *Reviews of Geophysics* 36, 143–182. <https://doi.org/10.1029/97RG02916>.
- Gilbert, L.A., Bona, M.L., 2016. Permeability of oceanic crustal rock samples from IODP Hole 1256D. *Geochem. Geophys. Geosyst.* 17, 3825–3832. <https://doi.org/10.1002/2016GC006467>.
- Gilbert, L.A., Salisbury, M.H., 2011. Oceanic crustal velocities from laboratory and logging measurements of Integrated Ocean Drilling Program Hole 1256D. *Geochem. Geophys. Geosyst.* 12, Q09001. <https://doi.org/10.1029/2011GC003750>.
- Gilgen, S.A., Diamond, L.W., Mercolli, I., Al-Tobi, K., Maidment, D.W., Close, R., Al-Towaya, A., 2014. Volcanostratigraphic controls on the occurrence of massive sulfide deposits in the Semail Ophiolite, Oman. *Economic Geology* 109, 1585–1610. <https://doi.org/10.2113/econgeo.109.6.1585>.
-

- Gilgen, S.A., Diamond, L.W., Mercolli, I., 2016. Sub-seafloor epidosite alteration: Timing, depth and stratigraphic distribution in the Semail Ophiolite, Oman. *Lithos* 260, 191–210. <https://doi.org/10.1016/j.lithos.2016.05.014>.
- Gillis, K.M., Sapp, K., 1997. Distribution of porosity in a section of upper oceanic crust exposed in the Troodos Ophiolite. *J. Geophys. Res.* 102, 10133–10149. <https://doi.org/10.1029/96JB03909>.
- Gillis, K.M., Banerjee, N.R., 2000. Hydrothermal alteration patterns in supra-subduction zone ophiolites. *Geol. Soc. Am. Spec.* 349, 283–298. <https://doi.org/10.1130/0-8137-2349-3.283>.
- Guilmette, C., Smit, M.A., van Hinsbergen, D.J.J., Gürer, D., Corfu, F., Charette, B., Maffione, M., Rabeau, O., Savard, D., 2018. Forced subduction initiation recorded in the sole and crust of the Semail Ophiolite of Oman. *Nat. Geosciences* 11, 688–695. <https://doi.org/10.1038/s41561-018-0209-2>.
- Hamano, Y., 1980. Physical properties of basalts from Holes 417D and 418A. Initial Rep. Deep Sea Drill. Proj. 51, 52, 53, 1457–1466. <https://doi.org/10.2973/dsdp.proc.515253.166.1980>.
- Hannington, M.D., Santaguida, F., Kjarsgaard, I.M., Cathles, L.M., 2003. Regional-scale hydrothermal alteration in the Central Blake River Group, western Abitibi subprovince, Canada: Implications for VMS prospectivity. *Miner. Deposita* 38, 393–422. <https://doi.org/10.1007/s00126-002-0298-z>.
- Harper, G. D., Bowman, J. R., & Kuhns, R., 1988. A field, chemical, and stable isotope study of subseafloor metamorphism of the Josephine Ophiolite, California-Oregon. *J. Geophys. Res.* 93, 4625–4656. <https://doi.org/10.1029/jb093ib05p04625>.
- Hasenclever, J., Theissen-Krah, S., Rüpke, L.H., Morgan, J.P., Iyer, K., Petersen, S., Devey, C.W., 2014. Hybrid shallow on-axis and deep off-axis hydrothermal circulation at fast-spreading ridges. *Nature* 508, 508–512. <https://doi.org/10.1038/nature13174>.
- Heap, M.J.J., Reuschlé, T., Farquharson, J.I.I., Baud, P., 2018. Permeability of volcanic rocks to gas and water. *J. Volcanol. Geotherm. Res.* 354, 29–38. <https://doi.org/10.1016/j.jvolgeores.2018.02.002>.
- Humphris, S.E., Klein, F., 2018. Progress in Deciphering the Controls on the Geochemistry of Fluids in Seafloor Hydrothermal Systems. *Annual Review of Marine Science* 10, 315–343.
- Hyman, J.D., Karra, S., Makedonska, N., Gable, C.W., Painter, S.L., Viswanathan, H.S., 2015. dfnWorks: A discrete fracture network framework for modeling subsurface flow and transport. *Comput. Geosci.* 84, 10–19. <https://doi.org/10.1016/j.cageo.2015.08.001>.
-

- Jarrard, R.D., Abrams, L.J., Pockalny, R., Larson, R.L., Hirono, T., 2003. Physical properties of upper oceanic crust: Ocean Drilling Program Hole 801C and the waning of hydrothermal circulation. *J. Geophys. Res. Solid Earth* 108, 1–26. <https://doi.org/10.1029/2001JB001727>.
- Johnson, D.M., 1980a. Fluid permeability of oceanic basalts. Initial Rep. Deep Sea Drill. Proj. 68, 1473–1477.
- Johnson, D.M., 1980b. Crack distribution in the upper crust and its effects upon seismic velocity, seismic structure, formation permeability and fluid circulation. Initial Rep. Deep Sea Drill. Proj. 51, 52, 53, 1457–1466. <https://doi.org/10.2973/DSDP.PROC.515253.169.1980>.
- Jowitt, S.M., Jenkin, G.R.T., Coogan, L.A., Naden, J., 2012. Quantifying the release of base metals from source rocks for volcanogenic massive sulfide deposits: Effects of protolith composition and alteration mineralogy. *J. Geochem. Explor.* 118, 47–59. <https://doi.org/10.1016/j.gexplo.2012.04.005>.
- Kusano, Y., Hayashi, M., Adachi, Y., Umino, S., Miyashita, S., 2014. Evolution of volcanism and magmatism during initial arc stage: Constraints on the tectonic setting of the Oman Ophiolite. In: Rollinson, H.R., Searle, M.P., Abbasi, I.A., Al-Lazki, A.I., Al Kindi, M.H. (Eds.), *Tectonic Evolution of the Oman Mountains*. Geol. Soc. London Spec. Pub. 392, 177 – 193. <https://doi.org/10.1144/SP392.9>.
- Kushnir, A.R.L., Martel, C., Champallier, R., Arbaret, L., 2017. In situ confirmation of permeability development in shearing bubble-bearing melts and implications for volcanic outgassing. *Earth Planet. Sci. Lett.* 458, 315–326. <https://doi.org/10.1016/j.epsl.2016.10.053>.
- Lowell, R.P., Seewald, J.S., 2008. *Magma to Microbe: Modeling Hydrothermal Processes at Oceanic Spreading Centers*. Washington D.C.
- MacLeod, C.J., Rothery, D.A., 1992. Ridge axial segmentation in the Oman ophiolite: Evidence from along-strike variations in the sheeted dyke complex. *Geol. Soc. London Spec. Pub.* 60, 39–63. <https://doi.org/10.1144/GSL.SP.1992.060.01.03>.
- MacLeod, C.J., Lissenberg, J.C., Bibby, L.E., 2013. “Moist MORB” axial magmatism in the Oman ophiolite: The evidence against a mid-ocean ridge origin. *Geology* 41, 459–462. <https://doi.org/10.1130/G33904.1>.
- Mottl, M.J., Wheat, G.C., 1994. Hydrothermal circulation through mid-ocean ridge flanks: Fluxes of heat and magnesium. *Geochim. Cosmochim. Acta* 58, 2225–2237. [https://doi.org/10.1016/0016-7037\(94\)90007-8](https://doi.org/10.1016/0016-7037(94)90007-8).
-

- Mordensky, S.P., Kennedy, B.M., Villeneuve, M.C., Lavallée, Y., Reichow, M.K., Wallace, P.A., 2019. Increasing the Permeability of Hydrothermally Altered Andesite by Transitory Heating. *Geochem. Geophys. Geosyst.* 20, 5251–5269. <https://doi.org/10.1029/2019GC008409>.
- Nehlig, P., Juteau, T., Bendel, V., Cotten, J., 1994. The root zones of oceanic hydrothermal systems: Constraints from the Samail ophiolite (Oman). *J. Geophys. Res.* 99, 4703–4713. <https://doi.org/10.1029/93JB02663>.
- Nicolas, A., Boudier, F., Ildefonse, B., Ball, E., 2000. Accretion of Oman and United Arab Emirates ophiolite – Discussion of a new structural map. *Mar. Geophys. Res.* 21, 147–180. <https://doi.org/10.1023/A:1026769727917>.
- Pezard, P. A., 1990. Electrical properties of mid-oceanic ridge basalt and implication for the structure of the upper oceanic crust in Hole 504B. *J. Geophys. Res.* 95, 9237–9264. <https://doi.org/10.1029/JB095iB06p09237>.
- Patten, C.G.C., Pitcairn, I.K., Teagle, D.A.H., Harris, M., 2016. Sulphide mineral evolution and metal mobility during alteration of the oceanic crust: Insights from ODP Hole 1256D. *Geochim. Cosmochim. Acta* 193, 132–159. <https://doi.org/10.1016/j.gca.2016.08.009>.
- Pearce, J.A., Lippard, S.J., Roberts, S., 1984. Characteristics and tectonic significance of supra-subduction zone ophiolites. In: Kokelaar, B.P., Howells, M.F. (Eds.), *Marginal Basins Geology: Volcanic and Associated Sedimentary and Tectonic Processes in Modern and Ancient Marginal Basins*. *Geol. Soc. London Spec. Pub.* 16, 77 – 94. <https://doi.org/10.1144/GSL.SP.1984.016.01.06>.
- Quon, S.H., Ehlers, E.G., 1963. Rocks of the northern part of the Mid-Atlantic Ridge. *Geol. Soc. Am. Bull.* 74, 1-8. [https://doi.org/10.1130/0016-7606\(1963\)74\[1:RONPOM\]2.0.CO;2](https://doi.org/10.1130/0016-7606(1963)74[1:RONPOM]2.0.CO;2).
- Richardson, C.J., Cann, J.R., Richards, H.G., Cowan, J.G., Siegel, J., 1987. Metal-depleted root zones of the Troodos ore-forming hydrothermal systems, Cyprus. *Earth Planet. Sci. Lett.* 84, 243–253. [https://doi.org/10.1016/0012-821x\(87\)90089-6](https://doi.org/10.1016/0012-821x(87)90089-6).
- Richter, L., 2020. Hydrothermal fluids in the oceanic crust and the genesis of volcanogenic massive sulfide (VMS) deposits: A fluid inclusion study of the Semail ophiolite, Oman. PhD thesis, Bern, Switzerland.
- Richter, L., Diamond, L.W., submitted. Characterization of hydrothermal fluids that alter the upper oceanic crust to spilite and epidosite: Fluid inclusion evidence from the Semail (Oman) and Troodos (Cyprus) ophiolites. *Geochim. Cosmochim. Acta.*, in review.
-

- Schiffman, P., Smith, B.M., 1988. Petrology and oxygen isotope geochemistry of a fossil seawater hydrothermal system within the Solea Graben, Northern Troodos Ophiolite, Cyprus. *J. Geophys. Res. Solid Earth* 93, 4612–4624. <https://doi.org/10.1029/JB093iB05p04612>.
- Searle, M., Cox, J., 1999. Tectonic setting, origin, and obduction of the Oman ophiolite. *Geol. Soc. Am. Bull.* 111, 104–122. [https://doi.org/10.1130/0016-7606\(1999\)111<0104:TSAOO>2.3.CO;2](https://doi.org/10.1130/0016-7606(1999)111<0104:TSAOO>2.3.CO;2).
- Shmonov, V.M., Vitovtova, V.M., Zarubina, I.V., 1995. Permeability of rocks at elevated temperatures and pressures. In: Shmulovich, K.I., Yardley, B.W.D., Gonchar, G.G. (Eds.), *Fluids in the Crust: Equilibrium and Transport Properties*. Springer, Netherlands, Dordrecht, pp. 285–313. [https://doi.org/10.1007/978-94-011-1226-0\\_11](https://doi.org/10.1007/978-94-011-1226-0_11).
- Staudigel, H., 2014. Chemical Fluxes from Hydrothermal Alteration of the Oceanic Crust. In: Holland, H.D., Turekian, K.K. (Eds.), *Treatise on Geochemistry* 2nd edition. vol. 4. Elsevier, Oxford, pp. 583–603. <http://doi.org/10.1016/B978-0-08-095975-7.00318-1>.
- Sweeney, M.R., Gable, C.W., Karra, S., Stauffer, P.H., Pawar, R.J., Hyman, J.D., 2019. Upscaled discrete fracture matrix model (UDFM): An octree-refined continuum representation of fractured porous media. *Comput. Geosci.* 24, 293–310. <https://doi.org/10.1007/s10596-019-09921-9>.
- van Everdingen, D.A., 1995. Fracture characteristics of the Sheeted Dike Complex, Troodos ophiolite, Cyprus: Implications for permeability of oceanic crust. *J. Geophys. Res.* 100, 19957–19972. <https://doi.org/10.1029/95JB01575>.
- Weber, S., 2020. Hydrothermal epidosite and pumpellyosite alteration in oceanic crust, Semail ophiolite, Oman: A combined field, petrographic, geochemical and numerical modelling study. PhD thesis, Bern, Switzerland.
- Weber, S., Diamond, L.W., Alt-Epping, P., Brett-Adams, A.C., submitted. Reaction mechanism and water/rock ratios involved in epidosite alteration of the oceanic crust. *J. Geophys. Res. Solid Earth*, in review.



## 2. Influence of in-situ temperatures and pressures on the permeability of hydrothermally altered basalts in the oceanic crust

Alannah C. Brett-Adams<sup>a,\*</sup>, Larryn W. Diamond<sup>a</sup>, Claudio Petrini<sup>b,1</sup>, Claudio Madonna<sup>b</sup>

<sup>a</sup>Institute of Geological Sciences, University of Bern, Baltzerstrasse 1+3, 3012, Switzerland

<sup>b</sup>Rock Physics and Mechanics Laboratory, ETH Zurich, Switzerland

In revision for resubmission in *Tectonophysics*.

*Author contributions:* Alannah Brett carried out experiments on a Paterson permeability apparatus at ETH-Zurich, calculated permeabilities and prepared the manuscript. Larryn Diamond, as thesis supervisor, guided the research and edited the manuscript. Claudio Petrini and Claudio Madonna supervised the experiments and provided the data-reduction code and guidance to calculate the permeability results.

### Abstract

Hydrothermal circulation through the oceanic crust, and all the transfers of mass and heat caused by this circulation, are controlled by the evolving permeability of the altered basaltic rocks at in-situ pressures ( $P$ ) and temperatures ( $T$ ). Numerical models designed to elucidate these processes therefore rely on knowledge of the rock-matrix permeabilities as a function of  $P$  and  $T$  and degree of hydrothermal alteration. We provide the first measurements of changes in permeability of two major types of high-temperature alteration of basalts, i.e., spilites and epidiosites, over the  $P$ – $T$  range relevant to hydrothermally active oceanic crust. Experiments were performed on microcrack-free samples of pervasively altered pillow lavas and sheeted dykes from the Semail (Oman) and Troodos (Cyprus) ophiolites. Gas permeameter measurements at room temperature show that compression to ~55 MPa effective pressure reduces the permeabilities of spilites and epidiosites by up to ~80% and 70%, respectively. Measurements at 50 MPa effective pressure using an oscillating flow apparatus show that heating spilites and epidiosites from 25 to 450 °C reduces their permeabilities by ~40% and 50%, respectively. However, duplicate measurements on cores drilled from the same hand samples reveal that all these effects are outweighed by the natural heterogeneity of permeability in spilites and epidiosites at the centimetre scale. It follows that the temperature effect on permeability can be ignored in numerical simulations of hydrothermal flow without incurring large errors. Nonetheless, our study provides quantitative temperature–permeability correlations to predict the temperature effect for spilites and epidiosites. The excellent reversibility of our heating experiments allows us to speculate on the mechanism of the permeability changes. We suggest that thermoelastic expansion of the mineral grains surrounding pores in the spilites and epidiosites reversibly seals off a fraction of the pore throats during heating, and that these throats progressively open again during cooling.

## 2.1. Introduction

Quantitative understanding of how seawater infiltrates the magmatically active oceanic crust and develops hydrothermal circulation cells requires knowledge of the permeability of the basaltic rock-matrix and the fracture networks (Fisher, 1998; Hasenclever et al., 2014). Previous laboratory measurements of permeability have been performed on oceanic basalt samples that are fresh or that show weak, low-temperature hydrothermal alteration to clay- and zeolite-bearing mineral assemblages (Gilbert and Bona, 2016; Jarrard et al., 2003; Johnson, 1980; Karato, 1983). These experiments have been complemented by in-situ hydraulic tests in seafloor drill holes and by fracture maps in ophiolites, in order to capture the combined effects of rock matrix and fracture permeability (Anderson et al., 1985; Becker and Fisher, 2000; Nehlig, 1994; van Everdingen, 1995). However, little is known about the permeability of basalts that have been hydrothermally altered at temperatures ( $T$ ) up to 450 °C at pressures ( $P$ ) of 30–70 MPa hydrostatic.

At such elevated  $P$ – $T$  conditions, basalts are transformed into two main assemblages of hydrothermal minerals. Along seawater downflow paths, assemblages of albite + chlorite  $\pm$  actinolite are stabilised, producing rocks that can be termed 'spilites' (e.g., Cann, 1969). In contrast, reactions along the upflow path can lead to partial or complete replacement of the spilite assemblage by epidote + quartz, producing rocks known as 'epidosites' (e.g., Richardson et al., 1987; Gilgen et al., 2016). Rock cores from the deepest drill holes in in-situ oceanic crust typically show only partial alteration to spilite, and epidotes are rare (e.g., Staudigel, 2014). In contrast, basalts altered to end-member spilites and epidotes are common in ophiolites and Archean greenstone belts (Alabaster and Pearce, 1985; Galley, 1993; Hannington et al., 2003; Gillis and Banerjee, 2000; Coehlo et al., 2015; Gilgen et al., 2014).

The water–rock interaction driving spilite and epidosite alteration has important consequences for mass and heat transfer between the crust and the oceans, including buffering of the chemical and isotopic composition of seawater (e.g., Mottl and Wheat, 1994; Bach et al., 2003). Leaching of base and precious metals during spilite or epidosite alteration may lead to formation of valuable massive sulphide ore deposits where the hydrothermal fluids discharge at the seafloor (e.g., Hannington, 2014; Jowitt et al., 2012; Patten et al., 2016). Progress in understanding these processes via numerical thermal–hydraulic–chemical modelling would be facilitated by knowing the permeability of the altered rocks along the high  $P$ – $T$  flow paths.

Samples of basalts that have undergone high temperature alteration are obtainable from drill holes in present-day oceanic crust and from outcrops in ophiolites. In both cases, the question arises as to what extent laboratory measurements of rock matrix permeability at room temperature and pressure are valid for the elevated in-situ temperatures and pressures at which the alteration occurred. Subjecting basalts to effective pressures up to 50 MPa at room temperature is known to reduce their permeability by up to half an order of magnitude (Christensen and Ramanantoandro, 1988; Gilbert and Bona, 2016; Karato, 1983). Experiments on the response of permeability to elevated temperatures have been



conducted on a few fresh basalts and weakly altered andesites (Aksyuk et al., 1992; Heap et al., 2018; Kushnir et al., 2017; Mordensky et al., 2019; Shmonov et al., 1995), but the results are in part contradictory, hindering recognition of clear temperature–permeability trends. To our knowledge no studies have tested the effect of increasing temperature on altered basalts.

As part of a wider investigation of the variation of permeability of the altered oceanic crust (to be published elsewhere) the present study focuses on how changes in pressure and temperature affect the permeability of spilite and epidosite samples from the pillow lavas and sheeted dyke complexes of the Semail and Troodos ophiolites, which experienced temperatures of 170–450 °C (Richter and Diamond, 2019). We first report room temperature experiments carried out over a range of pressures using an unsteady-state gas permeameter. We then present isobaric permeability experiments at 50 MPa effective pressure over temperatures between 25 and 450 °C using the oscillating flow method in a Paterson triaxial gas apparatus (Paterson, 1970). The results allow us to derive empirical correlations between temperature and permeability, which permit standard permeability measurements performed at room temperature and in-situ pressure to be corrected to the in-situ, high  $P$ – $T$  conditions of hydrothermal circulation in the oceanic crust. Furthermore, the correlations are suitable for use in numerical simulations of hydrothermal flow. Although our experiments were not designed to elucidate the mechanisms of permeability changes at elevated  $P$ – $T$  conditions, our observations nevertheless provide some insights into these phenomena.

## **2.2. Materials and Methods**

### *2.2.1. Geological setting of sampled spilites and epidosites*

Our samples derive from the sheeted dyke complexes and comagmatic pillow lavas that formed during the spreading-axis stages of crustal growth in the Semail and Troodos ophiolites. We have sampled spilites and epidosites from these units to ensure relevance of our results to in-situ oceanic crust. However, unlike modern mid-ocean ridge settings, the axial basalt to basaltic-andesite volcanic rocks in the Semail and Troodos ophiolites are overlain by a 1–2 km thick sequence of off-axis to post-axis primitive basalts, island-arc tholeiitic lavas and boninitic lavas (Belgrano et al., 2019; Osozawa et al., 2012). Owing to this additional overburden and its thermal insulation effect, the pressures and temperatures of hydrothermal alteration in the axial lavas and sheeted dykes may have been higher than those in in-situ crust. Whereas volcanic glass is commonly preserved in the altered Troodos lavas (Gillis and Robinson, 1990), hydrothermal alteration of the Semail lavas is stronger and glass is extremely rare (Alabaster and Pearce, 1985; Kusano et al., 2017). In general, epidosites are known to form by replacing pre-existing spilites (e.g., Gilgen et al., 2016) and therefore partially epidotised spilites are common in both Troodos and Semail.

### 2.2.2. Sample material and selection

For our experiments we collected from the Semail ophiolite a pillow lava altered to spilite, a pillow lava altered to epidosite (both belonging to the axial Geotimes volcanostratigraphic unit; Belgrano et al., 2019) and two dykes altered to spilite within the comagmatic sheeted dyke complex. From the Troodos ophiolite we obtained a dyke sample partially altered to epidosite, which was collected from the axial sheeted dyke complex by Coehlo et al. (2015) and used for their Paterson piston-cylinder experiments (their runs PP332 and PP308). We drilled out two new cores from that sample for our experiments.

Fig. 2.1 shows textures and pore types of the samples used in this study. Pores in the spilitised pillow lava (Fig. 2.1A) are of three types: (1) very small ( $< 10\ \mu\text{m}$  diameter) interstitial pores at the grain boundaries of chlorite, albite and clinopyroxene, (2) sub-micrometre pores within chlorite (observable only at high magnification in SEM), and (3) macroscopically visible volcanic vesicles. The latter contribute to porosity only where their filling by hydrothermal chlorite or quartz is incomplete. The spilitised dyke is coarser grained and contains predominantly interstitial pores of  $< 50\ \mu\text{m}$  diameter between actinolite, albite and clinopyroxene (Fig. 2.1B). As chlorite is less abundant than in the pillow lava, this spilitised dyke sample contains fewer micropores. In contrast, the epidotised pillow lava and dyke have a more granoblastic texture of interlocking epidote and quartz, with large intercrystalline pores (50–200  $\mu\text{m}$  in diameter; Fig. 2.1C and D). Significant amounts of relict actinolite and chlorite are preserved in the epidosites from the precursor spilites and so the epidosites used in this study are best viewed as partial epidosites rather than mineralogically complete epidosites. Accordingly, their porosities (6–10 vol.%) are notably lower than those of complete epidosites (typically 10–26 vol.%), but for convenience we refer to these samples in this paper simply as ‘epidosites’. Very small amounts of much younger, obduction-related calcite occasionally clog pores in the Semail samples (e.g., Fig. 2.1C). Hence, even in experiments that reproduce the original in-situ pressure and temperature of hydrothermal alteration, the porosities and permeabilities of these samples will be very slightly lower than their original values.

Outcrops of lavas with microcrack pore space occur abundantly in the Semail ophiolite but samples with microcracks were excluded from this study for two reasons. First, it is not always clear when the cracks formed, e.g., during subseafloor hydrothermal alteration or during later obduction of the ophiolite and/or subaerial weathering. Second, even if the microcracks formed during the hydrothermal processes of interest, their apertures (and hence their permeability) are likely to have been enlarged during subaerial exposure and weathering prior to our sampling in outcrops.

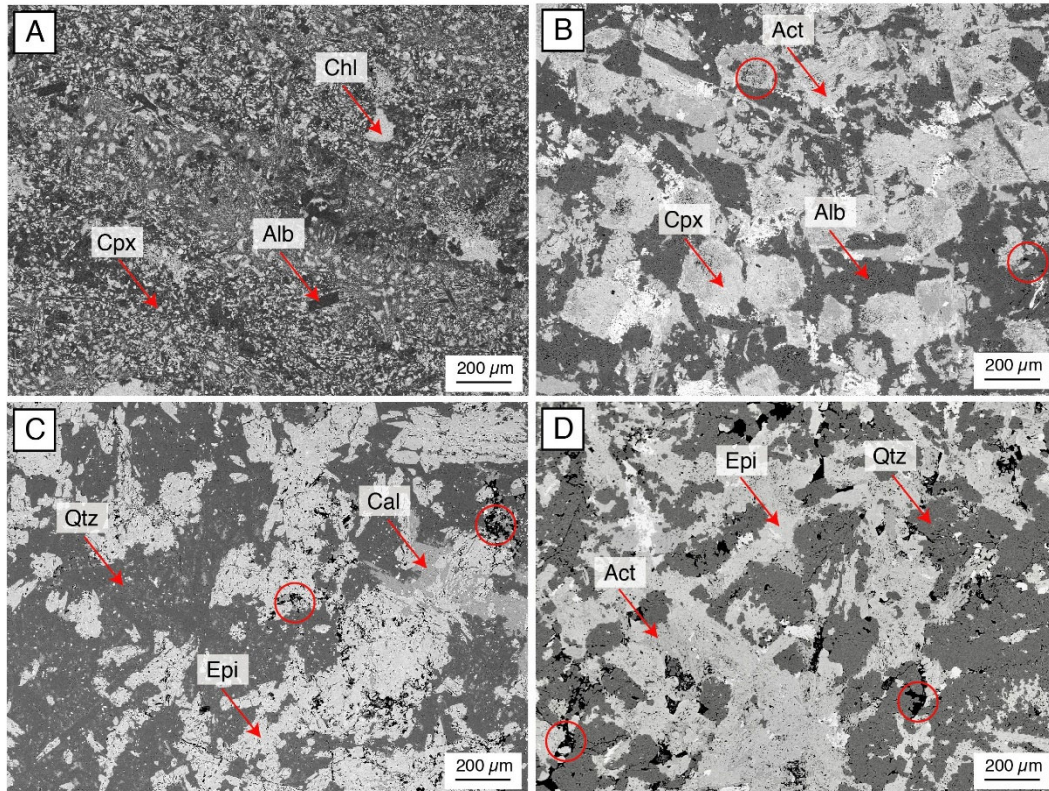


**Figure 2.1.** Scanning electron microscope (SEM) backscattered-electron images of four of the five samples used in this study. Red circles mark examples of pores (black). Abbreviations: Chl = chlorite, Ab = albite, Cpx = clinopyroxene, Ep = epidote, Qtz = quartz, Act = actinolite, Cal = calcite. (a) Spilitised pillow lava LD10-104-3. (b) Spilitised dyke AB17-32-spl. (c) Epidotised pillow lava SG14-56. (d) Partially epidotised dyke CO-51e (same specimen as CO-51s).

### 2.2.3. Preliminary sample measurements for sample selection

Prior to the high temperature experiments, cylindrical cores of 25 mm diameter were drilled from our samples and their porosity and permeability were measured at room temperature. The gas-accessible porosity was measured in our laboratory in Bern using a helium pycnometer (Micromeritics™ AccuPyc II 1340), and permeability was measured in a commercial laboratory using an unsteady-state gas permeameter at an effective pressure of 50 MPa (described in Section 2.2.5.). The properties of the measured samples are listed in Table 2.1.

The above preparatory measurements helped determine which samples were suitable for experiments at high temperatures, as the employed oscillating flow method (described in Section 2.4) can measure only a limited range of permeabilities. Two high-temperature scoping experiments on altered basalts with room-temperature permeabilities of  $\sim 1 \times 10^{-19} \text{ m}^2$  and  $\sim 4 \times 10^{-15} \text{ m}^2$  showed that these samples are too impermeable and too permeable, respectively, to be accurately measured by the oscillating flow method. Therefore, for further experiments, samples were selected from within this permeability range.

**Table 2.1***Samples used in this study, including porosity and unsteady-state permeameter measurements at 25 °C*

Sample name	Ophiolite	Lithostratigraphic unit	Location (UTM zone; coordinates mN, mE)	Rock type <sup>a</sup>	He-accessible porosity (vol.%)	Permeability <sup>b</sup> at 25 °C and $P_e = 50 \text{ MPa}^c$ (m <sup>2</sup> )
CO-51-e <sup>d</sup>	Troodos	Dyke complex	36N; 496904 3869828	Partial- epidosite dyke	10.0	$1.60 \times 10^{-16}$
CO-51-s <sup>d</sup>	Troodos	Dyke complex	36N; 496904 3869828	Partial- epidosite dyke	6.0	$3.36 \times 10^{-18}$
SG14-56	Semail	Geotimes lavas	40N; 431785 2739627	Epidosite pillow lava	4.1	$9.85 \times 10^{-17}$
AB17-32C-spl	Semail	Geotimes dyke complex	40N; 538351 2608870	Spilite dyke	4.8	$2.46 \times 10^{-19}$
LD10-104-3	Semail	Geotimes lavas	40N; 468748 2656024	Spilite pillow lava	5.1	$5.56 \times 10^{-19}$

<sup>a</sup> Glass-free hydrothermally altered basalts (see Table A2.1 for chemical composition and mineral abundances). <sup>b</sup> Measured by unsteady-state gas permeameter on 25 mm diameter cylindrical cores. Note that the high- $T$  experiments (Table 2.2) were performed on smaller cores. <sup>c</sup>  $P_e$  is the effective pressure = confining pressure minus pore pressure. <sup>d</sup> Samples drilled from same hand-specimen used in experiments by Coehlo et al. (2015; their runs PP332 and PP308).

#### 2.2.4. Selection of experimental conditions

The spilites and epidiosites in the Semail and Troodos ophiolites formed by hydrothermal alteration at temperatures of ~170–430 °C (Richter and Diamond, 2019), thus this is the experimental range of primary interest. A practical requirement of our high- $T$  apparatus is that the sample must first be briefly heated to 500 °C to seal a copper jacket around the sample before commencing permeability measurements. This elevated temperature is still within the thermal stability field of the minerals in the samples, as confirmed by our thermodynamic calculations using the data in Holland and Powell (2011). Accordingly, no mineralogical changes are expected during the relatively short-term, nominally water-free experiments. A further requirement of our experimental procedure was to end our high- $T$  experiments with final measurements at room temperature, in order to facilitate comparison of the results with conventional permeameter measurements at 25 °C and at elevated pressures. Our measurements were therefore made in four discrete steps between 25 and 450 °C.

The hydrostatic pressure during spilite and epidiosite alteration in the Troodos and Semail ophiolites is estimated to have been between 27 and 70 MPa (Juteau et al., 2000; Richardson et al., 1987; Richter and Diamond, 2019). In in-situ oceanic crust, hydrostatic pressures of approximately 50 MPa are widely taken to represent high- $T$  alteration conditions (e.g., Seyfried et al., 1988). We therefore chose to perform all our isobaric temperature–permeability experiments at 50 MPa effective pressure, achieved

by applying a confining pressure of 100 MPa and a pore pressure of 50 MPa. Our isothermal pressure–permeability experiments covered the effective pressure range from 5 MPa to 55 MPa at room temperature.

### 2.2.5. Permeability measurements at room temperature and elevated pressure

The effect of pressure on permeability at room temperature was measured in a CMS™-300 unsteady-state pressure-decay permeameter using helium as the pore fluid (Honarpour et al., 2018) at CoreLab, Aberdeen. Samples were measured at effective pressures of ~5, 34 and 55 MPa by increasing the confining pressure while maintaining pore fluid pressure at ~0.2 MPa. The detection limit of permeability measurements using the device is  $\sim 9.8 \times 10^{-20} \text{ m}^2$ .

### 2.2.6. Permeability measurements at elevated pressure and temperature

#### 2.2.6.1. Principle of the oscillating flow method

An internally heated Paterson gas apparatus (Petrini 2019; similar to that in Paterson, 1970) at ETH-Zurich was used to measure the permeability of cylindrical rock cores by the oscillating flow method (Bernabé et al., 2006; Fischer, 1992; Kranz et al., 1990) at various temperatures under constant confining and pore pressures. During the experiments the cylindrical surface of the core sample is sealed by a malleable copper jacket. Meanwhile, the ends of the core are open to upstream and downstream argon gas reservoirs at the selected pore pressure. A computer-controlled pump induces sinusoidal pressure oscillations of ~2 MPa amplitude in the upstream gas reservoir, which traverse the sample and are detected in the downstream reservoir. Owing to the rock sample characteristics, to the gas properties and to the characteristics of the experimental setup, the pressure oscillations in the downstream reservoir show an attenuated amplitude and a phase shift. The amplitude ratio and phase shift of the recorded signals are then employed to calculate the permeability of the sample by solving the following equation (Bernabé et al. 2006):

$$Ae^{i\theta} = \left( \frac{1+i}{\sqrt{\xi\eta}} \sinh \left[ (1+i) \sqrt{\frac{\xi}{\eta}} \right] + \cosh \left[ (1+i) \sqrt{\frac{\xi}{\eta}} \right] \right)^{-1} \quad (1)$$

where  $A$  is the amplitude ratio,  $\theta$  the phase shift, and  $\eta$  and  $\xi$  the non-dimensional permeability and storativity as follows:

$$\eta = \frac{S\tau k}{\pi L \mu \beta_D} \quad (2)$$

$$\xi = \frac{SL\beta}{\beta_D} \quad (3)$$

where  $S$  is the sample cross-sectional area,  $L$  the sample length,  $\mu$  the fluid viscosity,  $\Delta t$  the time period,  $\beta_D$  the downstream storage capacity,  $\beta$  the sample storativity, and  $k$  the sample permeability. A detailed discussion of the associated calculations, limitations and uncertainties of the oscillating flow method are given by Bernabé et al. (2006) and Petrini (2019).

#### 2.2.6.2. Sample preparation and experimental assembly

Samples were prepared and assembled according to the methodology in Petrini (2019). As the apparatus requires core samples of 15 mm diameter, new cores of 16–20 mm length were drilled from the 25 mm diameter cores previously measured for porosity and permeability at room temperature. In cases where the original 25 mm diameter core had been damaged, a 15 mm diameter core was drilled from the original hand-specimen directly adjacent to the 25 mm drill hole. The cores were precision-ground at both ends on a lathe under running water, then dried in an oven at 60 °C for at least 48 hours.

For each experiment a core was placed into the sample column between zirconia and alumina pistons, which each contain a central 2 mm hole to permit the flow of argon. Even distribution of the gas at the upstream and downstream ends of the sample was facilitated by a cross groove in each of the alumina spacers in contact with the sample. A copper jacket of 15 mm inner diameter was fitted snugly around the sample to isolate the pore-fluid gas from the gas used to transmit the confining pressure. The sample column was then inserted into a furnace and the furnace lowered into a pressure cell. Finally, the pressure cell was closed, and anodes were attached to control the furnace temperature, along with a thermocouple to monitor the temperature directly above the sample.

#### 2.2.6.3. Permeability measurements

After sample loading, both the confining and pore pressure systems were flushed five times with argon to saturate them and to clear any residual air. The confining pressure ( $P_c$ ) was first increased to 100 MPa and then the pore pressure ( $P_p$ ) was raised to 50 MPa. The copper jacket was sealed around the sample by increasing the temperature from 25 to 500 °C over ~1 hour and maintaining this temperature for 15 minutes. The first experimental run was then executed by allowing the sample to cool for isothermal measurements at 450 °C, 400 °C, 300 °C, 150 °C and 25 °C, while maintaining  $P_c$  at 100 MPa via a gas intensifier. Heating and cooling rates varied between ~4 °C/min and 10 °C/min. Prior to each measurement, the temperature was held constant for 10 minutes to equilibrate the desired temperature across the sample.

At the start of each experiment, test oscillations were induced to optimise the attenuated amplitude and phase offset within the limits required for best accuracy, as recommended by Bernabé et al. (2006 and references therein). The optimal settings for each sample are listed in Table 2.2. Thereafter at each temperature step, twenty-five pressure oscillations were recorded in the downstream reservoir, entailing 27–60 minutes of measurement time.

In addition to the initial cooling runs, measurements were repeated on three samples at the same temperature and pressure conditions during subsequent heating and cooling runs. These runs were carried out to test for reproducibility and for any hystereses dependent on the direction of temperature change. The spilitised pillow and dyke samples required several days for these measurements owing to their low permeability. During the 2–3 days between each run the sample was held for safety reasons at room temperature and  $P_c$  was decreased to  $\sim 30$  MPa and  $P_p$  to 5 MPa. Once the elevated pressures were restored after such breaks, measurements were carried out at 25 °C and then during heating at 150 °C, 300 °C and 400 °C. Additional measurements on the spilite dyke were made at 300 °C, 150 °C and 25 °C during a second cooling run on the same day. Similarly, the high permeability of the epidosite pillow sample required only short measurement times (Table 2.2). Thus, its initial cooling run was followed by a heating run to 400 °C on the same day, yielding seven measurements. After the 2–3 day pause, a second run of heating and cooling measurements was performed, totalling 14 measurements for this sample.

**Table 2.2**

*Sample dimensions and pressure oscillation parameters used in high temperature experiments*

Sample	Core diameter <sup>a</sup> (mm)	Core length (mm)	Pressure pulse amplitude (MPa)	Pressure pulse frequency (Hz)	Amplitude ratio <sup>b</sup>	Phase offset (cycles)	Time for 25 oscillations (min)
CO-51-e	15	20.01	2	0.010	0.27	0.21	40
CO-51-s	15	19.00	2	0.010	0.25	0.24	40
SG14-56	15	20.00	2	0.015	0.20	0.23	27
AB17-32C-spl	15	16.04	2	0.009	0.08	0.31	46
LD10-104-3	15	17.25	2	0.007	0.04	0.35	59

<sup>a</sup> Note that these cores are smaller than those used for the gas permeameter measurements at 25 °C (Table 2.1).

<sup>b</sup> Downstream/upstream pressure ratio.

#### 2.2.6.4. Calculation of permeability

Of the 25 oscillations recorded at each temperature step, the first six were discarded to avoid any early transient effects on the recorded downstream signal (Bernabé et al., 2006). Ten cycles were then used for the permeability calculation. The oscillation data were processed with the MATLAB™ code and procedure described in Petrini (2019). The code solves Eq. (1) numerically for permeability and storativity by applying an iterative gradient-based optimisation method with adaptive step size to improve convergence of the solution. Due to the high downstream reservoir storage of the employed pump, the storativity may attain unphysical values and was therefore not considered in our measurements (Bernabé et al., 2006).



## 2.3. Results

### 2.3.1. Effect of elevated pressure on the permeability of spilites and epidiosites

Applying increasing effective pressure to the samples at room temperature in the gas permeameter decreased the permeability of the two cores from the spilitised dyke (SG14-43-1 and SG14-43-2) and the two cores from the epidotised dyke (Co-51e and Co-51s; Fig. 2.2 and Table 2.3). Between 5 and 55 MPa effective pressure the permeability of the epidiosites decreased by absolute values of  $7.3 \times 10^{-17} \text{ m}^2$  (31% relative decrease; Co-51e) and  $7.2 \times 10^{-18} \text{ m}^2$  (68%, CO-51s). The spilitised dyke samples showed larger relative decreases in permeability between 5 and 33 MPa of at least  $4.0 \times 10^{-19} \text{ m}^2$  (80% relative decrease; SG14-43-1) and  $9.9 \times 10^{-20} \text{ m}^2$  (50%; SG14-43-2). The experimental detection limit at  $9.8 \times 10^{-20} \text{ m}^2$  (labelled LOD in Fig. 2.2) was reached at 33 MPa, therefore the quoted decreases in absolute and relative permeabilities of the two spilite samples are minimum values.

**Table 2.3**

*Permeabilities of spilitised and epidotised dykes at 20 °C over a range of effective pressures.*

Sample	Sample Type <sup>a</sup>	Confining pressure (MPa)	Mean pore pressure (MPa)	Effective pressure (MPa)	Permeability <sup>b</sup> (m <sup>2</sup> )
SG14-43-1	Spilitised dyke	5.5	0.25	5.3	$4.93 \times 10^{-19}$
SG14-43-1		33.5	0.25	33.3	Below detection
SG14-43-1		55.2	0.25	54.9	Below detection
SG14-43-2		5.5	0.26	5.2	$1.97 \times 10^{-19}$
SG14-43-2		33.5	0.26	33.2	Below detection
SG14-43-2		55.2	0.26	54.9	Below detection
CO-51e	Partial-epidosite dyke	5.5	0.17	5.3	$2.34 \times 10^{-16}$
CO-51e		33.5	0.17	33.3	$1.74 \times 10^{-16}$
CO-51e		55.2	0.17	55.0	$1.60 \times 10^{-16}$
CO-51s		5.5	0.20	5.3	$1.06 \times 10^{-17}$
CO-51s		33.5	0.20	33.3	$5.53 \times 10^{-18}$
CO-51s		55.2	0.20	54.9	$3.36 \times 10^{-18}$

<sup>a</sup> See Table A2.1 for chemical composition and mineral abundances. <sup>b</sup> Detection limit is  $\sim 9.8 \times 10^{-20} \text{ m}^2$ .



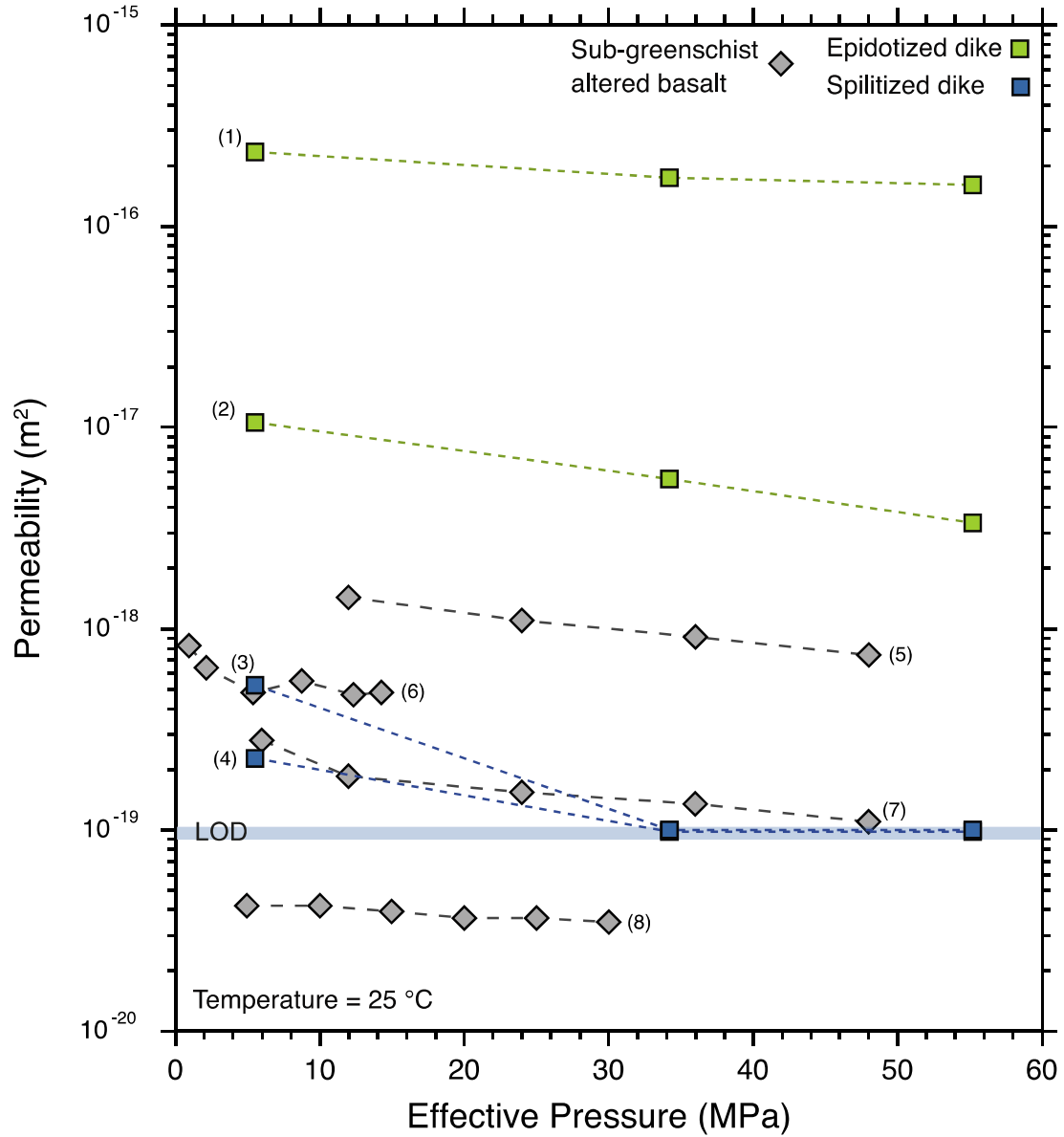


**Figure 2.2.** Permeability measured by standard permeameter as a function of effective pressure at 25 °C. (1), (2) dykes altered to epidosite (green, this study). (3), (4) dykes altered to spilite (blue, this study; LOD denotes limit of detection for our study). Literature data from basalts altered at sub-greenschist conditions: (5), (7) Christensen and Ramanantoandro (1988), (6) Karato (1983), (8) Gilbert and Bona (2016).

### 2.3.2. Experiments at elevated temperatures

#### 2.3.2.1 Response of spilite and epidosite permeability to elevated temperatures

During the initial cooling runs in the oscillating flow experiment, the permeability of each sample increased from the initial measurement at either 450 or 400 °C to the final measurement at 25 °C, thereby defining a systematic trend of increasing permeability with decreasing temperature (Fig. 2.3; Table 2.4). The only exception to this trend was a near constant permeability recorded for the spilite dyke sample at 400 °C and 300 °C, after which the permeability followed the trend of the other samples.

In the epidosite dykes, permeabilities increased upon cooling from 450 °C to 25 °C by absolute values of  $1.3 \times 10^{-18} \text{ m}^2$  (45% relative increase) and  $1.4 \times 10^{-18} \text{ m}^2$  (50%), and similarly the permeability of the epidosite pillow lavas increased by  $1.1 \times 10^{-18} \text{ m}^2$  (44%). Over the same cooling range, the permeabilities of the spilite dyke and spilite pillow samples increased by  $1.1 \times 10^{-19} \text{ m}^2$  (37%) and  $7.7 \times 10^{-20} \text{ m}^2$  (36%), respectively.

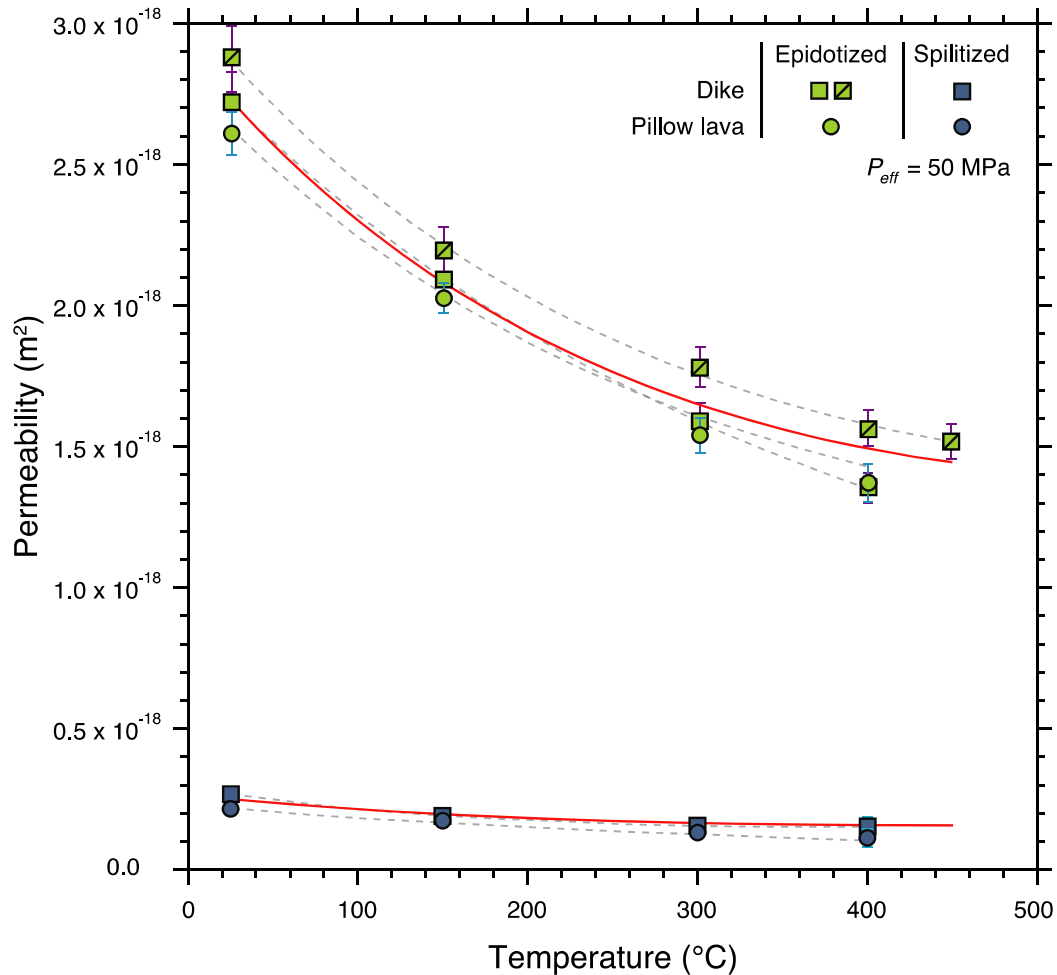


**Figure 2.3.** Measured permeability of spilitised and epidotised pillow lavas and dykes at 50 MPa effective pressure. Note that the y-axis scale is linear. Data for the epidotised dykes are from initial cooling runs, with analytical uncertainties shown by purple error bars. Data for the spilites and the epidotised pillow lava are mean values from repeat heating and cooling cycles, with standard deviations shown by blue error bars where larger than the data symbols. See Table 2.4 for all data. Red curves show fits for each alteration type according to equations (4) and (5) in the text.

### 2.3.2.2. *Production of water during experiments*

Upon disassembling the two experiments on the epidotised dyke (Co-51e and Co-51s), a thin film of water was found between the alumina spacer and the top of the sample. The samples themselves appeared slightly darker and greyer after the experiments but without any reddish tinge. No water was found in the other experiments.

### 2.3.3. *Behaviour and uncertainty of permeability over multiple cooling and heating cycles*

The results of repeated heating and cooling experiments on the epidosite pillow, spilite dyke and spilite pillow samples are shown in Table 2.4 and Fig. A2.1. The repeats exhibited the same trend as that observed in the initial cooling runs. However, the absolute values of the permeabilities shifted very slightly between runs. Based on the data in Table 2.4 the means of the repeat measurements and their associated standard deviations were calculated for the two spilites and the epidotised pillow lava and plotted in Fig. 2.3. These standard deviations for individual samples are comparable to the analytical uncertainty calculated by the MATLAB™ code (Section 2.2.6.4), and they have values 2–3 orders of magnitude lower than the measured permeabilities. The overall reproducibility of measurements of all samples of each alteration type at any given temperature is at most 17.5% in the epidiosites and 35% in the spilites.

### 2.3.4. *Temperature–permeability correlations*

The temperature–permeability data for individual samples describe smooth logarithmic trends that are well fitted by second-order polynomial functions of the  $\log_{10}(k)$  values (grey dashed curves in Fig. 2.3). Because the differences between the samples of each alteration type are small and their fitted curves are subparallel, we present a mean correlation for each alteration type (red curves in Fig. 2.3), corresponding to the following for epidiosites:

$$\log(k) = -17.5370 - 0.00111T + 9.5626 \times 10^{-7}T^2 \quad (4)$$

and the following for spilites:

$$\log(k) = -18.5780 - 0.00109T + 1.2853 \times 10^{-6}T^2 \quad (5)$$

where  $k$  is permeability ( $\text{m}^2$ ) and  $T$  is temperature between 0 and 450 °C.

**Table 2.4**

*Permeabilities of spilites and epidiosites measured at elevated temperatures at 50 MPa effective pressure in initial cooling runs and following heating and cooling runs*

Sample and sample type	Run type	Run day	Temperature <sup>a</sup> (°C)	Permeability (m <sup>2</sup> )	Analytical uncertainty <sup>b</sup> (m <sup>2</sup> )	$\square k^c$ (%)
CO-51-e Partial-epidosite dyke	Cooling	Day 1	400	$1.57 \times 10^{-18}$	$6.31 \times 10^{-20}$	—
			300	$1.78 \times 10^{-18}$	$7.18 \times 10^{-20}$	12
			150	$2.19 \times 10^{-18}$	$8.82 \times 10^{-20}$	19
			26	$2.88 \times 10^{-18}$	$1.16 \times 10^{-19}$	24
CO-51-s Partial-epidosite dyke	Cooling	Day 1	400	$1.35 \times 10^{-18}$	$5.45 \times 10^{-20}$	—
			300	$1.59 \times 10^{-18}$	$6.40 \times 10^{-20}$	15
			150	$2.10 \times 10^{-18}$	$8.45 \times 10^{-20}$	24
			26	$2.72 \times 10^{-18}$	$1.09 \times 10^{-19}$	23
SG14-56 Epidiosite pillow lava	Cooling	Day 1	400	$1.44 \times 10^{-18}$	$5.81 \times 10^{-20}$	—
			300	$1.62 \times 10^{-18}$	$6.54 \times 10^{-20}$	11
			150	$1.99 \times 10^{-18}$	$8.03 \times 10^{-20}$	19
			26	$2.57 \times 10^{-18}$	$1.03 \times 10^{-20}$	22
	Heating	Day 1	150	$2.05 \times 10^{-18}$	$8.27 \times 10^{-20}$	−25
			300	$1.55 \times 10^{-18}$	$6.24 \times 10^{-20}$	−33
			400	$1.36 \times 10^{-18}$	$5.48 \times 10^{-20}$	−14
	Heating	Day 2	26	$2.70 \times 10^{-18}$	$1.09 \times 10^{-19}$	—
			150	$2.09 \times 10^{-18}$	$8.40 \times 10^{-20}$	−29
			300	$1.51 \times 10^{-18}$	$6.06 \times 10^{-20}$	−39
			400	$1.31 \times 10^{-18}$	$5.26 \times 10^{-20}$	−15
	Cooling	Day 2	300	$1.49 \times 10^{-18}$	$5.98 \times 10^{-20}$	12
			150	$1.98 \times 10^{-18}$	$7.80 \times 10^{-20}$	25
			26	$2.56 \times 10^{-18}$	$1.03 \times 10^{-19}$	23
AB17-32C-spl Spilite dyke	Cooling	Day 1	400	$1.79 \times 10^{-19}$	$7.21 \times 10^{-21}$	—
			300	$1.82 \times 10^{-19}$	$7.31 \times 10^{-21}$	1
			150	$2.13 \times 10^{-19}$	$8.57 \times 10^{-21}$	15
			26	$2.86 \times 10^{-19}$	$1.15 \times 10^{-20}$	26
	Heating	Day 2	26	$2.76 \times 10^{-19}$	$1.11 \times 10^{-20}$	—
			150	$1.85 \times 10^{-19}$	$7.43 \times 10^{-21}$	−49
			300	$1.52 \times 10^{-19}$	$6.12 \times 10^{-21}$	−21
			400	$1.48 \times 10^{-19}$	$5.95 \times 10^{-21}$	−3
	Cooling	Day 2	300	$1.55 \times 10^{-19}$	$6.22 \times 10^{-21}$	4
			150	$1.89 \times 10^{-19}$	$7.60 \times 10^{-21}$	18
			26	$2.52 \times 10^{-19}$	$1.01 \times 10^{-20}$	25
LD10-104-3 Spilite pillow lava	Cooling	Day 1	400	$1.38 \times 10^{-19}$	$5.54 \times 10^{-21}$	—
			300	$1.42 \times 10^{-19}$	$5.71 \times 10^{-21}$	3

		150	$1.82 \times 10^{-19}$	$7.32 \times 10^{-21}$	22
		26	$2.15 \times 10^{-19}$	$8.64 \times 10^{-21}$	15
Heating	Day 2	26	$2.21 \times 10^{-19}$	$8.90 \times 10^{-21}$	–
		150	$1.66 \times 10^{-19}$	$6.68 \times 10^{-21}$	–33
		300	$1.22 \times 10^{-19}$	$4.93 \times 10^{-21}$	–36
		400	$8.96 \times 10^{-20}$	$3.61 \times 10^{-21}$	–37

<sup>a</sup> From top to bottom in order of measurement. <sup>b</sup> Permeability uncertainty resulting from measurements and experimental parameters inaccuracies. <sup>c</sup> Relative permeability change with respect to previous temperature step  $(k_{\text{step 2}} - k_{\text{step 1}}) / k_{\text{step 1}}$

## 2.4. Discussion

### 2.4.1. Effects of pressure on permeability

The mostly gradual reduction of permeability with increasing pressure observed in our spilite and epidosite samples is similar to that found in previous studies on fresh and altered basalts (Fig. 2.2; Christensen and Ramanantoandro, 1988; Karato, 1983a; and Gilbert and Bona, 2016). In contrast to our samples, all previous measurements were made on fresh to sub-greenschist altered basalts that contain glass, clays and zeolites. The markedly different absolute permeabilities and the minor differences in pressure–permeability slopes between the datasets in Fig. 2.2 are presumably due to these differences in sample mineralogy and texture. The data of Gilbert and Bona (2016) follow the same pressure–permeability trend as the other studies even though the measurements were made on brine-saturated samples rather than using dry gas as the pressure medium, which could have resulted in mineral reactions. Only the results of Karato (1983a) show a sharp kink with increasing pressure below 5 MPa. This may be a real property of the samples or an artefact due to initially incomplete sealing of the sample jacket. All the other studies used a minimum confining pressure of 5 MPa to ensure a good seal.

### 2.4.2. Effects of temperature on permeability

#### 2.4.2.1 Systematic changes in permeability with temperature

Accepting that the measured temperatures, pressures and permeabilities in the oscillating flow experiments are accurate, the repeated heating and cooling experiments demonstrate that the thermally induced changes in permeability of both the spilites and the epidiosites are essentially reversible (Fig. A2.1). The absence of systematic hystereses implies that the mean permeabilities of individual samples ( $\pm 9\%$  in epidiosites and  $\pm 17.5\%$  in spilites) at each  $P$ – $T$  point represent values at thermomechanical equilibrium, i.e., the values are independent of the rate and direction of temperature change.

The samples undoubtedly expand upon isobaric heating, as dictated by the weighted sum of the thermodynamic expansivities of their constituent minerals. The coefficients of compression and thermal expansion given in the thermodynamic database of Holland and Powell (2011) show that the epidiosites

steadily expand by 1.20 vol.% between room temperature and 450 °C at 50 MPa effective pressure, and the spilites expand by 1.19 vol.% over the same interval. Expansion of the rock matrix during heating implies that the pore spaces expand by the same relative amounts as well. Therefore, the observed systematic reduction in permeability exhibited by our samples (Fig. A2.1), although slight, is counter intuitive. Though our experiments were not designed to elucidate the mechanisms behind this behaviour, several possibilities can be envisaged, as discussed in the following.

#### *2.4.2.2. Thermally induced processes that reduce permeability*

Experimental studies on a wide range of rock types have revealed both positive and negative correlations between permeability and temperature (Bakker et al., 2015; Guo et al., 2017; Liu et al., 2018; Nahhas et al., 2019; Kozusnikova and Konečný, 2011; Kushnir et al., 2017; Mordensky et al., 2019; Shmonov et al., Sun et al., 2016 1995; Zاراisky and Balashov, 1995). Among these studies, several have suggested explanations for the reduction of permeability with temperature increase. In experiments in water at elevated temperatures one mechanism proposed is that permeability can be reduced by crack-sealing due to mineral precipitation (Kushnir et al., 2017). Other mechanisms are that pressure solution leads to grain boundary closures (e.g., in granites: Zاراisky and Balashov, 1995) or that ductile flow closes pores (e.g., in limestones: Bakker et al., 2015). These effects are not expected to occur in our experiments because we used a non-reactive gas rather than water, the hydrothermal minerals in our samples are thermodynamically stable at the imposed pressures and temperatures (Section 2.2.4), and the imposed differential pressures were well outside the regime of ductile deformation.

However, water was produced in our two experiments on epidotised dyke samples. This finding is similar to that described by Coehlo et al. (2015) in an experiment on a strongly chloritised metadiabase dyke at high temperature (400–500 °C) in a Paterson apparatus using dry argon over ~30 hours. Coehlo et al. (2015) noticed that the chlorite in that sample had turned red during the experiments and that its lattice *d*-spacing had increased. Coehlo et al. (2015) attributed these changes to oxidation of chlorite via dehydrogenation and dehydroxylation (e.g., Borggard et al., 1982; Lempart et al., 2018) and suggested that the expansion of chlorite could reduce sample porosity. The samples CO-51e and CO-51s provided to us by Coehlo et al. (2015) are epidiosites rather than chloritised metadiabase but they still contain relict chlorite (e.g. Fig. 2.1). The chlorite in these samples may have undergone the same changes as described by Coehlo et al. (2015) despite our shorter experimental duration of only ~2 hours at > 400 °C and despite the chlorite not having changed its macroscopic colour. Nevertheless, pore clogging by expanded chlorite cannot account for the reversibility of our observed temperature–permeability trends. The preservation of water after the experiments proves that any dewatering reaction was irreversible. Moreover, no water was observed in our other three experiments and not all our investigated samples contain chlorite, yet all the samples describe the same temperature–permeability trends. Thus, none of the thermally induced processes described above, i.e., ductile flow, pressure

solution, precipitation of minerals and dehydrogenation–hydroxylation of chlorite can explain the reversibility of our results.

The formation or growth of micro-cracks upon heating is known to increase permeability (e.g., Kozusnikova and Konečný, 2011; Liu et al., 2018; Mordensky et al., 2019; Shmulovich et al., 1995; Sun et al., 2016), whereas their closure is expected to reduce permeability (Guo et al., 2017). Thermally induced micro-cracking has been observed in a few studies in real-time SEM experiments or by comparing high-resolution photographs before and after the experiments (Guo et al., 2017; Liu et al., 2018; Nahhas et al., 2019; Shmonov et al., 1995). In contrast, observations by SEM of three fresh basalt samples during heating to 715 °C revealed neither growth of pre-existing micro-cracks nor formation of new micro-cracks (Shmonov et al., 1995). Similarly, altered andesites experienced only minor lengthening and increase in the abundance of micro-cracks upon heating (Mordensky et al., 2019). Formation of new micro-cracks in our experiments is conceivable as the heating rates we used (up to ~10 °C/min) were above the 2 °C/min rate recommended to prevent thermally induced cracking in granites (Richter and Simmons, 1974). However, formation of microcracks during heating at such rates (Richter and Simmons, 1974 and references therein) cannot explain our observed reduction of permeability. We expect the extremely fine-grained texture of the altered basalts and their high chlorite contents to reduce or prevent microcrack propagation in our study. Our thin-section petrography showed that our spilite and epidosite samples initially contained no or rare micro-cracks, hence possible closure of pre-existing micro-cracks can be ruled out as an explanation of the observed negative temperature–permeability trend.

We suggest an alternative mechanism to explain the net closure of connected pores. The minerals that make up our samples undergo different bulk thermoelastic expansions upon heating at 50 MPa (Table A2.1), and they also undergo different anisotropic expansions along their crystallographic axes. As examples of the latter effect, igneous plagioclase and hydrothermal albite expand by 70% more along their *c*-axes than along their other axes (Tribaudino et al., 2010) and epidote shows a 77% difference (Diego Gatta et al., 2011). Given the heterogeneous orientations of minerals that surround the pore spaces in our samples (Fig. 2.1), it is conceivable that anisotropic expansion could close a portion of pore throats upon heating, thereby reducing permeability even though the bulk pore space is increasing. As bulk and anisotropic thermoelastic expansions are reversible thermodynamic properties, they might also explain the observed reversibility of the temperature–permeability trends of our rock samples.

#### 2.4.2.3. *Non-systematic changes in permeability*

Superimposed on the main permeability–temperature trend in Fig. A2.1 are the much smaller, non-systematic shifts in permeability, which occurred during and between our heating and cooling runs. These shifts are presumably due to subtle drift of our experimental equipment. With values an order of

magnitude lower than the main permeability–temperature trends, we consider them negligible for the present study.

#### *2.4.2.4. Comparison of temperature–permeability trends in altered and unaltered basalts*

The negative temperature–permeability correlation found in the present study is consistent with the overall trend found by Shmonov et al. (1995) in a hydrothermally unaltered (i.e. "fresh"), submarine, massive flow basalt between 25 and 250 °C at effective pressures of 30, 50 and 120 MPa (Fig. 2.4). However, this sample exhibits small deviations in the trend over narrow temperature intervals (25–50 °C and 150–200 °C; Fig. 2.4). Furthermore, upon heating to 250 °C, the permeability drops by a factor of ~20, some 12 times more than that observed in the spilite and epidosite samples in this study (Fig. 2.4). The experiments of Aksyuk et al. (1992) on a different sample of fresh, submarine, massive flow basalt found a negative correlation between 25 and 100 °C, similar to our results, but a positive temperature–permeability correlation between 100 and 600 °C. Again, the overall change in permeability is vastly larger than that of our spilites and epidosites. Unfortunately, as only these two mutually contrasting studies on fresh basalts are available, no systematic comparison can be drawn with the behaviour of our spilite and epidosite samples.



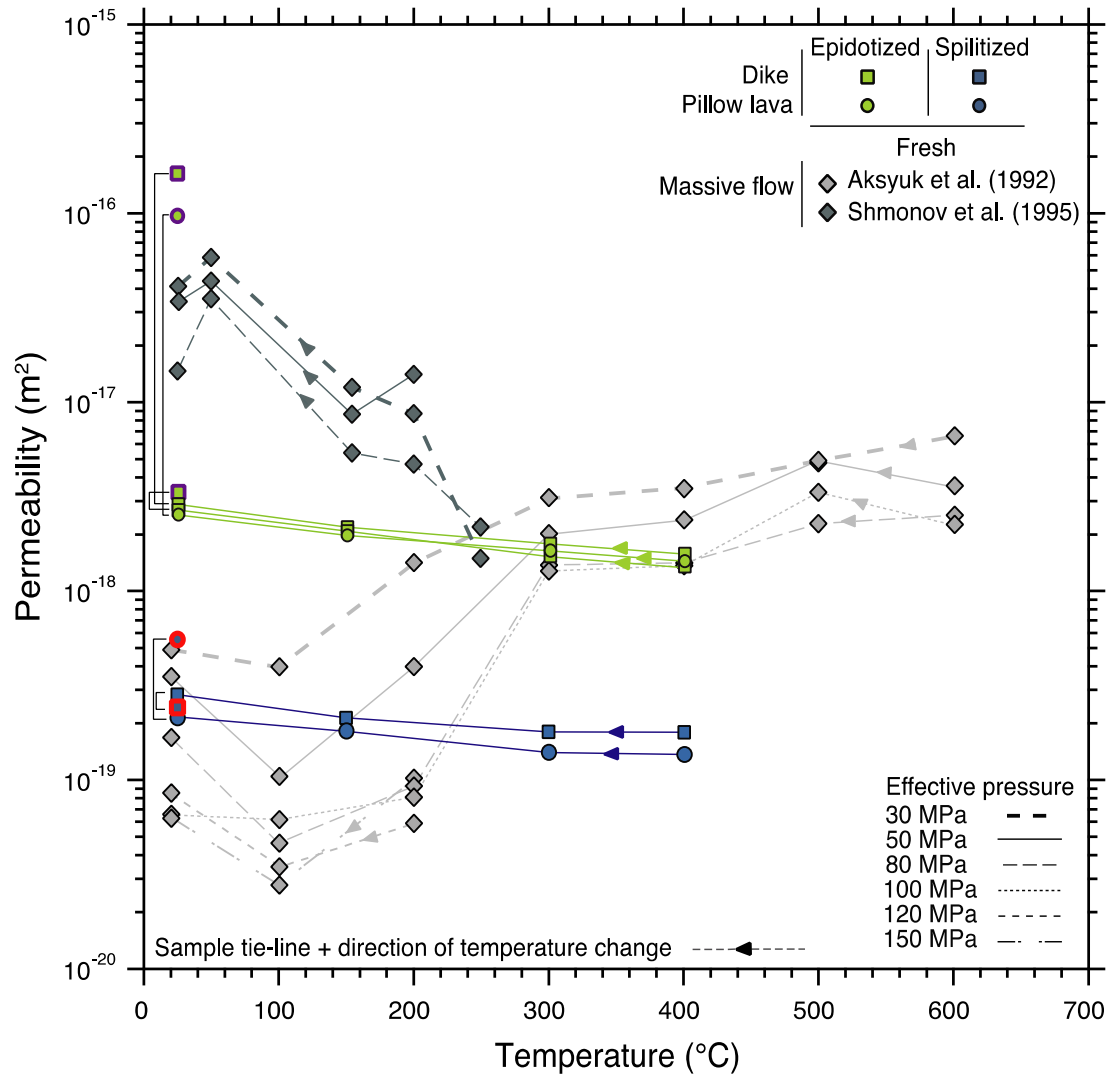


**Figure 2.4.** Comparison of temperature–permeability trends along various isobars of effective pressures in fresh basaltic massive flows (Shmonov et al., 1995; Aksyuk et al., 1992) and in spilite and epidosite altered basalt dykes and lavas (this study; 15 mm diam. cores). Room-temperature measurements at 55 MPa effective pressure on larger samples of spilites and epidiosites (25 mm diam. cores) are shown with thick red and purple outlines around symbols. Solid black brackets join measurements of 25 mm and 15 mm cores from the same hand sample.

### 2.4.3. Significance of measured changes in permeability

We have demonstrated that increasing temperature to 450 °C reduces the permeability of spilites and epidiosites by at most half an order of magnitude. Are these changes significant compared to the natural variation in permeability of spilites and epidiosites at the hand-specimen scale? Fig. 2.4 compares the room-temperature permeability at ~50 MPa effective pressure of 15 mm and 25 mm cores drilled from the same hand samples. Among these duplicate measurements only the spilitised dyke (AB17-32C-spl) and the partially epidiotised dyke (CO-51s) show similar permeabilities between the 25 mm and 15 mm cores. The duplicates of the other three samples (LD10-104-3, SG14-56, and CO-51e) differ in permeability by 0.5–1.5 orders of magnitude. Thus, the changes in permeability due to heating to 450 °C are in fact only minor compared to the natural heterogeneity of permeability in typical spilites and epidiosites. This conclusion is corroborated by the experiments of Coehlo et al. (2015), who measured permeability on cores from the same epidiotised dyke sample as our samples CO-51e and CO-51s using the steady-state flow method at 400 °C and 50 MPa. They obtained  $\sim 1.1 \times 10^{-18} \text{ m}^2$  when using argon as the pore fluid and  $\sim 6.5 \times 10^{-19}$  when using water. Both values are at least an order of magnitude lower than our measurements on the 15 mm cores at the same  $P$ – $T$  conditions. By contrast, the pressure–permeability effect from near atmospheric (5 MPa) to typical in-situ pressures (33–55 MPa) is about twice that of the temperature–permeability effect at 50 MPa effective pressure. As the inter-sample variability of permeability in spilites and epidiosites markedly outweighs the effect of heating the rocks to in-situ hydrothermal conditions, ignoring the thermal effect in numerical simulations of hydrothermal flow is unlikely to incur significant errors. However, it makes sense to conduct routine gas permeameter measurements at the relevant in-situ pressure to ensure that the pressure effect is taken into account.

### 2.4.4. Temperature–permeability correlations

As suggested above, it may be justified to ignore the thermal effects on permeability for certain modelling projects. However, for other projects it may still be desirable to average the room- $T$  permeabilities of numerous rock samples to obtain a representative mean and deviation and then apply a correction for the elevated temperatures of the simulations. A suitable correction function for temperature can be derived from the average temperature–permeability correlations expressed by equations (4) and (5). For example, permeabilities measured at 25 °C and at an effective pressure of ~50 MPa can be corrected as follows:

$$\log(k_T)_{\text{epidosite}} = \log(k_{25}) + 0.02644 - 0.0011056T + 9.5626 \times 10^{-7}T^2 \quad (6)$$

$$\log(k_T)_{\text{spilite}} = \log(k_{25}) + 0.02598 - 0.0010872T + 1.2853 \times 10^{-6}T^2 \quad (7)$$

where  $T$  is temperature between 25 and 450 °C,  $k_{25}$  is the permeability ( $\text{m}^2$ ) measured at 25 °C, and  $k_T$  is the permeability ( $\text{m}^2$ ) at the desired subscripted  $T$  at 50 MPa effective pressure. For permeabilities ( $k_{\text{exp}}$ ) measured at an experimental temperature ( $T_{\text{exp}}$ ) other than 25 °C, new values of the first

polynomial coefficient  $a'$  can be determined by rearranging equations (5) or (6) below, using the known  $k_{exp}$  and  $T_{exp}$ :

$$\log(k_{exp})_{epidosite} = a' - 0.0011056T_{exp} + 9.5626 \times 10^{-7}T_{exp}^2 \quad (8)$$

$$\log(k_{exp})_{spilite} = a' - 0.0010872T_{exp} + 1.2853 \times 10^{-6}T_{exp}^2 \quad (9)$$

The new  $a'$  values can then be inserted back into the equations (8) or (9) with the desired high temperature in place of  $T_{exp}$  to calculate the corrected permeabilities (valid at 50 MPa effective pressure).

#### 2.4.5. Influence of pressure on the temperature–permeability effect

Our experimental description of the temperature effect on permeability is strictly valid only for an effective pressure of 50 MPa. However, spilites and epidiosites form at a variety of stratigraphic depths (Gilgen et al., 2016) and therefore in-situ pressures vary. A study on sandstones and shales (Guo et al., 2017) demonstrated that the magnitude of the temperature–permeability effect varies systematically with pressure: the absolute reduction in permeability is more pronounced at low effective pressures (5 MPa) than at high effective pressures (40 MPa). In the studies on fresh basalts by Aksyuk et al., (1992) and Shmonov et al. (1995), the data are too scattered to recognise a systematic relationship (Fig. 2.4). The quantitative correlation of the permeability of spilites and epidiosites with pressure at elevated temperature therefore remains open.

### 2.5. Summary and conclusions

Our experiments have defined the first quantitative pressure–permeability and temperature–permeability trends for spilites and epidiosites – two major types of high temperature, hydrothermally altered basalts in the oceanic crust. The experiments cover the range of in-situ  $P$ – $T$  conditions in the most hydrothermally active portion of the crust: up to 55 MPa effective pressure at temperatures up to 450 °C.

At room temperature the permeabilities of spilites decrease by a minimum of ~50–80% upon compression to 35 MPa effective pressure, and the permeabilities of epidiosites decrease by up to ~70% upon compression to 55 MPa. These magnitudes and the smooth trends of the changes are similar to those previously reported for lower temperature, clay- and zeolite-altered basalts from present-day oceanic crust. Heating the spilites and epidiosites to 450 °C at 50 MPa effective pressure steadily lowers their permeabilities by ~40% and 50%, respectively, somewhat less than that caused by room-temperature compression to 55 MPa effective pressure.

Both the above pressure- and temperature-effects on permeability are outweighed by the natural heterogeneity of permeability in spilites and epidiosites at the centimetre scale. Nevertheless, routine room-temperature gas permeameter measurements are easy to perform at in-situ pressures and they

account for more than half of the  $P$ – $T$  effect in restoring samples to in-situ conditions. If such high-pressure measurements are used in numerical modelling of hydrothermal flow through the oceanic crust, only minor errors would be incurred if our observed temperature–permeability trends were not incorporated in the simulations. On the other hand, our correlation Eqs. (6–9) provide a convenient means to quantitatively predict the effects of temperature on the permeability of spilites and epidiosites, if required.

Although our study was not designed to reveal the mechanisms by which permeability decreases upon heating, the excellent reversibility of our experiments points to a thermodynamic property as the likely cause. We speculate that differences between the thermoelastic expansions of the mineral grains surrounding pores in the spilites and epidiosites leads to constriction of the pore throats during heating, and then to re-opening of these throats during cooling.

### Acknowledgements

We gratefully acknowledge the logistical support during field work in the Sultanate of Oman by Khalid al-Tobi (Earth Secrets Co., Muscat) and Mohammed Al Araimi and Mohammed Al-Battashi (Public Authority for Mining, Muscat). Samuel Gilgen (University of Bern) assisted with sample collection in Oman, and Stanislas Sizaret (University of Orléans, France) kindly provided us with an epidiosite sample from the Troodos ophiolite. This work was supported by Swiss National Science Foundation (SNSF) Grants 200020-169653 and -188567 to L.W.D.

### References

- Aksyuk, A.M., Vitovtova, V.M., Pustovoy, A.A., Kharin, G.S., Shmonov, V.M., 1992. The permeability of oceanic basalts and some questions of the formation of hydrothermal springs in the rift zone of the Atlantic Ocean. *Oceanol. Engl. Transl.* 32, 1115–1122.
- Alabaster, T., Pearce, J., 1985. The Interrelationship between Magmatic and Ore-Forming Hydrothermal Processes in the Oman Ophiolite. *Econ. Geol.* 80, 1–16.  
<https://doi.org/10.2113/gsecongeo.80.1.1>.
- Anderson, R.N., Zoback, D.M., Hickman, S.H., Newmark, R.L., 1985. Permeability Versus Depth in the Upper Oceanic Crust: In Situ Measurements in DSDP Hole 504B, Eastern Equatorial Pacific. *J. Geophys. Res.* 90, 3659–3669. <https://doi.org/10.1029/JB090iB05p03659>.
- Bakker, R.R., Violay, M.E.S., Benson, P.M., Vinciguerra, S. C., 2015. Ductile flow in sub-volcanic carbonate basement as the main control for edifice stability: New experimental insights. *Earth Planet. Sci. Lett.* 430, 533–541. <https://doi.org/10.1016/j.epsl.2015.08.017>.
- Bach, W., Peucker-Ehrenbrink, B., Hart, S.R., Blusztajn, J.S., 2003. Geochemistry of hydrothermally altered oceanic crust: DSDP/ODP Hole 504B - Implications for seawater-crust exchange budgets

- and Sr- and Pb-isotopic evolution of the mantle. *Geochem. Geophys. Geosyst.* 4, 1–29.  
<https://doi.org/10.1007/s00269-010-0415-y>.
- Becker, K., Fisher, A.T., 2000. Permeability of upper oceanic basement on the eastern flank of the Endeavor Ridge determined with drill-string packer experiments. *J. Geophys. Res.* 105, 897–912. <https://doi.org/10.1029/1999JB900250>.
- Belgrano, T.M., Diamond, L.W., Vogt, Y., Biedermann, A.R., Gilgen, S. A., 2019. A revised map of volcanic units in the Oman ophiolite: insights into the architecture of an oceanic proto-arc volcanic sequence. *Solid Earth* 10, 1181–1217. <https://doi.org/10.5194/se-10-1181-2019>.
- Bernabé, Y., Mok, U., Evans, B., 2006. A note on the oscillating flow method for measuring rock permeability. *Int. J. Rock Mech. Min. Sci.* 43, 311–316.  
<https://doi.org/10.1016/j.ijrmms.2005.04.013>.
- Borggaard, O.K., Lindgreen, H.B., Mørup, S., 1982. Oxidation and reduction of structural iron in chlorite at 480 °C. *Clays Clay Minerals* 30, 353–364.  
<https://doi.org/10.1346/CCMN.1982.0300506>.
- Cann, J.R., 1969. Spilites from the Carlsberg Ridge, Indian Ocean. *J. Petrol.* 10, 1–19.  
<https://doi.org/10.1093/petrology/10.1.1>.
- Christensen, N.I., Ramanantoandro, R., 1988. Permeability of the oceanic crust based on experimental studies of basalt permeability at elevated pressures. *Tectonophysics* 149, 181–186.  
[https://doi.org/10.1016/0040-1951\(88\)90126-6](https://doi.org/10.1016/0040-1951(88)90126-6).
- Coelho, G., Branquet, Y., Sizaret, S., Arbaret, L., Champallier, R., Rozenbaum, O., 2015. Permeability of sheeted dykes beneath oceanic ridges: Strain experiments coupled with 3D numerical modeling of the Troodos Ophiolite, Cyprus. *Tectonophysics* 644, 138–150.  
<https://doi.org/10.1016/j.tecto.2015.01.004>.
- Diego Gatta, G., Merlini, M., Lee, Y., Poli, S., 2011. Behavior of epidote at high pressure and high temperature: a powder diffraction study up to 10 GPa and 1,200 K. *Phys. Chem.* 38, 419–428.  
<https://doi.org/10.1007/s00269-010-0415-y>.
- van Everdingen, D.A., 1995. Fracture characteristics of the Sheeted Dike Complex, Troodos ophiolite, Cyprus: Implications for permeability of oceanic crust. *J. Geophys. Res.* 100, 19957–19972. <https://doi.org/10.1029/95JB01575>.
- Fischer, G.J., 1992. The Determination of Permeability and Storage Capacity: Pore Pressure Oscillation Method. In: Evans, B., Wong, T. (Eds.), *Fault Mechanics and Transport Properties of*

- Rocks 1<sup>st</sup> edition. vol. 51. Academic Press, Cambridge, MA, pp. 187–211.  
[https://doi.org/10.1016/S0074-6142\(08\)62823-5](https://doi.org/10.1016/S0074-6142(08)62823-5).
- Fisher, A.T., 1998. Permeability within basaltic ocean crust. *Reviews of Geophysics* 36, 143–182.  
<https://doi.org/10.1029/97RG02916>.
- Galley, A.G., Bailes, A.H., Kitzler, G., 1993. Geological setting and hydrothermal evolution of the Chisel Lake and North Chisel Zn-Pb-Cu-Ag-Au massive sulfide deposits, Snow Lake, Manitoba. *Exploration and Mining Geology* 2, 271–295
- Gilbert, L.A., Bona, M.L., 2016. Permeability of oceanic crustal rock samples from IODP Hole 1256D. *Geochem. Geophys. Geosyst.* 17, 3825–3832. <https://doi.org/10.1002/2016GC006467>.
- Gilgen, S.A., Diamond, L.W., Mercolli, I., Al-Tobi, K., Maidment, D.W., Close, R., Al-Towaya, A., 2014. Volcanostratigraphic controls on the occurrence of massive sulfide deposits in the Semail Ophiolite, Oman. *Economic Geology* 109, 1585–1610.  
<https://doi.org/10.2113/econgeo.109.6.1585>.
- Gilgen, S.A., Diamond, L.W., Mercolli, I., 2016. Sub-seafloor epidosite alteration: Timing, depth and stratigraphic distribution in the Semail Ophiolite, Oman. *Lithos* 260, 191–210.  
<https://doi.org/10.1016/j.lithos.2016.05.014>.
- Gillis, K.M., Banerjee, N.R., 2000. Hydrothermal alteration patterns in supra-subduction zone ophiolites. *Geol. Soc. Am. Spec.* 349, 283–298. <https://doi.org/10.1130/0-8137-2349-3.283>.
- Gillis, K.M., Robinson, P.T., 1990. Patterns and processes of alteration in the lavas and dykes of the Troodos Ophiolite, Cyprus. *J. Geophys. Res. Solid Earth* 95, 21523–21548.  
<https://doi.org/10.1029/JB095iB13p21523>.
- Guo, X., Zou, G., Wang, Y., Wang, Y., Gao, T., 2017. Investigation of the temperature effect on rock permeability sensitivity. *J. Pet. Sci. Eng.* 156, 616–622.  
<https://doi.org/10.1016/j.petrol.2017.06.045>.
- Hannington, M.D., 2014. Volcanogenic massive sulfide deposits. In: Holland, H.D., Turekian, K.K. (Eds.), *Treatise on Geochemistry*, 2nd edition. Elsevier, Oxford, pp. 463–488.
- Hannington, M.D., Santaguida, F., Kjarsgaard, I.M., Cathles, L.M., 2003. Regional-scale hydrothermal alteration in the Central Blake River Group, western Abitibi subprovince, Canada: Implications for VMS prospectivity. *Miner. Deposita* 38, 393–422.  
<https://doi.org/10.1007/s00126-002-0298-z>.

- 
- Hasenclever, J., Theissen-Krah, S., Rüpke, L.H., Morgan, J.P., Iyer, K., Petersen, S., Devey, C.W., 2014. Hybrid shallow on-axis and deep off-axis hydrothermal circulation at fast-spreading ridges. *Nature* 508, 508–512. <https://doi.org/10.1038/nature13174>.
- Heap, M.J.J., Reuschlé, T., Farquharson, J.I.I., Baud, P., 2018. Permeability of volcanic rocks to gas and water. *J. Volcanol. Geotherm. Res.* 354, 29–38. <https://doi.org/10.1016/j.jvolgeores.2018.02.002>.
- Holland, T.J.B., Powell, R., 2011. An improved and extended internally consistent thermodynamic dataset for phases of petrological interest, involving a new equation of state for solids. *J. Metamorph. Geol.* 29, 333–383. <https://doi.org/10.1111/j.1525-1314.2010.00923.x>.
- Honarpour, M., Koederitz, L., Harvey, A.H., 1986. Measurement of Rock Relative Permeability. In: *Relative Permeability of Petroleum Reservoirs*. CRC Press, Boca Raton, FL. pp. 1–12.
- Jarrard, R.D., Abrams, L.J., Pockalny, R., Larson, R.L., Hirono, T., 2003. Physical properties of upper oceanic crust: Ocean Drilling Program Hole 801C and the waning of hydrothermal circulation. *J. Geophys. Res. Solid Earth* 108, 1–26. <https://doi.org/10.1029/2001JB001727>.
- Johnson, D.M., 1980. Fluid permeability of oceanic basalts. Initial Rep. Deep Sea Drill. Proj. 68, 1473–1477.
- Jowitt, S.M., Jenkin, G.R.T., Coogan, L.A., Naden, J., 2012. Quantifying the release of base metals from source rocks for volcanogenic massive sulfide deposits: Effects of protolith composition and alteration mineralogy. *J. Geochem. Explor.* 118, 47–59. <https://doi.org/10.1016/j.gexplo.2012.04.005>.
- Juteau, T., Manac'h, G., Moreau, O., Lécuyer, C., Ramboz, C., 2000. The high temperature reaction zone of the Oman ophiolite: New field data, microthermometry of fluid inclusions, PIXE analyses and oxygen isotopic ratios. *Mar. Geophys. Res.* 21, 351–385. <https://doi.org/10.1023/A:1026798811446>.
- Karato, S., 1983. Physical properties of basalts from Deep Sea Drilling Project Hole 504B, Costa Rica Rift. Initial Rep. Deep Sea Drill. Proj. 69, 687–695.
- Kozusnikova, A., Konečný, P., 2011. Influence of temperature on the permeability of rocks. *Geotechnique* 61, 1081–1085. <https://doi.org/10.1680/geot.8.T.034>.
- Kranz, R.L., Saltzman, J.S., Blacic, J.D., 1990. Hydraulic diffusivity measurements on laboratory rock samples using an oscillating pore pressure method. *Int. J. Rock Mech. Min. Sci.* 27, 345–352. [https://doi.org/10.1016/0148-9062\(90\)92709-N](https://doi.org/10.1016/0148-9062(90)92709-N).
-

- 
- Kusano, Y., Umino, S., Shinjo, R., Ikei, A., Adachi, Y., Miyashita, S., Arai, S., 2017. Contribution of slab-derived fluid and sedimentary melt in the incipient arc magmas with development of the paleo-arc in the Oman Ophiolite. *Chemical Geology* 449, 206–225. <https://doi.org/10.1016/j.chemgeo.2016.12.012>.
- Kushnir, A.R.L., Martel, C., Champallier, R., Wadsworth, F.B., 2017. Permeability Evolution in Variably Glassy Basaltic Andesites Measured Under Magmatic Conditions. *Geophys. Res. Lett.* 44, 10, 262–10,271. <https://doi.org/10.1002/2017GL074042>.
- Lempart, M., Derkowski, A., Luberd-Durnaś, K., Skiba, M., Błachowski, A., 2018. Dehydrogenation and dehydroxylation as drivers of the thermal decomposition of Fe-chlorites. *American Mineralogist* 103, 1837–1850. <https://doi.org/10.2138/am-2018-6541>.
- Liu, J., Li, B., Tian, W., Wu, X., 2018. Investigating and predicting permeability variation in thermally cracked dry rocks. *Int. J. Rock Mech. Min. Sci.* 103, 77–88. <https://doi.org/10.1016/j.ijrmms.2018.01.023>.
- Mordensky, S.P., Kennedy, B.M., Villeneuve, M.C., Lavallée, Y., Reichow, M.K., Wallace, P.A., 2019. Increasing the Permeability of Hydrothermally Altered Andesite by Transitory Heating. *Geochem. Geophys. Geosyst.* 20, 5251–5269. <https://doi.org/10.1029/2019GC008409>.
- Mottl, M.J., Wheat, G.C., 1994. Hydrothermal circulation through mid-ocean ridge flanks: Fluxes of heat and magnesium. *Geochim. Cosmochim. Acta* 58, 2225–2237. [https://doi.org/10.1016/0016-7037\(94\)90007-8](https://doi.org/10.1016/0016-7037(94)90007-8).
- Nahhas, T., Py, X., Sadiki, N., 2019. Experimental investigation of basalt rocks as storage material for high-temperature concentrated solar power plants. *Renew. Sust. Energ. Rev.* 110, 226–235. <https://doi.org/10.1016/j.rser.2019.04.060>.
- Nehlig, P., Juteau, T., Bendel, V., Cotten, J., 1994. The root zones of oceanic hydrothermal systems: Constraints from the Samail ophiolite (Oman). *J. Geophys. R.* 99, 4703–4713. <https://doi.org/10.1029/93JB02663>.
- Osozawa, S., Shinjo, R., Lo, C.H., Jahn, B.M., Hoang, N., Sasaki, M., Wakabayashi, J., 2012. Geochemistry and geochronology of the Troodos ophiolite: An SSZ ophiolite generated by subduction initiation and an extended episode of ridge subduction? *Lithosphere* 4, 497–510. <https://doi.org/10.1130/L205.1>.
- Paterson, M.S., 1970. A high-pressure, high-temperature apparatus for rock deformation. *Int. J. Rock Mech. Min. Sci.* 7, 517–526. [https://doi.org/10.1016/0148-9062\(70\)90004-5](https://doi.org/10.1016/0148-9062(70)90004-5).
-



- 
- Patten, C.G.C., Pitcairn, I.K., Teagle, D.A.H., Harris, M., 2016. Sulphide mineral evolution and metal mobility during alteration of the oceanic crust: Insights from ODP Hole 1256D. *Geochim. Cosmochim. Acta* 193, 132–159. <https://doi.org/10.1016/j.gca.2016.08.009>.
- Petrini, C., 2019. Fluid Controls on Subduction Thrust Seismicity: Seismo-Hydro-Mechanical Modelling Combined with Experimental Studies. PhD Dissertation, Swiss Federal Institute of Technology (ETH) Zurich. 203 pp. <https://doi.org/10.3929/ethz-b-000387985>.
- Richardson, C.J., Cann, J.R., Richards, H.G., Cowan, J.G., Siegel, J., 1987. Metal-depleted root zones of the Troodos ore-forming hydrothermal systems, Cyprus. *Earth Planet. Sci. Lett.* 84, 243–253. <https://doi.org/10.1097/Ol.ta.0000220385.34197.f9>.
- Richter, L., Diamond, L.W. 2019. Identifying deep hydrothermal fluids that leach metals from the oceanic crust and generate seafloor VMS deposits. SGA Biennial Meeting: Proceedings of the 15<sup>th</sup> SGA Biennial Meeting, The Society for Geology Applied to Mineral Deposits (SGA), Scotland (2019), pp. 76–79.
- Richter, D., Simmons, G., 1974. Thermal expansion behavior of igneous rocks. *Int. J. Rock Mech. Min. Sci.* 11, 403–411. [https://doi.org/10.1016/0148-9062\(74\)91111-5](https://doi.org/10.1016/0148-9062(74)91111-5).
- Seyfried, W.E., Berndt, M.E., Seewald, J.S., 1988. Hydrothermal alteration processes at mid-ocean ridges; constraints from diabase alteration experiments, hot-spring fluids and composition of the oceanic crust. *Canadian Mineralogist* 26, 787–804.
- Shmonov, V.M., Vitovtova, V.M., Zarubina, I.V., 1995. Permeability of rocks at elevated temperatures and pressures. In: Shmulovich, K.I., Yardley, B.W.D., Gonchar, G.G. (Eds.), *Fluids in the Crust: Equilibrium and Transport Properties*. Springer, Netherlands, Dordrecht, pp. 285–313. [https://doi.org/10.1007/978-94-011-1226-0\\_11](https://doi.org/10.1007/978-94-011-1226-0_11).
- Staudigel, H., 2014. Chemical Fluxes from Hydrothermal Alteration of the Oceanic Crust. In: Holland, H.D., Turekian, K.K. (Eds.), *Treatise on Geochemistry* 2nd edition. vol. 4. Elsevier, Oxford, pp. 583–603. <http://doi.org/10.1016/B978-0-08-095975-7.00318-1>.
- Sun, Y.Z., Xie, L.Z., He, B., Gao, C., Wang, J., 2016. Effects of effective stress and temperature on permeability of sandstone from CO<sub>2</sub>-plume geothermal reservoir. *J. Rock Mech. Geotech. Eng.* 8, 819–827. <https://doi.org/10.1016/j.jrmge.2016.07.004>.
- Tribaudino, M., Angel, R.J., Cámara, F., Nestola, F., Pasqual, D., Margiolaki, I., 2010. Thermal expansion of plagioclase feldspars. *Contrib. Mineral Petrol.* 160, 899–908. <https://doi.org/10.1007/s00410-010-0513-3>.
-

Zaraisky, G.P., Balashov, V.N., 1995. Thermal decompaction of rocks. In: Shmulovich, K.I., Yardley, B.W.D., Gonchar, G.G., (Eds.), *Fluids in the Crust: Equilibrium and Transport Properties*. Springer, Netherlands, pp. 253–284. [https://doi.org/10.1007/978-94-011-1226-0\\_10](https://doi.org/10.1007/978-94-011-1226-0_10).

### 3. Rock-matrix porosity and permeability in the hydrothermally altered, upper oceanic crust, Oman ophiolite

Alannah C. Brett-Adams<sup>a</sup>, Larryn W. Diamond<sup>a</sup>, Samuel Weber<sup>a</sup> and Samuel A. Gilgen<sup>a</sup>

<sup>a</sup>*Institute of Geological Sciences, University of Bern, Baltzerstrasse 1+3, Bern CH-3012, Switzerland*

Unpublished manuscript

*Author contributions:* Alannah Brett collected the samples in Oman, carried out petrographic examinations, conducted the porosity and geochemical measurements, and prepared the manuscript. Permeability measurements were made at a commercial laboratory, but interpretations were made by the first author. Larryn Diamond, as thesis supervisor, guided the research, assisted with field sampling and edited the manuscript. Samuel Weber assisted with field sampling, simulated the evolution of porosity and mineralogy due to the spilite-to-epidosite reaction using the Flotran code, and performed 2D hydraulic simulations in PFlotran to calculate the permeability of spilite interpillow hyaloclastites. Samuel Gilgen collected and measured an initial set of sample porosities and permeabilities during his PhD thesis (Gilgen, 2016) and together with Diamond made the first field observations that constrain the relative permeabilities of lava types and the mechanism of epidosite formation.

#### Abstract

The distribution of permeability in magmatically active, upper oceanic crust controls hydrothermal circulation and all the water–rock interaction processes that this induces. Whereas data are available on the rock-matrix porosity and permeability of fresh basalts and of low-temperature hydrothermally altered basalts, little is known about these properties in high-temperature altered basalts. The role of these rocks in crustal-scale permeability and in hydrothermal flow paths is therefore unclear. To fill this gap, we conducted the first systematic study of rock-matrix porosities and permeabilities of oceanic basalts pervasively altered to greenschist-facies hydrothermal minerals. Samples were taken from the sheeted dyke complex and the comagmatic, axial Geotimes lavas in the Semail ophiolite, Oman, and measured by pycnometry and high-pressure gas permeameter. These glass-free rocks represent regionally distributed spilite alteration (chlorite–albite  $\pm$  actinolite) attributable to fluid downflow paths with modest water–rock ratios, and more localised epidosite alteration (epidote–quartz) characteristic of upflow paths with extremely high water–rock ratios. Different lava morphologies altered to spilite generally obey the following order of decreasing porosity and permeability: interpillow hyaloclastites (3–26 vol.%,  $10^{-17}$  to  $10^{-15}$  m<sup>2</sup>) > pillow cores (4–12 vol.%;  $\sim 10^{-19}$  to  $6 \times 10^{-18}$  m<sup>2</sup>) > pillow rims (4–11 vol.%;  $\sim 10^{-19}$  to  $2 \times 10^{-18}$  m<sup>2</sup>) > massive flows (5–9 vol.%;  $\sim 10^{-19}$  m<sup>2</sup>) > dykes (1–5 vol.%;  $\sim 10^{-19}$  to  $4 \times 10^{-19}$  m<sup>2</sup>). These new values for pillows, massive flows and dykes overlap with existing data on fresh and low-temperature altered basalts, suggesting that even extreme spilite alteration causes little change

to rock-matrix hydraulic properties. The new data on spilite-altered interpillow hyaloclastites are unique. Their remarkably high permeabilities raise the bulk permeabilities of pillow stack sequences to  $\sim 10^{-16} \text{ m}^2$ , within the range required by numerical simulations to explain observed heat and fluid discharge from the seafloor, even without considering a contribution from fracture permeability. Epidosites form by replacing spilites in the same strict order of rock types as defined by their permeabilities (above). The spilite-to-epidosite reaction increases porosity by 9–14 vol.% and permeability by 4.5 orders of magnitude, imparting permeabilities of  $\sim 10^{-15} \text{ m}^2$  to endmember epidosites, regardless of their lava morphology. This enormous reaction-enhanced permeability explains how huge water–rock ratios are attained during pervasive porous-medium alteration of  $\text{km}^3$ -sized epidosite bodies along hydrothermal upflow paths.

### 3.1. Introduction

Understanding hydrothermal transport of heat and mass through the basaltic, upper oceanic crust depends on a quantitative and realistic model of crustal permeability (Alt, 1995; Coogan & Gillis, 2018; Fisher, 1998; Hasenclever et al., 2014). Previous numerical models of this hydrothermal system invoke high bulk permeabilities ( $10^{-16}$ – $10^{-11} \text{ m}^2$ ; Fisher, 1998 and references therein; Hasenclever et al., 2014) to explain heat flow and fluid discharge, but whether these values represent both fracture permeability and rock-matrix permeability is unclear. Fracture networks are undoubtedly important and have often been viewed as the dominant form of permeability with estimates as high as  $\sim 10^{-12}$ – $10^{-6} \text{ m}^2$  (van Everdingen, 1995; Nehlig, 1994), but these estimates cannot be reconciled with permeabilities determined by *in-situ* hydraulic tests, which indicate  $1 \times 10^{-18}$  to  $1 \times 10^{-13} \text{ m}^2$  (e.g., Anderson et al., 1985; Becker, 1989; Becker & Fisher, 2000; Fisher, 1998). On the other hand, the importance of rock-matrix permeability in sub-seafloor circulation systems is testified by the intense and pervasive hydrothermal alteration of the upper crust and by the accompanying metasomatism and scavenging of metals by the hydrothermal fluid to form seafloor volcanic massive sulphide (VMS) deposits (Jowitt et al., 2012; Patten et al., 2016; Richter & Diamond, 2019). Despite the ubiquity of altered rocks in the upper crust, very little is known about their rock-matrix porosity and permeability and hence their hydraulic role in fluid convection systems

Basaltic dykes and lavas in ophiolites show two main types of pervasive rock-matrix alteration due to hydrothermal metasomatism at sub- to greenschist-facies conditions ( $\sim 200$ – $450^\circ \text{C}$ ). Volumetrically dominant by far are “spilites” (Cann, 1969; Honnorez, 2003), which show hydrothermal assemblages of albite + chlorite  $\pm$  actinolite  $\pm$  Fe-oxide. These formed during crustal-scale seawater downwelling, which enriched the rocks in Mg and Na and depleted them in Ca (Alt, 1995). The second type, “epidosites”, occur in more localised zones. They are former spilites metasomatised via Ca enrichment and Mg and Na depletion to assemblages of epidote + quartz + titanite + Fe-oxide by upwelling fluids at  $\sim 230$ – $420^\circ \text{C}$  (Richardson et al., 1987; Schiffman & Smith, 1988; Coelho et al., 2015; Richter & Diamond, 2019; Seyfried et al., 1988; Weber et al., submitted). Spilites and epidosites appear to be rare

in *in-situ* mid-oceanic ridge (MOR) settings compared to low-temperature zeolite and clay alterations (Staudigel, 2014), but they are common in Archean to Cretaceous ophiolites (Alabaster & Pearce, 1985; Coehlo et al., 2015; Galley et al., 1993; Gilgen et al., 2014; Gillis & Banerjee, 2000; Hannington et al., 2003; Richardson et al., 1987). The water–rock interaction that converts the rock-matrix to spilites or epidiosites is important, because it leads to transfers of mass and heat through the crust, to buffering of seawater chemistry (e.g., Mottl & Wheat, 1994; Bach et al., 2003) and to leaching of base and precious metals for VMS deposits (e.g., Richardson et al., 1987; Hannington, 2014; Jowitt et al., 2012; Patten et al., 2016).

Epidiosites are well known from the sheeted dyke complex in the Troodos ophiolite, Cyprus, where they were first recognised as markers of extreme fluid flux along upflow paths (Richardson et al., 1987; Schiffman & Smith, 1988). However, the Semail ophiolite, Oman, hosts epidiosites mostly in its extrusive lavas, where bodies occur up to 1 km<sup>2</sup> in outcrop without obvious fracture controls on fluid flow (Gilgen et al., 2016). This implies that epidiosites have sufficient rock-matrix permeability to permit large-scale alteration of their rock-matrix. Thus far we know that epidiosites can have a moderate permeability of  $\sim 1 \times 10^{-18}$  m<sup>2</sup>, based measurements on one sample by Coehlo et al. (2015). Other workers have described the granoblastic and highly porous texture of epidiosites, suggesting that the spilite-to-epidosite reaction could increase rock-matrix porosity by 10–20 vol.%, potentially enhancing permeability and permitting self-propagation of the hydrothermal fluid (Cann et al., 2014; Harper et al., 1988). This porosity increase has since been supported by rock composition analyses and reactive transport simulations by Weber et al. (submitted), but to date no study has measured the porosity or permeability changes associated with the spilite-to-epidosite reaction.

Few porosity and permeability measurements of spilitised basalts exist despite their abundance in ophiolites and their occurrence in drill cores from *in-situ* oceanic crust. Spilite dykes have porosities of ~0.4–4 vol.% (Gilbert & Salisbury, 2011; Pezard, 1990; Violay et al., 2010) and permeabilities from  $\sim 5 \times 10^{-21}$  to  $1 \times 10^{-15}$  m<sup>2</sup> (Gilbert & Bona, 2016; Coehlo et al., 2015). The only other spilites measured are a few pillow basalts with porosities of 3–5 vol.% (Christensen & Smewing, 1981) and a breccia with 8.7 vol.% (Pezard, 1990).

To fill these gaps in knowledge, the present study provides new measurements of rock-matrix porosity and permeability of spilites and epidiosites from the MOR-type lavas and comagmatic sheeted dyke complex (SDC) generated by ridge-axis spreading in the Semail ophiolite. Such measurements provide most insight into fluid circulation and fluid–rock interaction in the oceanic crust once they are integrated into crustal-scale thermal–hydraulic–chemical simulations. Accordingly, our aim is to provide a robust dataset of rock-matrix porosity and permeability, corrected for any post-alteration artefacts, that is suitable for future numerical simulations. This includes providing constraints on the dependency of permeability on porosity in the major rock types in the upper crust (dykes, massive flows, pillow flows, hyaloclastites), all as function of the extent of the spilite-to-epidosite reaction. To establish these relationships we interpolate our laboratory measurements and constrain unknowns by

performing small-scale hydraulic and reactive-transport simulations. Our results quantify the porosity and permeability required to explain the vast volumes of pervasive alteration in the Semail upper crust, and they show that the spilite-to-epidosite reaction enhances porosity and permeability enormously, facilitating the pervasive, high-flux upflow already deduced qualitatively for epidiosites. The comparatively minor role of fracture permeability in spilite and epidiosite alteration is addressed in Chapter 4 of this thesis.

### **3.2. Geological Setting and Hydrothermal Alteration**

The Semail ophiolite represents a slice of oceanic lithosphere formed in a proto-arc, subduction-initiation setting in the Upper Cretaceous (Belgrano & Diamond, 2019; Guilmette et al., 2018; MacLeod et al., 2013; Pearce et al., 1984). The crust first formed at a fast-spreading ridge axis, producing gabbros, a sheeted dyke complex (SDC) and overlying comagmatic basalt to basaltic-andesite lavas (Geotimes unit, also known as V1) with MORB-type major-element chemistry. Despite its suprasubduction zone setting, the morphology, igneous stratigraphy and structural characteristics of the axial upper crustal rocks are comparable to that at modern, fast-spreading mid-ocean ridges, such as the East Pacific Rise (e.g., Einaudi et al., 2000; Kusano et al., 2014; Nicolas et al., 2000). Owing to these similarities, our study focuses on the axial SDC and Geotimes units. In addition to the axial units, the Semail crust contains a thick sequence of younger, compositionally distinct lavas, which have no accompanying sheeted dyke complex but are instead fed by localised dyke swarms: off-axial primitive lavas of the Lasail unit, overlain by the post-axial Tholeiitic Alley and Boninitic Alley units (Belgrano et al., 2019).

Spilite alteration overprints the SDC, although there are variations in intensity from pervasively altered dykes in which only relicts of igneous clinopyroxene are preserved through to rare, weakly altered dykes (Miyashita et al., 2003). In contrast, the Geotimes and Lasail lavas are very strongly altered to spilite throughout the ophiolite (Alabaster et al., 1982; Alabaster & Pearce, 1985), with glass being preserved extremely rarely (Kusano et al., 2017). Spilite alteration increases from lower to upper greenschist facies assemblages with depth, whereas the post-axial Tholeiitic Alley and Boninitic Alley lavas are regionally altered to zeolite–celadonite–smectite  $\pm$  chlorite–albite assemblages (Alabaster & Pearce, 1985). The Geotimes, Tholeiitic Alley and Boninitic Alley lavas all host Cyprus-type VMS deposits, attesting to the intensity of their hydrothermal alteration (Gilgen et al., 2014).

Epidiosite bodies overprint spilite alteration in the SDC and in the overlying Geotimes and Lasail lavas. The lava-hosted bodies are much larger and more numerous (Gilgen et al., 2016). Epidiosite alteration of cross-cutting dykes of known volcanostratigraphic affinity shows that the majority of epidiosites formed during Tholeiitic Alley time, with a minority during Lasail time (Gilgen et al., 2016). This mostly post-axial timing of epidiosite alteration is unimportant for the present study, in that the changes in porosity and permeability induced by the spilite-to-epidosite alteration are independent of absolute age.

In the Geotimes pillow outcrops, a spectrum from spilite to complete epidosite alteration can be readily distinguished. Gilgen et al. (2016) mapped three stages of progressive alteration that develop over distances of up to 200 m perpendicular to the margins of major epidosite bodies ( $\leq 1 \text{ km}^2$ ). Their systematic concentric arrangement around the epidosite bodies shows that the stages correspond to the following temporal sequence: (1) *incipient epidosites*, in which only the interpillow hyaloclastite is converted to epidosite, leaving spilite assemblages in the pillow cores and rims. The total area of epidosite in such outcrops is 5–10 area% (Figure 3.1a); (2) *intermediate epidosites*, in which the interpillow hyaloclastite and the pillow cores are converted to epidosite, but the pillow rims retain spilite alteration (10–80 area% epidosite; Figure 3.1b); and (3) *complete epidosites*, in which interpillows, pillow cores and pillow rims are all converted to epidosite ( $> 80$  area% epidosite; Figure 3.1c). Although epidosites mapped as "complete" exhibit an intense pistachio-green colour in outcrop owing their high epidote content, they only rarely consist of mineralogical endmembers composed of 100 vol.% quartz + epidote + Fe-Ti-oxides, but rather contain minor relict augite and/or chlorite (Weber et al., submitted). Spilitised massive flows in the Geotimes unit are typically only weakly converted to epidosite, displaying epidosite only along the margins of joints or along the centres of cooling columns, rarely summing to more than 10 vol.% epidosite in outcrops. Complete or stripy epidosite alteration of dykes (Figure 3.1d) is common in the Semail SDC (Gilgen et al., 2016), similar to that in the Troodos ophiolite (Cann et al., 2015).

In addition to sub-seafloor spilite and epidosite alteration, the SDC and Geotimes units also show later features of importance in our study: (1) cross-cutting hydrothermal veins of coarsely crystalline calcite and spatially associated pore-fillings in their wall rocks. These veins formed at  $\sim 70\text{--}90^\circ\text{C}$  from waters with 0.2–0.7 wt.  $\text{NaCl}_{\text{equiv.}}$ , well below the 3.2 wt.%  $\text{NaCl}_{\text{equiv.}}$  seawater-like salinity of the spilite-forming and epidosite-forming fluids (Richter & Diamond, submitted); (2) fine-grained calcite travertine deposited by evaporation of shallow wadi groundwaters during exposure of the outcrops. Both the calcite veins and travertine are referred to hereafter as "late calcite"; (3) open fractures induced during obduction and weathering.



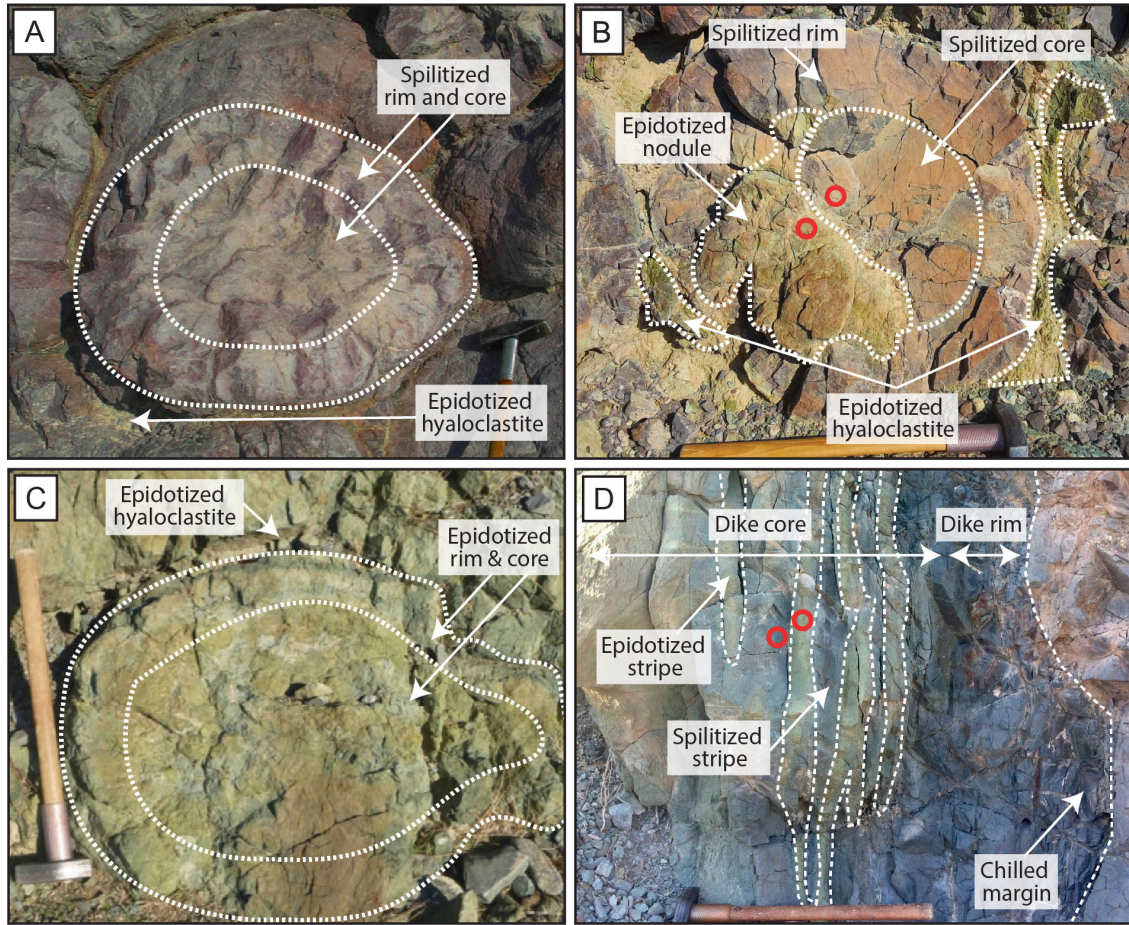


**Figure 3.1.** Field photographs showing stages of spilite-to-epidosite alteration in pillow lavas and a dyke. Dashed white lines outline boundaries between different zones within the pillows and dyke. Red circles indicate potential locations for sampling “conjugate pairs” of spilite and epidosite samples. (a) Incipient epidosite, in which only the interpillow hyaloclastite is epidotised whereas the pillows display epidote-free spilite alteration. (b) Intermediate epidosite, in which the interpillow hyaloclastite and part of the pillow core is altered to epidosite. (c) Complete epidosite. (d) Stripy intermediate epidosite alteration of the core of a spilite dyke. The grey stripes in the core and the chilled margin show spilite alteration.

### 3.3. Approach

Reconstruction of laboratory measurements of rock-matrix porosity and permeability to their values at the time of sub-seafloor hydrothermal alteration requires a targeted sampling and measurement approach to recognise and correct for post-alteration overprinting processes and for  $P$ – $T$  reequilibration to laboratory conditions. For the samples from the Oman ophiolite, overprinting processes include formation of new pores, fractures and mineral precipitates during post-spilite and post-epidosite hydrothermal activity, obduction, uplift and finally subaerial weathering. We therefore provide petrographic observations to characterise the various pore-types and their fillings and to establish their relative ages and relevance to our reconstruction. In addition to the mappable (outcrop-scale) stages in progressive epidosite alteration mentioned in Section 3.2 (incipient, intermediate and complete), we have classified our hand samples according to an index of epidosite alteration intensity into



(1) *endmember spilites* (epidote-free), (2) *weak epidosites* (< 20 vol.% epidote + quartz), (3) *partial epidosites* (20–90 vol.% epidote + quartz) and (4) the uncommon *endmember epidosites* (90–100 vol.% epidote + quartz). This mineralogical classification enables precise monitoring of changes in porosity and permeability due to the spilite-to-epidosite reaction.

We present new porosity measurements on samples from dykes, massive flows, interpillow hyaloclastites, pillow cores and pillow rims, of both alteration types (spilite and epidosite). These values are then corrected for clogging by late calcite and the effect of  $P$ – $T$  reequilibration is quantified by thermoelastic calculations. New permeability measurements on the same samples are presented, except for interpillow hyaloclastites in spilite lavas, which are too friable for conventional measurements. Unfortunately, the permeability measurements could not be corrected for calcite clogging, therefore weight is given to results from the subset of calcite-free samples. The effects of  $P$ – $T$  reequilibration on permeability are quantified by reference to the measurements reported in Chapter 2 of this Thesis. To assess the permeability of the hyaloclastites we performed hydraulic simulations to find the range of possible values. From this dataset, trends can be recognised between different lava types, zones within pillows (i.e. core versus rim), and extents of igneous fractional crystallization.

Our reconnaissance work showed that, even for a given extent of igneous fractionation and intensity of hydrothermal alteration, the measured porosity and permeability varies between different outcrops of the same rock types, e.g. massive flows and dykes, and even between pillows within the same outcrop. This indicates that changes induced by the spilite-to-epidosite reaction can be quantified only by comparing samples that were situated adjacent to each other (within 30 cm) within the same individual pillows, dykes or massive flows. We therefore sampled such closely situated spilites and epidosites, which we refer to as “conjugate pairs” (Figure 3.1b and d), and based on quantitative analyses of their mineralogy, we used them to quantify specific steps in the reaction-induced porosity and permeability. Reactive transport simulations were then used to predict the evolution of porosity continuously throughout the spilite-to-epidosite reaction.

### 3.3.1. Samples

Samples were collected from spilite and epidosite outcrops of the axial Geotimes lavas and comagmatic sheeted dyke complex in the Semail ophiolite. The samples cover the small variation of vesicularity in these units. Outcrops were chosen with as little post-epidosite hydrothermal calcite veining, open fractures and wadi travertine as possible. Most samples were retrieved as cylindrical plugs using a portable, water-cooled drill equipped with a diamond-tipped core bit of 2.54 cm diameter. The remainder were collected as oversized samples where outcrop conditions allowed extraction by leverage with chisels without heavy hammering, to avoid inducing fractures. These samples were subsequently cored in the laboratory. Interpillow hyaloclastites altered to epidosite have the same high tenacity as other epidosites and were sampled as above. However, the spilitised hyaloclastites were too fragile to drill and so samples were carefully prized out of the outcrops, wrapped in padding and placed in rigid

containers for transport. All the samples were carefully examined under a hand lens and any showing fractures or calcite veins were discarded, leaving only a small subset of high quality samples for measurement of rock-matrix properties. The characteristics and location of each sample are summarised in Table 3.1.

**Table 3.1.** Hand sample petrophysical and alteration characteristics, and sample locations

Sample ID	UTM mE	UTM mN	Morphology	Alteration	Total <sup>a</sup> epidote + quartz content (vol.%)	Porosity A <sup>b</sup> (vol.%)	Average <sup>c</sup> calcite in sample powder (vol.%)	Fracture <sup>d</sup> correction (1.5 = common fracture, 0.5 rare fractures)	Porosity B <sup>e</sup> (vol.%)	Permeability <sup>f</sup> (m <sup>2</sup> )	Bulk density (g/cm <sup>3</sup> )
AB17-42F-spl/e-a	432358	2739423	Flow	Spilitised	33	3.61	5.57	—	9.18	$9.87 \times 10^{-20}$	2.80
AB17-42F-epi-a	432358	2739423	Flow	Epidotised	91	6.11	4.62	0.5	10.23	$5.07 \times 10^{-18}$	2.93
AB17-31C-spl-b	538351	2608870	Dyke	Spilitised	18	1.61	0.22	—	1.83	$9.87 \times 10^{-20}$	2.78
AB17-31C-epi	538351	2608870	Dyke	Epidotised	66	8.13	5.81	—	13.94	$3.04 \times 10^{-18}$	3.00
AB17-32C-spl	538351	2608870	Dyke	Spilitised	20	4.81	0.43	—	5.24	$2.46 \times 10^{-19}$	2.81
AB17-32C-epi	538351	2608870	Dyke	Epidotised	63	4.99	2.78	—	7.77	$1.90 \times 10^{-18}$	3.01
AB17-33C-spl	538351	2608870	Dyke	Spilitised	19	0.59	0.28	—	0.88	$9.87 \times 10^{-20}$	2.79
AB17-33C-epi	538351	2608870	Dyke	Epidotised	61	8.02	0.45	—	8.47	$3.43 \times 10^{-17}$	2.77
AB17-33R-epi	538351	2608870	Dyke	Epidotised	88	9.03	1.55	1.5	9.08	$3.98 \times 10^{-15}$	3.02
AB17-37C-spl	443641	2715879	Pillow core	Spilitised	9	0.60	4.79	—	5.39	$9.93 \times 10^{-19}$	2.81
AB17-37C-epi-a	443641	2715879	Pillow core	Epidotised	100	15.93	4.11	1.5	18.54	$1.91 \times 10^{-15}$	2.67
AB17-39C-spl	435338	2725271	Pillow core	Spilitised	29	11.40	0.30	—	11.70	$6.53 \times 10^{-18}$	2.59
AB17-40C-spl-a	435338	2725271	Pillow core	Spilitised	30	11.35	0.48	2.0	9.83	$7.43 \times 10^{-18}$	2.53
AB17-41C-spl-a	432249	2739587	Pillow core	Spilitised	17	7.42	9.62	1.5	9.14	$6.26 \times 10^{-18}$	2.61
AB17-41C-epi-b	432249	2739587	Pillow core	Epidotised	96	7.39	13.07	—	20.45	$1.94 \times 10^{-17}$	2.86
AB17-44C-spl	432150	2739701	Pillow core	Spilitised	25	7.92	1.78	—	9.70	$9.87 \times 10^{-20}$	2.56
AB17-44R-spl	432150	2739701	Pillow rim	Spilitised	16	5.07	0.69	—	5.76	$9.87 \times 10^{-20}$	2.62
AB17-44C-epi	432150	2739701	Pillow core	Epidotised	100	8.84	17.76	0.5	26.10	$1.64 \times 10^{-17}$	2.93
AB16-4272c	443182	2716103	Pillow core	Spilitised	12	3.26	4.71	—	7.97	$9.87 \times 10^{-20}$	2.77
AB16-427R	443182	2716103	Pillow rim	Spilitised	12	0.63	7.57	—	3.16	$9.87 \times 10^{-20}$	2.77
AB16-4273c	443182	2716103	Pillow core	Epidotised	72	10.70	3.06	—	13.76	$1.32 \times 10^{-16}$	2.86
AB17-25C	431934	2739740	Pillow core	Epidotised	81	13.00	0.80	—	13.80	$3.51 \times 10^{-16}$	2.79
AB17-25R	431934	2739740	Pillow rim	Epidotised	76	5.24	0.47	—	5.71	$1.64 \times 10^{-19}$	2.77
AB16-4431bR-1_A	431979	2739807	Pillow rim	Epidotised	66	9.68	9.03	—	18.72	$6.52 \times 10^{-17}$	2.91
LD10-120-3	444490	2739546	Pillow core	Epidotised	59	9.36	9.36	—	18.72	$4.32 \times 10^{-18}$	2.84
AB16-4131C	431926	2739580	Pillow core	Epidotised	79	6.23	2.17	—	8.40	$1.89 \times 10^{-18}$	3.02
SG14-56	431785	2739627	Pillow core	Epidotised	—	4.13	7.15	—	11.28	$9.85 \times 10^{-17}$	3.04
LW5C	431950	2740730	Pillow core	Epidotised	—	10.08	0.00	—	10.08	$2.92 \times 10^{-15}$	2.72
LW7-IP	432080	2739611	Hyaloclastite (IP)	Epidotised	—	10.81	6.33	—	17.14	$2.70 \times 10^{-15}$	2.78
AB16-4133a	431927	2739580	Hyaloclastite (IP)	Epidotised	—	6.20	11.02	—	17.23	$1.31 \times 10^{-17}$	3.00
SWOM-1885	432184	2737889	Hyaloclastite (IP)	Epidotised	—	6.78	1.44	—	8.21	$4.70 \times 10^{-16}$	2.98

Sample ID	UTM mE	UTM mN	Morphology	Alteration	Total <sup>a</sup> epidote + quartz content (vol.%)	Porosity A <sup>b</sup> (vol.%)	Average <sup>c</sup> calcite in sample powder (vol.%)	Fracture <sup>d</sup> correction (1.5 = common fracture, 0.5 rare fractures)	Porosity B <sup>e</sup> (vol.%)	Permeability <sup>f</sup> (m <sup>2</sup> )	Bulk density (g/cm <sup>3</sup> )
NZ-40	432971	2739532	Flow	Spilitised	–	1.94	2.86	–	4.80	$9.87 \times 10^{-20}$	2.80
SG14-43	431747	2739254	Dyke	Spilitised	–	0.57	3.90	–	4.46	$3.90 \times 10^{-19}$	2.78
SG14-33A	431747	2739254	Dyke	Spilitised	–	0.59	0.60	–	1.18	$3.34 \times 10^{-19}$	2.89
AB16-4231	449116	2691867	Pillow rim	Spilitised	–	10.18	0.95	–	11.13	$6.58 \times 10^{-20}$	2.45
SG13-29B	431965	2739360	Pillow core	Spilitised	–	7.30	2.10	–	9.40	$3.64 \times 10^{-18}$	2.67
AB16-4232	449116	2691867	Pillow core	Spilitised	–	4.72	2.47	–	7.18	$9.87 \times 10^{-20}$	2.58
LD10/105	438374	2686042	Pillow rim	Spilitised	–	10.14	1.12	–	11.26	$2.17 \times 10^{-18}$	2.46
AB16-4394T	435337	2725271	Pillow rim	Spilitised	–	7.40	1.04	–	8.44	$4.63 \times 10^{-19}$	2.53
LD10-104-1b	468748	2656024	Pillow core	Spilitised	–	8.97	0.22	–	9.19	$1.57 \times 10^{-18}$	2.60
LD10-104-2c	468748	2656024	Pillow core	Spilitised	–	7.15	0.22	–	7.37	$1.14 \times 10^{-18}$	2.65
LD10-104-3b	468748	2656024	Pillow rim	Spilitised	–	5.06	0.22	–	5.28	$5.56 \times 10^{-19}$	2.68
LD10-104-3c	468748	2656024	Pillow crust	Spilitised	–	9.55	0.22	–	9.77	–	2.60
LD10-145-2	449105	2691860	Hyaloclastite (IP)	Spilitised	–	13.97	0.23	–	14.20	–	2.55
SG14-9	431959	2741288	Hyaloclastite (IP)	Spilitised	–	7.72	19.60	–	27.32	–	2.58

<sup>a</sup> Total epidote plus quartz content is normalised to 100 to exclude calcite, hematite, titanite, titanomagnetite and porosity. <sup>b</sup> Porosity A: raw porosity value uncorrected for calcite clogging pores and empty microfractures. <sup>c</sup> Average calcite calculated from carbon value in CNS analysis, sample powder from the core used for porosity and permeability or from zone in the same hand specimen adjacent to the core. <sup>d</sup> Qualitative fracture correction applied to correct porosity based on SEM observation of relative fracture abundance in thin sections. <sup>e</sup> Porosity B: Porosity corrected for late calcite and empty microfractures. <sup>f</sup> Permeabilities unable to be corrected for late calcite or empty microfractures.

### 3.4. Analytical and Simulation Methods

#### 3.4.1. Bulk-rock geochemistry, mineralogy and petrography

Mineral abundances in the texturally isotropic samples were determined by combining results of several methods: element mapping of thin-sections by electron microprobe recast into mineral abundances using XMapTools (Lanari et al., 2018); standard powder x-ray diffraction; and calculation of calcite contents from the total carbon content of rock powders determined in a Thermo Scientific FlashSmart™ carbon–nitrogen–sulphur (CNS) elemental analyser.

Descriptions of pores types, igneous features, alteration mineralogy and textures were made based on transmitted-light microscopy and scanning electron microscopy in back-scattered electron mode (BSE-SEM) on carbon-coated petrographic thin-sections. A Zeiss Evo50 environmental SEM at the University of Bern was used with a beam acceleration voltage of 20 kV, current of 2.5 mA in variable-pressure mode (28 Pa). Mineral identification was aided by Raman spectroscopy with a Jobin–Yvon LabRam HR800 instrument equipped with a 532.120 nm laser focused through a petrographic microscope (100X objective) at the University of Bern.

Bulk rock samples were homogenised into pressed powder pellets for elemental analysis by laser-ablation inductively coupled plasma mass spectroscopy (LA-ICP-MS) following the technique of Peters and Pettke (2016).

#### 3.4.2. Porosity

Bulk sample porosity was measured with an uncertainty of < 1 vol.% using a Micromeritics AccuPyc™ 1340 helium-gas pycnometer at the University of Bern. Cylindrical core samples (4 – 17 cm<sup>3</sup>) were measured for skeletal volume and density by pycnometer, and for bulk volume by caliper measurements. The skeletal volumes of irregularly shaped and fragile specimens were obtained from density measurements using a standard paraffin immersion method. All measurements were made at room pressure and temperature. Since the masses of the dry bulk and skeletal samples are identical, porosity was calculated by:

$$\phi = 100 - 100 \left[ \frac{m_{skel} \rho_{bulk}}{m_{bulk} \rho_{skel}} \right] \quad (1)$$

where  $\phi$  is porosity (vol.%),  $m_{bulk}$  and  $m_{skel}$  are the masses of the samples (g),  $\rho_{bulk}$  is dry bulk density (g/cm<sup>3</sup>) and  $\rho_{skel}$  is skeletal density (g/cm<sup>3</sup>). The results for each sample were corrected for pore-clogging by late calcite by subtracting the sample's volume-fraction of calcite (~0.2–18 vol.%; Table 3.1) as determined after the pycnometer measurements by crushing the sample and performing CNS analysis.

Thin-sections of each sample were imaged in SEM-BSE to evaluate the presence of any microfractures. Seven of the 48 imaged samples contained rare or a few open fractures that cross-cut, and hence post-date, the spilite and epidosite alteration minerals. Based on the abundance of these

fractures in the thin-sections we corrected the measured porosities of the samples by 0.5 – 1.5 vol% (Table 3.1).

### 3.4.3. Simulation of Spilite-to-Epidosite alteration

The evolution of porosity and mineralogy during the spilite-to-epidosite reaction was simulated numerically with the approach and thermodynamic data in Weber et al. (submitted) using the software FLOTRAN (Lichtner, 2007). A model fluid in equilibrium with epidote, quartz and hematite ( $pH = 4.75$ , molal Na/Ca = 10,  $T = 300$  °C and  $P = 35$  MPa) was set to flow through the measured spilite starting compositions, producing trajectories of porosity and mineralogy as a function of reaction progress (monitored by the time-integrated water/rock ratio).

### 3.4.4. Permeability

Permeabilities were measured at CoreLab, Aberdeen using a Core Measurement System CMST<sup>TM</sup>-300 unsteady-state (transient) permeameter with He-gas at a confining pressure of 55 MPa at room temperature (lower detection limit  $\sim 9.8 \times 10^{-20}$  m<sup>2</sup>). Measurement uncertainties are < 10%. As sub-seafloor *in-situ* pressures are known to affect permeability (Christensen & Ramanantoandro, 1988; Karato, 1983; and Gilbert and Bona, 2016), all measurements were performed at 50 MPa effective pressure, typical of other studies on mid-ocean ridge settings (e.g., Coehlo et al., 2015; Seyfried et al., 1988).

As described above (Section 3.4.2), our samples are essentially free of open microfractures induced by outcrop weathering. However, for a few of the samples, the above measurements underestimate the rock-matrix permeability at the time of spilite and epidosite alteration owing to the presence of later microveinlets (microfracture fillings) of calcite, which may block otherwise permeable pathways through the rock matrix. After first measuring the permeability of test samples we removed their calcite by leaching the plugs in acetic acid and then remeasured their permeability. Unfortunately, this unclogging of the calcite-generation microfractures led to unrealistically high permeabilities, and so we abandoned this approach. The samples that contain calcite veinlets are therefore identified in our results and their reported permeabilities are treated as minimum values.

### 3.4.5. Simulations of hyaloclastite permeability

Fluid flux along a geometrically simplified 2D pillow stack was simulated numerically to constrain the permeability of interpillow hyaloclastites, which were not amenable to laboratory measurements. The model setup consists of three stacks of four pillow tubes, offset vertically by half the tube height and connected via interpillow matrix (Figure 3.2). The bounding tubes are 1 m and the central pillows 2 m long, each 48 cm high. Each tube consists of a core enveloped by symmetrical rims, all assigned their measured permeabilities. The geometric model was discretised into a fine mesh and Darcy's Law was implemented using the software PFLOTRAN (Lichtner et al., 2015). Estimates of the water–rock ratios required to generate incipient, intermediate and complete alteration stages via the spilite-to-epidosite

reaction were adopted from Section 3.4.3. The range of possible permeabilities of the hyaloclastite zones was then found by trial and error, such that the required water–rock ratios could be reproduced (Figure 3.1a and b).

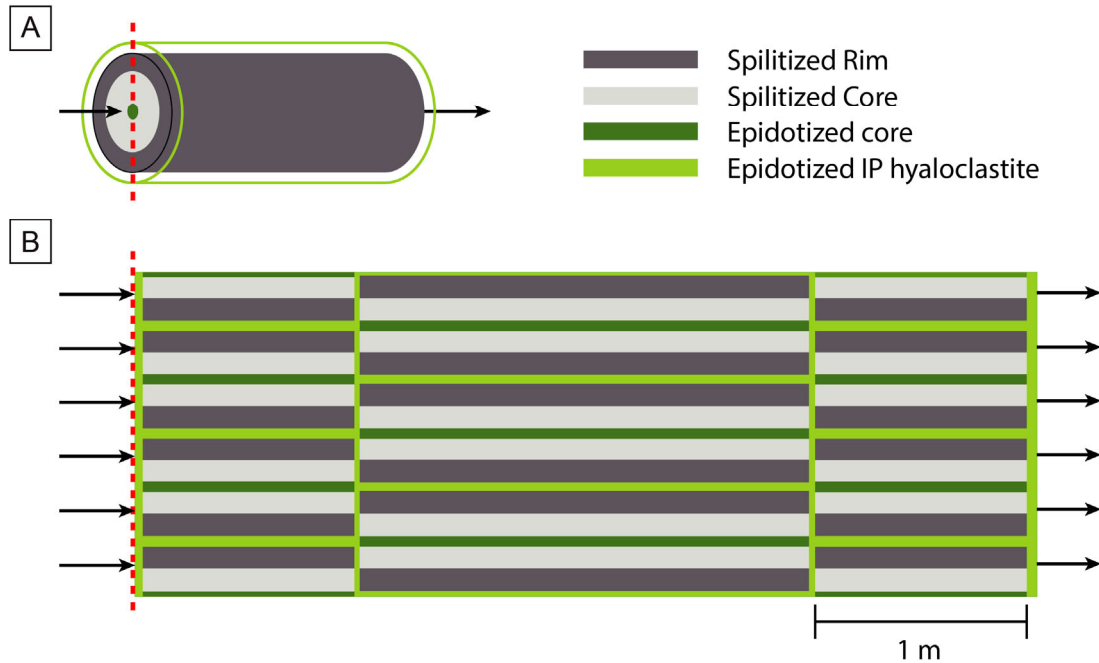


**Figure 3.2.** Simplified geometry of a partially epidotised pillow stack, with cores, rims and interpillow (IP) hyaloclastites of different permeabilities, as used for hydraulic simulations (arrows show flow direction). (a) Single 3D pillow tube surrounded by hyaloclastite (here shown as an envelope indicated by the light green line around the pillow rim). (b) 2D section of pillow stack parallel to long axes of pillow tubes, showing 7 whole-width and 4 half-width pillows.

### 3.5. Results

#### 3.5.1. Petrography of pillow lavas and hyaloclastites

##### 3.5.1.1. Textures and geochemistry of spilitised basalts

The porosity of the sampled spilites are strongly influenced by the igneous textures inherited from their MORB-like basalt precursors. Thin-section petrography of the ghost igneous textures and examination of immobile trace-element ratios distinguished two types of pillow lavas. Type 1 ("evolved") pillows are most common: they erupted with more abundant vesicles, high glass abundance (now entirely altered to chlorite intergrown with other fine-grained hydrothermal minerals), their plagioclase microphenocrysts (now completely metasomatised pseudomorphically to albite) crystallised after their rare augite microphenocrysts, and their whole-rock Zr/Y concentration ratios (Figure A3.1) indicate evolved degrees of igneous fractionation. The vesicles in this pillow type are now empty or partly to completely filled by chlorite, and the groundmass is composed of fine-grained, pseudomorphic albite laths, occasionally small relict augites and interstitial chlorite (Figure 3.3a and b).

Type 2 ("primitive") pillows are less common; they contain rare vesicles and initially less glass (now entirely altered to chlorite) and they have lower Zr/Y concentration ratios (Figure A3.1) indicating less evolved fractionation. They are also coarser-grained and have an ophitic texture of late augite microphenocrysts surrounding early plagioclase laths (now entirely metasomatised pseudomorphically to albite), with minor interstitial chlorite (Figure 3.3c). The volumetric ratio of albite to relict augite in evolved pillows varies from 20:1 to augite-free, whereas in primitive pillows the ratio is closer at 2:1 to 3:1. In both pillow types, the rims (outer 5–20 cm of the pillows; Figure 3.3a) are composed of finer relict igneous and hydrothermal crystals than the pillow cores (Figure 3.3b).

The vesicles in the pillows lavas vary from 50  $\mu\text{m}$  to 2 mm diameter (Figure 3.3g), but they generally are not abundant. Thus, micropores at crystal boundaries and between plates and fans of chlorite are the dominant pore types (Figure 3.3g). Micropore sizes vary between spilitised pillows (< 20  $\mu\text{m}$  diameter), massive flows (< 50  $\mu\text{m}$  diam.) and dykes (< 50  $\mu\text{m}$  diam.). In both evolved and primitive spilites, porosity distribution is essentially isotropic, with only occasional elongation of vesicles owing to continued lava movement during gas exsolution.



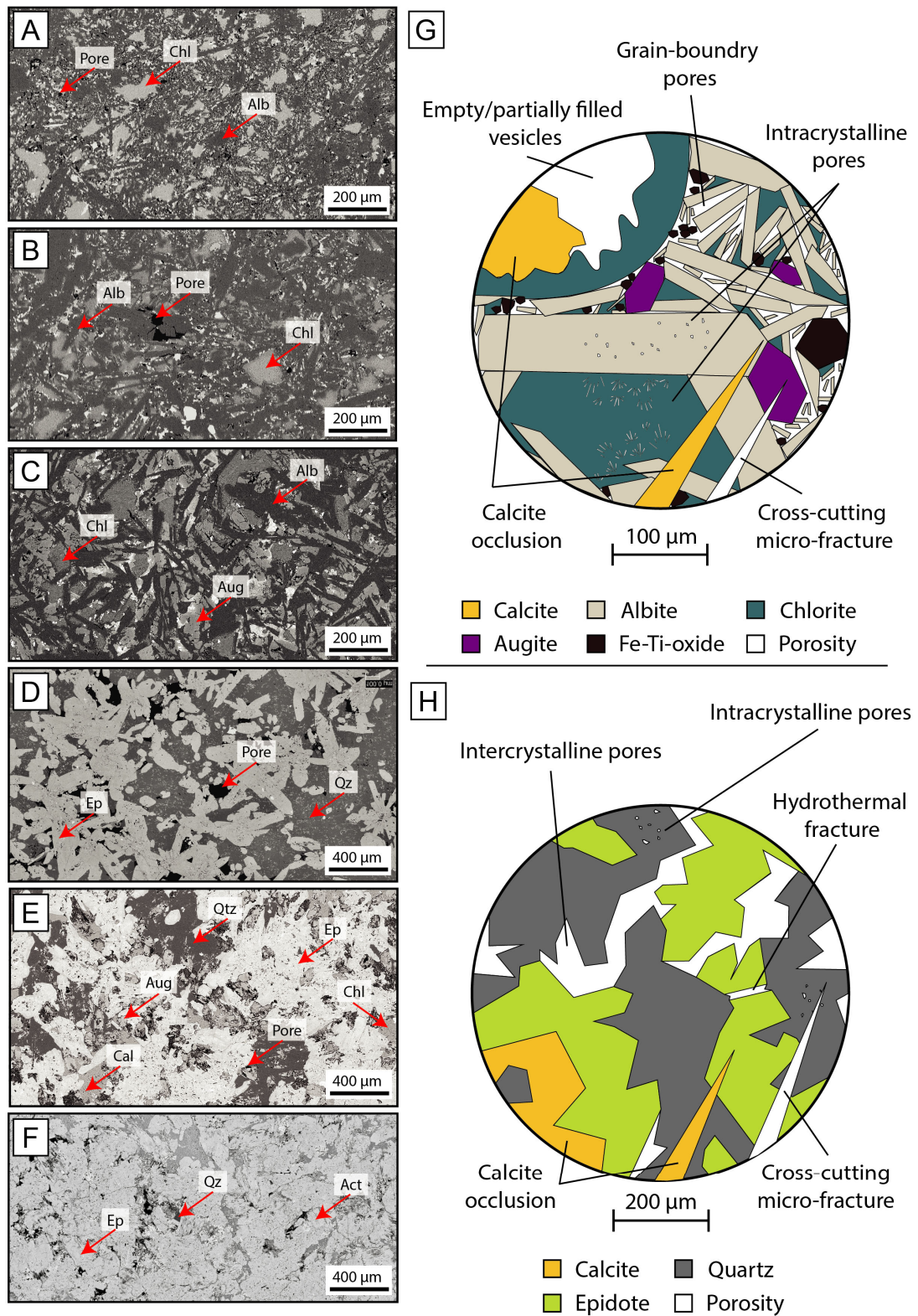


**Figure 3.3.** SEM-BSE microphotographs of spilite and epidosite textures and diagrams showing their pore types including post-seafloor (obduction and weathering) features. Note different scales between subfigures. (a) Spilite alteration in rim of evolved pillow lava. (b) Spilite alteration in core of evolved pillow lava. (c) Spilite alteration of primitive pillow lava core. (d) End-member epidosite alteration of pillow lava. (e) Partial epidosite alteration of pillow lava showing relict augite and chlorite. (f) Partial epidosite alteration of dyke showing relict actinolite. (g) Pore types and their fillings in spilites. (h) Pore types and their fillings in spilite in epidosites.

### 3.5.1.2. Textures of epidosites

Endmember epidosites have isotropic, coarsely crystalline textures that appear essentially identical in pillows lavas, massive flows and dykes. They are composed of intergrowths of euhedral quartz and epidote arranged in idioblastic to granoblastic textures with large intercrystalline pores of 50 to 200  $\mu\text{m}$  diameter (Figure 3.3d and h; see also Gilgen et al., 2016). Inherited igneous textures are still manifested by the slight decrease in crystal sizes from pillow cores to pillow rims, by the presence of vesicles (either open or more commonly filled with epidote fans and euhedral quartz), and by the ghost groundmass texture revealed by titanite crystallites within epidote and quartz, which trace the outlines of former albite laths (Figure 3.3d). Epidote and quartz are free of these titanite inclusions only where they replace former phenocrysts or vesicles (easily seen in transmitted light. Inclusions of earthy hematite and relict igneous titanomagnetite are present in epidote in some samples but are limited to a few volume percent. Partial epidosites have finer crystal sizes, they rarely show idioblastic textures, and they commonly contain chlorite, augite and actinolite inherited from the spilite precursors (Figure 3.3e and f).

In partially altered epidosites, dissolution of some of the spilite-stage albite and chlorite has enlarged pores along crystal boundaries. In near-endmember epidosites, pores are particularly noticeable around augite and actinolite (Figure 3.3e and f). In endmember epidosites, the granoblastic texture of euhedral epidote and quartz crystals is associated with large intercrystalline pores (50 – 200  $\mu\text{m}$  diameter; Figure 3.3d and h). Other minor pore types are hydrothermal fractures in epidote and quartz grains that have been partly or completely filled by further epidote and quartz precipitation, and pores in epidote fans that fill former vesicles (Figure 3.3h). Typical post-epidosite macro- and microfractures and clogging of pores by late calcite are shown in Figure 3.3g and h. In our fracture-free epidosite samples, the distribution of matrix porosity is isotropic.

### 3.5.1.3. Hyaloclastite textures

Hyaloclastites in spilitised interpillow zones are highly chloritised, they contain platy and angular chloritised pseudomorphs of former glass shards and they contain amygdules of chlorite  $\pm$  zeolite  $\pm$  quartz (Figure 3.4a). The amygdules and shards are aligned parallel to the pillow rims, imparting a preferred planar orientation to former pore spaces. In addition to the former vesicles, micro-porosity around chlorite is common. Zones of porous hematitic jasper occur occasionally within the interpillow hyaloclastites. Hand samples and thin sections of hyaloclastite contain many open microfractures and although some of these were likely open during hydrothermal circulation, they are indistinguishable from late weathering fractures. Rare, larger accumulations of massive hyaloclastite (0.3–3 m thick zones) in the pillow stacks are finer grained, highly vesicular and lack the large platy shards observed in interpillow zones (Figure 3.4b).

Hyaloclastites that have been intensely altered to epidosite (Figure 3.4b) have high tenacity, in contrast to their fragile, chloritised precursors. The pale shards in Figure 3.4b are strikingly similar in



texture to the chloritised shards in Figure 3.4a; they may consist of quartz, epidote + quartz, or epidote + chalcedony, often with late pore fillings of calcite (Fig. 3.4c,d,e). The fine-grained matrix surrounding the shards is replaced by epidote  $\pm$  quartz (Figure 3.4d). Large intercrystalline pores are observed between euhedral quartz and epidote. As in the spilite hyaloclastites, microfractures are frequent, in some cases appearing to be hydrothermal, e.g., formed during epidotisation as evidenced by epidote + quartz fillings. More often the micro-fractures are younger, as they cross-cut the epidosite mineralogy and are either open or filled by late calcite.

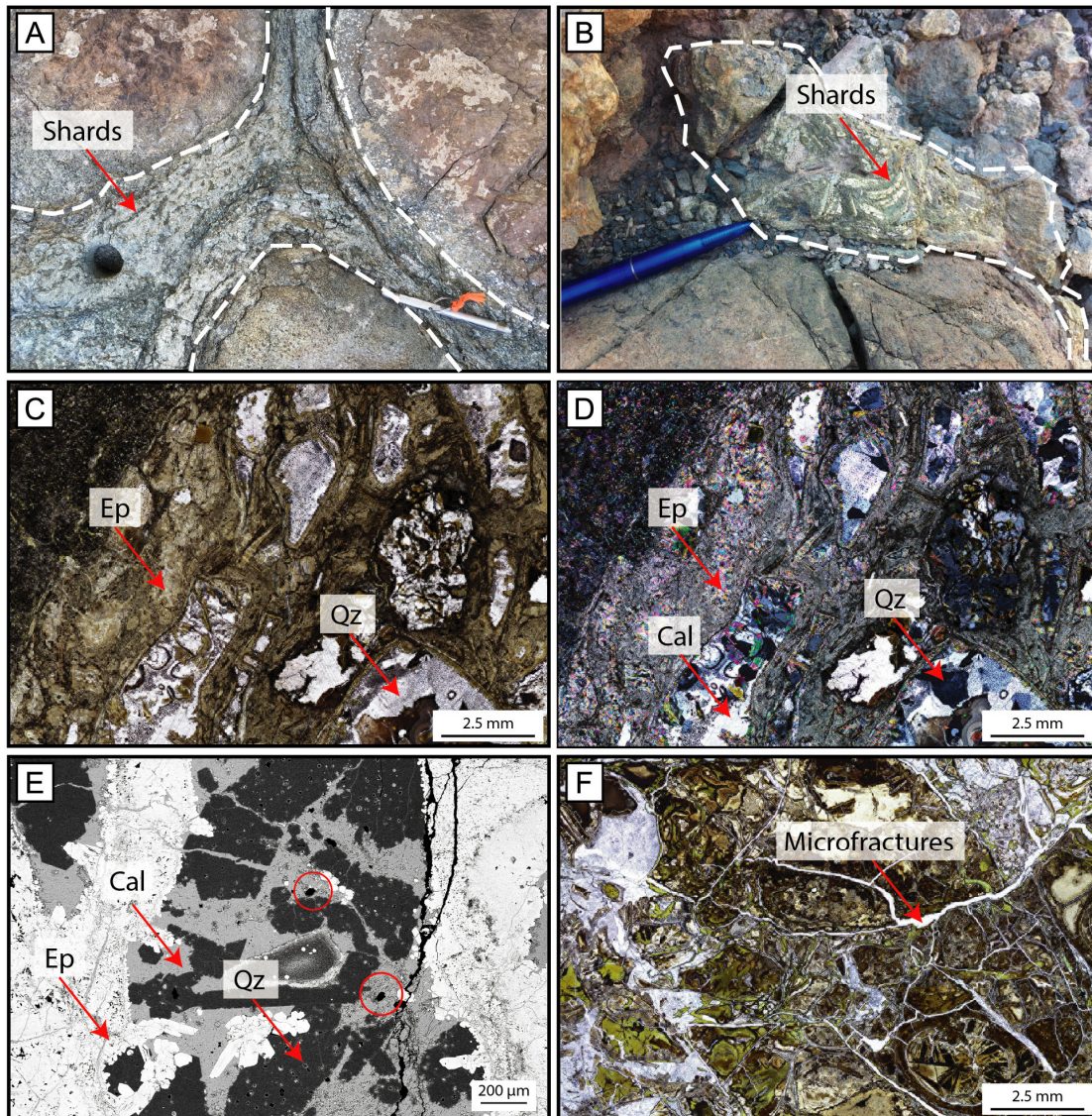


**Figure 3.4.** Textures of interpillow hyaloclastites. Hyaloclastites are outlined in field photographs. Examples of pores are outlined with red circles in microphotographs. (a) Spilite alteration of interpillow hyaloclastite (outlined) showing dark chlorite pseudomorphs of former glass shards altered to dark chlorite. (b) Epidosite alteration of interpillow hyaloclastite showing pale pseudomorphs of former glass shards. (c) Microphotograph of epidosite alteration of hyaloclastite in plane-polarised light. Green epidote matrix surrounding quartz-calcite pseudomorphs of former glass shards. (d) Same view as (c) in cross-polarised light. (e) Close-up SEM-BSE image of a pale shard pseudomorph in (b), showing epidosite-stage quartz replaced by late calcite. (f) Microphotograph of spilite alteration of hyaloclastite in plane-polarised light, showing numerous open microfractures potentially caused by outcrop weathering.

### 3.5.2. Rock-matrix porosity and permeability

Results of our measurements of rock-matrix porosity and permeability are shown in Figure 3.5, categorised by alteration type and lava morphology (pillow cores, pillow rims, interpillow hyaloclastites, massive flows, and dykes). Spilite dykes and dykes altered to weak epidosite (<10 vol.% epidote + quartz) have relatively low porosities (<5 vol.%), whereas massive flows and pillow lavas both have higher values of 4.5–12 vol.% (Figure 3.5a). Within individual spilitised pillows, rims are less porous than cores. Additionally, evolved pillow lavas have higher average porosities than primitive pillows, consistent with their differences in vesicularity. The highest porosities among spilites are in interpillow hyaloclastites (13–26 vol.%).

Epidotised interpillow hyaloclastites have similar or lower porosities than their spilitised precursors (Figure 3.5a). All other types of epidosites have porosities up to two times larger than their spilite equivalents. The ranges of values from epidotised dykes, massive flows and primitive pillow cores overlap and their averages are also similar (~14 vol.%). Evolved pillow rims and pillow cores have slightly higher averages, again presumably reflecting higher inheritance of degassing vesicles.

Permeability trends mimic porosity trends in spilite and partial spilite pillow lavas (Figure 3.5b). Within each individual pillow the rim is less permeable than the core and evolved pillows are more permeable than primitive pillows. Additionally, dykes and massive flows have permeabilities at the lower range of values for pillow lavas. Permeabilities of partial and endmember epidosites have a larger range than those of spilites. The highest permeabilities ( $\sim 3.5 \times 10^{-16}$  to  $3 \times 10^{-15}$  m<sup>2</sup>) are from endmember epidosites free of any calcite clogging. The values for samples containing 4–10 vol.% calcite (represented by orange rings in Figure 3.5b) represent minimum permeabilities for the spilites and epidosites.

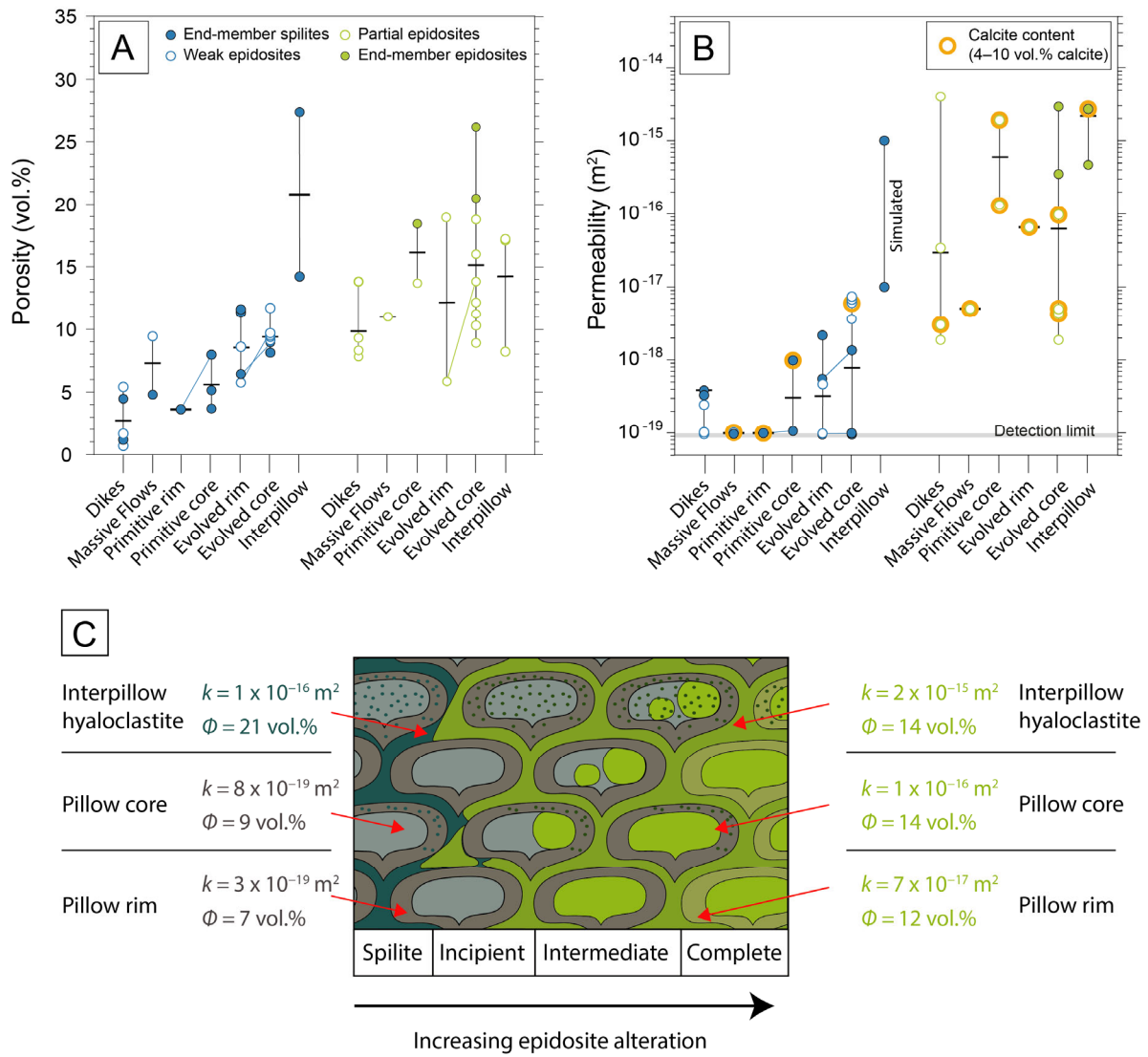


**Figure 3.5.** Rock-matrix porosity and permeability categorised according to lava morphology and extent of magmatic fractionation (primitive vs. evolved). All values from measurements of plug samples, except for simulated permeabilities of spilite interpillow hyaloclastite (see text). Diagonal tie-lines join rim–core pairs from individual pillows. (a) Rock-matrix porosities, corrected for clogging by late calcite. Horizontal bars denote medians of indicated ranges. (b) Rock-matrix permeabilities. Horizontal bars denote geometric means of indicated ranges. No calcite correction could be made, therefore samples containing calcite are marked by orange rings. (c) Schematic diagram of progressive epidosite alteration of pillow outcrops with field-scale zones identified by Gilgen et al. (2016), summarising average porosities and permeabilities from (a) and (b) (combined primitive and evolved data) for pillow cores, pillow rims and interpillow hyaloclastites. Note:  $k$  = permeability ( $\text{m}^2$ ),  $\phi$  = porosity (vol.%).

The relationship between porosities and permeabilities of most samples in this study is shown in Figure 3.6. Pristine samples with no post-epidosite artefacts are highlighted in Figure 3.6. Permeability values of samples with late calcite clogging are included in Figure 3.6, but those with late fractures are excluded. The porosity–permeability trend of spilites shows a positive correlation, but the spread of spilite porosities at the LOD of permeability precludes a meaningful trend line being fitted to our



dataset. Pristine epidiosites also follow a positive porosity–permeability trend, broadly represented by the following exponential fit ( $R = 0.458$ ):

$$k = 10^{(0.212\phi - 18.29)} \quad (2)$$

where  $k$  is the permeability ( $\text{m}^2$ ) and  $\phi$  is the porosity (vol.%).

No systematic difference in the porosity–permeability relationship is observed between different lava morphologies. However, pillow lavas and the epidiotised interpillow hyaloclastites are generally shifted to higher permeabilities than dykes, as already shown in Figure 3.5. Spilites clogged by minor late calcite generally overlap with the pristine spilites. In contrast, clogged epidiosites lie to the right of the pristine epidiosite field, reflecting their generally higher porosities.

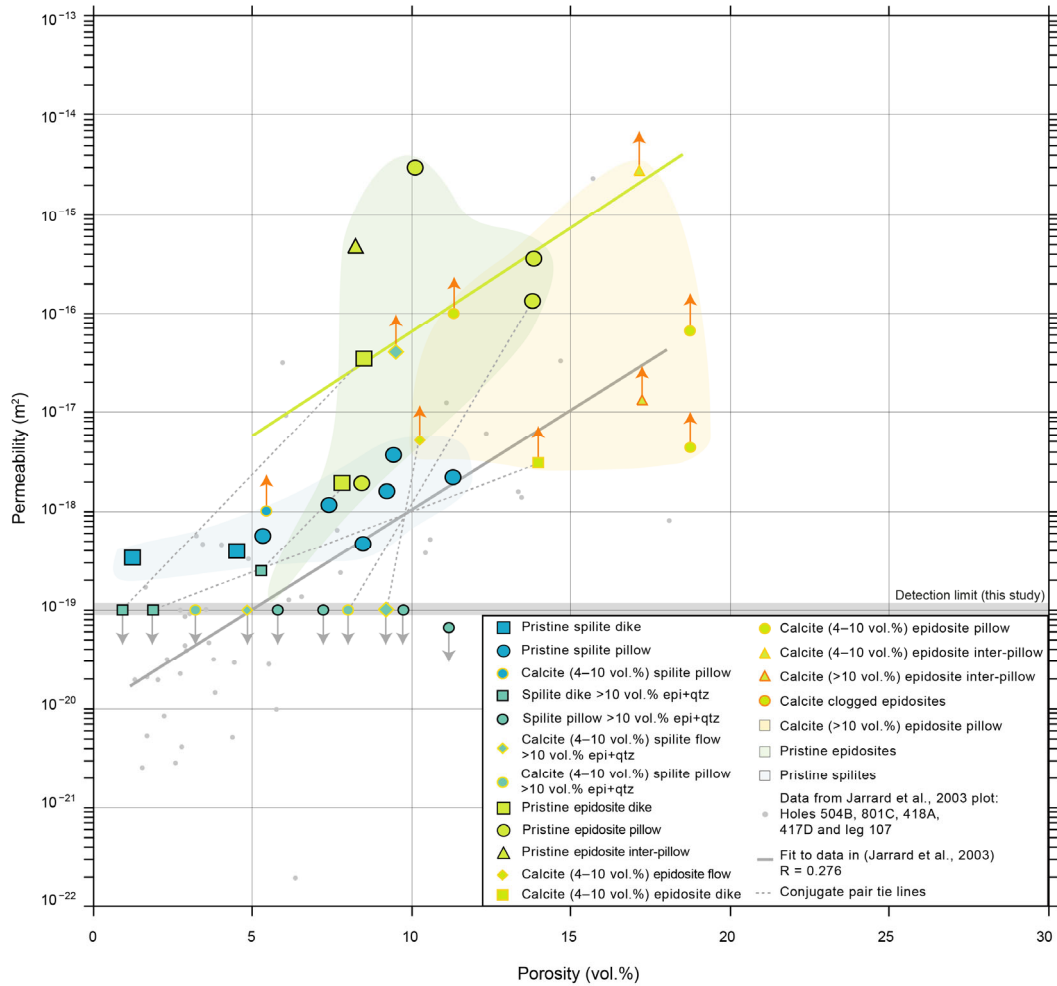


**Figure 3.6.** Relationship between permeability and porosity for spilite and epidiosite samples from this study, compared to fresh or low temperature altered basalts recovered from drill holes in *in-situ* seafloor (Jarrard et al., 2003 and references therein). Large symbols denote pristine samples from our study that are free of post-spilite and post-epidiosite calcite and microfractures. Coloured fields are visual guides only. Porosity values are corrected for calcite; permeability is uncorrected (arrowheads denote minimum or maximum values). Samples with > 4 vol.% calcite are shown in small symbols, (those with 4–10 vol.% calcite have yellow outlines; those with 10–13 vol.% calcite have orange outlines). Partial spilites (in this case 10–35 vol.% epi+qtz) are shown in turquoise.

#### 3.5.2.1. *Hyaloclastite permeability*

Our hydraulic simulations of the schematic pillow stack in Figure 3.2b are based on the field- and petrographic findings that epidosite alteration occurs after spilite alteration, and that interpillow hyaloclastites are epidotised before pillow cores and pillow rims (Section 3.2). The simulations show that this sequence of alteration will occur only if the spilite interpillows have permeabilities between  $10^{-17}$  and  $10^{-15}$  m<sup>2</sup> (plotted in Figure 3.5b).

Simulations were repeated throughout the range of measured permeabilities in pillow cores. These iterations confirmed that, for our simplified model geometry, the ratio of volumetric fluxes through the core and interpillow regions during epidotisation is essentially a function of their permeability ratio.

#### 3.5.3. *Epidotisation: reaction porosity and permeability*

Our reactive-transport simulations predict the gradual changes in porosity and alteration index (abundance of epidote + quartz) during progress of the spilite-to-epidosite reaction. A simulation was carried out for each spilite in our set of spilite–epidosite conjugate sample pairs. A calculated trajectory curve (Figure 3.7a) emanates from each spilite sample and rises to a model endmember epidosite (arrowheads in Figure 3.7a). Kinks in these trajectories correspond to the replacement of spilite minerals (albite then chlorite; Weber et al., submitted), depending on their initial abundance in the spilites. The measured porosities and alteration indices of the conjugate partial and endmember epidosites coincide very well with the simulated trajectories. Porosity increases from spilites to endmember epidosites: in pillow lavas by ~9–14 vol.% and in dykes by ~9–12.2 vol.%.

Complete epidotisation shown by some conjugate pairs also dramatically increases permeability (Figure 3.7b). Endmember pillow and dyke epidosites have permeabilities up to 4–4.5 orders of magnitude higher than their conjugate spilites, reaching  $2 \times 10^{-15}$  to  $4 \times 10^{-15}$  m<sup>2</sup>. Similarly to the change in porosity, partial epidotisation moderately and variably increases permeability by 2–3 orders of magnitude.

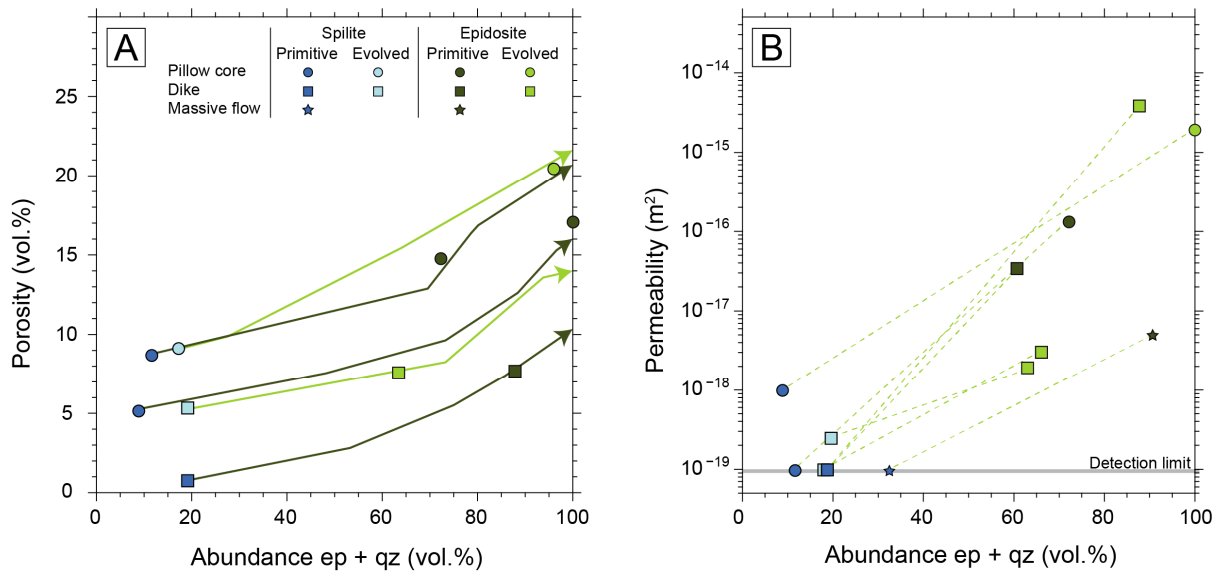


**Figure 3.7.** Effect of spilite-to-epidosite reaction on porosity and permeability for conjugate (spatially adjacent) sample pairs. Increasing extent of reaction correlates with increasing abundance of epidote + quartz (x-axes). (a) Measured porosities (symbols) and modelled evolution of porosity (lines) based on reactive-transport simulations (see text). Some epidosites show only partial alteration (60–90 vol.% epi + qz), others are endmembers (> 90 vol.% epi + qz). Simulated trajectories start at each spilite and terminate at a model endmember epidosite (arrowheads). (b) Measured permeabilities (not all samples are identical to those in (a)). Conjugate pairs are linked visually by tie-lines (not simulated).

### 3.6. Discussion

#### 3.6.1. Reliability of results

Only a limited set of 32 samples could be analysed for porosity and permeability in our study (Figure 3.5). This is the result of our stringent sample selection criteria, designed to avoid the abundant weathering fractures in the Oman outcrops and to minimise the presence of late calcite. Nevertheless, based on our extensive field experience in the Semail ophiolite, we are confident that this final set of samples is typical of the alteration and volcanic rock types in the axial Geotimes lavas and comagmatic SDC.

Our estimates of fracture volumes based on SEM-BSE imaging enabled correction of the measured porosities (by 0.5–1.5 vol.%) in the seven samples that contain minor late fractures. Similarly, the porosity filled by late calcite could be quantitatively corrected based on bulk calcite analyses of the samples performed after the porosity and permeability measurements. Unfortunately, such corrections could not be applied to the permeability results of the affected samples. Their permeabilities are therefore likely to be slightly underestimated owing to pore clogging by their minor calcite.

It remains possible that our small sample set does not capture the full range of rock-matrix porosity and permeability in the investigated units. However, the systematic differences in porosity and permeability between the various rock types (Figure 3.5), which correlate with the intensities of alteration visible in the field, suggests that our reported ranges are likely to be realistic and representative.



### 3.6.2. Porosities and permeabilities representative of *in-situ* hydrothermal conditions

As our porosity measurements were conducted at room temperature and pressure, the question arises as to whether the values are valid for the *in-situ*  $P$ – $T$  conditions of spilite and epidosite alteration during magmatism in the Semail crust. Stratigraphic reconstructions to the base of the SDC (Belgrano et al., 2019), ocean-depth estimates (Belgrano et al., submitted) and fluid inclusion data (Richter and Diamond, submitted) suggest that the studied alteration occurred at temperatures in the range of 200–450 °C and that maximum and minimum pressures through to the base of the SDC varied as follows:  $P_{\text{confining}} = P_{\text{ocean}} + P_{\text{lithostatic}} = 44\text{--}190$  MPa and  $P_{\text{effective}} = P_{\text{confining}} - P_{\text{hydrostatic}} = 8\text{--}90$  MPa. As epidosite alteration mostly occurred during post-axial Tholeiitic Alley time (Section 3.2), the maxima of these pressure ranges include the Tholeiitic Alley overburden above the axial SDC and Geotimes lavas.

Calculations using the thermoelastic properties of the spilite and epidosite mineral assemblages show that the porosity of both alteration types increases by at most 2.4 vol.% during heating and compression to the *in-situ* conditions (Chapter 2 of this Thesis). Compared to the variation in porosity between samples, this change is negligible.

Regarding the effect of *in-situ* pressure on permeability, our measurements were made at an effective pressure of 50 MPa, equal to the mean  $P_{\text{effective}}$  estimated for the Semail upper crust during spilite and epidosite alteration. Room-temperature permeability measurements on an epidotised dyke as a function of confining pressure (Chapter 2 of this Thesis) show values of  $1.0 \times 10^{-17}$  at 5.3 MPa,  $5.5 \times 10^{-18}$  at 33.3 MPa and  $3.4 \times 10^{-18}$  at 55 MPa. Extrapolating this trend suggests that the permeability would fall to about  $1\text{--}2 \times 10^{-18}$  at 90 MPa, the maximum  $P_{\text{effective}}$  for the Semail ophiolite. This difference of at most 0.3 of order of magnitude in permeability is significantly less than the 3 orders of magnitude variation in the results for epidosite dykes in Figure 3.5b.

The effect of temperature on permeability on our samples was addressed in a separate experimental study (Chapter 2 of this Thesis). Upon heating the spilite and epidosite dykes and lavas at 50 MPa, their permeabilities decrease by less than 0.2 of an order of magnitude at 400 °C. This change is also negligible compared to the inter-sample variation in permeability.

We conclude that the porosities and permeabilities reported in Figures 3.5, 3.6 and Table 3.1 can be taken at face value as closely representative of the studied ophiolite units during spilite and epidosite alteration at the *in-situ* hydrothermal  $P$ – $T$  conditions.

### 3.6.3. Controls on porosity and permeability of different rock types and their consequences for progressive epidosite alteration

Within each alteration type, the range and trends in rock-matrix porosity and permeability mainly depend on the inherited igneous texture (Figure 3.5). Dykes are consistently the least porous and permeable. In the extrusive rocks, the permeability correlates with the macroscopically visible porosity and matrix grain size. Within individual pillow lavas, the coarse-grained cores are more porous and

permeable than the finer-grained rims. In addition, primitive lavas have lower porosities and permeabilities than evolved lavas, which are more vesicular and richer in chlorite (initially glass).

Within each pillow, the grain size increase from the pillow rim to core causes a porosity and permeability zonation in spilites and epidiosites; low values in the rims and higher values in the cores (Figure 3.5). This decimetre-scale zonation in spilites explains the 100 m-scale concentric outcrop patterns of progressive epidosite alteration described by Gilgen et al. (2016) and shown schematically in Figure 3.5c. Large epidosite bodies up to 1 km<sup>2</sup> in the Geotimes lavas have complete epidiosites in their centres, surrounded by zones of intermediate epidosite, and rimmed by incipient alteration. This spatial zonation has been interpreted to result from a temporal evolution (Gilgen et al., 2016), and this is nicely confirmed by our measurements. In accord with previous qualitative deductions (e.g. Seyfried et al., 1978; Coogan & Gillis, 2018), we have demonstrated that the most permeable component of the spilitised pillow stacks are the interpillow hyaloclastites, with values of  $1 \times 10^{-15} \text{ m}^2$  to  $1 \times 10^{-17} \text{ m}^2$ . Consequently, they are the first parts of pillow stacks to be altered to epidosite. Spilitised pillow cores are next epidotised because their permeability is 1–2 orders of magnitude lower, yet ~0.5 orders of magnitude higher than spilitised pillow rims. The presence of such intermediate epidosite alteration (i.e. epidotised hyaloclastite and pillow cores) is highly systematic in the Geotimes pillows, even though the pillow rims are in contact with the highly permeable hyaloclastite. Evidently, epidosite-forming fluids infiltrate pillow cores at the base of pillow stacks, presumably via fractures or hyaloclastites, and then migrate up through the branching cores to the top of the stacks. Finally, the low permeability pillow rims are also epidotised, forming completely altered pillow stacks.

#### 3.6.4. Porosity–permeability correlations

The positive correlation between the porosity and permeability of pristine spilites (Figure 3.6) is similar to that of fresh and low-temperature altered basalts extracted from ocean drill-holes (grey points in Figure 3.6), as summarised by Jarrard et al. (2003; and references therein). Jarrard et al. (2003) described the trend by the following fit:

$$k = 10^{(0.201\phi - 20.003)} \quad (3)$$

$k = 10$  where  $k$  is the permeability (m<sup>2</sup>) and  $\phi$  is the porosity (vol.%). The R value is only 0.276, reflecting the high scatter in the data. We expect that our spilite samples on the detection limit would fall in the same ultra-low permeability region as that measured for many of the drill-hole samples (indicated by downward arrows in Figure 3.6). Thus, our spilite data would clearly overlap well with the literature data, based on which we suggest that the same fit line (Eqn. 3) could be used to approximate spilite porosity and permeability. The similarity of the porosity–permeability trends between our spilites and the fresh and low-temperature clay-altered basalts indicates that the properties of the connected pore network does not change significantly upon overprinting by new greenschist-facies spilite minerals.

Epidosites generally have much higher permeabilities than spilites for a given porosity between ~7 and 12 vol% (Figure 3.6). This may reflect the interconnectedness of the large pores in the relatively coarse-grained granoblastic epidiosites compared to the fine-grained, tortuous spilite texture. The porosities of the epidiosites to the right of the pristine samples in Figure 3.6 have been corrected for calcite clogging, but their permeabilities have not (indicated by upward arrows). Since the late-stage, low-salinity fluid that precipitated calcite would have preferentially infiltrated the most permeable of the epidiosites, it can be assumed that the clogged samples had pre-calcite permeabilities some 1–3 orders of magnitude higher than their measured values. Extrapolating the epidiosite porosity–permeability trend-line in Figure 3.6 therefore suggests that some epidiosites could have had permeabilities between  $1 \times 10^{-14}$  and  $1 \times 10^{-13}$  m<sup>2</sup>.

The conjugate pair tie-lines connecting spilites and epidiosites from individual pillows marked in Figure 3.6 do not represent fitted trends, yet these tie-lines do follow a positive trend not unlike the epidiosite and literature porosity–permeability lines. In detail, the evolution of these trends during progress of the spilite-to-epidiosite reaction is likely to be non-linear in log(permeability)–porosity space (as observed in Figure 3.7a), which may explain the variations in slopes of the tie-lines in Figure 3.6.

### *3.6.5. Implications for permeability of the upper crust*

#### *3.6.5.1. Reaction-enhanced permeability in epidiosites*

The spilite-to-epidiosite reaction was previously predicted to increase porosity by 10–20 vol.%, based on estimates of the reaction stoichiometry and observations of the abundant porosity in thin-sections of epidiosites (Cann et al., 2015; Harper et al., 1988). The results of our measurements and simulations in Figure 3.7a confirm and constrain these previous estimates to ~9–14 vol.% for both pillow lavas and dykes.

The partial epidiosites in our study have low permeabilities comparable to the one previous measurement of  $\sim 8 \times 10^{-18}$  m<sup>2</sup> by Coehlo et al. (2015; their sample contains abundant relict chlorite, which corresponds to our definition of "partial" epidiosite). However, endmember epidiosites in our conjugate pairs have permeabilities up to  $4 \times 10^{-15}$  m<sup>2</sup> (Figure 3.7b). The conjugate spilite of the most permeable epidiosite lies on the detection limit at  $1 \times 10^{-19}$  m<sup>2</sup>, therefore the increase in permeability in this case must be in excess of 4.5 orders of magnitude. The other epidiosites show increases of 1–3 orders of magnitude. As the conjugate pairs unequivocally represent samples with the same initial chemical composition, the increase in permeability can be entirely attributed to the spilite-to-epidiosite reaction itself.

The huge enhancement of permeability due to the spilite-to-epidiosite reaction must have consequences for fluid circulation through the oceanic crust. As epidiosite bodies evolve towards endmember compositions they clearly become high permeability channels compared to the surrounding spilites, which may provide positive feedback between permeability and fluid flow. This self-

propagation of flow presumably facilitates attainment of the exceedingly high water/rock ratios (700–40,000) required to form endmember epidiosites, as quantified by Weber et al. (submitted). Self-propagation may explain how lavas in the Semail ophiolite and dykes in the Semail and Troodos sheeted dyke complexes become converted to epidiosite in the absence of significant fracture-controlled fluid flow at the outcrop scale (Gilgen et al., 2016; Cann et al., 2015). At a larger scale, the same phenomenon may explain how km<sup>3</sup>-size bodies of upper crustal spilites in the Semail and Troodos ophiolites become pervasively altered to epidiosite (Gilgen et al., 2016; Jowitt et al., 2012), without necessarily being close to major, high-permeability feeder faults (Gilgen et al., 2016). These conclusions underscore the proposals of earlier workers (Richardson et al., 1987; Schiffman & Smith, 1988; Harper et al., 1988) that epidiosite bodies are the markers of focused upflow in the hydrothermally active oceanic crust. Whereas the fluid focusing itself has traditionally been attributed purely to buoyancy forces in the context of crustal-scale free convection (e.g., Jupp & Schulz, 2004), our results show that permeability enhancement by the spilitic-to-epidiosite reaction is an additional, important factor that reinforces focusing of hydrothermal fluid along the upflow path.

#### 3.6.5.2. Comparison of spilites to fresh and low temperature altered basalts

Figure 3.8 compares our newly determined porosities and permeabilities of spilites with those of previously measured spilites, fresh oceanic basalts and oceanic basalts altered at low temperature to clay and zeolite assemblages. The literature data come from the Semail and Troodos ophiolites, and from several DSDP drill holes in *in-situ* oceanic crust.

In dykes and massive flows, our porosities and permeabilities are generally consistent with previous studies of spilites. The exception is one permeability value of  $1.1 \times 10^{-15} \text{ m}^2$  for a dyke (Gilbert & Bona, 2016); however, this value was measured using a Tiny-Perm II device, which in the same study on pillow lavas produced very high permeabilities compared to a standard permeameter, and therefore we do not consider this value to be accurate. Despite the low temperature alteration of all the previously measured massive flow samples, their values are consistent with our spilitic massive flow values. The one massive flow from the Troodos ophiolite with a higher porosity of ~17 vol.% is likely a vesicle-rich sample (Gillis & Sapp, 1997).

The larger range of values in pillow lavas compared to massive flows and dykes also agrees with the variation we measured between individual pillow lavas. Those pillow lavas with the highest porosities and permeabilities have high vesicularity, e.g. the Troodos samples have up to 20 vol% vesicles (Gillis & Sapp, 1997) and lavas from 801C are described as tholeiites, which again have higher vesicularity (Jarrard et al., 2003). The extremely high permeability values from Hole 1256D were measured using the same Tiny-Perm II device as the high permeability dyke (Gilbert & Bona, 2016), and so the accuracy of those measurements is unclear. Otherwise, our spilitic values overlap with the central range of previous measured porosities and permeabilities. This comparison shows that the

vesicle-poor Semail Geotimes lavas are more similar to MORB lavas than the andesite to dacite lavas from the Troodos ophiolite, which contain up to 15 vol.% vesicles (Gillis & Sapp, 1997).

What can these differences and similarities tell us about the petrophysical properties and changes between alteration types? Previous authors have reported that the porosity and permeability of fresh basalts is reduced by seafloor weathering and by shallow hydrothermal clay alteration (Gillis & Sapp, 1997; Jarrard et al., 2003, Johnson, 1980a), but that carbonate and zeolite precipitation may potentially increase permeability (Jarrard et al., 2003). Our observations of partially or completely filled vesicles in hand specimens and thin sections imply spilites have lower porosities than fresh basalts with open vesicles. However, in agreement with the conclusion in Section 3.6.4, the overlap between values from most dykes, massive flows and pillow lavas shows that, at a crustal scale, the greenschist-facies spilite alteration found in ophiolites is unlikely to markedly change the bulk porosities and permeabilities of fresh or low-temperature altered basalts.

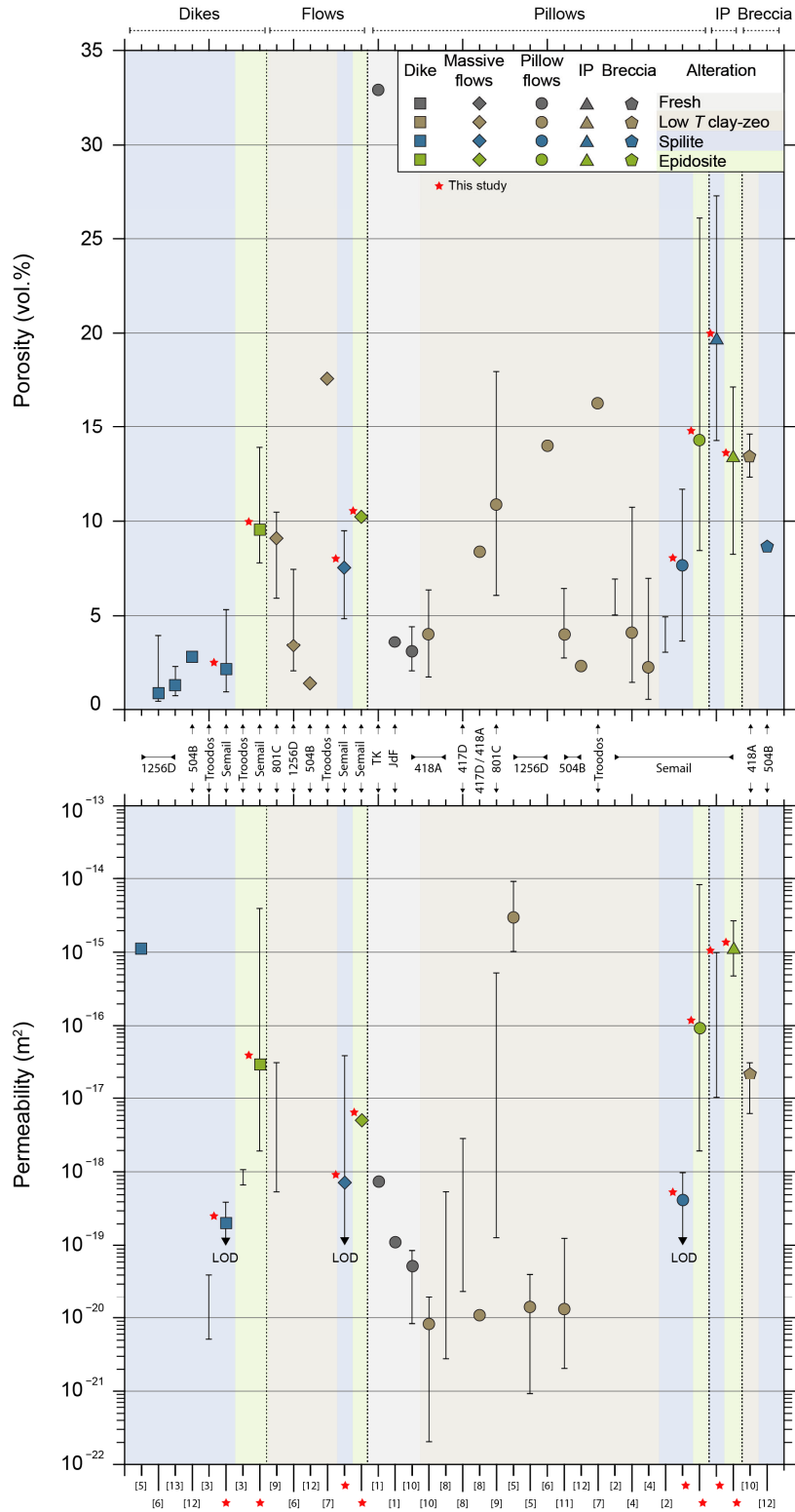


**Figure 3.8.** Comparison of porosity and permeability of basaltic rocks (dykes, massive flows, pillow lavas, interpillow hyaloclastite = IP, breccias) in upper oceanic crust as a function of alteration type (fresh basalt, low temperature clay–zeolite, spilitite, epidosite) and locality. Data from this study (red asterisks; pillow data combine cores and rims) and literature (sources in x-axis of b). Range bars include averages (symbols) where available. (a) Porosity. (b) Permeability, including limit of detection (LOD) for our data. <sup>[1]</sup>Christensen and Ramanantoandro (1988), <sup>[2]</sup>Christensen & Smewing (1981), <sup>[3]</sup>Coehlo et al. (2015), <sup>[4]</sup>Einaudi et al. (2000), <sup>[5]</sup>Gilbert & Bona (2016), <sup>[6]</sup>Gilbert & Salisbury (2011), <sup>[7]</sup>Gillis & Sapp (1997), <sup>[8]</sup>Hamano (1980), <sup>[9]</sup>Jarrard et al. (2003), <sup>[10]</sup>Johnson (1980a), <sup>[11]</sup>Karato (1983), <sup>[12]</sup>Pezard (1990), <sup>[13]</sup>Violay et al. (2010).

### 3.6.5.3. Significance of interpillow hyaloclastites as fluid pathways

Gillis and Sapp (1997) estimated the macroscopic porosity (basaltic clast porosity + palagonite porosity + porosity equivalent to calcite zones) of fresh interpillow hyaloclastites in basaltic andesites to be 25–55 vol.%, and 14–28 vol.% for basalts altered at low temperature, in the Troodos ophiolite. The latter values are comparable to our measurements of spilite interpillows at 14–27 vol.% (Figure 3.8a). In Figure 3.8a and b our interpillow zones are clearly the most porous and permeable non-epidotised rocks in the altered upper crust, even higher than the breccias from DSDP Holes 418A and 504B. Moreover, interpillow zones surround every pillow, constituting a connected network throughout the pillow stacks. In contrast, massive flows and feeder dykes have much lower permeabilities (Figure 3.8b) and they tend to act as hydraulic barriers to fluid flow. This is evident at the field scale in the Geotimes lavas, where transformation of spilite pillow stacks to complete epidiosites occurs with only minor epidiosite alteration of the cross-cutting feeder dykes and intervening massive flows (Gilgen et al., 2016).

### 3.6.5.4. Application of rock-matrix permeabilities to hydrothermal circulation in the upper crust

The main application of measured permeabilities is in coupled numerical thermal–hydraulic and thermal–hydraulic–chemical simulations of fluid flow through the oceanic crust. However, rock-matrix permeabilities measured at the hand-specimen scale, as done in the present study, are currently not used in numerical simulations. In fact, there is a longstanding discrepancy of more than 3–4 orders of magnitude between hand-specimen permeabilities and the much higher crustal-scale values used by modellers (as recently highlighted by Gilbert & Bona, 2016). Most numerical models use crustal-scale permeabilities of  $\sim 1 \times 10^{-16}$  to  $4 \times 10^{-11} \text{ m}^2$ , which have been adjusted to reproduce known heat flow or fluid discharge (Fisher, 1998 and references therein; Hasenclever et al., 2014). Attempts have been made to measure crustal-scale permeabilities that corroborate these values, using a number of approaches. The highest values of  $1 \times 10^{-12}$  to  $4 \times 10^{-6} \text{ m}^2$  were found by permeability modelled from fracture data using the parallel plate method (e.g. Semail ophiolite by Nehlig, 1994; on-axis crust in the Troodos ophiolite by van Everdingen, 1995; DSDP Hole 418A by Johnson, 1980b). However, this and other indirect methods, such as permeability calculated from heat flow, may be semi-quantitative and overestimate permeability according to the comprehensive review by Fisher (1998). In contrast to fracture-based permeabilities, values measured *in-situ* with drill-string packer tests yield a lower range of crustal scale permeabilities of  $1 \times 10^{-18}$  to  $1 \times 10^{-13} \text{ m}^2$  (e.g., Anderson et al., 1985; Becker, 1989; Becker and Fisher, 2000; Fisher, 1998). Nonetheless, this range of crustal-scale values is still orders of magnitude higher than the permeabilities of most hand specimens from ophiolites and *in-situ* oceanic crust. Figure 3.8b shows that fresh basalts, most low temperature altered basalts, and spilitised dykes and pillows have permeabilities between  $1 \times 10^{-21}$  and  $1 \times 10^{-18} \text{ m}^2$ . What aspect of permeability in the crust can reconcile these differences?

Although parallel plate models for fracture permeability appear to produce erroneously high values, fracture permeability is a clear candidate to fill the permeability gap and fractures mapped in the sheeted

dyke complexes of the Troodos and Semail ophiolites by Nehlig (1994) and van Everdingen (1995), respectively, support this explanation. Gilbert and Bona (2016) similarly concluded that fracture permeability must make up the gap between hand specimen and modelled permeabilities at Hole 1256D. Fractures have been documented in the extrusive lavas in ophiolites and drill holes (e.g., Christensen & Smewing, 1981; Gilbert & Bona, 2016; Gillis & Sapp, 1997; Johnson, 1980) but lack regionally representative quantification and reasonable permeability estimates. Additionally, other authors have observed large tracts of relatively unfractured lavas in the Semail ophiolite (Gilgen et al., 2016). Alternatively, the epidiosites, breccias and hyaloclastites in Figure 3.8 are permeable enough to explain the low end of *in-situ* crustal-scale estimates. Although epidiosites undoubtedly constitute high permeability pathways, their role is debatable, as so far they have been found very rarely in *in-situ* oceanic crust (Staudigel, 2014). By contrast, hyaloclastites and breccias are common and have the highest permeabilities of all upper crust lava types. For example breccias compose ~19% of the extrusive Hole 1256D (Tominaga et al., 2009) and hyaloclastites make up 7.5–18 area% of pillow outcrops mapped in Troodos by Gillis and Sapp (1997). We hypothesise that extensive and permeable hyaloclastites networks throughout pillow stacks may be the fundamental flow paths in relatively unfractured areas, away from seafloor faults.

We make a first order estimate on the permeability of a spilitised pillow stack that takes into account hyaloclastite permeability, by assuming flow parallel to the hyaloclastite and pillow zones, respectively (as in Figure 3.2). Using average values from our study combined at the proportion of interpillow zones mapped by Gillis and Sapp (1997) gives a permeability range for spilite pillow stacks between  $\sim 8 \times 10^{-17}$  and  $\sim 2 \times 10^{-16} \text{ m}^2$ . This range overlaps with values measured by packer tests and is 2–3 orders of magnitude higher than the average permeabilities of pillow lava hand specimens. To reach permeabilities over  $\sim 10^{-16} \text{ m}^2$ , as measured by packer tests and as required by numerical simulations to reproduce heat flow, large and frequent zones of beccias and fracture networks would have to exist at the crustal scale.

### 3.7. Summary and Conclusions

Our investigation has defined how rock-matrix porosities and permeabilities influence hydrothermal fluid circulation through the spilitised and epidotised upper oceanic crust, as abundantly exposed in ophiolites. The study has assessed the rock-matrix porosity and permeability by carefully avoiding or correcting for artefacts due to processes that post-date the hydrothermal alteration of interest.

Spilite porosity and permeability is controlled by grain size, vesicularity and chlorite content inherited from fresh basalts, which produces the following order of decreasing permeability: interpillow hyaloclastites > pillow cores > pillow rims > massive flows > dykes.

The bulk permeability of the volcanic stack is strongly influenced by the highly permeable interpillow hyaloclastites. Nevertheless, the remaining rock types have significant permeabilities, such that the above order of decreasing permeabilities is followed during the progressive alteration of spilite



pillow stacks to epidiosites, via the stages of incipient, intermediate and complete outcrops as observed by Gilgen et al. (2016). The reaction stoichiometry and molar volumes of the phases involved in the spilite-to-epidosite transformation generates, up to 9–14 vol.% of new porosity and enhances permeability by 4 – 4.5 orders of magnitude, reaching  $5 \times 10^{-15} \text{ m}^2$ . The feedback of this enhancement on rock-matrix flow explains the formation of  $\text{km}^3$ -size bodies of pervasive epidiosites in the absence of significant fracture networks. Moreover, this positive feedback mechanism between permeability and fluid discharge facilitates the huge water–rock ratios (Weber et al., submitted) needed to quantitatively leach Mg and Na and form endmember epidiosites.

At the crustal scale we have shown that the bulk porosities and permeabilities of spilites, fresh basalts and low-temperature altered basalts are comparable despite their mineralogical differences, and that their porosity–permeability correlations are broadly similar. Additionally, we have demonstrated that the results of hydraulic tests in *in-situ* upper crust can be reconciled with the individually heterogenous rock-matrix permeabilities by combining the permeable network of interpillow hyaloclastites with pillow interiors, yielding a pillow stack permeability of up to  $\sim 10^{-16} \text{ m}^2$ . This implies that the minimum permeabilities of  $\sim 10^{-16} \text{ m}^2$  required to numerically simulate the observed heat flow and fluid discharge at the seafloor most likely reflect a strong component of flow through the rock-matrix. Nevertheless, a full assessment of bulk permeability still requires integration of the effects of fracture networks. The comprehensive data set in this study is a solid basis for a forthcoming study (Chapter 4) that upscales our rock-matrix porosities and permeabilities into a decametre-scale equivalent porous medium for the lavas and combines this with new fracture distributions mapped in the Semail ophiolite, to simulate the bulk permeability of the extrusive lavas in the upper crust.

### **Acknowledgements**

We gratefully acknowledge the logistical support during field work in the Sultanate of Oman from Khalid al-Tobi (Earth Secrets Co., Muscat) and the Public Authority for Mining, Muscat. Lisa Richter (University of Bern) assisted with sample collection in Oman. This work was supported by Swiss National Science Foundation (SNSF) Grants 200020-169653 and -188567 to L.W.D.

## References

- Aksyuk, A.M., Vitovtova, V.M., Pustovoy, A.A., Kharin, G.S., Shmonov, V.M., 1992. The permeability of oceanic basalts and some questions of the formation of hydrothermal springs in the rift zone of the Atlantic Ocean. *Oceanol. Engl. Transl.* 32, 1115–1122.
- Alabaster, T., Pearce, J., 1985. The Interrelationship between Magmatic and Ore-Forming Hydrothermal Processes in the Oman Ophiolite. *Econ. Geol.* 80, 1–16.  
<https://doi.org/10.2113/gsecongeo.80.1.1>.
- Alabaster, T., Pearce, J.A., & Malpas, J., 1982. The volcanic stratigraphy and petrogenesis of the Oman ophiolite complex. *Contrib. Mineral. Petr.* 81, 168–183.  
<https://doi.org/10.1007/BF00371294>.
- Alt, J.C., 1995. Subseafloor processes in mid-ocean ridge hydrothermal systems. *Geophysical Monograph* 91, 85–114. <https://doi.org/10.1029/GM091p0085>.
- Anderson, R.N., Zoback, D.M., Hickman, S.H., Newmark, R.L., 1985. Permeability Versus Depth in the Upper Oceanic Crust: In Situ Measurements in DSDP Hole 504B, Eastern Equatorial Pacific. *J. Geophys. Res.* 90, 3659–3669. <https://doi.org/10.1029/JB090iB05p03659>.
- Amstutz, G.C., 1974. *Spilites and spilitic rocks*. Springer-Verlag, Heidelberg, Germany.
- Bach, W., Peucker-Ehrenbrink, B., Hart, S.R., Blusztajn, J.S., 2003. Geochemistry of hydrothermally altered oceanic crust: DSDP/ODP Hole 504B - Implications for seawater-crust exchange budgets and Sr- and Pb-isotopic evolution of the mantle. *Geochem. Geophys. Geosyst.* 4, 1–29.  
<https://doi.org/10.1007/s00269-010-0415-y>.
- Becker, K., 1989. Measurements of the permeability of the sheeted dikes in Hole 504B, ODP Leg 111. *Proc. ODP, Sci. Results* 111, 317–325. <https://doi.org/10.2973/odp.proc.sr.111.156.1989>.
- Becker, K., Fisher, A.T., 2000. Permeability of upper oceanic basement on the eastern flank of the Endeavor Ridge determined with drill-string packer experiments. *J. Geophys. Res.* 105, 897–912. <https://doi.org/10.1029/1999JB900250>.
- Belgrano, T.M., Diamond, L.W., Vogt, Y., Biedermann, A.R., Gilgen, S. A., 2019. A revised map of volcanic units in the Oman ophiolite: Insights into the architecture of an oceanic proto-arc volcanic sequence. *Solid Earth* 10, 1181–1217. <https://doi.org/10.5194/se-10-1181-2019>.
- Belgrano, T.M., Tollan, P.M., Marxer, F., Diamond, L.W., submitted. Paleobathymetry of submarine lavas in the Samail and Troodos ophiolites: Insights from volatiles in glasses and implications for hydrothermal systems. *J. Geophys. Res. Solid Earth*, in review.

- 
- Bird, P., 2003. An updated digital model of plate boundaries. *Geochem. Geophys. Geosyst.* 4, 1–52. <https://doi.org/10.1029/2001GC000252>.
- Cann, J.R., 1969. Spilites from the Carlsberg Ridge, Indian Ocean. *J. Petrol.* 10, 1–19. <https://doi.org/10.1093/petrology/10.1.1>.
- Cann, J.R., Mccaig, A.M., Yardley, B.W.D., 2015. Rapid generation of reaction permeability in the roots of black smoker systems, Troodos ophiolite, Cyprus. *Geofluids* 15, 179–192. <https://doi.org/10.1111/gfl.12117>.
- Christensen, N.I., Smewing, J.D., 1981. Geology and seismic structure of the northern section of the Oman ophiolite. *J. Geophys. Res.* 86, 2545–2555. <https://doi.org/10.1029/JB086iB04p02545>.
- Christensen, N.I., Ramanantoandro, R., 1988. Permeability of the oceanic crust based on experimental studies of basalt permeability at elevated pressures. *Tectonophysics* 149, 181–186. [https://doi.org/10.1016/0040-1951\(88\)90126-6](https://doi.org/10.1016/0040-1951(88)90126-6).
- Coelho, G., Branquet, Y., Sizaret, S., Arbaret, L., Champallier, R., Rozenbaum, O., 2015. Permeability of sheeted dykes beneath oceanic ridges: Strain experiments coupled with 3D numerical modeling of the Troodos Ophiolite, Cyprus. *Tectonophysics* 644, 138–150. <https://doi.org/10.1016/j.tecto.2015.01.004>.
- Coogan, L.A., Gillis, K.M., 2018. Low-temperature alteration of the seafloor: Impacts on ocean chemistry. *Annu. Rev. Earth Planet. Sci.* 46, 21–45. <https://doi.org/10.1146/annurev-earth-082517-010027>.
- Einaudi, F., Pezard, P. A., Cochemé, J.-J., Coulon, C., Laverne, C., Godard, M., 2000. Petrography, geochemistry and physical properties of a continuous extrusive section from the Sarami Massif, Semail ophiolite. *Mar. Geophys. Res.* 21, 387–407.
- Fisher, A.T., 1998. Permeability within basaltic ocean crust. *Reviews of Geophysics* 36, 143–182. <https://doi.org/10.1029/97RG02916>.
- Fleet, A.J., Robertson, A.H.F., 1980. Ocean-ridge metalliferous and pelagic sediments of the Semail Nappe, Oman. *J. Geol. Soc.* 137, 403–422. <https://doi.org/10.1144/gsjgs.137.4.0403>.
- Galley, A.G., Bailes, A.H., Kitzler, G., 1993. Geological setting and hydrothermal evolution of the Chisel Lake and North Chisel Zn-Pb-Cu-Ag-Au massive sulfide deposits, Snow Lake, Manitoba. *Exploration and Mining Geology* 2, 271–295.
- Gilbert, L.A., Bona, M.L., 2016. Permeability of oceanic crustal rock samples from IODP Hole 1256D. *Geochem. Geophys. Geosyst.* 17, 3825–3832. <https://doi.org/10.1002/2016GC006467>.
-

- Gilbert, L.A., Salisbury, M.H., 2011. Oceanic crustal velocities from laboratory and logging measurements of Integrated Ocean Drilling Program Hole 1256D. *Geochem. Geophys. Geosyst.* 12, Q09001. <https://doi.org/10.1029/2011GC003750>.
- Gilgen, S.A., Diamond, L.W., Mercolli, I., 2016. Sub-seafloor epidosite alteration: Timing, depth and stratigraphic distribution in the Semail Ophiolite, Oman. *Lithos* 260, 191–210. <https://doi.org/10.1016/j.lithos.2016.05.014>.
- Gilgen, S.A., Diamond, L.W., Mercolli, I., Al-Tobi, K., Maidment, D.W., Close, R., Al-Towaya, A., 2014. Volcanostratigraphic controls on the occurrence of massive sulfide deposits in the Semail Ophiolite, Oman. *Economic Geology* 109, 1585–1610. <https://doi.org/10.2113/econgeo.109.6.1585>.
- Gillis, K.M., Banerjee, N.R., 2000. Hydrothermal alteration patterns in supra-subduction zone ophiolites. *Geol. Soc. Am. Spec.* 349, 283–298. <https://doi.org/10.1130/0-8137-2349-3.283>.
- Gillis, K. M., Sapp, K., 1997. Distribution of porosity in a section of upper oceanic crust exposed in the Troodos Ophiolite. *J. Geophys. Res.* 102, 10133–10149. <https://doi.org/10.1029/96JB03909>.
- Guilmette, C., Smit, M.A., van Hinsbergen, D.J.J., Gürer, D., Corfu, F., Charette, B., Maffione, M., Rabeau, O., Savard, D., 2018. Forced subduction initiation recorded in the sole and crust of the Semail Ophiolite of Oman. *Nat. Geosciences* 11, 688–695. <https://doi.org/10.1038/s41561-018-0209-2>.
- Hacker, B.R., Mosenfelder, J.L., Gnos, E., 1996. Rapid emplacement of the Oman ophiolite; Thermal and geochronological constraints. *Tectonics* 15, 1230–1247. <https://doi.org/10.1029/96TC01973>.
- Hamano, Y., 1980. Physical properties of basalts from Holes 417D and 418A. Initial Rep. Deep Sea Drill. Proj. 51, 52, 53, 1457–1466. <https://doi.org/10.2973/dsdp.proc.515253.166.1980>.
- Hannington, M.D., 2014. Volcanogenic massive sulfide deposits. In: Holland, H.D., Turekian, K.K. (Eds.), *Treatise on Geochemistry*, 2nd edition. Elsevier, Oxford, pp. 463–488.
- Hannington, M.D., Santaguida, F., Kjarsgaard, I.M., Cathles, L.M., 2003. Regional-scale hydrothermal alteration in the Central Blake River Group, western Abitibi subprovince, Canada: Implications for VMS prospectivity. *Miner. Deposita* 38, 393–422. <https://doi.org/10.1007/s00126-002-0298-z>.
- Harper, G. D., Bowman, J. R., & Kuhns, R., 1988. A field, chemical, and stable isotope study of subseafloor metamorphism of the Josephine Ophiolite, California-Oregon. *J. Geophys. Res.* 93, 4625–4656. <https://doi.org/10.1029/jb093ib05p04625>.
-

- Hasenclever, J., Theissen-Krah, S., Rüpke, L.H., Morgan, J.P., Iyer, K., Petersen, S., Devey, C.W., 2014. Hybrid shallow on-axis and deep off-axis hydrothermal circulation at fast-spreading ridges. *Nature* 508, 508–512. <https://doi.org/10.1038/nature13174>.
- Heap, M.J.J., Reuschlé, T., Farquharson, J.I.I., Baud, P., 2018. Permeability of volcanic rocks to gas and water. *J. Volcanol. Geotherm. Res.* 354, 29–38. <https://doi.org/10.1016/j.jvolgeores.2018.02.002>.
- Honnorez, J., 2003. Hydrothermal alteration vs. ocean-floor metamorphism. A comparison between two case histories: The TAG hydrothermal mound (Mid-Atlantic Ridge) vs. DSDP/ODP Hole 504B (Equatorial East Pacific). *C. R. Geosci.* 335, 781–824. <https://doi.org/10.1016/j.crte.2003.08.009>.
- Jarrard, R.D., Abrams, L.J., Pockalny, R., Larson, R.L., Hirono, T., 2003. Physical properties of upper oceanic crust: Ocean Drilling Program Hole 801C and the waning of hydrothermal circulation. *J. Geophys. Res. Solid Earth* 108, 1–26. <https://doi.org/10.1029/2001JB001727>.
- Johnson, D.M., 1980a. Fluid permeability of oceanic basalts. Initial Rep. Deep Sea Drill. Proj. 68, 1473–1477.
- Johnson, D.M., 1980b. Crack distribution in the upper crust and its effects upon seismic velocity, seismic structure, formation permeability and fluid circulation. Initial Rep. Deep Sea Drill. Proj. 51, 52, 53, 1457–1466. <https://doi.org/10.2973/DSDP.PROC.515253.169.1980>.
- Jowitt, S.M., Jenkin, G.R.T., Coogan, L.A., Naden, J., 2012. Quantifying the release of base metals from source rocks for volcanogenic massive sulfide deposits: Effects of protolith composition and alteration mineralogy. *J. Geochem. Explor.* 118, 47–59. <https://doi.org/10.1016/j.gexplo.2012.04.005>.
- Jupp, T.E., Schultz, A., 2004. Physical balances in subseafloor hydrothermal convection cells. *J. Geophys. Res. Solid Earth* 109, B5, 1–12. <https://doi.org/10.1029/2003JB002697>.
- Juteau, T., Manac'h, G., Moreau, O., Lecuyer, C., Ramboz, C., 2000. The high temperature reaction zone of the Oman ophiolite: New field data, microthermometry of fluid inclusions, PIXE analyses and oxygen isotopic ratios. *Mar. Geophys. Res.* 21, 351–385. <https://doi.org/10.1023/A:1026798811446>.
- Karato, S., 1983. Physical properties of basalts from Deep Sea Drilling Project Hole 504B, Costa Rica Rift. Initial Rep. Deep Sea Drill. Proj. 69, 687–695. <https://doi.org/10.2973/dsdp.proc.69.143.1983>.

- Kusano, Y., Adachi, Y., Miyashita, S., Umino, S., 2012. Lava accretion system around mid-ocean ridges: Volcanic stratigraphy in the Wadi Fizh area, northern Oman ophiolite. *Geochem. Geophys. Geosyst.* 13, 1–25. <https://doi.org/10.1029/2011GC004006>.
- Kusano, Y., Umino, S., Shinjo, R., Ikei, A., Adachi, Y., Miyashita, S., Arai, S., 2017. Contribution of slab-derived fluid and sedimentary melt in the incipient arc magmas with development of the paleo-arc in the Oman Ophiolite. *Chemical Geology* 449, 206–225. <https://doi.org/10.1016/j.chemgeo.2016.12.012>.
- Kushnir, A.R.L., Martel, C., Champallier, R., Wadsworth, F.B., 2017. Permeability Evolution in Variably Glassy Basaltic Andesites Measured Under Magmatic Conditions. *Geophys. Res. Lett.* 44, 10262–10271. <https://doi.org/10.1002/2017GL074042>.
- Lanari, P., Vho, A., Bovay, T., Airaghi, L., Centrella, S., 2018. Quantitative compositional mapping of mineral phases by electron probe micro-analyser. *Geological Society of London Special Publications* 478, SP478-4. <https://doi.org/10.1144/SP478.4>.
- Lanphere, A.M., 1981. K-Ar ages of metamorphic rocks at the base of the Semail ophiolite, Oman. *J. Geophys. Res.* 86, 2777–2782. <https://doi.org/10.1029/JB086iB04p02777>.
- Lichtner, P.C., 2007. FLOTRAN User’s manual: Two-phase nonisothermal coupled thermal hydrologic-chemical (THC) reactive flow & transport code, version 2. Los Alamos National Laboratory, Los Alamos, New Mexico.
- Lippard, S.J., Shelton, A.W., Gass, I.G., 1986. The ophiolite of northern Oman. Blackwell Scientific Publications Ltd, London, United Kingdom.
- MacLeod, C.J., Lissenberg, J.C., Bibby, L.E., 2013. “Moist MORB” axial magmatism in the Oman ophiolite: The evidence against a mid-ocean ridge origin. *Geology* 41, 459–462. <https://doi.org/10.1130/G33904.1>.
- Miyashita, S., Adachi, Y., Umino, S., 2003. Along-axis magmatic system in the northern Oman ophiolite: Implications of compositional variation of the sheeted dike complex. *Geochem. Geophys. Geosyst.* 4. <https://doi.org/10.1029/2001GC000235>.
- Mordensky, S.P., Kennedy, B.M., Villeneuve, M.C., Lavallée, Y., Reichow, M.K., Wallace, P.A., 2019. Increasing the Permeability of Hydrothermally Altered Andesite by Transitory Heating. *Geochem. Geophys. Geosyst.* 20, 5251–5269. <https://doi.org/10.1029/2019GC008409>.
- Mottl, M.J., Wheat, G.C., 1994. Hydrothermal circulation through mid-ocean ridge flanks: Fluxes of heat and magnesium. *Geochim. Cosmochim. Acta* 58, 2225–2237. [https://doi.org/10.1016/0016-7037\(94\)90007-8](https://doi.org/10.1016/0016-7037(94)90007-8).
-

- Nehlig, P., Juteau, T., Bendel, V., Cotten, J., 1994. The root zones of oceanic hydrothermal systems: Constraints from the Samail ophiolite (Oman). *J. Geophys. Res.* 99, 4703–4713.  
<https://doi.org/10.1029/93JB02663>.
- Nicolas, A., 1989. Structures of ophiolites and dynamics of oceanic lithosphere. Kluwer Academic Publisher, Dordrecht, Netherlands.
- Nicolas, A., Boudier, F., Ildefonse, B., Ball, E., 2000. Accretion of Oman and United Arab Emirates ophiolite – Discussion of a new structural map. *Mar. Geophys. Res.* 21, 147–180.  
<https://doi.org/10.1023/A:1026769727917>.
- Patten, C.G.C., Pitcairn, I.K., Teagle, D.A.H., Harris, M., 2016. Sulphide mineral evolution and metal mobility during alteration of the oceanic crust: Insights from ODP Hole 1256D. *Geochim. Cosmochim. Acta* 193, 132–159. <https://doi.org/10.1016/j.gca.2016.08.009>.
- Pearce, J.A., Lippard, S.J., Roberts, S., 1984. Characteristics and tectonic significance of supra-subduction zone ophiolites. In: Kokelaar, B.P., Howells, M.F. (Eds.), *Marginal Basins Geology: Volcanic and Associated Sedimentary and Tectonic Processes in Modern and Ancient Marginal Basins*. *Geol. Soc. London Spec. Pub.* 16, 77 – 94.  
<https://doi.org/10.1144/GSL.SP.1984.016.01.06>.
- Peters, D., Pettke, T., 2016. Evaluation of Major to Ultra Trace Element Bulk Rock Chemical Analysis of Nanoparticulate Pressed Powder Pellets by LA-ICP-MS. *Geostand. Geoanal. Res.* 41, 5–28. <https://doi.org/10.1111/ggr.12125>.
- Pezard, P. A., 1990. Electrical properties of mid-oceanic ridge basalt and implication for the structure of the upper oceanic crust in Hole 504B. *J. Geophys. Res.* 95, 9237–9264.  
<https://doi.org/10.1029/JB095iB06p09237>.
- Richardson, C.J., Cann, J.R., Richards, H.G., Cowan, J.G., Siegel, J., 1987. Metal-depleted root zones of the Troodos ore-forming hydrothermal systems, Cyprus. *Earth Planet. Sci. Lett.* 84, 243–253.  
[https://doi.org/10.1016/0012-821x\(87\)90089-6](https://doi.org/10.1016/0012-821x(87)90089-6).
- Richter, L., Diamond, L.W., 2019. Identifying deep hydrothermal fluids that leach metals from the oceanic crust and generate seafloor VMS deposits. *Proceedings of the 15th Biennial SGA Meeting* 1, 76–79.
- Richter, L. Diamond, L.W., submitted. Characterization of hydrothermal fluids that alter the upper oceanic crust to spilite and epidosite: Fluid inclusion evidence from the Semail (Oman) and Troodos (Cyprus) ophiolites. *Geochim. Cosmochim. Acta.*, in review.
-

- 
- Searle, M.P., Malpas, J., 1980. Structure and metamorphism of rocks beneath the Semail ophiolite of Oman and their significance in the ophiolite obduction. *Transactions of the Royal Society of Edinburgh: Earth Sciences* 71, 247–262.
- Seyfried, W.E., Berndt, M.E., Seewald, J.S., 1988. Hydrothermal alteration processes at mid ocean ridges: Constraints from diabase alteration experiments, hot-spring fluids and composition of the oceanic crust. *Canadian Mineralogist* 26, 787–804.
- Schiffman, P., Smith, B.M., 1988. Petrology and oxygen isotope geochemistry of a fossil seawater hydrothermal system within the Solea Graben, Northern Troodos Ophiolite, Cyprus. *J. Geophys. Res. Solid Earth* 93, 4612–4624. <https://doi.org/10.1029/JB093iB05p04612>.
- Seyfried, W.E., Mottl, M.J., Bischoff, J.L., 1978. Seawater/basalt ratio effects on the chemistry and mineralogy of spilites from the ocean floor. *Nature* 275, 211–213. <https://doi.org/10.1038/275211a0>.
- Shmonov, V.M., Vitovtova, V.M., Zarubina, I.V., 1995. Permeability of rocks at elevated temperatures and pressures. In: Shmulovich, K.I., Yardley, B.W.D., Gonchar, G.G. (Eds.), *Fluids in the Crust: Equilibrium and Transport Properties*. Springer, Netherlands, Dordrecht, pp. 285–313. [https://doi.org/10.1007/978-94-011-1226-0\\_11](https://doi.org/10.1007/978-94-011-1226-0_11).
- Staudigel, H., 2014. Chemical Fluxes from Hydrothermal Alteration of the Oceanic Crust. In: Holland, H.D., Turekian, K.K. (Eds.), *Treatise on Geochemistry* 2nd edition. vol. 4. Elsevier, Oxford, pp. 583–603. <http://doi.org/10.1016/B978-0-08-095975-7.00318-1>.
- Tominaga, M., Teagle, D.A.H., Alt, J.C., Umino, S., 2009. Determination of the volcanostratigraphy of oceanic crust formed at superfast spreading ridge: Electrofacies analyses of ODP/IODP Hole 1256D. *Geochem. Geophys. Geosyst.* 10, 1–31. <https://doi.org/10.1029/2008GC002143>.
- van Everdingen, D.A., 1995. Fracture characteristics of the Sheeted Dike Complex, Troodos ophiolite, Cyprus: Implications for permeability of oceanic crust. *J. Geophys. Res.* 100, 19957–19972. <https://doi.org/10.1029/95JB01575>.
- Violay, M., Pezard, P.A., Ildefonse, B., Belghoul, A., Laverne, C., 2010. Petrophysical properties of the root zone of sheeted dikes in the ocean crust: A case study from Hole ODP/IODP 1256D, Eastern Equatorial Pacific. *Tectonophysics*, 493, 139–152. <https://doi.org/10.1016/j.tecto.2010.07.013>.
- Weber, S., Diamond, L.W., Alt-Epping, P., Brett-Adams, A.C., submitted. Reaction mechanism and water/rock ratios involved in epidosite alteration of the oceanic crust. *J. Geophys. Res. Solid Earth*, in review.
-



## 4. Permeability of hydrothermally altered and fractured lavas in the oceanic crust at centimetre to kilometre scales, Oman ophiolite: from field mapping to flow simulations

Alannah C. Brett<sup>a</sup> & Larryn W. Diamond<sup>a</sup>

<sup>a</sup>Institute of Geological Sciences, University of Bern, Bern, Switzerland

Unpublished manuscript

*Author contributions:* Alannah Brett mapped and structurally characterised fracture networks and documented the igneous and hydrothermal features of lava outcrops in Oman; made petrographic examinations; upscaled the rock-matrix porosity and permeabilities determined in Chapter 3 to outcrop-scale; created 3D discrete fracture models in the *dfnWorks* software; conducted flow simulations in the *dfnWorks* to calculate bulk fracture–matrix permeabilities; and prepared the manuscript. Larryn Diamond, as thesis supervisor, guided the research, assisted with field work and edited the manuscript.

### Abstract

Exchange of chemical elements and heat between the oceanic crust and the oceans is controlled by the complex permeable interface of extrusive lavas. A prevailing view is that the lavas behave as a fractured aquifer in which permeability to hydrothermal fluids is dominated by extensional faults and fracture networks. However, little is known about the nature and hydraulic efficiency of fracture networks in the km-wide blocks of crust that lie between major faults and their damage zones. Based on field mapping of hydrothermal veins in pervasively altered ridge-axis lavas in the Semail ophiolite, Oman, this study characterises the fracture distribution in such distal blocks and compares it to a fault-proximal damage zone. Fracture intensities in distal blocks are only  $\sim 0.005$  m of fracture per  $\text{m}^2$  of outcrop, but over an order of magnitude higher ( $\sim 0.063$ ) in fault damage zones. Rock-matrix porosities and permeabilities at the outcrop scale (combining weighted values for hyaloclastite, pillow rim and pillow core components) are  $\sim 10\text{--}12$  vol.% and  $\sim 2.5 \times 10^{-16} \text{ m}^2$ , respectively. Numerical hydraulic simulations using *dfnWorks* software, which simultaneously couples fracture- and matrix flow, yield a bulk permeability of  $\sim 10^{-11} \text{ m}^2$  for damage zones, confirming their role as efficient fluid conduits. For distal blocks, simulations yield a bulk permeability of  $\sim 5 \times 10^{-16} \text{ m}^2$ , within the range of published results of hydraulic tests in *in-situ* oceanic crust. This demonstrates that the rock-matrix in distal blocks is just as permeable as the sparse and unconnected fracture network, consistent with the thoroughly pervasive, rather than fracture-controlled, nature of greenschist-facies hydrothermal alteration observed in the distal Semail lavas. Moreover, our bulk values confirm those required by numerical models of crustal-scale hydrothermal circulation aiming to reproduce known heat and fluid discharge at the seafloor. Our observations and calculated bulk permeabilities provide an updated view of fluid flow through the upper

crustal aquifer, in which matrix-flow controls circulation through large blocks of lavas, enhanced by fault-damage zones spaced at km-scale intervals. This new perspective readily explains how the entire layer of oceanic lavas is accessible for isotopic exchange and for intimate leaching of metals for seafloor sulphide deposits.

#### 4.1. Introduction

Basaltic lavas in the upper layer of the oceanic crust behave as an aquifer through which seawater circulates in response to heating by magma bodies. Seafloor faults, rifts and transform zones that accommodate tectonic extension and magmatism are usually considered to be the main channels for fluid flow through the volcanic sequence (Hayman and Karson, 2007; 2009; Karson, 2002; Karson et al., 2002). However, the amount of fluid flow through the large blocks of lavas that lie between the km-spaced faults, here termed *distal zones*, is less well understood. Observations of such zones exposed in ophiolites show that the lavas are pervasively altered to hydrothermal mineral assemblages, attesting to considerable porous-medium type fluid flow. On the other hand, permeable networks of extensional fractures are also thought to be widespread in MOR-type crust. Whether the lava alteration can be explained exclusively by the permeability of the rock-matrix, or whether fracture networks play a decisive role in distributing flow, is unknown. A better understanding of this aspect of the dual permeability architecture of oceanic lavas is of broad interest because it determines the pathways available to hydrothermal fluids that leach metals and form volcanogenic massive sulphide deposits (VMS; Hannington, 2014; Jowitt et al., 2012; Patten et al., 2016), and that cycle mass and heat between the crust and the oceans (e.g. Mottl and Wheat, 1994; Bach et al., 2003).

Rock-matrix permeabilities measured in samples from ophiolites and *in-situ* crust generally yield rather low values of  $\sim 10^{-21}$  to  $10^{-14}$  m<sup>2</sup> (e.g., Christensen and Ramanantoandro, 1988; Brett et al., Chapter 2 of this thesis; Einaudi et al., 2000; Gilbert and Bona, 2016; Gilbert and Salisbury, 2011; Gillis and Sapp, 1997; Hamano, 1980; Jarrard et al., 2003; Johnson, 1980a; Pezard, 1990). In contrast, hydraulic tests in *in-situ* oceanic crust have indicated bulk permeabilities (i.e., those that integrate the contributions of rock-matrix and fracture networks) of  $\sim 10^{-18}$  and  $10^{-13}$  m<sup>2</sup> (e.g., Anderson et al., 1985; Becker, 1989; Becker & Fisher, 2000; Fisher, 1998). However, no single best estimate is available and the relative contributions of fracture and rock-matrix permeabilities remains unclear. The only quantitative fracture and permeability study of oceanic lavas is from DSDP Hole 418, for which a high permeability of  $\sim 3.9 \times 10^{-8}$  m<sup>2</sup> was modelled (Johnson, 1980b). The porosity of fractures within the pillow lavas in the Troodos ophiolite has been estimated at 1–3.5 vol.% (Gillis and Sapp, 1997) but no estimate is available for permeability.

The permeability of fractures has previously been calculated based on variants of the parallel plate method (e.g. Lister, 1974), but the assumption of infinite fracture length tends to overestimate the true permeability (Fisher, 1998; van Everdingen, 1995). In the context of the oceanic crust, this method has been used to calculate the permeability due to fractures in Hole 418 (Johnson, 1980b), in the sheeted

dyke complexes (SDC) of the Semail and Troodos ophiolites (Nehlig, 1994; van Everdingen, 1995). This approach has been superseded by numerical simulation software that allows models of discrete fracture networks (DFN) to be generated stochastically from field data (measurements of orientations, lengths and apertures of fractures). Hydraulic flow through the DFN can then be simulated to yield improved permeability estimates for connected fractures (e.g., the MAFIC approach in the *FracMan* software; Dershowitz et al., 1991; Miller, 1990). This method was also applied by van Everdingen (1995) to the Troodos SDC, resulting in much lower permeabilities than those calculated using the parallel plate approach. Continuum approaches to calculate permeability by flow modelling have been used in other settings, but thus far they have been unable to capture the geometry and connectivity of natural fracture networks (Sweeney et al., 2019). A recent development is the upscaled discrete fracture–matrix (UDFM) modelling code (Sweeney et al., 2019), as implemented in the *dfnWorks* parallelised computation software for subsurface flow and transport modelling (Hyman et al., 2015). This enables simulations of combined flow through fracture-networks within a permeable rock-matrix, while retaining fracture geometry and connectivity. Implementation of this approach has the potential to describe the dual porosity and dual permeability of the lavas in the upper crust.

This study aims to estimate the bulk permeability of distal zones of lavas in the oceanic crust. In doing so, we also aim to show whether the traditional concept of extrusive lavas as a fracture-network aquifer holds, or if a porous-medium aquifer with a relatively sparse fracture component is a more accurate description. To achieve this, we investigate the axial MORB-like Geotimes volcanic unit of the Semail ophiolite, Oman. This site presents an opportunity to observe and map vast areas of relatively undeformed extrusive lavas, providing an areal perspective that cannot be achieved yet in *in-situ* oceanic crust. We present new field characterisations of fractures in several distal areas of lavas and in a fault-proximal damage zone, and then use these structural observations to create DFN models using the UDFM code. Average values of rock-matrix porosities and permeabilities of the Geotimes lavas, as determined by Brett et al. (Chapter 3 of this thesis), are upscaled and used to define the hydraulic properties of the lava bodies that host the DFNs. Flow simulations in *dfnWorks* then yield the bulk permeability of the distal and fault-proximal zones. These results provide robust input parameters for future numerical simulations that investigate coupled thermal–hydraulic–chemical processes in the hydrothermally active oceanic crust (e.g., Fisher, 1998 and references therein; Hasenclever et al., 2014).

## 4.2. Geological setting

The Semail ophiolite is a well preserved and complete section of oceanic lithosphere formed in a proto-arc setting between 97–93 Ma and obducted onto the Arabian margin at ~70 Ma (Belgrano & Diamond, 2019; Coleman, 1981; Glennie et al., 1974; Guilmette et al., 2018; Searle & Cox, 1999). The volcanic stratigraphy dips on average ~30° to the east, constituting an oblique cross-section through the upper crust that stretches over 500 km along Oman’s northern coast and into U.A.E. It includes a 4–6 km thickness of lower oceanic crust, 3–4 km of SDC and extrusive lavas, capped by a layer of pelagic

sediments (Belgrano et al., 2019; Lippard et al., 1986). The volcanic section is composed of four distinct lavas units; at the base is the MORB-like basaltic to basaltic-andesitic Geotimes unit, which formed at a fast-spreading ridge axis and which was fed by the SDC. This is overlain by the primitive off-axis Lasail unit, and by post-axial Thoeilitic Alley and Boninitic Alley units. The post-axial units were fed by dyke swarms that crosscut the SDC, Geotimes and Lasail units with NW–SE to E–W orientations (e.g. Belgrano et al., 2019). Detailed descriptions of the lavas units are given by Belgrano et al. (2019). The nascent supra-subduction zone setting of ridge-axis volcanism in Oman imparted trace element and igneous water contents to the Geotimes lavas that differ from those in typical MORB (Belgrano & Diamond, 2019 and references therein; Guilmette et al., 2018; MacLeod et al., 2013). However, the volcanic and structural features of the Geotimes lavas, with their vast stacks of weakly vesicular pillow lavas and minor massive flows, are a good analogue of MORB lavas in in-situ fast-spreading ridges, e.g. the East Pacific Rise (e.g., Einaudi et al., 2000; Nehlig et al., 1995).

The Semail upper crust was not penetratively deformed during its obduction, but localised faulting caused block rotations and some reactivation of seafloor faults. Emplacement of the ophiolite resulted in segmentation of the Semail nappe into massifs along thrusts and normal faults, but the internal structure of these massifs remained intact (MacLeod and Rothery, 1992; Nicolas et al., 2000; Searle and Cox, 1999). In some areas, the volcanic rocks are crosscut by quartz–hematite–pyrite veins with chloritised alteration haloes and by later calcite veins, both attributed to post-magmatic and syn-obduction processes (Gilgen et al., 2014; Richter & Diamond, submitted).

Geological maps of the Semail upper crust show at least one major rift graben and numerous syn-volcanic, normal faults (Belgrano et al., 2019; MacLeod and Rothery, 1992; Searle and Cox, 1999). Kilometre-scale syn-volcanic faults orientated NW–SE and E–W are common across the ophiolite, occurring at a spacing of roughly 0.5–2 km (e.g. in maps by Lippard et al., 1986 and Belgrano et al., 2019). Importantly for the present study, the syn-volcanic timing of these faults can usually be distinguished by their alteration mineralogy (e.g., epidote, quartz, and sulphides), by offsets and up-section onlaps of the volcanostratigraphy, and by the presence of tonalites, gabbros and swarms of mafic dykes injected along the faults (e.g., Belgrano et al., 2019; MacLeod and Rothery, 1992). The hot and metal-rich hydrothermal fluids tapped by the fault zones are key ingredients needed to form VMS deposits, a relationship which has been previously suggested and indicated at a number of sites, e.g. the Yanqul area Rakah and Hayl al Safil deposits and the Safwa deposits south of Wadi Rajmi (Belgrano et al., 2019; Gilgen et al., 2014; Haymon et al., 1989; Smewing et al., 1977). However, this relationship is not always systematic because of the variable timing of VMS deposits relative to different stages of volcanism (e.g. Gilgen et al., 2014). For example, the Aarja deposit extends in a NW–SE direction, but the nearby Bayda deposit is crosscut by NW–SE and E–W faults (Lippard et al., 1986). The timing of fractures and regional faults relative to magmatism and VMS formation is therefore a key aspect that requires further investigation (Belgrano et al., 2019).

At a 10–100 m scale the transition from the gabbros to the lower SDC is characterised by fracture densities (marked by actinolite and epidote + quartz veins) of 0.01–0.5 fractures per metre (Nehlig, 1994). However, in the Geotimes lavas the fracture distribution in fault-damage zones and between faults has never been mapped. Despite this, the extrusive crust is clearly permeable, given the regionally pervasive hydrothermal alteration of the SDC and all the overlying lavas (Lippard et al., 1986). In the Geotimes unit, the pervasive background alteration is of greenschist-facies “spilite” type (Cann, 1969; Honnorez, 2003), characterised by hydrothermal assemblages of albite + chlorite ± actinolite, typical of downwelling seawater that leaches Ca and enriches the lavas in Mg and Na. The Geotimes, Lasail and Tholietic Alley lavas also host large (~1 km<sup>2</sup>) zones of the high temperature, Ca-rich alteration known as “epidosite”, which is a metasomatic replacement of spilites by epidote + quartz + Fe-Ti-oxides (Gilgen et al., 2016; Richter & Diamond, 2019; Seyfried et al., 1988). The relationship between these pervasively altered rocks and fractures containing hydrothermal minerals is important for our understanding of hydrothermal fluid flow through the oceanic crust.

### **4.3. Approach**

Our principle aim was to generate a bulk permeability value that accurately represents both fracture and rock-matrix permeability in the distal zones of the axial lavas. The workflow developed in Fig. 4.1 was focused on the volcanic lavas of the Semail ophiolite but could be applied to other settings. Fracture and rock-matrix properties were treated in separate upscaling paths: the fracture upscaling quantified fracture distributions and produced inputs for the DFN component of the UDFM model, and the rock-matrix upscaling produced bulk matrix porosities and permeabilities (per cubic metre of outcrop) for the UDFM (Fig. 4.1). The rock-matrix upscaling relied on the average rock-matrix porosities and permeabilities produced in Chapter 3 (see Section 4.1 below). Prerequisites for the fracture upscaling were the choice of mapping locations and the relevant fracture types.

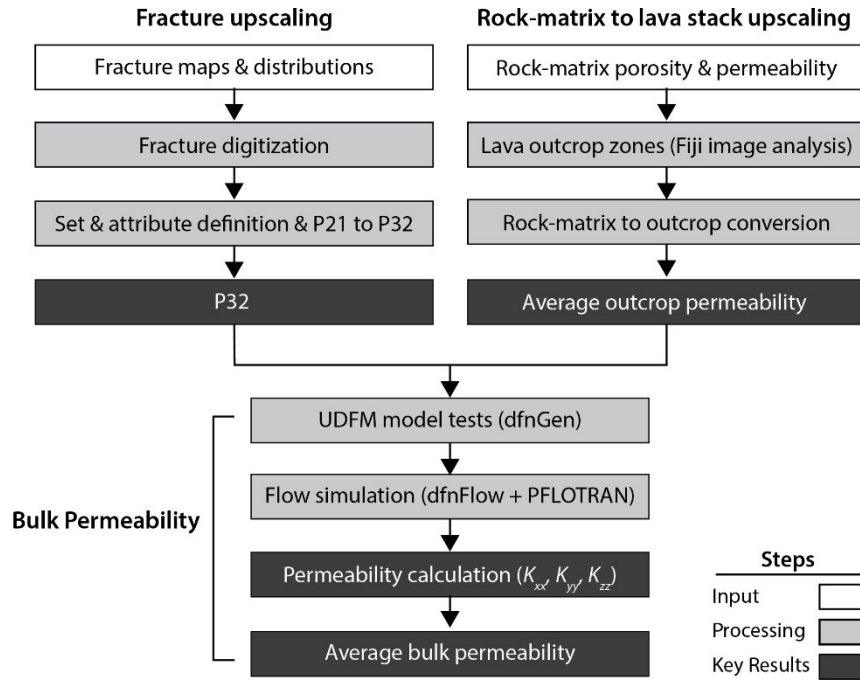


**Figure 4.1.** Workflow of fracture and rock-matrix upscaling, showing steps to create UDFM models. Bulk permeability path shows key steps to calculate bulk permeabilities of the pillow lavas in zones distal to faults and in fault-proximal damage zones.

Four locations of distal zones were chosen based on the recent geological map of Belgrano et al. (2019). The first three locations, ‘Aswad’, ‘Hilti’ and ‘Rusays’, are zones of mainly Geotimes lavas, plus a region of Lasail lavas at Rusays, without major through-going syn-volcanic faults (Figure 4.2a,b,c). Preliminary scouting of these locations showed a damage zone of intense fracturing in the SW boundary of the Hilti location and in the NE corner of the Aswad location. Both of these zones are adjacent to the syn-volcanic faults indicated in Figure 4.2a and b; however, the wadi gravel cover over fault zones meant no fault-zone characterisation could be made. The fourth area, ‘Ajeeb’ (Fig. 4.2d), was chosen because of its outcropping ~2 km long damage zone around a syn-volcanic fault, for which an alteration map is available (Gilgen et al., 2016). At Ajeeb the difference between the fault damage zone and surrounding distal zone was documented and subsequently the zones were separated into the Ajeeb Damage Zone and the Ajeeb Distal Zone for the UDFM models.

As a basis for mapping, we also distinguished the fracture types open during seafloor hydrothermal circulation. Existing descriptions of fracture types by Gilgen (2014) distinguished syn-volcanic fractures as those filled with the hydrothermal minerals epidote, epidote + quartz, prehnite, and prehnite + quartz. Previous mapping studies identified kilometre-scale syn-volcanic faults with similar assemblages. These are sub-vertical extensional structures commonly trending NW–SE to E–W, ~2 km long and surrounded by  $\pm$  ~50–100 m wide damage zones, e.g. the fault in the Ajeeb area first described by Gilgen (2014). Fractures filled with calcite or quartz + hematite were identified as post-

volcanic features. Additionally, in line with previous studies on fracture mapping in ophiolites (e.g., van Everdingen, 1995), we assumed that any empty fractures in the outcrops were either hydraulically isolated and hence insufficiently conductive to become filled with hydrothermal minerals, or they were created after the calcite veins, i.e., during obduction or weathering. Accordingly, only fractures filled with syn-volcanic hydrothermal minerals were mapped. Such fractures could alternatively be termed veins, but we refer to them hereafter as fractures.

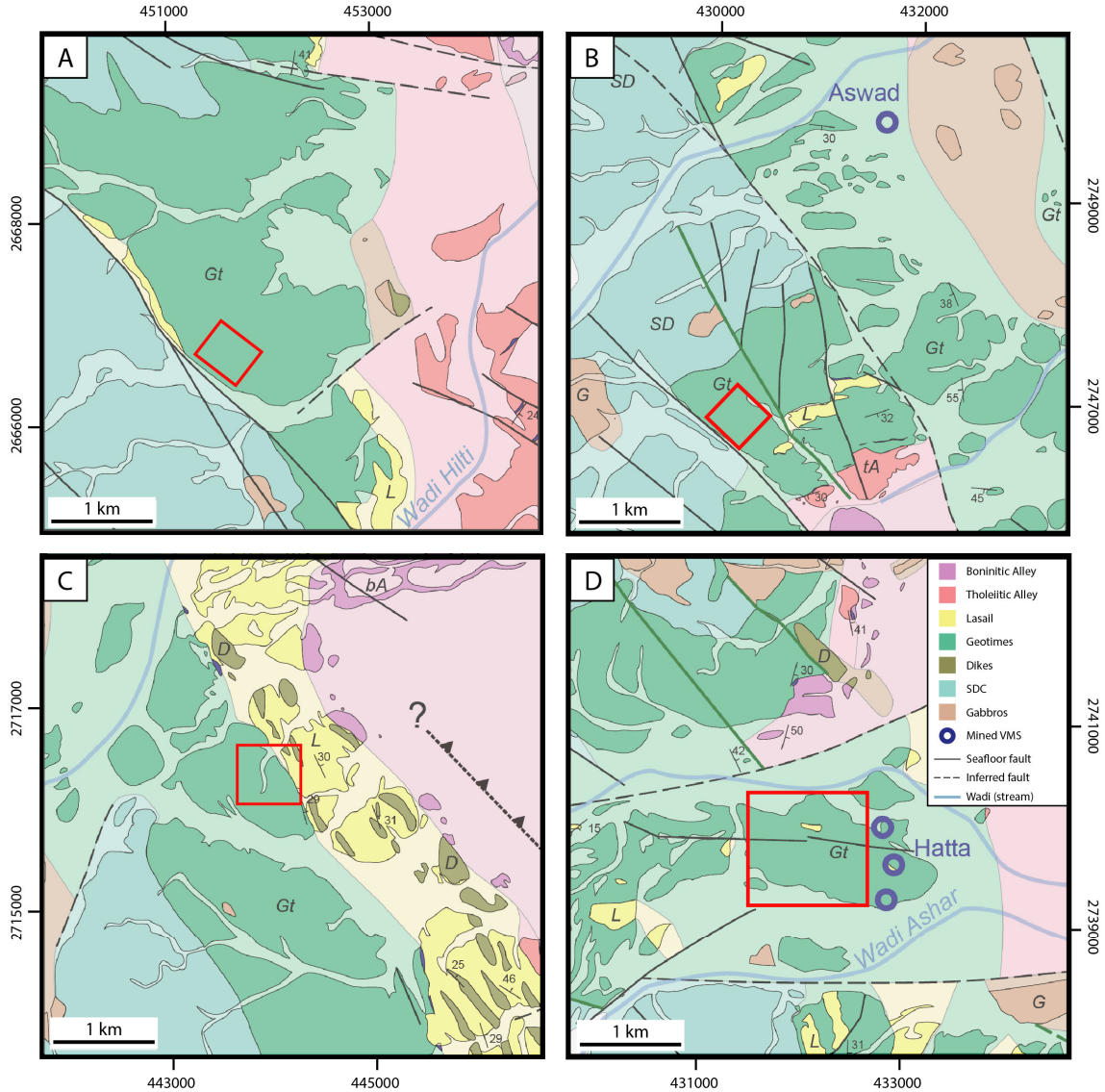


**Figure 4.2.** Maps of the Semail ophiolite volcanic units modified after Belgrano et al. (2019), showing overviews of the chosen fracture mapping areas (red rectangles) in the Geotimes and some Lasail lavas. Note UTM coordinates are unique for each map. (a) Hilti. (b) Aswad. (c) Rusays. (d) Ajeeb.

An important aspect of the fracture upscaling was a customised mapping approach that best acquires the *fracture intensity* value “P21” (fracture length per unit area of outcrop;  $m^{-1}$ ), which is essential input for the DFN and UDFM models. Although we also acquired traditional *fracture density*

values “P10” (number of fractures per unit length of outcrop;  $\text{m}^{-1}$ ), P21 is advantageous because it describes the lengths of fractures and is independent of direction (Giuffrida et al., 2019; Wang, 2005). Using the method of Wang (2005), the measured P21 values were converted to the *volumetric fracture intensity* value “P32” (area of fractures per unit volume of outcrop;  $\text{m}^{-1}$ ) required to generate stochastic fracture distributions.

On the basis of representative upscaled rock-matrix values and fracture distributions, the UDFM model was constructed and implemented in the *dfnWorks* code. Flow simulations were then carried out across the UDFM and the bulk permeability of each model was calculated with an appropriate version of Darcy’s law. A detailed description of the modelling steps follows in the methods Section 4.

## 4.4. Methods

### 4.4.1. Rock-matrix porosity and permeability upscaling

To determine the rock-matrix porosity and permeability of pillow lava stacks, we developed a method to upscale standard measurements on cylindrical 2.5 cm diameter drill plugs from the hydraulically distinct rock components that make up pillow stacks, i.e. pillow cores, pillow rims and interpillow hyaloclastites, as determined in Chapter 3 of this Thesis. Digital field photographs of outcrops orientated perpendicular to the lava extrusion direction (e.g. Fig. 4.3a) were used to determine the proportions of the pillow components. The pillows are approximated as cylinders along their long axes as in Fig. 4.3b and therefore the cross-sectional area fractions of the component rocks is approximately equal to their volume fractions. Three outcrop images were chosen with variable abundances of interpillow hyaloclastites.

In Chapter 3 (this Thesis) we showed from thin-section microscopy that spilitised pillow cores and rims have different permeabilities owing to their different grain-sizes. Unfortunately, the boundary between cores and rims is often indistinguishable in the field. Therefore, to find the fractions of rim and core zones in an average Geotimes pillow, we analysed an image of a pillow stack that shows preferential alteration of the cores to epidosite (Fig. 4.3a). Gilgen et al. (2016) and our work in Chapter 3 of this Thesis showed that such “intermediate epidosite” outcrops reliably distinguish pillow cores from pillow rims. We digitised this chosen pillow stack into separate layers of polygons for the core and for the entire pillows (core + rim). The separate layers files (Figure 4.3c,d) were then converted into black and white binary images and processed to find their surface areas ( $\text{m}^2$ ) in *Fiji/ImageJ*.

To determine the average fraction of hyaloclastite zones in a pillow outcrop, the three pillow outcrop images with different hyaloclastite abundances were digitised in *Adobe Illustrator* into two layers of polygons; the entire pillows (rim + core) and the entire outcrop (e.g. Fig. 4.3e,f). These images were processed for their respective surface areas ( $\text{m}^2$ ) in *Fiji/ImageJ* (Fig. 4.3d).

We assume that these area fractions are equal to volume fractions and that these proportions apply for both spilite and epidosite lava stacks because no indications of pillow-volume change during



epidotisation have been observed. Additionally, our observations of epidosite alteration patterns show flow occurred mainly parallel to the core, rim and interpillow zones along the long axes of the pillow tubes, rather than perpendicular to them. The porosity and permeability per cubic metre of outcrop were therefore calculated by the arithmetic means (rather than harmonic mean used for cross-flow permeability; Maasland, 1957) of the average pillow zone values from Chapter 3 weighted by the core, rim and interpillow proportions.

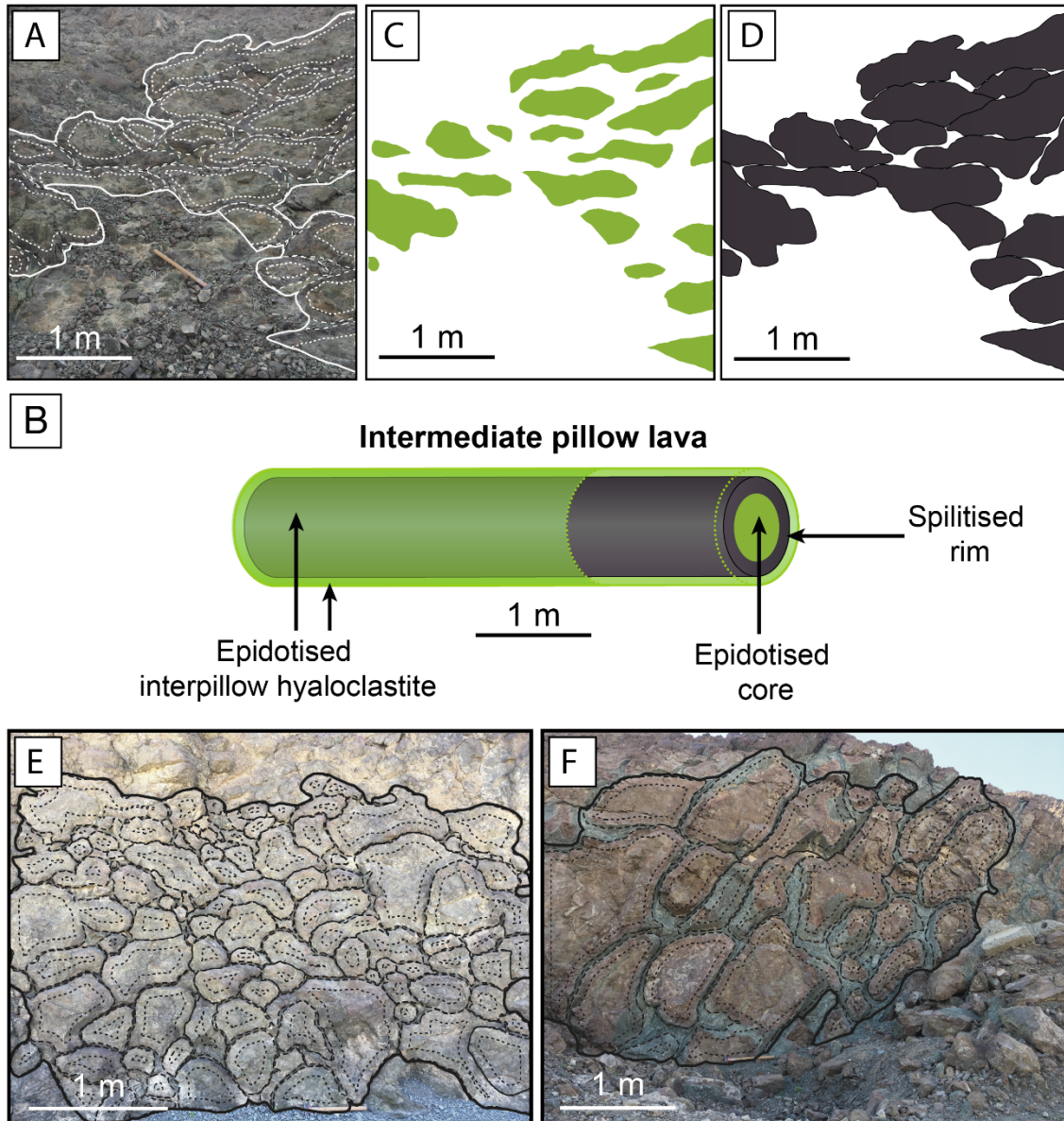


**Figure 4.3.** Outcrop images and polygon layers used for upscaling from drill plug analyses to outcrop rock-matrix porosity and permeability, along with a schematic pillow tube. (a) Intermediate pillow outcrop, with epidotised pillow cores and spilitised pillow rims. (b) 3D diagram of intermediate-type pillow tube. (c) Polygons of pillow core areas. (d) Polygons of pillow area (core + rim). (e) Spilite outcrop with thin interpillow hyaloclastites. (f) Spilite outcrop of large pillows with thick interpillow hyaloclastites.

#### 4.4.2. Fracture mapping

Fracture mapping was conducted in four areas of  $\sim 0.25\text{--}0.5\text{ km}^2$  in the Geotimes and Lasail volcanic units over two field seasons (2018 and 2020; Fig. 4.2a,b,c,d). Instead of the traditional line or circular transect maps (e.g. Fig. 4.4a,b), areas termed “swaths” were mapped. Swath maps as shown in Fig. 4.4c,d provide the fracture intensity P21 and eliminate most of the directional bias caused by line transects.

Swaths were defined in GPS-guided mapping tablets with the software *Field Move*<sup>TM</sup> and marked by a central line. Each mapper followed a central line, looking and mapping  $\pm 5\text{ m}$  of either side and documenting any fractures in the swath area. Swaths were between 50 and 800 m long and spaced 30–50 m apart where possible. Mainly swaths following a grid pattern were mapped (Fig. 4.4c); however, in areas with limited outcrop, non-linear swaths were followed to maximise the amount of mapped outcrop (Fig. 4.4d).

The location of each fracture was marked on the GPS-guided mapping tablet, and the aperture (min, max, mode), length, orientation, mineral assemblage, termination type (in outcrop or under gravel cover) and other features, such as kinematic indicators and alteration haloes, were recorded in *Field Move*<sup>TM</sup>. To accurately represent fracture length distributions the full fracture lengths were recorded, i.e. including the lengths of segments extending outside of the swath area, where exposed. Fracture traces were mostly  $< 30\text{ m}$  long and a minimum cut-off length of 30 cm was applied. Most fracture terminations could be mapped within outcrops.

Mapping was limited to fractures visually discernible from up to  $\sim 5\text{ m}$  distance in the field and therefore the proportion of fractures  $\leq 1\text{ mm}$  wide is under-represented. Reconstruction of the fracture apertures at the time of hydrothermal circulation required interpretation. For typical fractures this was taken as the thickness of the single generation of hydrothermal minerals that fills the fracture. In less common cases, the aperture could only be roughly estimated, where: (1) fine grained space-filling assemblages (commonly with chlorite, hematite, pumpellyite and sometimes fine-grained epidote) display diffuse rather than sharp boundaries against the surrounding alteration haloes in the wall rocks, (2) syn-volcanic fractures are overprinted by obduction-related quartz–hematite veins, which widen the apparent aperture of the precursor fracture, and (3) the apertures are widened by multiple generations of mineral precipitation or by breccias. These apertures were estimated as best as possible and thin sections were made to check true aperture widths where required.

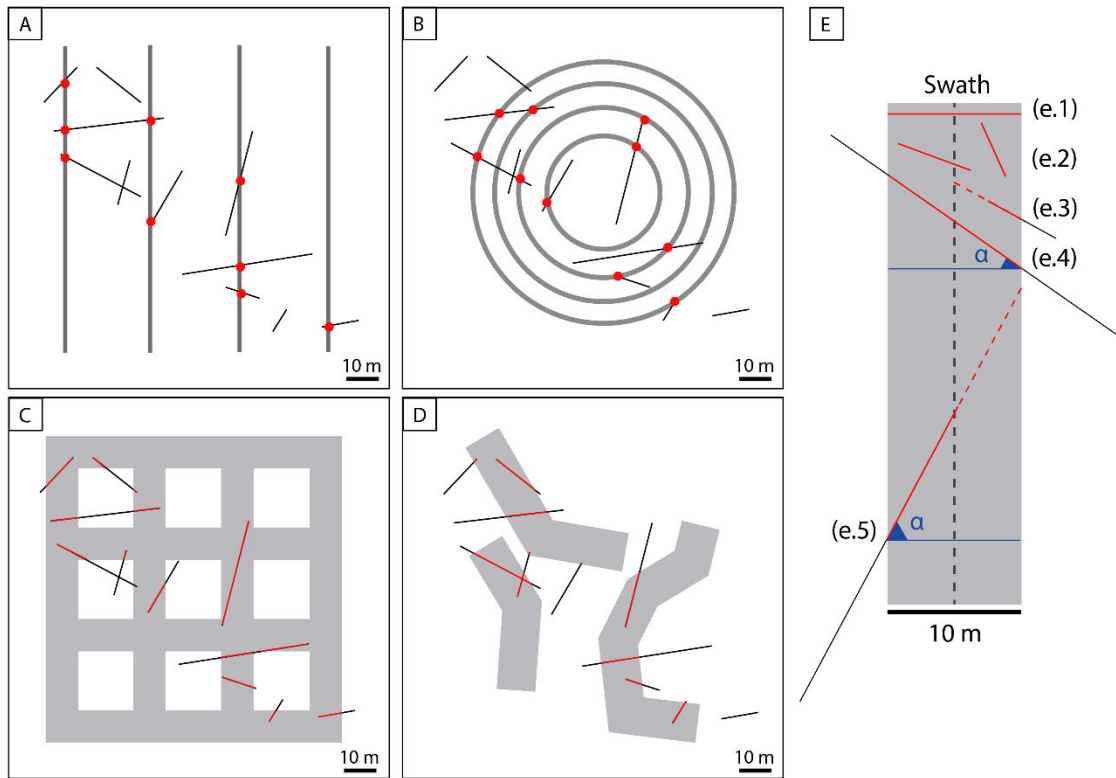


**Figure 4.4.** Fracture mapping approaches to measure P10 and P21 values. Examples of line transects and swath areas are shown in light grey; fractures in black; intercepts of transects and fractures shown in red dots. Lengths of fractures within swath areas shown by solid red lines; additional lengths projected within swath shown in red dotted lines. Blue lines in E show diameter of swath perpendicular to long axis. Note different scale between (e) and other diagrams. (a) Parallel line transects. (b) Circular transects. (c) Orientated swaths. (d) Un-orientated swaths. (e) Fracture types characterised by their relationship with the swath. Fracture types: (e.1) Fracture of 10 m length within the swath. (e.2) Fractures < 10 m length inside swath. (e.3) Fracture of  $\leq 10$  m length partly inside and partly outside the swath. (e.4) Fracture of > 10 m length crosscutting the swath. (e.5) Fracture of > 10 m length cutting into the swath.

#### 4.4.3. Fracture distribution analysis

##### 4.4.3.1. Classification of fractures into geometric groups

Fracture attributes recorded in *Field Move*<sup>TM</sup> for each mapped area were exported for processing into the *Fracture Modeling* module of *Move*<sup>TM</sup> and into *Stereonet* (Allmendinger et al., 2013). Prior to analysing the data, fracture orientations were restored to their original seafloor orientations by rotating the local dip of the volcanic stratigraphy to horizontal (Table 4.1). In most studies, stochastic generation of fracture networks is based on the statistical properties of structurally distinguishable fracture *sets*. However, no clear structural distinction between fractures could be made in the present case because none of the mapped fractures show kinematic indicators. Therefore, to permit statistical characterisation of the fracture orientations, we simply identified groups based on the positions of fracture poles on the stereonet of each map. We therefore refer to these as “geometric groups” rather than traditional “fracture sets”. For each geometric group a Fisher distribution and principal mean pole were calculated (Fisher, 1953).

The fracture length and aperture data from each mapping location were analysed to choose the length and aperture distribution parameters required to construct the DFN models. The low number of fractures in each geometric group meant that it was not viable to make distribution fits based on the individual lengths and apertures of the fractures. Among the options in the employed UDFM code, we chose to fit our length data by log-normal distributions. For the distribution of apertures, we found that length-aperture plots showed no meaningful correlation and that a  $\log_{10}$  function did not reveal a normal distribution. However, since apertures clearly vary, we used a log-normal distribution as the best approximate representation from the available options.

These distribution fits required mean, minimum, maximum and standard deviation of fracture radii data and the mean and standard deviation of aperture data. Each geometric group was assigned its individual values of fracture radii. One of the geometric groups contained fractures of constant length, for which a constant distribution parameter was applied. The UDFM code allows only one type of aperture distribution per model. Therefore, the average and standard deviation values combined from all fractures at a given location were assigned to each geometric group at that location.

#### *4.4.3.2. Fracture intensity: conversion of P21 to P32*

The *volumetric fracture intensity* P32, is a principle input parameter required for each geometric group of fractures to build a representative UDFM model. To calculate a P32 value we first calculated P21 from mapped fracture lengths and outcrop area data, and then converted P21 to P32 using the method of Wang (2005).

P21 was determined in two steps. The total area of outcrop was calculated by subtracting the recorded area of gravel cover from the total swath area mapped. A trace map of fracture lengths could not be made due to limitations in reproducibility of the GPS locations, e.g. short fractures  $< 1$  m were within GPS uncertainty. Therefore, we manually determined the lengths of fractures inside the swaths based on the length value recorded for each fracture, as follows. The full lengths of fractures  $\leq 10$  m long (e.g., Fig. 4.4 e.1, e.2 and e.3) were automatically included. This covers the majority of fractures mapped. This may slightly overestimate fracture length, for example in Fig. 4.4 e.3 where the dotted red portion of the fracture that might have been outside the swath was projected into the swath. The length of fractures  $> 10$  m were individually adjusted using trigonometry, knowing the angle  $\alpha$  of the fracture with respect to the swath line (Fig. 4.4 e.4, e.5). The resulting value was the maximum length to occur within the swath. This approach may overestimate the length in cases where long fractures were mainly mapped outside of the swath and for which part of the length is projected inside the swath (Fig. 4.4 e.5), but fortunately, this rarely occurred. After these steps, the sum of fracture lengths for each geometric group of fractures was calculated. The P21 value was then determined for each geometric group by the total length of fractures per geometric group divided by the total outcrop area mapped.

To convert from the planar fracture intensity P21 to volumetric fracture intensity P32 we used the method provided by Wang (2005), which multiplies P21 by a conversion factor, C23. Wang (2005) produced equations to find C23 based on any Fisher distribution and the corresponding angle ( $\rho$ ) between the lines of the pole of the sampling plane and the Fisher mean pole (details in Wang, 2005). In our case the sampling plane followed the topography of the mapping sites and although this was in fact undulating, we treated the sampling plane as horizontal. This means that the sampling plane normal is orientated vertically and therefore the  $\rho$ -angle is approximately equal to the Fisher mean dip. Thus, C23 was calculated for each of our fracture sets, and used to generate P32 values.

**Table 4.1.** Orientations of local lava stratigraphy at each location used to restore field data to seafloor dip orientation in *Stereonet* (Allmendinger et al., 2013).

Location	Azimuth of rotation axis <sup>1</sup>	Plunge of rotation axis <sup>2</sup>	Magnitude of rotation <sup>3</sup>	Stratigraphy orientation source
Hilti	088	0	-26	BRGM (1993)
Aswad	072	0	-30	Belgrano et al. (2019)
Rusays	165	0	30	Belgrano et al. (2019)
Ajeeb	037	0	-23	Gilgen (2014)

<sup>1</sup>Azimuth of rotation is the strike of the local stratigraphy; <sup>2</sup>Plunge is set to zero as rotating around the horizontal strike line; <sup>3</sup>Magnitude of rotation is in the anticlockwise direction looking in the dip direction.

#### 4.4.4. *dfnWorks* workflow: DFN, domain build and flow simulation

The open source software *dfnWorks* (Hyman et al., 2015) was used to build a UDFM model and simulate flow in order to calculate bulk permeabilities (also known as effective permeability) of the mapped lavas. Created at Los Alamos National Laboratory (LANL), *dfnWorks* is a parallelised computation suite, which provides a framework for existing codes, such as the meshing code *Los Alamos Grid Toolbox* (*LaGriT*; also developed at LANL) and the massively parallel reactive-transport and flow finite volume flow code *PFLOTRAN* (Hammond et al., 2014; Lichtner et al., 2015) to be implemented with UDFM models generated by *dfnWorks*.

The first step was to use the *dfnGen* module in *dfnWorks* to generate a DFN that stochastically models the fracture properties and their distributions at each mapped location. The minimum length scale, which determines the smallest possible feature in the model (e.g., fracture intersection length; distance between lines of fracture intersection), was set to 0.2 m.

To incorporate our outcrop rock-matrix porosities and permeabilities into the DFN's, the UDFM model developed by Sweeney et al., (2019) was implemented. The UDFM model is a new code that overcomes the challenges of meshing between highly permeable fractures and a surrounding porous matrix, while preserving network geometry and connectivity. It requires a starting mesh size, which we set to 25 m, equivalent to the diameter of an average pillow outcrop. A mesh refinement level of 3–4 steps was chosen; this increases the mesh resolution around fractures by an octree division of the mesh

volumes containing fractures and immediately adjacent volumes. The meshing of the DFN and the surrounding matrix was carried out using the integrated *LaGriT* module which builds an unstructured grid for the UDFM.

The *dfnFlow* module was then used to simulate fluid flow through the UDFM models. The initial boundary conditions for pressure were set to Dirichlet with a constant atmospheric pressure ( $1.0325 \times 10^5$  Pa). A Dirichlet pressure gradient was then applied at the inflow and outflow domain boundaries, equivalent to 1 m hydraulic head ( $9.81 \times 10^3$  Pa). The flow simulations were run with inflow and outflow boundaries in the three principal permeability tensor directions,  $x$ ,  $y$ , and  $z$ . Key outputs of these simulations were the inflow and outflow fluid masses (kg), the inflow and outflow rates (kg/d) and domain density. Finally, to calculate the bulk permeability across the entire domain in each principle direction, an additional python script was run with the following form of Darcy's law:

$$k = \frac{q \times \mu}{\Delta P} \quad (1)$$

where  $k$  is the effective permeability ( $\text{m}^2$ ),  $q$  is the output value of total Darcy flux ( $\text{m}^3/\text{m}^2/\text{s}$ ) that exits the domain boundary,  $\mu$  the dynamic viscosity of water ( $\text{m}^2/\text{s}$ ) and  $\Delta P$  the pressure gradient (Pa).

These steps were carried out for each of the four mapped distal zones and at the Ajeeb Damage Zone using spilite rock-matrix properties. An additional model and set of flow simulations was made with epidosite rock-matrix properties combined with the fracture distribution from the Hilti location. For each model a geometric mean of permeability across the three main flow directions was calculated for each of the spilite and distal zone models, and these were combined again using the geometric mean into a bulk permeability for distal zone models.

## 4.5. Results

### 4.5.1. Bulk rock-matrix porosity and permeability

Based on the image analysis areas we calculated that cores composes ~52 area% and rims ~48 area% of an average pillow. The hyaloclastites compose 8.7, 25.4 and 16.8 area% in the three outcrops, with an average of ~17.0 area%. Therefore, as a proportion of the total outcrop, the cores compose ~43 area%, the rims ~40 area% and the interpillows ~17 area%. Pillow lavas stacks have bulk rock-matrix porosities ( $\phi$ ) and permeabilities ( $k$ ) that are composed of these contributions. Therefore, for each  $\text{m}^3$  of pillow stack, spilitised lavas are calculated to have  $\phi \approx 10$  vol.% and  $k \approx 2 \times 10^{-16} \text{ m}^2$ , and epidotised lavas have  $\phi \approx 12$  vol.% and  $k \approx 3 \times 10^{-16} \text{ m}^2$ .

### 4.5.2. Syn-volcanic fault structures

The main type of syn-volcanic structures observed in the mapping areas are extensional fractures with hydrothermal mineral fillings (i.e. veins), which typically cut across several individual pillows. The host fractures thus formed after cooling of the pillow flow and they are not to be confused to cooling

joints (see below). In fault-damage zones the fractures are sub-vertical and strike NW–SE to E–W, with variable lengths of ~0.3–50 m and apertures of ~0.1–4 cm. Fractures in fault-distal zones have similar orientations, are sub-vertical, and have lengths of ~0.3–30 m and apertures of ~0.1–3 cm. A few fractures longer than 30 m were also observed. None of the fractures show shear offsets of the pillows, as evidenced by the geometry of the pillow boundaries (e.g., Fig. 4.5a). The field appearance and variety of hydrothermal minerals that fill these fractures are shown in Fig. 4.5. Mineral assemblages such as epidote, epidote + quartz and prehnite are the most common, although chlorite, pyrite and pumpellyite have also been observed. The apertures of these fractures vary. Some epidote  $\pm$  quartz fractures are < 1 mm wide with an intense epidote alteration halo making them appear up to 2 cm thick (Fig. 4.5c,e). Other fractures have multiple quartz and epidote generations and may contain breccias zones including clasts of epidotised wall rock and of epidote  $\pm$  quartz vein with a surrounding epidote  $\pm$  quartz matrix (Fig. 4.5b,g,h). Epidote-bearing mineral assemblages are particularly common close to large pervasive epidotes and epidotised fault zones as at Ajeeb, but are also found in fault-distal zones of spilite lavas. Prehnite- (Fig. 4.5d,f) and chlorite-bearing fractures are more commonly found in spilite lavas.

Aside from the above mineralised, post-cooling fractures, the majority of Geotimes pillows are free of lava cooling joints. This is a key characteristic of the Geotimes unit, which contrasts with the commonly jointed pillows in the Lasail unit. Nevertheless, radial and concentric cooling joints are occasionally present (Fig. 4.6a,b), creating a honeycomb-like pattern on pillow crusts. Each joint typically penetrates only 10–15 cm into the pillow interior, hence the jointed pillows remain robustly intact and the joints do not constitute a connected flow network that traverses the pillows. The joints have apertures of < 1 mm and are bordered by alteration haloes up to 1 cm wide. The main joint-filling minerals are prehnite and epidote  $\pm$  quartz (Fig. 4.6 c,d,e). Where prehnite is present, it often fills only short ( $\leq$  3 cm) segments of the joints, leaving the remainder open (Fig 4.6c). The most famous pillow stacks in Oman at the type locality of the Geotimes unit (Suhaylah Road bridge over Wadi Jizi) exemplify the uncommon jointed pillows with minor prehnite fillings. Examples of the common joint-free Geotimes lavas are shown in Fig. 4.6f.



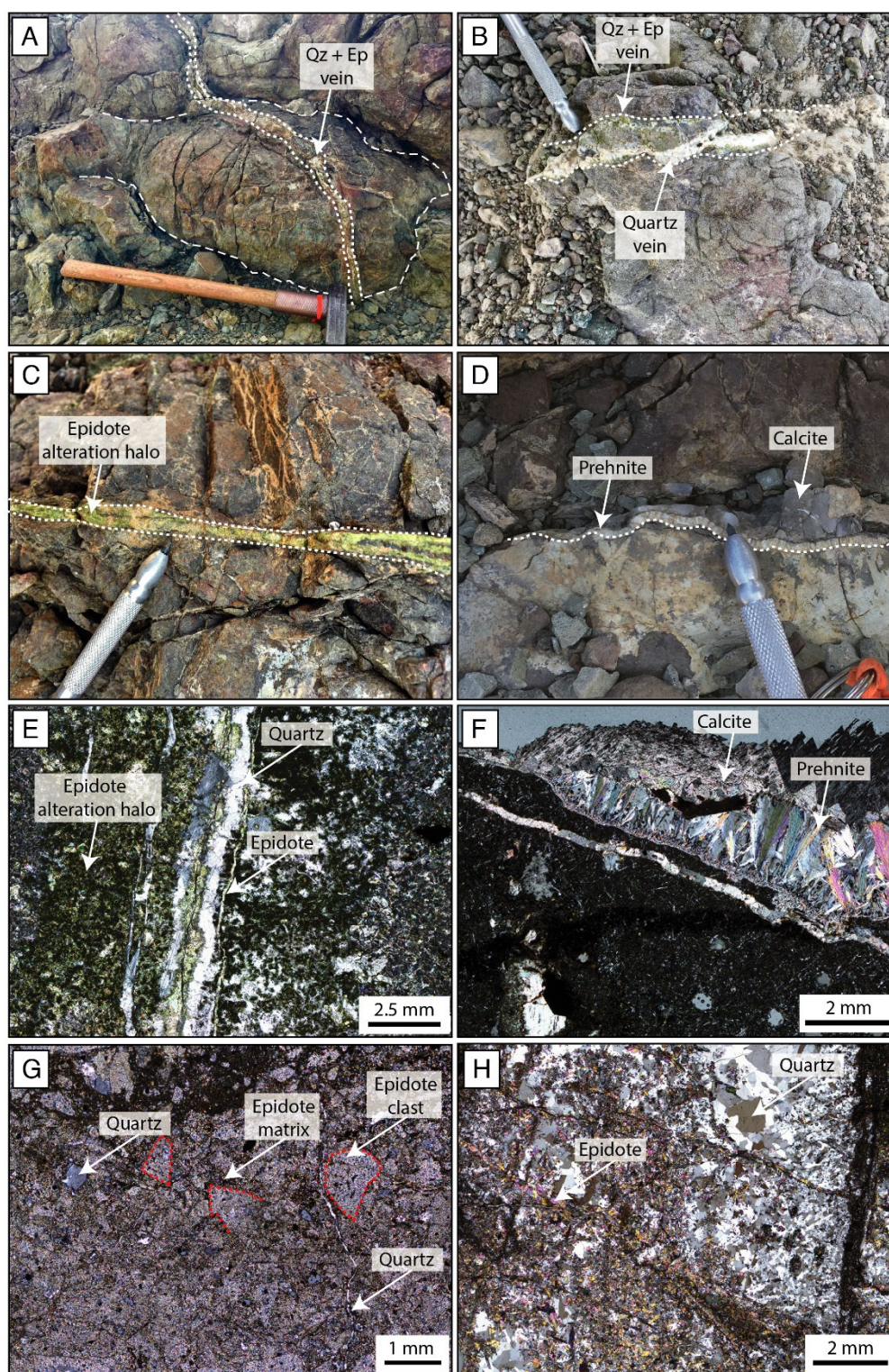


**Figure 4.5.** Field photographs and plane-polarised, transmitted-light microphotographs of fracture types (i.e., hydrothermal veins) observed in the Geotimes pillow lavas. Dotted white lines highlight fracture boundaries and pillow outlines. (a) Large epidote  $\pm$  quartz vein crosscuts pillow lava without any shear displacement of pillow boundary. (b) Vein with multiple generations of coarse-grained epidote + quartz. (c) Bright green epidote halo bordering a  $< 1$  mm wide vein of epidote + quartz. (d) Vein filled with coarse-grained prehnite and later cross-cutting calcite. (e) Microphotograph of type (c) epidote vein showing epidote alteration of wall rock beside epidote + quartz vein. (f) Microphotograph of vein in (d) showing late calcite overgrowing early prehnite. (g) Microphotograph of a quartz + epidote vein with breccia clasts. (h) Microphotograph of a multi-generation epidote + quartz vein with crosscutting epidote veinlets.



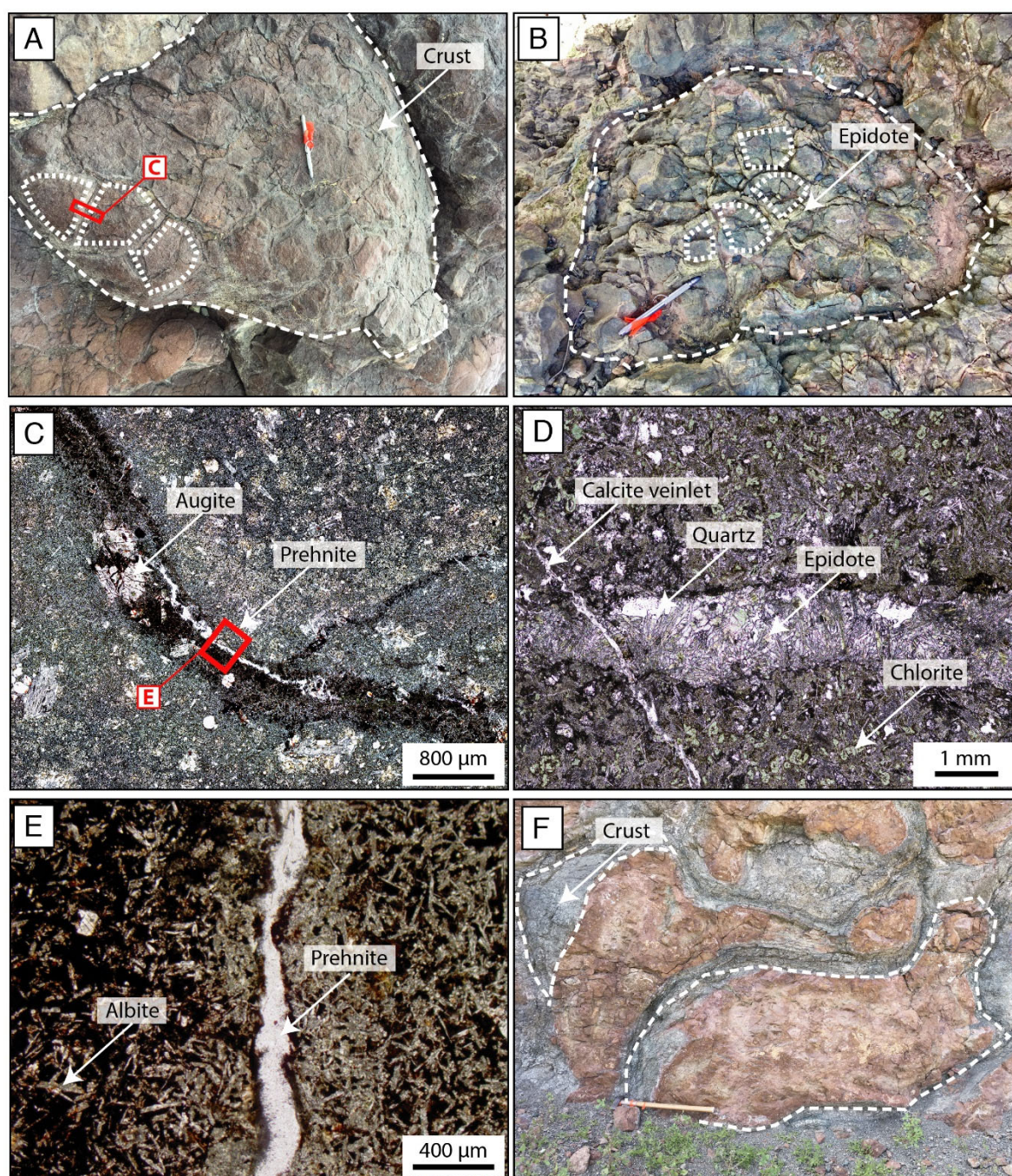


**Figure 4.6.** Uncommon radial and concentric cooling joints filled with hydrothermal minerals in the Geotimes volcanic unit. Dotted white lines outline pillow and polygonal sectors of pillow crust bounded by cooling joints. All microphotographs in plane-polarised, transmitted light. (a) Cooling joints in a spilitised Geotimes pillow. (b) Green epidotised joints in a partially epidotised pillow. Epidotised zones up to 1 cm wide on either side of the joints are matrix-replacement halos. (c) Microphotograph of prehnite-filled cooling joint from pillow (a). Joint is marked by dark hematite and by finer grain-size of wall rock (chilled margin). Only a short segment of the joint contains prehnite. (d) Joint from (b) showing epidote + quartz filling and epidote replacing the rock matrix bordering the joint. (e) Close-up of prehnite in (c), showing grain-size reduction of the albite-rich rock matrix in the chilled margin beside the joint. (f) Common Geotimes pillow lavas with no cooling joints in the lava crust or inside the lava.

#### *4.5.3. Fracture distributions*

##### *4.5.3.1. Hilti fracture map*

The total area mapped in the Hilti location was 41286 m<sup>2</sup> (0.041 km<sup>2</sup>) along 12 main swaths and ~20 additional outcrops, of which 52 area% was volcanic outcrop and 48 area% was covered in gravel (Fig. 4.7). The main volcanic morphology present is pillow lavas typical of the Geotimes volcanic unit. Around 49 dykes crosscut the lavas, with two sets of mean orientations (seafloor restored values: dip/dip azimuth) of 33/203 and 53/064 and an average thickness of 0.9 m. All the lavas and dykes are hydrothermally altered. The majority (~68 area%) are spilites but a few zones of incipient epidosite (~15 area%) and intermediate epidosite (~17 area%) are present.

A total of 36 fractures containing hydrothermal seafloor minerals were mapped in this area, producing a P21 value of 0.0039 m/m<sup>2</sup>. The main mineral assemblage is prehnite ± late calcite, and a few fractures have either coarse comb epidote + quartz, fine grained chlorite or quartz only. A summary of fracture data is provided in Table A4.1. These fractures are divided into two geometric groups summarised in Table 4.2. The main group with 33 fractures contains prehnite, epidote and quartz mineralogies and has a seafloor restored mean principal orientation of 86/230 and a fisher distribution of 13.1. The other group with only three parallel chlorite fractures is orientated 62/302.



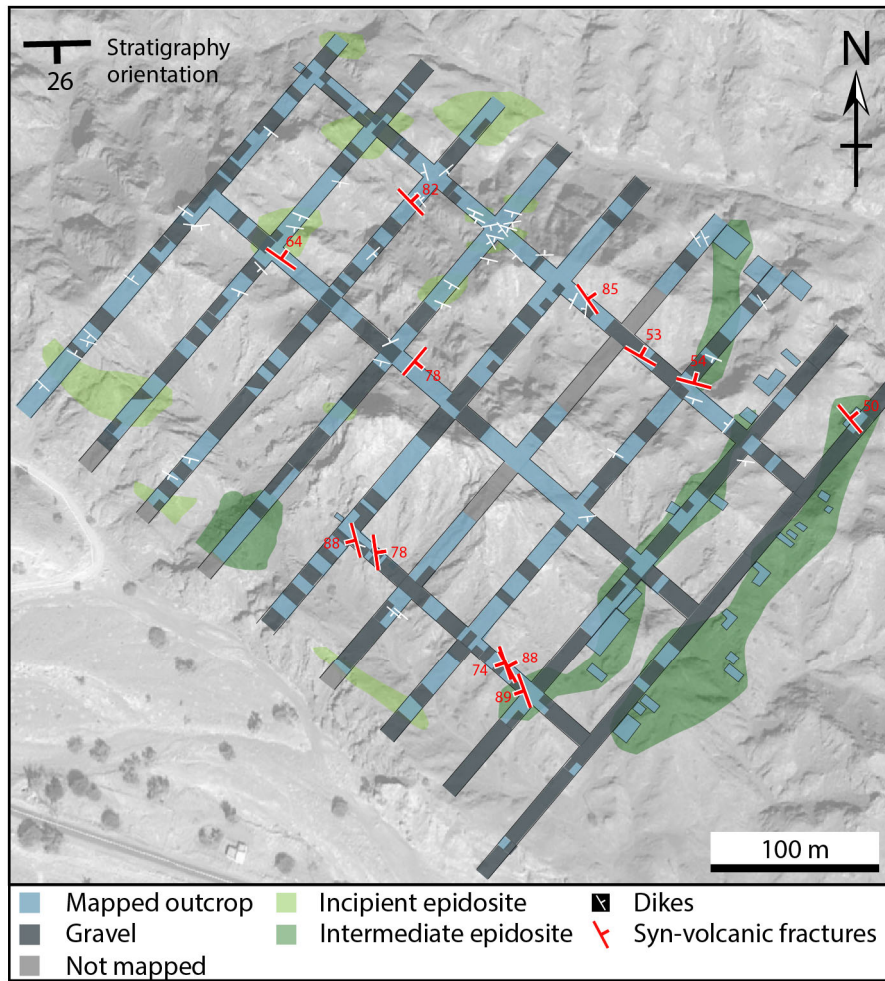


**Figure 4.7.** Hilti fault-distal zone showing mapped swaths of pillow lavas with outcrops and gravel cover. Underlay is a greyscale satellite image. Dyke orientations shown with white strike/dip symbols; fractures shown with red strike/dip symbols with associated dip angles. Parallel fractures too small to distinguish as this scale are indicated by a single strike/dip symbol (for full fracture data see Table A4.1).

#### 4.5.3.2. Aswad fracture map

At the Aswad location, 11236 m<sup>2</sup> (0.011 km<sup>2</sup>) were mapped along 5 main swaths, in which 56 area% was volcanic outcrop and 43 area% was gravel cover (Fig. 4.8). This area is composed of Geotimes pillow lavas and massive lava flows with only rare dykes. A total of 16 massive flow outcrops were mapped, with a total of ~250 m and about ~29 area% of the mapped outcrop. All the rocks are hydrothermally altered; ~50 area% is spilites, ~26 area% is incipient epidiosites and ~24 area% is intermediate epidiosites. The damage zone to the NE takes up ~2750 m<sup>2</sup> of outcrop and ~14 area% of mapped swaths. It lies parallel to a large kilometre-scale seafloor fault in an adjacent wadi (Fig. 4.1b). This zone was excluded from fracture density calculations because it could not be completely quantified but clearly had a significantly higher fracture density and probably represents the edge of a damage zone.

In the distal area of the map only nine seafloor fractures (Table A4.1) were identified, all with epidote  $\pm$  quartz mineralogies, giving a total P21 value of 0.0034 m/m<sup>2</sup>. Two geometric groups were distinguished (Table 4.2), one group with five fractures with a seafloor restored mean principal orientation of 71/222 and a Fisher distribution of 19.5, and the other group of four parallel fractures orientated 87/280.

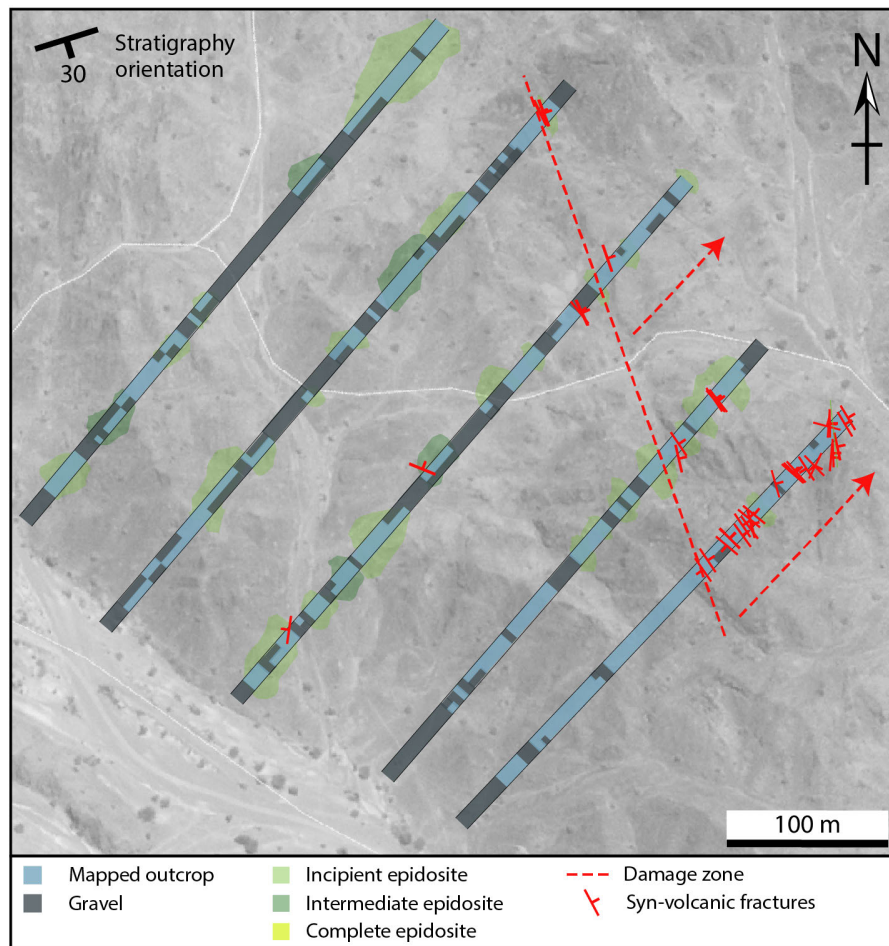


**Figure 4.8.** Aswad area showing mapped swaths of outcrop, gravel cover, hydrothermal alteration and fracture orientations. Underlay is a greyscale satellite image. Dotted red line divides a sparsely fractured, fault-distal zone in the SW from an intensely fractured fault-damage zone in the NE. The damage zone was not mapped in detail, but some fractures are shown to illustrate the high fracture density and the extent of the zone. Complete fracture data from the distal zone are in Table A4.1. At this map scale some of the 9 total fractures overlap and cannot be distinguished.

#### 4.5.3.3. *Rusays fracture map*

At the Rusays location, 38560 m<sup>2</sup> (~0.039 km<sup>2</sup>) were mapped along irregular swaths that followed available outcrop. Of the swath area 83 area% was volcanic outcrop and 17 area% was gravel cover (Fig. 4.9). This area is split between Geotimes and Lasail volcanic units, but contains predominantly pillow lavas. The geochemical and field characteristic differences between the pillow lavas types are described extensively by Belgrano et al. (2019), but for fracture mapping these units are similar. The background hydrothermal alteration is spilite but almost all outcrops have some incipient or

intermediate epidotisation and some complete epidosite was found in the north. The alteration zones shown in Fig. 4.9 are compiled from previous field mapping including the Master thesis work by Novakovic (2016), PhD thesis mapping from Gilgen (2014) and additional notes from our own fieldwork.

In Rusays, 27 seafloor fractures were mapped all with epidote  $\pm$  quartz fillings (Table A4.1), resulting in a P21 value of 0.0053 m/m<sup>2</sup>. From this data only one geometric group was distinguished that has a seafloor restored mean principal orientation of 82/243 and a Fisher distribution of 7.1. Most fractures strike NW–SE; however, two outlier fractures that strike NNE–SSW and E–W were also included in the main geometric set (Table 4.3).

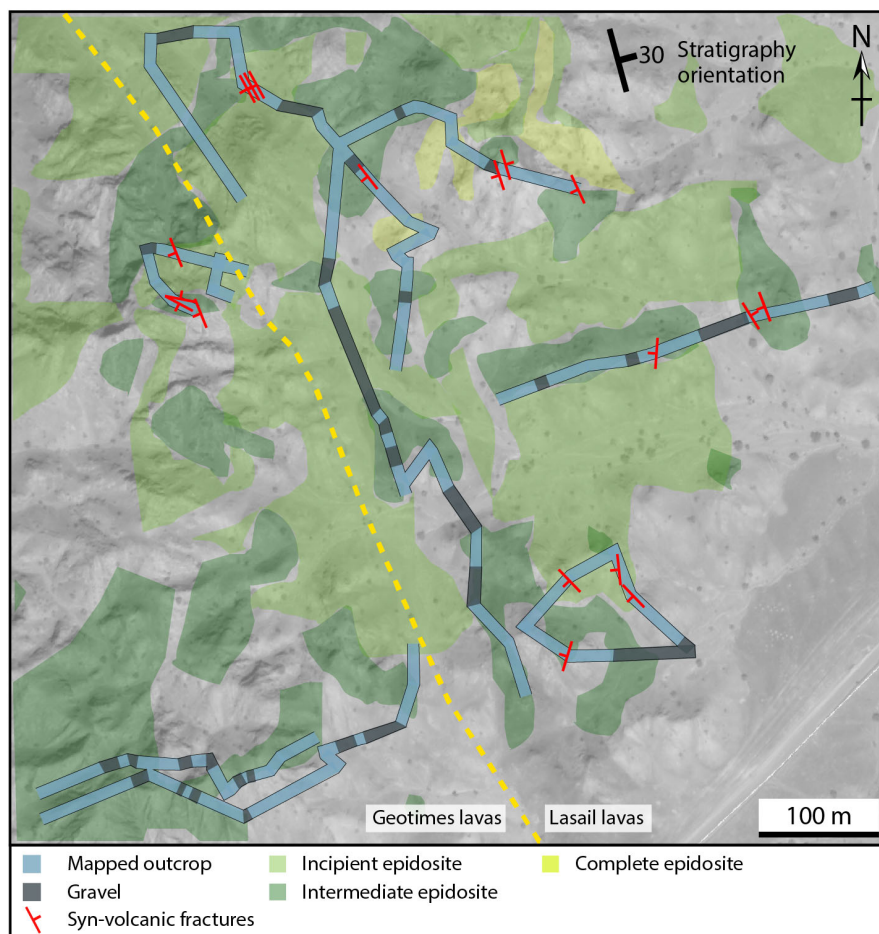


**Figure 4.9.** Mapped swaths at Rusays showing outcrop, gravel cover, alteration and fracture orientations. Yellow dashed line separates Geotimes and Lasail lavas. Complete fracture data are available in Table A4.1.

#### 4.5.3.4. Ajeeb fracture map

The largest of the four areas, Ajeeb, was mapped in 36 swaths, ~100–800 m in length and mostly orientated N–S across the central seafloor fault (Fig. 4.10a). The outcrop area is ~32780 m<sup>2</sup> (excluding gravel cover) and includes mainly Geotimes lavas but also some intercalations of Lasail lavas (Gilgen et al., 2016). Extensive epidosite alteration was mapped and described in detail by Gilgen (2014), but

is broadly summarised in Fig. 4.10a as an E–W striking zone of complete and intermediate epidosite, grading into incipient epidosite and some spilites in the north and south. Pillow lavas are abundant with the exception of a few massive flow outcrops and occasional dykes.

At Ajeeb, 192 fractures were mapped and all contain an assemblage of epidote  $\pm$  quartz, with the exception of two pumpellyite  $\pm$  epidote fractures and one chlorite fracture (Table A4.1). The fracture distribution varies from a densely fractured zone trending E–W around the previously identified syn-volcanic fault, to less densely fractured areas to the north and south. The steep cumulative fracture density (Fig. 4.10b) either side of the main fault defines a distinct damage zone extending 100 m north and 50 m south. Data from this damage zone were separated from the distal areas to the north and south. North and south distal areas were combined to make a total “Ajeeb Distal Zone”.

The Ajeeb Damage Zone has a total mapped outcrop area of 8210 m<sup>2</sup> and total P21 value of  $\sim 0.063$  m/m<sup>2</sup>. The Ajeeb Distal Zone contains a mapped outcrop area of 24570 m<sup>2</sup> and a total P21 value of  $\sim 0.0073$  m/m<sup>2</sup>. In both the distal and damage zones three main orientation clusters were chosen to distinguish the geometric groups, which strike N–S, NW–SE and E–W. Some rotation of strikes is observed from fractures with NNW–SSE orientations in the N and S distal zones, converging towards a sub-parallel WNW–ESE strike in the damage zone. All geometric groups have steep mean dips ranging from  $\sim 66^\circ$  to vertical (Table 4.2).



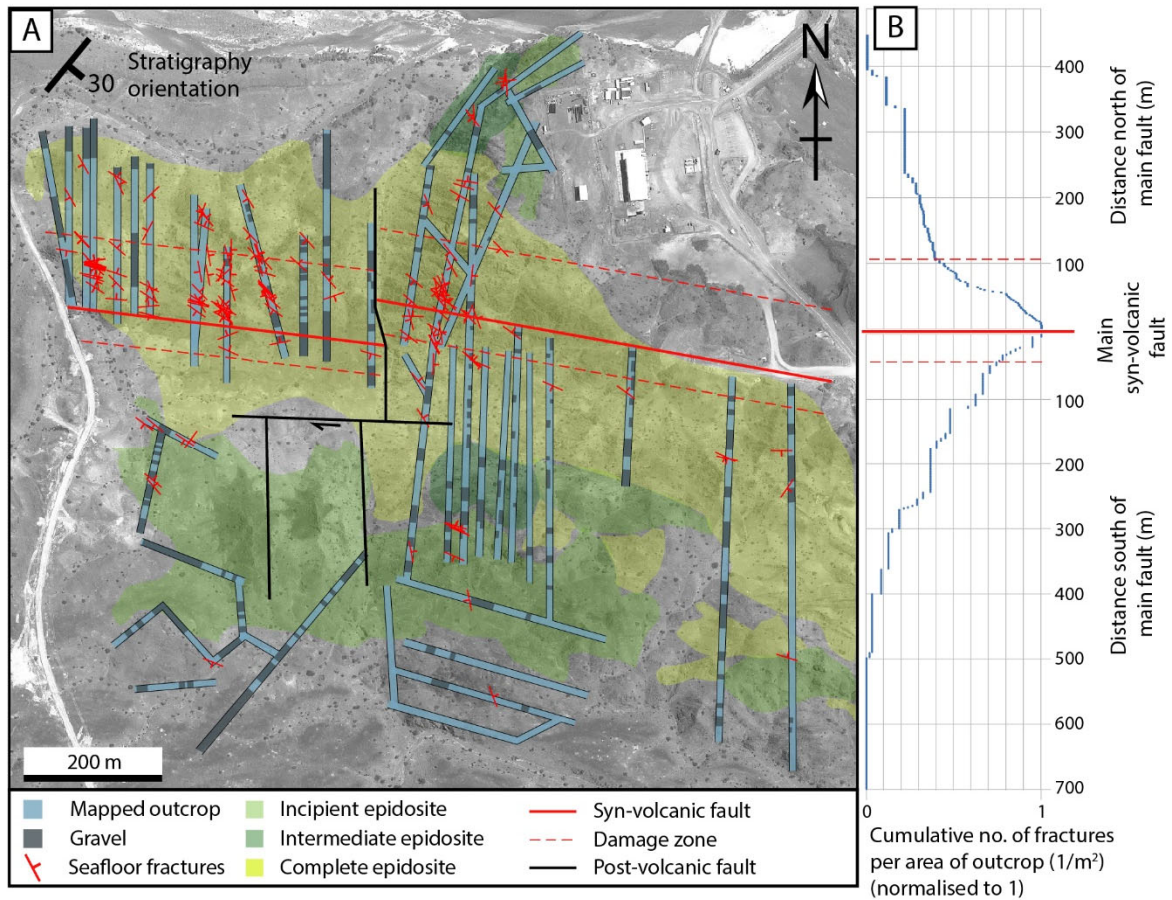


**Figure 4.10.** (a) Ajeeb fracture map showing mapped swaths, gravel cover, hydrothermal alteration and fracture orientations. A post-volcanic sinistral fault (black) offsets the main syn-volcanic fault (red) in the middle of the area. Alteration map modified and simplified after Gilgen (2016). (b) N–S aligned cumulative fracture frequency plot used to distinguish the fault-damage zone from the fault-distal zone.

In addition to the main fractures mapped in the Ajeeb Damage Zone, microfracture networks were also found (Fig. 4.11). Due to the  $< 1$  mm fracture size and short lengths, these could not be mapped at the chosen swath scale. Areas containing these fractures were sometimes as large as  $100 \text{ m}^2$ , however they were not present throughout the entire Ajeeb Damage Zone and were not mapped in detail. Figure 4.11 shows two examples of these anastomosing microfracture networks filled with epidote  $\pm$  quartz. The microfractures crosscut pillow lavas crusts (Fig. 4.11a). They do not seem to crosscut mineralised cooling joints and hyaloclastites (Fig. 4.11b) but their similar mineralogies and small scale made this timing relationship difficult to distinguish in the field.

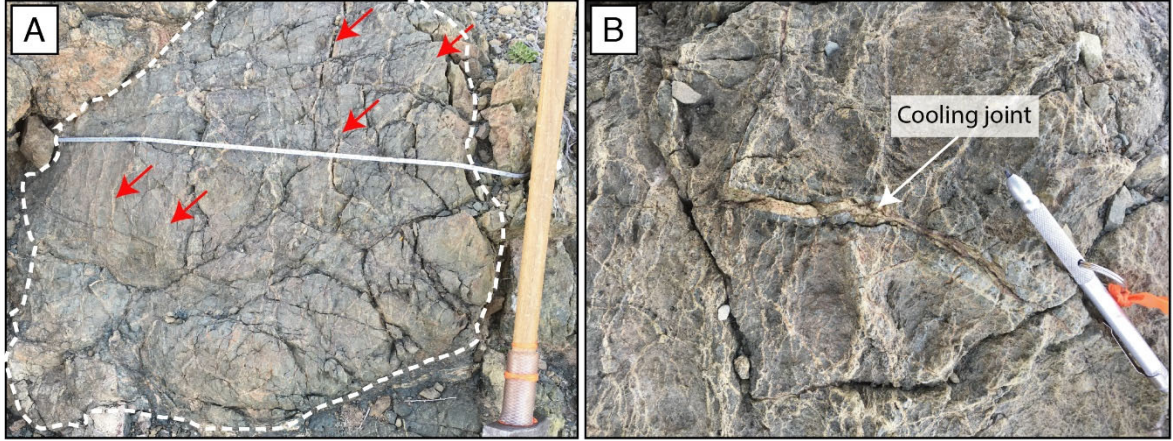


**Figure 4.11.** Hairline microfracture networks in the Ajeeb fault-damage zone. (a) Exterior crust of pillow is crosscut by abundant epidote  $\pm$  quartz  $\pm$  late calcite microfractures (five of the larger ones are indicated with red arrows). (b) Close-up field photograph of anastomosing microfractures orientated mostly perpendicular to an epidotised cooling joint.

#### 4.5.3.5. Distal zone characteristics for UDFM models

All four distal locations have syn-volcanic fractures at high angles with similar NW–SE, E–W and NNE–SSW orientations. The volumetric intensity P32 values calculated from the total data at each location have the same order or magnitude and range from 0.0044–0.0082  $\text{m}^2/\text{m}^3$ . More variation is present in P32 values of individual geometric groups. The P32 values, mean principal orientations, Fisher distribution, radius and aperture data used for UDFM generation are provided in Table 4.2.

#### 4.5.3.6. Fracture network characteristics in damage zones

The P32 values calculated for geometric groups in the Ajeeb Distal Zone range from 0.0026–0.0483  $\text{m}^2/\text{m}^3$ , and a total value of  $\sim 0.07 \text{ m}^2/\text{m}^3$ . The Fisher distribution, mean principal orientations, radius and aperture distributions are detailed in Table 4.2 for UDFM generation.



**Table 4.2.** Fracture distribution data for geometric groups at each location, including properties used to generate DFNs.

Location	Outcrop mapped (m <sup>2</sup> )	Geometric Group	No. of fractures <sup>1</sup>	Seafloor mean principal dip (°)	Seafloor mean principal dip. azimuth (°)	phi (°) <sup>2</sup>	theta (°) <sup>3</sup>	Kappa (FD) <sup>4</sup>	Total set length (m) <sup>5</sup>	P21 (m/m <sup>2</sup> ) <sup>6</sup>	P32 (m <sup>2</sup> /m <sup>3</sup> ) <sup>7</sup>	Radius min (m)	Radius max (m)	Radius average (m)	Radius SD (m) <sup>8</sup>	Aperture average (mm) <sup>9</sup>	Aperture SD (mm) <sup>10</sup>
Hilti	–	1	33	85.5	229.5	49.5	94.5	13.1	78.04	0.00367	0.00398	0.20	10.00	1.33	1.74	4.2	9.4
	–	2	3	90.0	302.4	302.4	61.7	∞	5.70	0.00027	0.00037	0.20	0.95	0.58	0.53	3.0	0.0
	21283.5	All fractures	36	83.1	234.1	54.1	96.9	7.9	83.74	0.00393	0.00435	–	–	–	–	4.1	9.0
Aswad	–	1	5	70.8	221.6	221.6	70.8	19.5	19.00	0.00221	0.00365	0.75	2.50	1.05	0.84	2.1	0.9
	–	2	4	87.1	279.9	279.9	87.1	∞	10.00	0.00117	0.00198	1.25	1.25	1.25	0.00	2.5	0.0
	5830.0	All fractures	9	76.6	248.6	248.6	76.6	5.4	29.00	0.00338	0.00562	–	–	–	–	2.3	0.7
Rusays	–	1	27	82.0	243.0	63.0	98.0	12.8	169.09	0.00526	0.00572	0.50	170.00	14.03	34.78	13.0	15.2
	32170.0	All fractures	27	82.0	243.0	63.0	98.0	12.8	169.09	0.00526	0.00572	–	–	–	–	13.0	15.2
Ajeeb Distal Z.	–	1	8	66.4	301.70	121.7	113.6	9.8	36.15	0.00147	0.00172	0.50	7.08	2.58	2.27	43.6	33.3
	–	2	11	88.6	18.00	18.0	88.6	37.9	26.90	0.00109	0.00115	0.15	2.00	1.12	0.64	23.4	9.6
	–	3	30	89.1	233.20	53.2	90.9	14.8	116.51	0.00474	0.00513	0.25	7.50	1.94	1.82	18.4	13.3
	24570.0	All fractures	49	81.6	223.0	43.0	98.4	4.5	179.56	0.00731	0.00823	–	–	–	–	23.2	20.1
Ajeeb Damage	–	1	5	67.6	303.0	123.0	112.4	9.6	18.50	0.00225	0.00261	0.75	3.50	1.85	1.14	3.7	6.5
	–	2	53	89.4	202.0	22.0	90.6	3.1	136.06	0.01657	0.01887	0.25	5.28	1.28	0.84	14.7	29.5
	–	3	85	79.5	229.8	49.8	100.5	11.7	361.09	0.04398	0.04825	0.25	10.22	2.12	1.83	22.6	24.8
	8210.0	All fractures	143	85.1	233.3	53.3	94.9	5.0	515.65	0.06281	0.07031	–	–	–	–	19.5	26.4

<sup>1</sup>Number of fractures in group and total at each location; <sup>2</sup>Spherical coordinate, phi, referring to the angle that the normal vector projected on the x-y plane makes with the x-axis; <sup>3</sup>Spherical coordinate, theta, the angle between the fracture normal vector and the positive z-axis. <sup>4</sup>The Fisher distribution, known as the kappa parameter in model inputs; <sup>5</sup>Total set length inside swath; <sup>6</sup>P21 value of area fracture intensity = fracture length per unit area of outcrop; <sup>7</sup>P32 value of volumetric fracture intensity = area of fracture per unit volume of outcrop; <sup>8</sup>Standard deviation of fracture radii for the geometric group all or all fractures; <sup>9</sup>Average of the fracture aperture for each geometric group, but only the average aperture of all fractures at a location was applied to the model for each location; <sup>10</sup>Standard deviation of the fracture aperture for each geometric group, but only the SD for all fractures at a location was applied to the model for each location.

#### 4.5.4. Distal zone UDFM models and bulk permeability

The bulk permeabilities calculated at each location in the principal flow directions ( $xx$ ,  $yy$ , and  $zz$ ) are displayed in Table 4.3. The associated graphical DFN models and the 3D liquid pressure flow fields and UDFM meshes at each location are reported in Fig. 4.12. The stereonet plots of field data and stochastically generated fractures for each model are shown in Fig. 4.13.

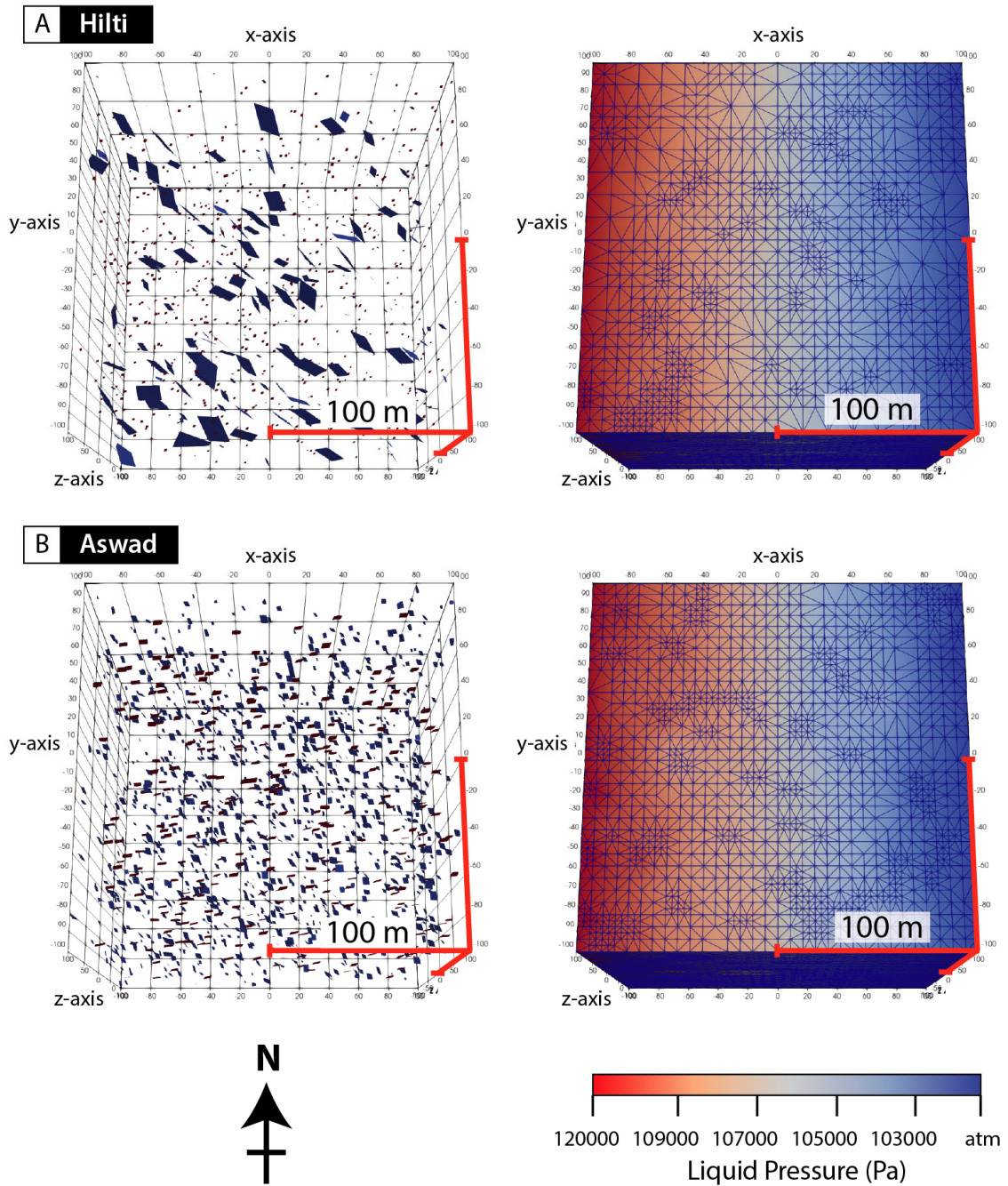
The bulk permeabilities of all spilite distal zones, across the three principal flow directions range from  $3.4\text{--}8.3 \times 10^{-16} \text{ m}^2$  and have a geometric mean of  $4.4 \times 10^{-16} \text{ m}^2$ . Bulk permeability of the epidosite Hilti model is higher than the spilite Hilti model by  $\sim 1\text{--}1.5 \times 10^{-16} \text{ m}^2$  in the  $k_{xx}$  and  $k_{zz}$  directions, and by  $\sim 4 \times 10^{-16} \text{ m}^2$  in the  $k_{yy}$  (Table 4.3). The geometric mean of bulk permeability for the epidosite Hilti model is  $\sim 5.9 \times 10^{-16} \text{ m}^2$ .

Figure 4.14 shows four additional examples of Rusays UDFM models from a total of 10 generated. One of the 10 models (Fig. 4.14a) contained long fractures that connected a pathway across the domain. This model has a very high bulk permeability ( $k_{xx}$  of  $3.4 \times 10^{-11} \text{ m}^2$  compared to the other nine models that range between  $5.5 \times 10^{-16}$  and  $8.0 \times 10^{-16} \text{ m}^2$  e.g. the three in Fig. 4.14,b,c,d, which are all similar to the other distal zones. The bulk permeability associated with the connected fracture model was not used to calculate the average bulk permeability of spilite distal zones above.

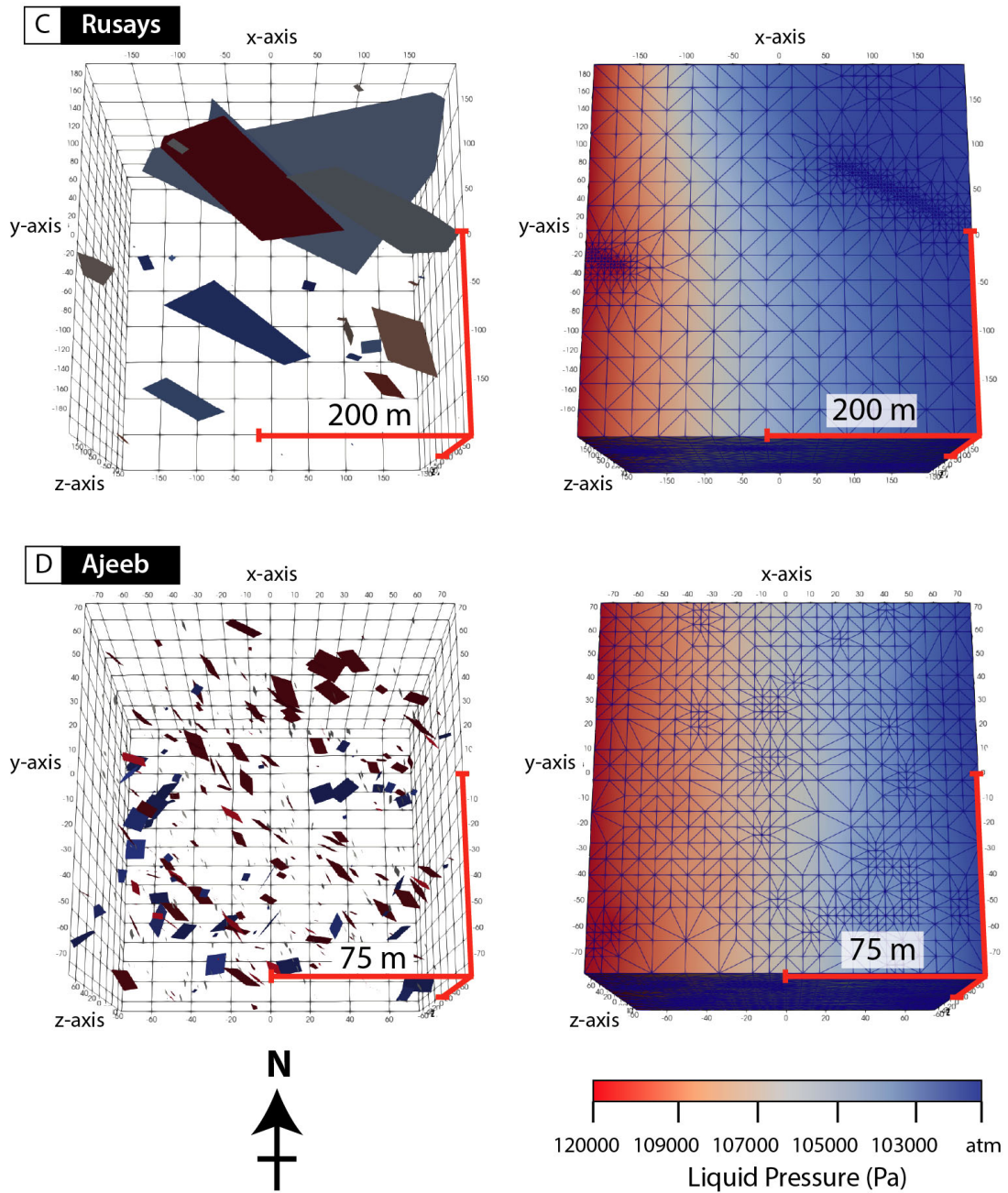
**Table 4.3.** Summary of UDFM outputs, flow simulation times, and bulk permeabilities calculated for each model

Location	Domain size (m)	Volume of model (m <sup>3</sup> )	Matrix Alteration <sup>1</sup>	Number of fractures <sup>2</sup>	Total P32 (m <sup>2</sup> /m <sup>3</sup> ) <sup>3</sup>	$K_{xx}$ (m <sup>2</sup> ) (W to E) <sup>4</sup>	$K_{yy}$ (m <sup>2</sup> ) (N to S) <sup>5</sup>	$K_{zz}$ (m <sup>2</sup> ) (T to B) <sup>6</sup>	Mean permeability (m <sup>2</sup> ) <sup>7</sup>	Time (simulated; days) <sup>8</sup>	Number of flow solve steps <sup>9</sup>	Steady-state reached in inflow and outflow rates	Time (wall clock; hours) <sup>10</sup>
Hilti	200 × 200 × 200	8000000	Spilite	879	0.00438	$3.56 \times 10^{-16}$	$3.45 \times 10^{-16}$	$4.38 \times 10^{-16}$	$3.77 \times 10^{-16}$	300, 200, 400	5325	Approximately	5
Hilti	200 × 200 × 200	8000000	Epidosite	879	0.00438	$4.69 \times 10^{-16}$	$5.02 \times 10^{-16}$	$8.81 \times 10^{-16}$	$5.92 \times 10^{-16}$	300, 300, 200	5347	Yes	5
Aswad	200 × 200 × 200	8000000	Spilite	720	0.00564	$4.04 \times 10^{-16}$	$4.81 \times 10^{-16}$	$4.67 \times 10^{-16}$	$4.49 \times 10^{-16}$	200, 200, 200	4228	Approximately	12
Rusays	399 × 399 × 399	63521199	Spilite	39	0.00601	$5.86 \times 10^{-16}$	$3.93 \times 10^{-16}$	$8.31 \times 10^{-16}$	$5.76 \times 10^{-16}$	2000, 2200, 2100	815	Yes	4
Ajeeb Distal	150 × 150 × 150	3375000	Spilite	477	0.00811	$3.39 \times 10^{-16}$	$3.57 \times 10^{-16}$	$4.64 \times 10^{-16}$	$3.83 \times 10^{-16}$	150, 150, 150	7132	Approximately	4.2
Ajeeb Damage	100 × 100 × 100	1000000	Spilite	670	0.07010	$2.43 \times 10^{-11}$	$3.83 \times 10^{-12}$	$8.82 \times 10^{-11}$	$2.02 \times 10^{-11}$	80, 40, 40	799	Yes	4–8

<sup>1</sup>Type of matrix alteration with properties corresponding to Section 4.5.1; <sup>2</sup>Total number of fracture generated in each model DFN; <sup>3</sup>P32 total volumetric fracture intensity (geometric groups at each location combined); <sup>4</sup>Permeability from the darcy flux across the x-axis, flow simulation from west to east of the domain; <sup>5</sup>Permeability from the darcy flux across the y-axis, flow simulation from north to south of the domain; <sup>6</sup>Permeability from the darcy flux across the z-axis, flow simulation from top to bottom of the domain; <sup>7</sup>Geometric mean of the three permeabilities associated with the main flow directions; <sup>8</sup>Number of simulation days that the flow simulation was run for, three numbers correspond to the simulations run for x-, y-, and x-axis permeability directions; <sup>9</sup>Total number of solutions run to reach or approximately reach steady-state flow; <sup>10</sup>Real wall clock time approximately required to finish each simulation.

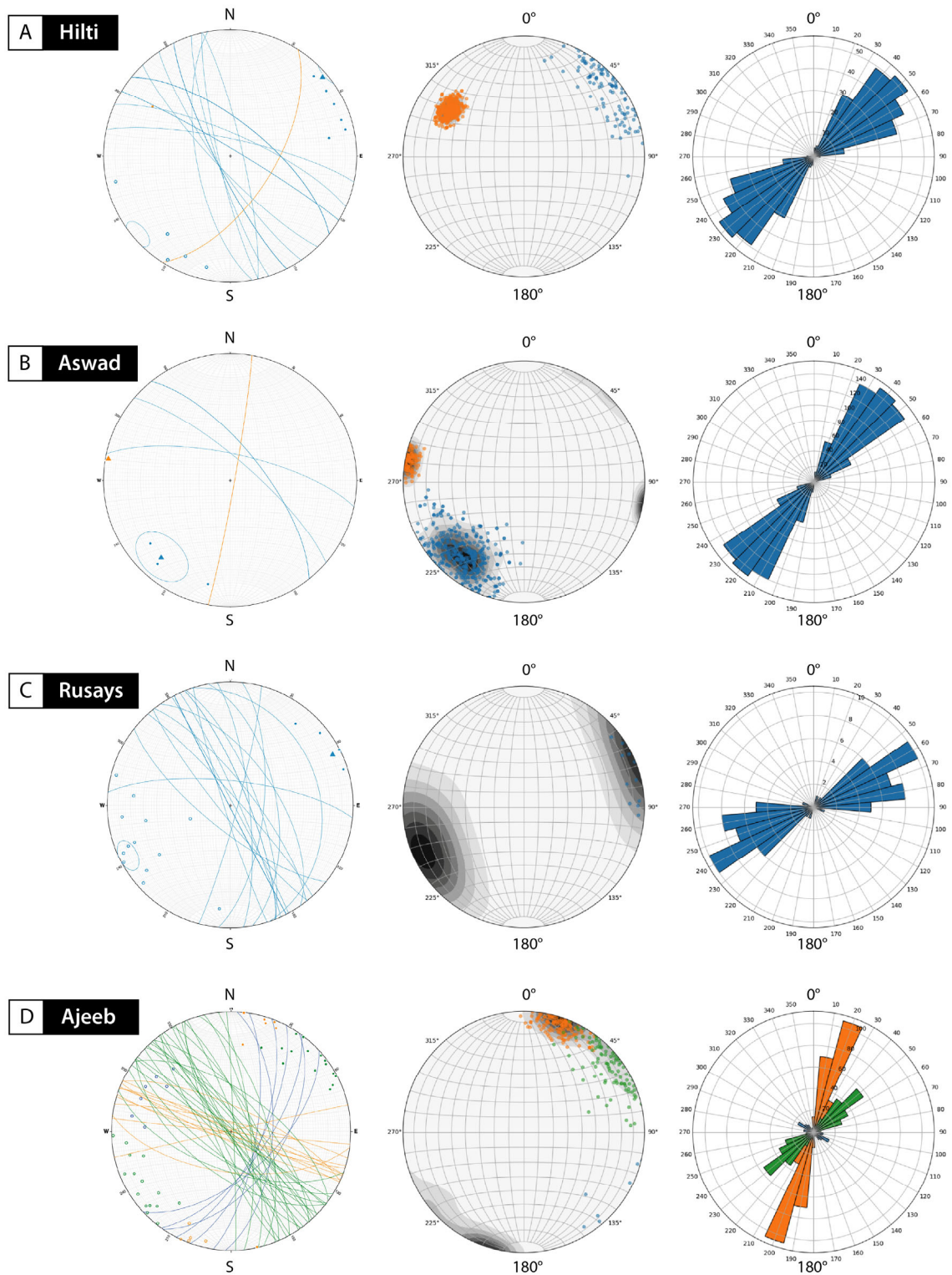


**Figure 4.12.** DFN models (left) and meshed block models (right) for the four mapped fault-distal lava zones. Block models show liquid pressure gradient (colours) during flow from W to E, with meshed volumes shown as polygons. Fracture colours in the DFN models show different geometric groups in (a), (b) and (d), but simply different fractures in (c). Detail of meshing increases where fractures intersect block surfaces. Largest mesh volume is 25 m diameter. All diagrams are orientated top to the north, with depth (z axis) into the page. Scales of the models vary between mapping locations and correspond to different model domain volumes. Liquid pressure varies from the inflow at western face to outflow at the eastern face by the equivalent of 1 m hydraulic head or 0.000981 MPa. (a) Hilti models. (b) Aswad models. Continued on following page.



**Figure 4.12.** Continued: (c) Rusays models. (d) Ajeeb Fault-Distal Zone models.





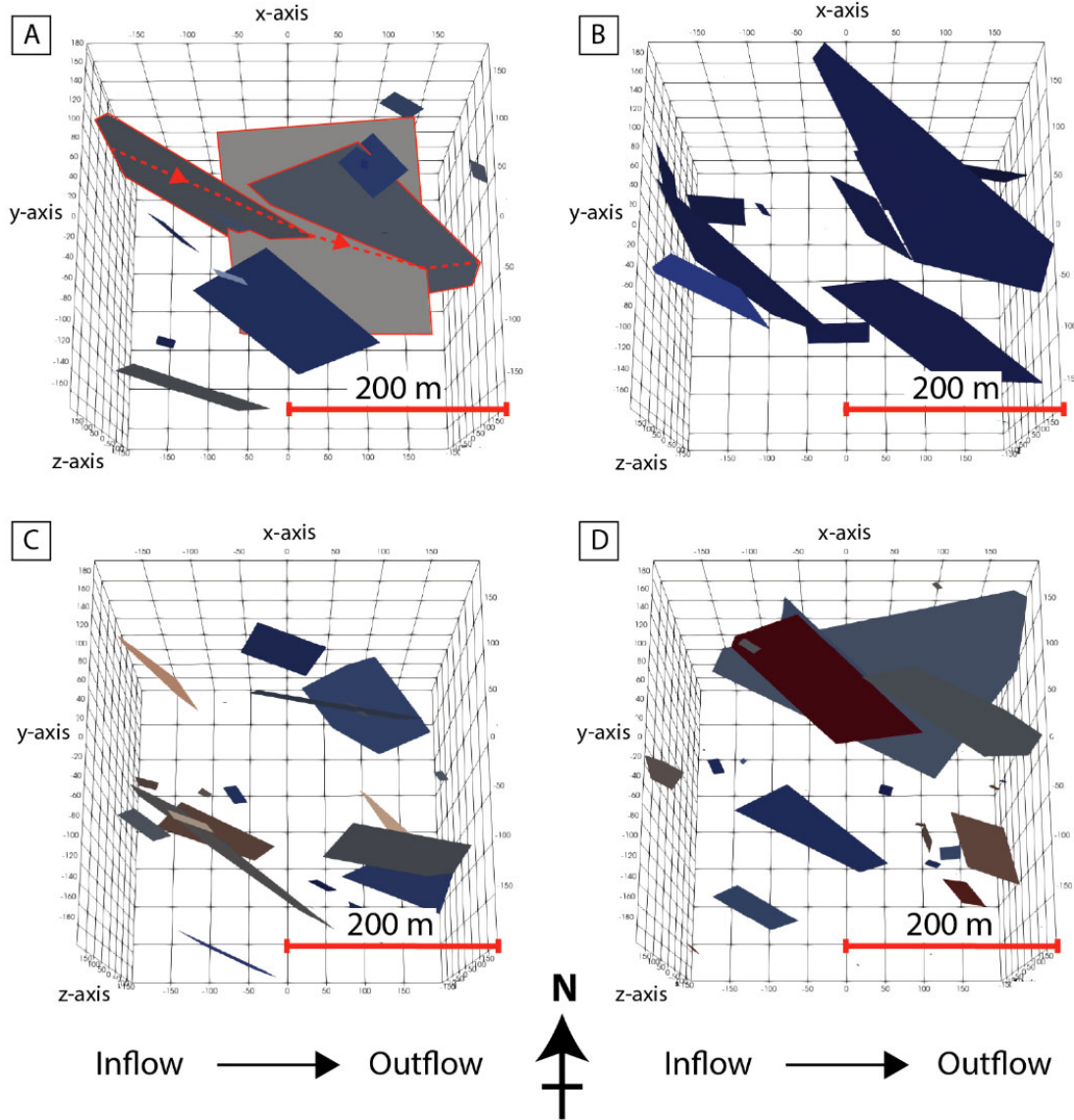


**Figure 4.14.** Block models of four DFNs produced with different model seed values for Rusays mapping site. Permeability described in text corresponds to the flow direction shown (inflow in west and outflow in east). Domain volume is  $\sim 400 \times 400 \times 400$  m. Scale on DFN marks the top surface. Domains in (a) and (b) were truncated slightly on the southern section of the y-axis in display software. (a) DFN with long fractures that form a connected path across domain. Connected fractures outlined in red, and a potential path is shown in a dashed red line along the flow direction. (b), (c), (d) Examples of stochastically generated DFNs showing no fracture connections across the domain.

#### 4.5.5. Damage zone DFN models and bulk permeability

Figure 4.15 shows a summary of the models for the Ajeeb Damage Zone. A total of 670 fractures were produced in three sets and these match the three geometric groups of field data (Fig. 4.15a,b,c). Bulk permeability for this zone varies between the principal flow directions;  $k_{xx} = 2.4 \times 10^{-11} \text{ m}^2$ ,  $k_{yy} = 3.8 \times 10^{-12} \text{ m}^2$ , and  $k_{zz} = 8.8 \times 10^{-11} \text{ m}^2$  (Table 4.3). The geometric mean of the Ajeeb Damage Zone bulk permeability is therefore  $\sim 2 \times 10^{-11} \text{ m}^2$ .

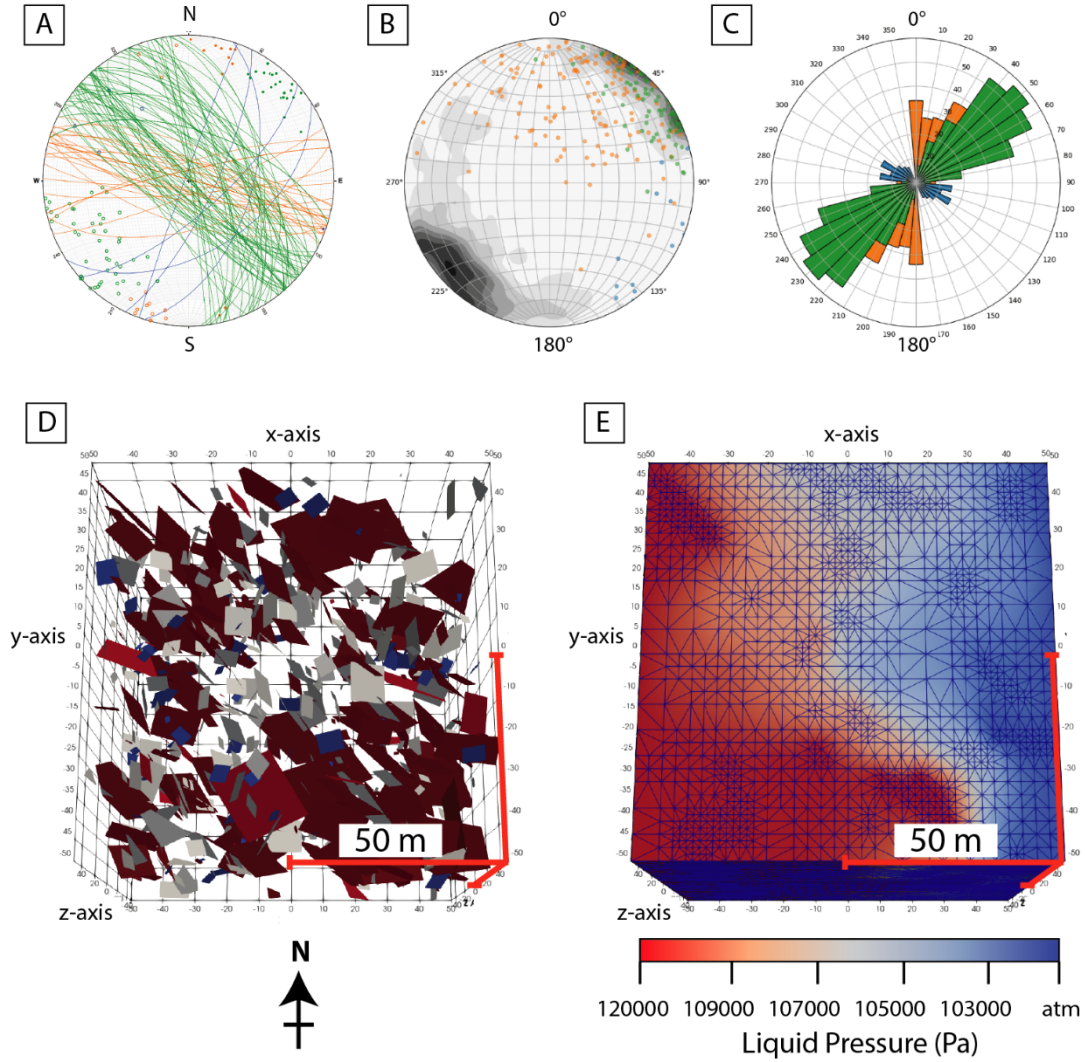


**Figure 4.15.** Ajeeb Fault-Damage Zone. Model domain volume is 100 x 100 x 100 m. Red scale bars indicate 50 m along the  $x$ -,  $y$ -, and  $z$ -axes. (a) Field data stereonet. (b) Stereonet of fractures in DFN. (c) Rose plot of fractures in DFN. (d) DFN of the damage zone. (e) Liquid pressure flow field (W to E) across the domain and meshed volumes (polygon outlines).

## 4.6. Discussion

### 4.6.1. Accuracy of upscaling from field observations to flow models

#### 4.6.1.1. Rock-matrix upscale

Our unique upscaling approach to determine rock-matrix porosities and permeabilities of pillow stacks relied on three assumptions; (1) that the average rock-matrix values for pillow rims, cores and interpillows are representative of Geotimes pillow lavas, (2) that the area fraction of the three zones represents an average pillow stack geometry and (3) that the area fractions of the pillow stack zones are equivalent to their volume fractions.

The datasets and average values determined in Chapter 3 of this study are representative of Geotimes pillow lavas with three limitations. Some spilite pillow rims were at the detection limit for



the permeameter, which means that the average rim value may be slightly lower than the one used. Additionally, only a few spilite interpillow hyaloclastites could be measured for porosity with an average value of ~20 vol.%. We expect that the porosities could be higher, because the most friable hyaloclastites could not be sampled and measured. Lastly, from the range of hydraulically modelled permeabilities of  $10^{-17}$  to  $10^{-15}$  m<sup>2</sup> for spilite hyaloclastites in Chapter 3 we chose the highest permeability for upscaling, based on the high porosities and friable textures we observed in the field. However, the permeability of spilite hyaloclastites may vary.

Assumption (2) is validated by the comparable average area fraction of interpillow zones calculated from outcrops in this study (~17 area%) and that for the Troodos ophiolite (~19 area%; Gillis and Sapp, 1997). Additionally, the ratio of pillow cores to pillow rim in intermediate epidiosites varies across epidosite zones, but alteration of pillow cores was frequently observed in the systematic way seen in Fig. 4.3a.

In support of assumption (3) the diagram of pillow tube geometry in Fig. 4.3b matches our observations of outcrops that expose lavas tubes along their long axis. Such outcrops may contain continuous lavas tubes 2–8 m long demonstrating that the area fractions observed in outcrops perpendicular to the lava extrusion direction are representative of their volume fractions.

These characteristics of lava outcrops may vary within the Semail and other ophiolites, especially with differing lava vesicularity, viscosity and morphology. Nevertheless, the assumptions are reasonable for most spilitised and epidotised Geotimes pillow lavas outcrops. Moreover, the axial spreading-ridge setting and the MORB-type compositions of Geotimes lavas ensure that our upscaled rock-matrix porosities and permeabilities at the outcrop/decametre-scale are relevant for other ophiolites and for *in-situ* extrusive lavas.

No values are calculated for intermediate epidosite lavas because the amount of epidotisation is variable. However, the small difference in porosity and permeability between spilite and epidosite altered lavas suggests intermediate compositions would also be similar.

#### 4.6.1.2. Advantages of the swath area approach

On the Hilti map we tested the directional independence of swath maps, by mapping two perpendicular swath directions (NW–SE and NE–SW; Fig. 4.7). The NW–SE swath direction contains NW–SE striking fractures, despite these fractures being parallel to the swath direction. These fractures, that would usually be missed by 1D transects, were readily measured within the swath areas. At Rusays, large gravel areas separate outcrops but being aware of the directional independence meant that unorientated swaths, and hence larger areas of outcrop, could be mapped with confidence. Furthermore, the P21 data acquired within swath areas, rather than P10, provide a robust description of the fracture networks, accounting for increased fracture intensity caused by long fractures and therefore increased network connectivity.

The swath method was especially suitable for our distal zone locations, which contain sparse fracture densities and good outcrop exposure. At the Ajeeb Damage Zone, mapping of the high fracture density was achievable with a large team. The time required to map densely fractured areas could possibly be reduced if such areas were suitable for digital fracture analysis of fracture trace maps (e.g. Darcel et al., 2009; Giuffrida et al., 2019).

#### 4.6.1.3. Fracture size uncertainty

Steps were taken to quantify and reduce uncertainty due to fracture-size sampling biases such as: (1) censoring, (2) truncation, and (3) topographic bias (Darcel et al., 2009; Einstein and Baecher, 1983).

We recorded the type of fracture end terminations, i.e., whether inside the outcrop or under gravel cover, to qualitatively assess the censoring bias. At the Hilti location nearly half of the fracture terminations were inside outcrops and half were covered by gravel, therefore a certain amount of censoring bias probably reduces the average value of our length data.

Truncation of fracture size occurs when small fractures are under-sampled because of measurement/sampling resolution, and when large fractures cannot be sampled because of limited outcrop or survey size (Einstein and Baecher, 1983). The lower length limit of 30 cm proved to be reasonable at the distal zone sites where small fractures were rare and isolated and unlikely to contribute to bulk permeability. However, the Ajeeb damage zone contains m<sup>2</sup>-size areas of fine hair-line epidote-filled fractures < 30 cm long and < 1 mm in diameter in connected networks. These microfractures were not included in the swath map fracture data for the Ajeeb Damage Zone, therefore the average length is potentially overestimated. In further work these microfracture networks (Fig. 4.11) could be quantified and added to the P21 and P32 values by converting outcrop images into digital trace maps following the steps of Giuffrida et al. (2019). Regarding truncation of large fractures, the large extent and frequent continuity of outcrop exposures over tens to hundreds of metres renders this effect negligible in most cases. Furthermore, of the 264 fractures measured, lengths are generally short: 223 fractures are < 5 m long, 23 are 5–10 m, 11 are 10–30 m, 4 are 50–80 m, and only 2 fractures were over 100 m long.

Truncation of fracture apertures certainly occurred to some extent because the geologists in the mapping team were only reasonably able to identify fractures of 1 mm diameter or larger. The identification of 1 mm scale fractures was possible because of the strong colour contrast of their mineral fillings (quartz, epidote, prehnite) with the surrounding dark spilite basalts. In areas with intense epidotisation of the rock matrix, fractures filled by epidote ± quartz fracture were more difficult to identify, as was the identification of chlorite-filled fractures in spilite areas.

The topographic relief at mapped locations varied over ~1–100 m. This facilitated the observation of low-angle fractures but may have caused fracture-length bias where fractures appear longer over rounded or uneven outcrops (Darcel et al., 2009). Where fractures run over rough topography we attempted to measure only their projected horizontal lengths, thereby reducing overestimates due to length bias.

#### 4.6.1.4. Geometric groups of fracture orientations

Our strategy to choose geometric groups of fractures rather than structurally defined fracture sets, was inevitable owing to the lack of kinematic indicators. A similar lack of kinematic indicators on individual fractures in fast-spreading oceanic crust was also reported by Hayman and Karson (2007) at Hess Deep. The use of multiple geometric groups at the mapped sites (except Rusays), rather than lumping the data, was necessary to ensure that representative fracture orientations and fracture intersections were created by the stochastic algorithm in the UDFM models.

Fracture intensities of each group are well described by P21 values and provide a good basis for generating P32 using the conversion factor from Wang (2005). It was not possible to convert P21 to P32 values for the NNE–SSW groups of parallel fractures at Hilti and Aswad because of their infinite Fisher distributions. Wang (2005) provides a modified conversion calculation for this scenario, but the values produced were illogically high compared to the total P32 value at the mapped locations. We also attempted to use very high Fisher distribution values in the normal conversion of Wang (2005) but this seemed to produce erroneous results. Instead, the P32 values for these parallel geometric groups were calculated by subtracting the P32 of the other geometric group at each location from the total P32 value at that location. With this calculation the ratio of P21 values for the two geometric groups at both Hilti and Aswad was maintained in their P32 data.

Our log–normal distribution for length data approximately fits the combined data from all locations and should approximately describe geometric group lengths. Hyman et al. (2016) showed that, although network geometry strongly influences bulk permeability, bulk permeability increases when length-correlated apertures are applied. Our data show a weak positive relationship between length and aperture with no simple mathematical form, therefore any applied relationship would be speculative. The log–normal distribution fit used for apertures, although approximate, was therefore more appropriate than any other correlated or constant function. The effect of internal fracture aperture variations are considered negligible in our models, but their effect on flow and transport have been investigated in detail using *dfnWorks* by Makedonska et al. (2016).

#### 4.6.1.5. Generation of UDFM models

The parameters implemented with the *genDFN* module reasonably describe our fracture data. Figure 4.13 shows that orientation data are well represented using the Fisher distribution, yielding similar trends and distributions of the mapped and generated fracture orientations for all geometric groups. The orange fracture groups from Hilti and Aswad that contain three and four parallel fractures were assigned Fisher values of 200. This value is used because we assume that these fractures are only approximately parallel in reality, although differences were not within the precision of the field tablet clinometer, and therefore these groups do not have infinite Fisher distributions. The P32 values of modelled fracture groups in Table 4.3 show that mapped fracture intensities are also well represented.

The rectangular shape and 1:1 aspect ratio are appropriate approximations for purely extensional fractures. The calculated internal permeability of fractures ( $10^{-12} \text{ m}^2$ ) is a preliminary value and could be further tested to evaluate its impact on bulk permeability. We expect that in distal zones, where permeability is mainly matrix-controlled, the P32 value has more influence than small variations in internal fracture permeability. However, in the Ajeeb Damage Zone the bulk permeability could be significantly influenced by even small changes.

#### 4.6.1.6. A brief comparison of UDFM with alternative approaches applied to oceanic crust

We successfully used the UDFM and *genFlow* modules to calculate bulk permeabilities of fault-distal and fault-damage zone blocks that simultaneously account for the effects of combined fractures and rock-matrix permeabilities. DFN models are usually treated separately from the rock-matrix as they usually vastly outweigh the contribution of rock-matrix permeability. However, our results show that UDFM models are essential in cases where high rock-matrix permeability competes with or dominates over the permeability of sparse fracture networks. Our estimates of bulk permeability were enabled by the octree-refined, matrix–fracture mesh unique to the UDFM approach in *dfnWorks*, versus the stochastic fracture models in *Move* and *FracMan*. *DfnWorks* is also advantageous over the parallel plate method used by Nehlig (1994) to calculate permeability in the Semail SDC, which produced extremely high values of  $10^{-12}$  to  $10^{-11} \text{ m}^2$ . This method is based on equation (2) from Lister (1974), which assumes infinite fracture radius and is highly dependent on fracture aperture:

$$k = \frac{W^3}{12Y} \quad (2)$$

where the  $k$  is permeability ( $\text{m}^2$ ),  $Y$  is crack spacing (m) and  $W$  is crack aperture (m). The parallel plate method is also implemented in the *Move* workflow but is known to overestimate permeability (Fisher, 1998; van Everdingen 1995).

#### 4.6.1.7. Flow simulations: challenges and adaptations

Although the *genFlow* module and PFLOTRAN facilitate finite element calculations of fluid flow, flow through a relatively low permeability matrix and largely unconnected fractures was a difficult numerical problem to solve. A number of simplifications and loosening of tolerances in the PFLOTRAN input parameters had to be made to approximately reach steady-state flow and achieve convergence of inflow and outflow rates across the domain in feasible time scales. Firstly, instead of sub-seafloor hydrostatic conditions, simple pressure conditions specified as Dirichlet boundary conditions were used. Secondly, the default PFLOTRAN tolerances ( $rtol = 10^{-8}$ ,  $atol = 10^{-50}$ ) had to be reduced to  $rtol = 10^{-4}$  and  $atol = 10^{-4}$ , and also an *itol* value of only 1 was used (an explanation of tolerance parameters can be found in *Petsc* documentation).

In models of Hilti (spilite) and Ajeeb Distal Zone inflow and outflow rates approximately reached steady state within 150–400 days simulation time, and under 5 hours wall clock time. Convergence of

inflow and outflow mass were nearly reached and accepted to calculate permeabilities within the available time restrictions. Despite the lowered tolerances, steady-state flow rates were still difficult to reach at Aswad. After 12 hours, simulations were stopped and permeability was calculated based on the associated fluxes, even though flow rates continued to gradually change. Additional time and computation power would be necessary to test alternative conditions to completely reach steady state and convergence for all models.

For Rusays, Hilti (epidosite) and Ajeeb Damage Zone the same tolerance and modifications were used, however steady-state was reached during every flow simulation. For the Ajeeb Damage Zone models this intuitively makes sense because fractures are abundant and well connected and mean fluid can easily pass across the domain. This suggests that the unconnected, short and sparse fractures within a relatively low permeability rock-matrix in the distal zones hinder achievement of steady-state and convergence. Flow simulations with stricter tolerances could be used to refine the Ajeeb Damage Zone bulk permeability and also to compare the impact of the tolerance level on bulk permeability.

#### *4.6.1.8. Representative domain size*

The domain volume of DFN and flow models was set at 200 x 200 x 200 m for the Hilti and Aswad locations. The cross-section area of this domain is larger than the total area mapped at any location and significantly longer in all directions than the maximum fracture length. For the Ajeeb Distal Zone the same domain volume was trialled at first and then was reduced to 150 x 150 x 150 m to reach accepted convergence and steady-state flow in under 12 hours computing time. Step-wise tests of increasing domain size should be made to check at which volume bulk permeabilities no longer change.

For the Rusays model, the maximum observed fracture length of 350 m meant that a 200 x 200 x 200 m domain volume was insufficient to include the fracture length distribution. The UDFM and flow simulation were therefore run with a ~400 x 400 x 400 m domain volume to account for the high fracture length. Although a reasonable P32 value was generated, the algorithm truncated long fractures against domain edges and only 39 fractures were produced. It is unlikely that this domain is large enough to have reached a representative volume and therefore requires further testing. However, the average thickness of the Geotimes unit, ~500 m, should be an upper limit to future model depths. Additionally, multiple DFN models and flow simulations at Rusays show that very high bulk permeabilities are produced when long fractures connect across the domain (Fig. 4.14). The permeability of  $3.4 \times 10^{-11} \text{ m}^2$  produced in this case seems too high given the internal fracture permeability of  $10^{-12} \text{ m}^2$ . An increased refinement level might be required to reduce mesh volumes containing false connections (mesh volumes that are accidentally assigned fracture- rather than matrix properties; Sweeney et al., 2019).

For the Ajeeb Damage Zone model, 670 fractures, many of which were connected, were generated in the 100 x 100 x 100 m domain volume. The permeabilities produced are also higher than the internal fracture permeability. With the current computational capacity only four refinement levels during

meshing could be applied to such a large number of fractures. This should also be checked for the highest refinement level (five) to reduce false connections in cell volumes.

#### 4.6.1.9. Validation of bulk permeabilities

The calculated bulk permeabilities are reasonable first estimates for our fault-distal zones despite the simplifications and loosened tolerances required to generate them. The consistent bulk permeabilities that are produced by similar fracture intensities from the models for Hilti, Aswad, Rusays and the Ajeeb Damage Zone supports this.

Although it was initially unclear how sensitive the flow simulations were to unconnected fractures, the difference between bulk permeability in the main flow directions (Table 4.3) demonstrates that flow is sensitive enough to reflect changes in unconnected fracture orientations. In all of the Hilti (spilite and epidosite), Rusays and Ajeeb Distal Zone models, higher bulk permeabilities are produced when flow is parallel to the fractures ( $k_{zz}$ ), despite their lack of connectivity, and lower values when flow is perpendicular to fractures ( $k_{xx}$  and  $k_{yy}$ ). In comparison, the Aswad model has similar permeabilities in all three principal directions. This could be due to the small fracture sizes, which do not enhance permeability in a particular direction compared to longer fractures in the other models. A similar anisotropic bulk permeability was produced at the Ajeeb Damage Zone, but the very high values may include false connections in the fracture meshes and should be re-evaluated.

Further, the statistical variation of the bulk permeability should be determined by calculating the bulk permeability for ~30 realisations of the UDFM models using different seeds to generate unique DFNs. For Hilti, Aswad, and Ajeeb Distal and Ajeeb Damage Zones, we expect only small variations of permeability will be observed. However, at Rusays the four test DFN's (Fig. 4.14) show that, for a domain with a few relatively long fractures, the bulk permeability can change dramatically when fractures connect across the domain.

#### 4.6.2. Implications of rock-matrix, fracture and bulk permeabilities for the hydrothermal circulation in the oceanic crust

##### 4.6.2.1. Rock-matrix permeability

Previous work on rock-matrix properties of extrusive lavas shows a range of porosity and permeability values  $\sim 10^{-21}$  to  $10^{-14}$  m<sup>2</sup> (e.g., Christensen and Ramanantoandro, 1988; Einaudi et al., 2000; Gilbert and Bona, 2016; Gilbert and Salisbury, 2011; Gillis and Sapp, 1997; Hamano, 1980; Jarrard et al., 2003; Johnson, 1980a; Pezard, 1990). In Chapter 3 of this study we showed that the bulk permeability of lava stacks needs to incorporate the highly permeable and porous hyaloclastite zones in order to be realistic. Our refined upscaling method in this Chapter produced new reliable estimates of bulk rock-matrix permeabilities ( $\phi \approx 10$  vol.% and  $k \approx 2 \times 10^{-16}$  m<sup>2</sup> in spilites and  $\phi \approx 12$  vol.% and  $k \approx 3 \times 10^{-16}$  m<sup>2</sup> in epidositites). These values are applicable to the outcrop scale, which translates well to their use for the 25 m diameter mesh for the rock matrix in the UDFM models. These values should also be applicable



to fresh basalts and to low-temperature alteration, as the rock-matrix values of spilites are similar to those of the more weakly altered rocks (Chapter 3).

The upscaled rock-matrix permeabilities and the UDFM models are based exclusively on the properties of pillow lava stacks, which vastly dominate the Geotimes unit. They do not take account of intercalations of the less permeable massive flows, which often act as barriers to flow (e.g. Fig. 4.16), or of the extremely permeable volcanic breccias and massive hyaloclastite zones. A number of massive flows were mapped at the Aswad location but generally they are uncommon in the Geotimes unit, appearing mostly near the top of the unit. Volcanic breccias and massive hyaloclastites are even less common in the Geotimes unit. Inclusion of these rock types in the models would obviously cause variations in the calculated outcrop-scale permeability. Such variations may be in part responsible for the  $\sim 10^{-18}$  to  $10^{-13}$  m<sup>2</sup> range of permeabilities measured in hydraulic tests in *in-situ* oceanic crust (Anderson et al., 1985; Becker, 1989; Becker & Fisher, 2000; Fisher, 1998).

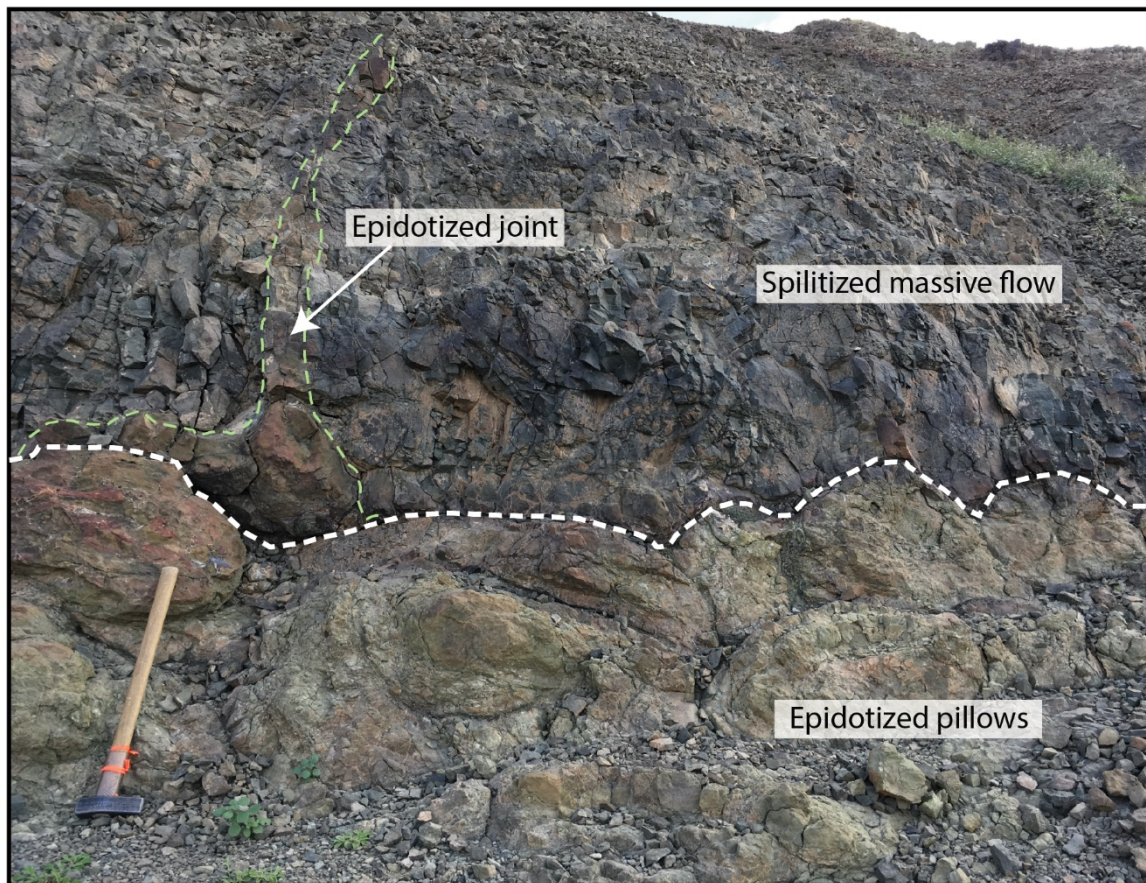


**Figure 16.** Field photograph of epidotised pillow lavas underlying a spilitised massive flow. Massive flow contains one epidotised joint. These field relations show that epidosite alteration post-dates spilite alteration, and that the pillow flows are more permeable than the massive flows.

#### 4.6.2.2 Fracture distributions in the Geotimes unit compared to other sites

Earlier works documented faults and fractures in the *in-situ* oceanic crust at km-scale transform faults (e.g. Hensen et al., 2019; Karson, 2002; Karson et al., 2002), at the Hess Deep and Pito Deep tectonic

windows in the eastern Pacific (Hayman & Karson, 2007; 2009), and in gabbros and in the SDC of the Semail and Troodos ophiolites (Nehlig, 1994; van Everdingen, 1995). Fracture porosity has also been reported for lavas in the Troodos ophiolite (Gillis and Sapp, 1997). At Hess Deep and Pita Deep, fault- and fault-damage zones were documented along with hydrothermal mineralisation (Hayman & Karson, 2007; 2009). These studies observed similar mineral fillings in fractures as we have documented in the Semail ophiolite. For example, quartz, epidote and prehnite were observed at both locations, along with more common chlorite- and actinolite-filled fractures at Hess Deep. Studies at both sites also report the pervasive alteration of the rock-matrix in non-faulted areas (Hayman & Karson, 2007; 2009; Heft et al., 2008), i.e., in areas that we have termed "fault-distal". However, fracture densities were not quantified at these locations. The only documented fracture distributions in oceanic lavas for fault-distal zones are from the DSDP H418 drill core (Johnson, 1980b) and in the Troodos ophiolite (Gillis and Sapp, 1997).

Johnson (1980b) measured all open (unfilled fractures) and carbonate- and smectite-filled fractures over the ~546 m drill core recovered from DSDP H418. The high recovery rate of this core (~72%) meant that a good proportion of fractures could be recorded, although the most intensely fractured and brecciated areas are likely to have been lost (Johnson, 1980b). The core was divided into 1.5 m intervals and total crack densities found vary between 0 to ~60 cracks per 1.5 m, with an average of around 30 cracks per 1.5 m, which is approximately a P10 value of  $20 \text{ m}^{-1}$ . This P10 values is 4–5 orders of magnitude higher than approximate P10 values from our distal zones of 0.015, 0.017, 0.008, and 0.020  $\text{m}^{-1}$  (uncorrected for line direction orientations) and two orders of magnitude higher than the ~0.174  $\text{m}^{-1}$  at the Ajeeb Damage zone. The reported average fracture lengths and apertures from Hole 418 of 150 mm and 2 mm, respectively, are significantly shorter, but they presumably represent truncated values owing to the limited diameter of the drill core.

Fracture mapping of drill core is likely more accurate for the distinction of fine <1–2 mm fractures than our areal outcrop maps, which could result in higher fracture densities. Another potential explanation for the difference between the fracture densities in this study and those from Hole 418 (Johnson, 1980b) is the high frequency of cooling joints described in *in-situ* oceanic lavas, whereas cooling joints are uncommon in the Geotimes unit. Intra-pillow cooling joints are the main type of fractures documented by Gillis and Sapp (1997), which are discussed in more detail below.

#### 4.6.2.3 Cooling joints in Geotimes pillow lavas

Basalts in *in-situ* oceanic crust and the Troodos ophiolite contain abundant open fractures that are attributed to cooling-induced shrinkage immediately after extrusion (e.g. Gillis and Sapp, 1997; Johnson 1980b). These fractures are immediately accessible to infiltrating and seawater, which precipitates a variety of clays, carbonates, zeolites, and celadonite (Gillis and Sapp, 1997; Johnson, 1980b). In individual lavas from the Troodos ophiolite, joint-fracture densities and fracture intensities (P10 and P21) were reported by Gillis and Sapp (1997). Their intra-pillow P10 values are ~10–120  $\text{m}^{-1}$ , P21 values (all open and filled fractures) are ~10–90  $\text{m}^{-1}$  and P21 values (filled fractures) are ~0–60



$\text{m}^{-1}$ . Based on these fracture distributions and fracture apertures, Gillis and Sapp (1997) calculated an intra-pillow fracture porosity of 1.5–3.7 vol.%.

In our mapped locations some pillow basalts show mineralised radial and concentric cooling joints but most pillows lack any open or mineralised fractures (e.g. Fig. 4.6). Therefore, we see two open questions regarding the contribution of thermal cooling joints to the permeability of the lavas; (1) what proportion of lavas contain cooling joints in the Geotimes unit and (2) what proportion of these cooling joints are open to fluids? In some parts of the Ajeeb map, Geotimes and Lasail pillows with patchy/intermediate epidotisation have epidotised cooling joints containing freely grown epidote with a surrounding halo (Fig. 4.6d). Also at the Geotimes type-locality, pillows contain partially prehnite filled cooling joints (Fig. 4.6a,c,e). The exact proportion of jointed to joint-free pillows is unknown, but the mineralised joints indicate that at least some joints were open to hydrothermal fluids.

Two possible explanations for the lack of joints in pillows are (1) there were no joints formed on the seafloor due to slow cooling rates, or a less likely scenario (2) joints were formed and then clogged by early lower temperature assemblages such as calcite, clay and zeolite, and these were later replaced by epidotising or spilitising fluids. Overprinted joints would then become indistinguishable from the surrounding host matrix and the pillow lavas might appear joint-free.

Cooling joints would significantly increase the permeability of pillow stacks. This contribution to permeability, along with the microfractures not mapped in the field (Fig. 4.11), could account for the difference between our modelled bulk permeabilities and those measured by *in-situ* hydraulic packer tests. Further study could attempt to quantify cooling joints following a similar method to Gillis and Sapp (1997) and calculate their permeability using flow simulations of simplified 2D or 3D models of pillow lava tubes with joints.

#### 4.6.2.4 Bulk permeability

Based on the similar bulk permeabilities calculated for the Aswad, Hilti, Rusays and Ajeeb Distal Zone models ( $\sim 3.5\text{--}8 \times 10^{-16} \text{ m}^2$ ) we draw three main conclusions regarding permeability in fault-distal lava zones: (1) the rock-matrix permeability of pillow stacks largely determines the order of magnitude of bulk permeability, (2) fractures increase bulk permeability by up to half an order of magnitude, which doubles the permeability, and (3) an average bulk permeability value of  $\sim 5 \times 10^{-16} \text{ m}^2$  represents the overall fractured rock mass. Additionally, bulk permeabilities increase slightly where the rock-matrix is altered to epidosite rather than spilite (e.g. Hilti location epidosite model, Table 4.3). Although fractures contribute to enhancing permeability as stated above, it is critical to acknowledge that without the rock-rock permeability, nearly all the fractures mapped would be isolated, and therefore not contribute to bulk permeability.

In the Ajeeb Damage Zone model the calculated bulk permeabilities  $3.85 \times 10^{-12}$  to  $8.82 \times 10^{-11} \text{ m}^2$  are considered preliminary and require further modelling to check for false connections in mesh

cells. At an order-of-magnitude scale they illustrate the intuitive result that permeability in damage zones is controlled by fractures rather than by the rock matrix.

#### *4.6.2.5 Applicable scale of bulk permeabilities*

The conclusions above are valid for Aswad, Hilti and Ajeeb Distal for domain volumes of  $\sim 200 \times 200 \times 200$  m, and we expect that they would be still valid at larger scales. In Rusays, variable bulk permeabilities were produced by the models over the  $\sim 400 \times 400 \times 400$  m volume, depending on fracture connectivity. High bulk permeabilities controlled by fractures were produced by connected fractures at this scale, and would also be produced at any domain volume smaller than the largest (350 m long) fracture. These results show that bulk permeability can vary depending on the scale of interest in models.

Considering all the mapped locations, these long fractures are uncommon. At Rusays the epidote + quartz vein mapped as the longest fracture (350 m) lies along the contact of a dyke, but despite the abundance of similar dykes at the Hilti location there are no notably long fractures there. Only a handful of other fractures out of the total 120 mapped in distal zones are  $> 30$  m long: three other fractures at Rusays (54, 88 and 120 m long) and two at Ajeeb Distal Zone (60 and 70 m long).

Below lava volumes of  $400 \times 400 \times 400$  m, these long fractures may become important fluid conduits but in the case of Rusays, this does not seem to be the case. The longest fracture only has a 2 mm aperture and lacks a significant epidotised halo. This indicates that the fluid flow to form the incipient and intermediate epidotisation in the surrounding lavas was controlled by the rock-matrix. One explanation for this is that the fracture became clogged by hydrothermal minerals soon after it formed.

In summary, the scale of interest is important for modelled bulk permeabilities but the complexity of opening, clogging and potential reactivation of fractures means that connected fractures may equate to high fracture permeability only during limited time intervals. For numerical models of hydrothermal circulation in the upper oceanic crust, the applicable scale for our bulk permeabilities is likely to be the average thickness of the Geotimes unit ( $\sim 500$  m), and the time-scale of its validity is likely to be very long (because the rock-matrix dominates the bulk permeability and the rocks are still permeable today). A low density of  $\leq 350$  m long fractures are unlikely to significantly increase bulk permeability at this scale and therefore, the average bulk permeability for distal zones in our study, (excluding bulk permeability from the connected Rusays model; Fig. 4.14a) of  $\sim 5 \times 10^{-16} \text{ m}^2$  is suitable for generic use.

#### *4.6.2.6 Absolute timing of fractures*

The timing and regional stress conditions under which mapped fractures formed are difficult to interpret due to the lack of kinematic indicators and crosscutting relationships. However, the mapped fracture orientations may be compared to larger scale, regionally distributed structural features with some axial and post-axial timing constraints. Many of the syn-volcanic faults mapped by Lippard et al. (1986) and

Belgrano et al. (2019) strike NW–SE to E–W, which match most of our fracture groupings and therefore the timing of those regional faults may reflect that of the mapped fractures. Several timing constraints were highlighted by Belgrano et al. (2019) during their recent remapping of the volcanic units; those and additional considerations from other authors are summarized to distinguish the axial and post-axial timing of regional fault offsets:

1. In the Western Fize blocks and Hilti block, the axial SDC and Geotimes lavas are offset to a greater extent than the conformably overlying Tholeiitic Alley and Boninitic Alley lavas along the same NW–SE to E–W faults.
2. Several of the axial-stage VMS deposits hosted in Geotimes lavas (e.g. Ghuzayn 3, Mahab, Zuha) formed along seafloor scarps of normal faults (Gilgen et al., 2014).
3. Some of the VMS deposits hosted in Geotimes lavas (e.g. Bayda, Hatta Main and Hatta Extended) are crosscut by NW–SE and E–W faults (Gilgen et al., 2014; Lippard et al., 1986).
4. Undeformed Boninitic Alley dikes sit within NW–SE and E–W faults in some areas, whereas in other areas (e.g., Hilti block), faults with the same orientations offset the Boninitic Alley lavas.

Constraints (1) to (4) indicate that faulting occurred during and after the axial-stage magmatism that formed the SDC and Geotimes units (Belgrano et al., 2019), and that it locally continued through to Boninitic Alley time, the latest period of volcanism.

A few NE–SW to N–S fractures were also found in our mapping areas; a group of three parallel chlorite-filled fractures in the Hilti area, one chlorite-filled fracture in the Ajeeb Distal Zone, and a few other epidote  $\pm$  quartz filled fractures at each location. These fractures run parallel to the strike of dikes in the axial SDC, and so may be related to axis-parallel extension during Geotimes volcanism. A separate UDFM model and bulk permeability analysis could not be made based on so few fractures, so these were lumped with the total fracture distributions at each location. It is possible that more such spilite-type fractures exist in the mapped areas, but those filled by chlorite or smectite are very thin and easily weathered out on the outcrops, such that they might have been overlooked while mapping the more obvious fractures filled by epidote + quartz.

The tectonic stress regime during the MOR stage of formation of the Semail crust is accepted as being extensional. Van Hinsbergen et al. (2019) propose that extension continued to dominate during post-axial volcanism as well, but Umino et al. (2019) offer an alternative theory of compression during the post-axial stage, induced by early plate rotation of the Semail lithosphere. The rather low intensity of fracturing in the Semail SDC was suggested by Nehlig (1994) to reflect a high magma-supply rate relative to the plate tectonic spreading rate, such that intervals of amagmatic spreading and faulting along the MOR were less prevalent. We do not discuss these possible far-field stress regimes further because fractures make such a minor contribution to the bulk permeability in our mapped distal zones. Nevertheless, future investigation of this topic might reveal interesting relationships. Regardless of the underlying controls on fracturing, the dominance of the rock-matrix permeability over sparse fractures

means that our distal zone observations and bulk permeabilities in the Semail MORB crust have relevance for *in-situ* MORB-type crust in the modern oceans.

#### 4.6.2.7. The relationship between fractures, pervasive rock-matrix alteration and bulk permeability

The bulk permeability determined by modelling is in one sense a maximum permeability estimate because it includes multiple fracture orientations and assemblages that were unlikely to all be open and permeable at the same time. Here we offer some insight as to when fracture permeability was open and if it was coupled or decoupled from pervasive rock-matrix flow.

The regional spilite alteration of the Geotimes lavas is thought to occur during the axial stage of magmatism, which is pervasive and replaces all fresh glass (Kusano et al., 2017). However, few fractures with spilite mineral assemblages were mapped, and few fractures overall seem to coincide with the axial regional stress regime. If axial fractures are sparse, this suggests spilite fluids alter the rock-matrix in fault-distal zones largely in the absence of fracture permeability.

In axial *in-situ* oceanic crust, epidote  $\pm$  quartz and prehnite fractures are typically reported without pervasive epidotisation of the rock-matrix (e.g. Hayman and Karson, 2007; 2009). Whereas most of our epidote  $\pm$  quartz fractures were observed in zones with some rock-matrix epidotisation, the same mineralised fractures are also found outside areas of epidosite (Gilgen et al., 2016). Thus, it is feasible that these fluids were actively circulating through fractures prior to pervasive epidotisation events.

In pervasively epidotised zones such as Ajeeb and to some extent Rusays, the following timing relationships are feasible between fracture flow and pervasive rock-matrix flow of the epidosite-forming fluid: (1) fractures formed first, then the epidotising fluids ascended through them and infiltrated the wall rocks to form the  $\sim\text{km}^3$ -sized bodies of metasomatised rock-matrix observed today; (2) fractures formed during pervasive alteration, (3) fractures formed at the waning and cooling stage of the hydrothermal system, or (4) fractures formed and were reactivated during multiple stages (1), (2), and (3) of the rock-matrix epidotisation.

In Chapter 3 of this study we showed that epidotising fluids produce a reaction permeability of up to 4.5 orders of magnitude. This indicates that epidotising fluids can create their own permeable pathways and thus do not require open fracture permeability to migrate. Therefore, this property removes the need to couple fracture and rock-matrix flow. Fractures could still transport some epidotising fluids, although the small (mm- to cm-scale) alteration halos surrounding mapped fractures suggest that they may be clogged by epidote  $\pm$  quartz early during fluid movement. This would prevent large halos from forming and mean epidotising fluids might be forced out into the rock-matrix. Clogging of fractures and faults by hydrothermal minerals has also been reported in *in-situ* oceanic crust (e.g. at Hess Deep by, Hayman and Karson, 2007).

In support of scenario (3) above, prehnite fractures at the exterior damage zones of the Ajeeb epidosite suggest that some fractures were open at a lower temperature stage, e.g., as epidotising fluids cooled. In support of scenario (4), the presence of multi-generation mineral precipitation in fractures

points to their reactivation over an extended hydrothermal history but could also be due to rapid clogging.

Based on these observations it is difficult to define one timing relationship between epidote  $\pm$  quartz fractures and pervasive epidotisation. All the 12 epidosite bodies in the Semail ophiolite with clear age constraints formed during or after Lasail volcanism, and 5 clearly formed during Tholeiitic Alley volcanism (Gilgen et al., 2016) but the relative age of the fractures to pervasive epidotisation is still unclear. The timing relationship at Ajeeb and Rusays could be investigated further by looking for crosscutting relationships: at a thin-section scale between epidote  $\pm$  quartz fractures and surrounding epidotised matrix, and at a field scale between epidote  $\pm$  quartz fractures and dykes of known volcanostratigraphic affinity and age.

#### 4.7. Conclusions

We have presented the fracture mapping, fracture network upscaling, and *dfnWorks* flow simulations used to calculate bulk permeability of the distal zones between seafloor faults in basaltic lavas of the oceanic crust. The important conclusions are summarised in three categories:

##### *Mapping approach*

Previous fracture distributions in extrusive lavas were based on fracture mapping from DSDP Hole 418, Troodos intra-pillow fracture and qualitative observations *in-situ* Hess Deep and Pito Deep tectonic windows (Gillis and Sapp, 1997; Hayman and Karson, 2007; 2009; Johnson, 1980b). These methods did not capture the regional scale variability of fracture distributions in distal zones, nor quantitative fracture distributions in fault damage-zones. Our study investigated the unique exposures of largely undisturbed extrusive lavas in the Semail ophiolite to quantify distal zone fracture distributions.

Swath mapping facilitated robust estimates of fracture intensity (P21), a technique that could be implemented in other ophiolites. Alongside this, the assignment of geometric groups to fracture orientations allowed a reasonable description of geological data that lack kinematic indicators. This approach provided a clear description of fracture properties and network geometry as reliable input parameters to build DFN and UDFM models.

##### *UDFM and flow simulations with dfnWorks*

From the available methods to calculate or model permeability, the UDFM model and flow simulation in *dfnWorks* (Hyman et al., 2015; Sweeney et al., 2019) was the only viable way to integrate fracture network geometry and connectivity with rock-matrix properties. This modelling approach was critical to calculate bulk permeability in a setting that has a permeable and porous matrix but sparse fractures, and to determine the contribution from both components. The challenges and adaptations made to the tolerances used in flow models that were needed to reach convergence and steady state in the flow simulations, should serve as a useful example and basis for improved models in further work and studies

of similar settings. The sensitivity of the flow simulation to unconnected fracture orientations in permeable domains validates our bulk permeability values and shows the effectiveness of the UDFM models and *dfnWorks* for similar settings.

#### *Bulk permeabilities of extrusive lavas*

Our mapping and models demonstrate that bulk permeability in distal zones of the extrusive lavas is dominated by the permeability of the rock-matrix. The rock-matrix permeability of the spilite pillow stacks is  $\sim 2 \times 10^{-16} \text{ m}^2$  and epidiosites pillow stacks  $\sim 3 \times 10^{-16} \text{ m}^2$ . The average bulk permeability value for fault-distal spilite and epidiosite zones including the rock-matrix and fractures is  $\sim 5 \times 10^{-16} \text{ m}^2$ . Therefore, fractures enhance the rock-matrix permeability by a factor of two; however, the isolated fractures would be unconnected with no fracture permeability if not for the surrounding permeable matrix. The bulk permeability values are applicable to cubic blocks of lava with sides between 200 m and 500 m long. However, the values might be slightly overestimated by our inclusion of all fractures from potentially multiple fracture generations associated with different alteration stages. Additionally, the intuitively high fracture intensity and high fracture-controlled permeability in fault-damage zones was confirmed. Bulk permeabilities in these zones likely depends on the internal fracture permeability and are on the order of  $10^{-12}$ – $10^{-11} \text{ m}^2$ . The traditional concept of the upper layer of the oceanic crust as a fractured aquifer should consequently be updated to a permeable rock-matrix aquifer that is enhanced at spaced intervals by intensely fractured fault-damage zones. This model is based on the km-scale permeability architecture of the pillow lavas in the Semail ophiolite, in which blocks of  $\sim 0.5$ – $1$  km width are dominated by rock-matrix flow, interspaced by seafloor faults surrounded by  $\sim 50$ – $100$  m wide damage zones.

The bulk permeabilities of distal zones found in this study are still  $\sim 2$  orders of magnitude lower than the highest values measured in *in-situ* hydraulic tests ( $\sim 10^{-14} \text{ m}^2$ ). Reasons for this difference might be (1) the under-sampling of breccia zones and/or underestimated hyaloclastite permeabilities in our rock-matrix upscaling, or (2) exclusion of cooling joints uncommon in the Geotimes unit but abundant in pillow lavas in *in-situ* drill sites. Despite this, a combination of distal and damage zone bulk permeabilities could account for the permeabilities of  $10^{-16}$ – $10^{-11} \text{ m}^2$  required by numerical models to reproduce seafloor heat and fluid discharge (e.g. values in Fisher, 1998 and references therein; Hasenclever et al., 2014).

The exact timing of the mapped NW–SE, E–W and N–S fractures and faults is difficult to constrain, but they are certainly syn-volcanic. Nevertheless, as fracture permeability in the fault-distal zones is any case so low, and as our mapped Geotimes lavas certainly formed via MOR-spreading, our deduced bulk permeabilities are still applicable to *in-situ* oceanic crust. Therefore, we suggest that our new values can be used as valid calibration targets for numerical models of hydrothermal circulation in both MOR and supra-subduction zone oceanic crust.

## Acknowledgements

We gratefully acknowledge the logistical support during field work in the Sultanate of Oman by Khalid al-Tobi (Earth Secrets Co., Muscat) and Mohammed Al Araimi and Mohammed Al-Battashi (Public Authority for Mining, Muscat). The University of Bern field mapping team including Tom Belgrano, Lisa Richter, Samuel Weber, Samuel Pierre, Nicolas Zuluaga Velasquez, Sarah Pein, Robin Wolf, Raphael Kuhn and Ludwik de Doliwa Zielinski. This work was supported by Swiss National Science Foundation (SNSF) Grants 200020-169653 and -188567 to L.W.D.

## References

- Allmendinger, R.W., Cardozo, N.C., Fisher, D., 2013. Structural Geology Algorithms: Vectors and Tensors. Cambridge University Press, Cambridge, England.
- Anderson, R.N., Zoback, D.M., Hickman, S.H., Newmark, R.L., 1985. Permeability Versus Depth in the Upper Oceanic Crust: In Situ Measurements in DSDP Hole 504B, Eastern Equatorial Pacific. *J. Geophys. Res.* 90, 3659–3669. <https://doi.org/10.1029/JB090iB05p03659>.
- Bach, W., Peucker-Ehrenbrink, B., Hart, S.R., Blusztajn, J.S., 2003. Geochemistry of hydrothermally altered oceanic crust: DSDP/ODP Hole 504B - Implications for seawater-crust exchange budgets and Sr- and Pb-isotopic evolution of the mantle. *Geochem. Geophys. Geosyst.* 4, 1–29. <https://doi.org/10.1007/s00269-010-0415-y>.
- Becker, K., 1989. Measurements of the permeability of the sheeted dikes in Hole 504B, ODP Leg 111. *Proc. ODP, Sci. Results* 111, 317–325. <https://doi.org/10.2973/odp.proc.sr.111.156.1989>.
- Becker, K., Fisher, A.T., 2000. Permeability of upper oceanic basement on the eastern flank of the Endeavor Ridge determined with drill-string packer experiments. *J. Geophys. Res.* 105, 897–912. <https://doi.org/10.1029/1999JB900250>.
- Belgrano, T.M., Diamond L.W., 2019. Subduction-zone contributions to axial volcanism in the Oman-U.A.E. ophiolite. *Lithosphere* 11, 399–411. <https://doi.org/10.1130/L1045.1>.
- Belgrano T.M., Diamond L.W., Vogt Y., Biedermann A.R., Gilgen S.A., 2019. A revised map of volcanic units in the Oman ophiolite: Insights into the architecture of an oceanic proto-arc volcanic sequence. *J. Geophys. Res. Solid Earth* 10, 1181–1217. <https://doi.org/10.5194/se-10-1181-2019>.
- Cann, J.R., 1969. Spilites from the Carlsberg Ridge, Indian Ocean. *J. Petrol.* 10, 1–19. <https://doi.org/10.1093/petrology/10.1.1>.



- Christensen, N.I., Ramananantoandro, R., 1988. Permeability of the oceanic crust based on experimental studies of basalt permeability at elevated pressures. *Tectonophysics* 149, 181–186. [https://doi.org/10.1016/0040-1951\(88\)90126-6](https://doi.org/10.1016/0040-1951(88)90126-6).
- Coleman, R.G., Bailey, E.H., 1981. Mineral deposits and geology of northern Oman as of 1974. USGS Open File Report 81-452. <https://doi.org/10.3133/ofr81452>.
- Darcel, C., Davy, C., Le Groc, R., de Dreuzy, J.R., Bour, O., 2009. Statistical methodology for discrete fracture model – including fracture size, orientation uncertainty together with intensity uncertainty and variability. Swedish Nuclear Fuel and Waste Management Co., Sweden.
- Dershowitz, W., Lee, G., Geier, J., 1991. FracMan Version 2.3. Interactive discrete feature data analysis, geometric modeling, and exploration simulation. User documentation. Golder Associates Inc, Redmond, Washington, USA.
- Einaudi, F., Pezard, P. A., Cochemé, J-J., Coulon, C., Laverne, C., Godard, M., 2000. Petrography, geochemistry and physical properties of a continuous extrusive section from the Sarami Massif, Semail ophiolite. *Mar. Geophys. Res.* 21, 387–407.
- Einstein, H.H., Baecher, G.B., 1983. Probabilistic and statistical methods in engineering geology. *Rock Mechanics and Rock Engineering*, 16, 39–72. <https://doi.org/10.1007/BF01030217>.
- Fisher, A.T., 1998. Permeability within basaltic ocean crust. *Reviews of Geophysics* 36, 143–182. <https://doi.org/10.1029/97RG02916>.
- Fisher, R., 1953. Dispersion on a sphere. *Proc. Math. Phys. Eng. Sci.* 217, 295–305. <https://doi.org/10.1098/rspa.1953.0064>.
- Gilbert, L.A., Bona, M.L., 2016. Permeability of oceanic crustal rock samples from IODP Hole 1256D. *Geochem. Geophys. Geosyst.* 17, 3825–3832. <https://doi.org/10.1002/2016GC006467>.
- Gilbert, L.A., Salisbury, M.H., 2011. Oceanic crustal velocities from laboratory and logging measurements of Integrated Ocean Drilling Program Hole 1256D. *Geochem. Geophys. Geosyst.* 12, Q09001. <https://doi.org/10.1029/2011GC003750>.
- Gilgen, S.A., Diamond, L.W., Mercolli, I., 2016. Sub-seafloor epidosite alteration: Timing, depth and stratigraphic distribution in the Semail Ophiolite, Oman. *Lithos* 260, 191–210. <https://doi.org/10.1016/j.lithos.2016.05.014>.
- Gilgen, S.A., Diamond, L.W., Mercolli, I., Al-Tobi, K., Maidment, D.W., Close, R., Al-Towaya, A., 2014. Volcanostratigraphic controls on the occurrence of massive sulfide deposits in the Semail Ophiolite, Oman. *Economic Geology* 109, 1585–1610. <https://doi.org/10.2113/econgeo.109.6.1585>.
-

- 
- Gillis, K.M., Sapp, K., 1997. Distribution of porosity in a section of upper oceanic crust exposed in the Troodos Ophiolite. *J. Geophys. Res.* 102, 10133–10149. <https://doi.org/10.1029/96JB03909>.
- Giuffrida, A., La Bruna, V., Castelluccio, P., Panza, E., Rustichelli, A., Tondi, E., Giorgioni, M., Agosta, F., 2019. Fracture simulation parameter of fractured reservoirs: Analogy with outcropping carbonates of the Inner Apulian Platform, southern Italy. *Journal of Structural Geology* 123, 18–41.
- Glennie, K.W., Boeuf, M.G., Hughes-Clarke, M.H.W., Moody-Stuart, M., Pilaar, W.F., Reinhardt, B., 1974. Geology of the Oman Mountains. *Geologisch Mijnbouwkundig Genootschap* no. 31, Netherlands.
- Guilmette, C., Smit, M.A., van Hinsbergen, D.J.J., Gürer, D., Corfu, F., Charette, B., Maffione, M., Rabeau, O., Savard, D., 2018. Forced subduction initiation recorded in the sole and crust of the Semail Ophiolite of Oman. *Nat. Geosciences* 11, 688–695. <https://doi.org/10.1038/s41561-018-0209-2>.
- Hamano, Y., 1980. Physical properties of basalts from Holes 417D and 418A. Initial Rep. Deep Sea Drill. Proj. 51, 52, 53, 1457–1466. <https://doi.org/10.2973/dsdp.proc.515253.166.1980>.
- Hammond, G.E., Lichtner, P.C., Mills, R.T., 2014. Evaluating the performance of parallel subsurface simulators: An illustrative example with PFLOTRAN. *Water Resour. Res.* 50, 208–228. <https://doi.org/10.1002/2012WR013483>.
- Hannington, M.D., 2014. Volcanogenic massive sulfide deposits. In: Holland, H.D., Turekian, K.K. (Eds.), *Treatise on Geochemistry*, 2nd edition. Elsevier, Oxford, pp. 463–488.
- Hayman, N.W., Karson, J.A., 2007. Faults and damage zones in fast-spread crust exposed on the north wall of the Hess Deep Rift: Conduits and seals in seafloor hydrothermal systems. *Geochem. Geophys. Geosyst.* 8, 1–31. <https://doi.org/10.1029/2007GC001623>.
- Hayman, N.W., Karson, J.A., 2009. Crustal faults exposed in the Pito Deep Rift: Conduits for hydrothermal fluids on the southeast Pacific Rise. *Geochem. Geophys. Geosyst.* 10, 1–26. <https://doi.org/10.1029/2008GC002319>.
- Haymon, R.M., Koski, R.A., Abrams, M.J., 1989. Hydrothermal discharge zones beneath massive sulfide deposits mapped in the Oman ophiolite. *Geology* 17, 531–535. [https://doi.org/10.1130/0091-7613\(1989\)017](https://doi.org/10.1130/0091-7613(1989)017).
- Heft, K.L., Gillis, K.M., Pollock, M.A., Karson, J.A., Klein, E.M., 2008. Role of upwelling hydrothermal fluids in the development of alteration patterns at fast spreading ridges: Evidence
-

- 
- from the sheeted dike complex at Pito Deep. *Geochem. Geophys. Geosyst.* 9, 1–26.  
<https://doi.org/10.1029/2007GC001926>.
- Hensen, C., Duarte, J. C., Vannucchi, P., Mazzini, A., Lever, M. A., Terrinha, P., ... Nuzzo, M., 2019. Marine Transform Faults and Fracture Zones: A joint perspective integrating seismicity, fluid flow and life. *Frontiers in Earth Science* 19. <https://doi.org/10.3389/feart.2019.00039>.
- Hyman, J.D., Aldrich, G., Viswanathan, H.S., Makedonska, N., Karra, S., 2016. Fracture size and transmissivity correlations: Implications for transport simulations in sparse three-dimensional discrete fracture networks following a truncated power law distribution of fracture size. *Water Resources Research* 52, 6472–6489. <https://doi.org/10.1002/2016WR018806>.
- Hyman, J.D., Karra, S., Makedonska, N., Gable, C.W., Painter, S.L., Viswanathan, H.S., 2015. dfnWorks: A discrete fracture network framework for modeling subsurface flow and transport. *Comput. Geosci.* 84, 10–19. <https://doi.org/10.1016/j.cageo.2015.08.001>.
- Isles, D.J., Witham, W.J.A., 1993. Batinah Coast region and Raki Hayl As Safil area, Airborne Geophysical Project: Final report on geological interpretation. Ministry of Petroleum and Minerals, Muscat, Sultanate of Oman.
- Jarrard, R.D., Abrams, L.J., Pockalny, R., Larson, R.L., Hirono, T., 2003. Physical properties of upper oceanic crust: Ocean Drilling Program Hole 801C and the waning of hydrothermal circulation. *J. Geophys. Res. Solid Earth* 108, 1–26. <https://doi.org/10.1029/2001JB001727>.
- Johnson, D.M., 1980a. Fluid permeability of oceanic basalts. Initial Rep. Deep Sea Drill. Proj. 68, 1473–1477.
- Johnson, D.M., 1980b. Crack distribution in the upper crust and its effects upon seismic velocity, seismic structure, formation permeability and fluid circulation. Initial Rep. Deep Sea Drill. Proj. 51, 52, 53, 1457–1466. <https://doi.org/10.2973/DSDP.PROC.515253.169.1980>.
- Jowitt, S.M., Jenkin, G.R.T., Coogan, L.A., Naden, J., 2012. Quantifying the release of base metals from source rocks for volcanogenic massive sulfide deposits: Effects of protolith composition and alteration mineralogy. *J. Geochem. Explor.* 118, 47–59.  
<https://doi.org/10.1016/j.gexplo.2012.04.005>.
- Karato, S., 1983. Physical properties of basalts from Deep Sea Drilling Project Hole 504B, Costa Rica Rift. Initial Rep. Deep Sea Drill. Proj. 69, 687–695.
- Karson, J. A., 2002. Geological structure of the uppermost oceanic crust created at fast- to intermediate-rate spreading centers. *Annu. Rev. Earth Planet. Sci.* 30, 347–384.  
<https://doi.org/10.1146/annurev.earth.30.091201.141132>.
-

- Karson, J.A., Tivey, M.A., Delaney, J.R., 2002. Internal structure of uppermost oceanic crust along the Western Blanco Transform Scarp: Implications for subaxial accretion and deformation at the Juan de Fuca Ridge. *J. Geophys. Res. Solid Earth* 107, B9. <https://doi.org/10.1029/2000JB000051>.
- Lichtner, P.C., 2007. FLOTRAN User's manual: Two-phase nonisothermal coupled thermal hydrologic-chemical (THC) reactive flow & transport code, version 2. Los Alamos National Laboratory, Los Alamos, New Mexico.
- Lippard, S.J., Shelton, A.W., Gass, I.G., 1986. The ophiolite of northern Oman. Blackwell Scientific Publications Ltd, London, United Kingdom.
- Lister, C.R.B., 1974. On the penetration of water into hot rock. *Geophys. J. R. astr. Soc.* 39, 465–509. <https://doi.org/10.1111/j.1365-246X.1974.tb05468.x>.
- Maasland, M., 1957. Soil anisotropy and soil drainage. In: Maddock, J.N. (Eds.), *Drainage of agricultural lands*. American Society of Agronomy, Madison, Wisconsin, pp. 216–285.
- MacLeod, C.J., Reuber, I., 1990. Complex rift geometry in the northern Oman ophiolite: A possible overlapping spreading center. In: Peter, T.J., Nicolas, A., Coleman, R.G. (Eds.), *Ophiolite Genesis and Evolution of the Oceanic Lithosphere*. Kluwer Acad., Norwell, Massachusetts, pp. 200–229.
- MacLeod, C.J., Rothery, D.A., 1992. Ridge axial segmentation in the Oman ophiolite: Evidence from along-strike variations in the sheeted dyke complex. *Geol. Soc. London Spec. Pub.* 60, 39–63. <https://doi.org/10.1144/GSL.SP.1992.060.01.03>.
- Makedonska, N., Hyman, J.D., Karra, S., Painter, S.L., Gable, C.W., Viswanathan, H.S., 2016. Evaluating the effect of internal aperture variability on transport in kilometer scale discrete fracture networks. *Advances in Water Resources* 94, 486–497. <http://dx.doi.org/10.1016/j.advwatres.2016.06.010>.
- Miller, I., 1990. MAFIC Version Beta 1.2 Matrix/Fracture Interaction Code with Solute Transport – User Documentation. Golder Associates, Inc, Redmond, WA.
- Morris, A., Meyer, M., Anderson, M.W., MacLeod, C.J., 2016. Clockwise rotation of the entire Oman ophiolite occurred in a suprasubduction zone setting. *Geology* 44, 1055–1058. <https://doi.org/10.1130/G38380.1>.
- Mottl, M.J., Wheat, G.C., 1994. Hydrothermal circulation through mid-ocean ridge flanks: Fluxes of heat and magnesium. *Geochim. Cosmochim. Acta* 58, 2225–2237. [https://doi.org/10.1016/0016-7037\(94\)90007-8](https://doi.org/10.1016/0016-7037(94)90007-8).
-

- 
- Nehlig, P., Juteau, T., Bendel, V., Cotten, J., 1994. The root zones of oceanic hydrothermal systems: Constraints from the Samail ophiolite (Oman). *J. Geophys. Res.* 99, 4703–4713. <https://doi.org/10.1029/93JB02663>.
- Nicolas, A., Boudier, F., Ildefonse, B., Ball, E., 2000. Accretion of Oman and United Arab Emirates ophiolite – Discussion of a new structural map. *Mar. Geophys. Res.* 21, 147–180. <https://doi.org/10.1023/A:1026769727917>.
- Patten, C.G.C., Pitcairn, I.K., Teagle, D.A.H., Harris, M., 2016. Sulphide mineral evolution and metal mobility during alteration of the oceanic crust: Insights from ODP Hole 1256D. *Geochim. Cosmochim. Acta* 193, 132–159. <https://doi.org/10.1016/j.gca.2016.08.009>.
- Perrin, M., Plenier, G., Dautria, J.-M., Cocuau, E., Prévot, M., 2000. Rotation of the Semail ophiolite (Oman): Additional paleomagnetic data from the volcanic sequence. *Mar. Geophys. Res.* 21, 181–194. <https://doi.org/10.1023/A:1026738313805>.
- Pezard, P. A., 1990. Electrical properties of mid-oceanic ridge basalt and implication for the structure of the upper oceanic crust in Hole 504B. *J. Geophys. Res.* 95, 9237–9264. <https://doi.org/10.1029/JB095iB06p09237>.
- Richter, L., Diamond, L.W., 2019. Identifying deep hydrothermal fluids that leach metals from the oceanic crust and generate seafloor VMS deposits. *Proceedings of the 15th Biennial SGA Meeting* 1, 76–79.
- Reuber, I., 1988. Complexity of the crustal sequence in the northern Oman ophiolite (Fizh and southern Aswad blocks): The effect of early slicing? *Tectonophysics* 151, 137–165. [https://doi.org/10.1016/0040-1951\(88\)90244-2](https://doi.org/10.1016/0040-1951(88)90244-2).
- Searle, M., Cox, J., 1999. Tectonic setting, origin, and obduction of the Oman ophiolite. *Geol. Soc. Am. Bull.* 111, 104–122. [https://doi.org/10.1130/0016-7606\(1999\)111<0104:TSOAOO>2.3.CO;2](https://doi.org/10.1130/0016-7606(1999)111<0104:TSOAOO>2.3.CO;2).
- Seyfried, W.E., Berndt, M.E., & Seewald, J.S., 1988. Hydrothermal alteration processes at mid ocean ridges: Constraints from diabase alteration experiments, hot-spring fluids and composition of the oceanic crust. *Canadian Mineralogist* 26, 787–804.
- Smewing, J.D., Simonian, K.O., Elboushi, I.M., and Gass, I.G., 1977. Mineralized fault zone parallel to the Oman ophiolite spreading axis. *Geology* 5, 534–538. [https://doi.org/10.1130/0091-7613\(1977\)5<534:MFZPTT>2.0.CO;2](https://doi.org/10.1130/0091-7613(1977)5<534:MFZPTT>2.0.CO;2).
-

- Sweeney, M.R., Gable, C.W., Karra, S., Stauffer, P.H., Pawar, R.J., Hyman, J.D., 2019. Upscaled discrete fracture matrix model (UDFM): An octree-refined continuum representation of fractured porous media. *Comput. Geosci.* 24, 293–310. <https://doi.org/10.1007/s10596-019-09921-9>.
- Umino, S., Kusano, Y., Yamaji, A., Fudai, T., Tamura, A., Arai, S., 2019. The conversion tectonics from spreading to subduction: Paleostress analysis of dike swarms during the subduction initiation in the Oman Ophiolite. *The Geological Society of America* 132, 1333–1343. <https://doi.org/10.1130/B35202.1>.
- van Everdingen, D.A., 1995. Fracture characteristics of the Sheeted Dike Complex, Troodos ophiolite, Cyprus: Implications for permeability of oceanic crust. *J. Geophys. Res.* 100, 19957–19972. <https://doi.org/10.1029/95JB01575>.
- van Hinsbergen, D.J.J., Maffione, M., Koorneef, L.M.T., Guilmette, C., 2019. Kinematic and paleomagnetic restoration of the Semail ophiolite (Oman) reveals subduction initiation along an ancient Neotethyan fracture zone. *Earth Planet. Sci. Lett.* 518, 183–196. <https://doi.org/10.1016/j.epsl.2019.04.038>.
- Wang, X., 2005. Stereological Interpretation of Rock Fracture Traces on Borehole Walls and Other Cylindrical Surfaces. PhD thesis, Blacksburg, Virginia.
- Weiler, P., 2000. Differential rotations in the Oman ophiolite: Paleomagnetic evidence from the southern massifs. *Mar. Geophys. Res.* 21, 195–210. <https://doi.org/10.1023/A%3A1026760331977>.





## 5. General Conclusions and Implications

The main findings of this Thesis bring to the forefront the importance of rock-matrix porosity and permeability in the circulation of hydrothermal fluids in the oceanic crust.

This Thesis set out to address the enigmatic nature of epidotising fluids, and although their origins still require research, the mechanism for their infiltration and extreme metasomatic replacement of  $\sim 1$  km<sup>2</sup> zones of the rock-matrix in volcanic lavas and the SDC is now clear. In transforming the spilite rock-matrix, the epidotising reaction hugely enhances porosity (9–14 vol.%) and permeability ( $\sim 10^{-15}$  m<sup>2</sup> and 4.5 orders of magnitude). This remarkable enhancement mechanism decouples flow from easily clogged fractures and instead provides a positive feedback mechanism that ultimately facilitates the extreme water–rock ratios required to create end-member epidiosites.

Spilites and epidiosites form at greenschist-facies pressures and temperatures but the effects of heating and compression to these conditions from laboratory conditions have only a minimal impact on standard measurement of rock-matrix permeability, compared to natural sample heterogeneity. Our experimental work showed that while *in-situ* effective pressures should be applied during permeability measurements whenever possible, large natural datasets can be considered robust representations of sub-seafloor hydrothermal conditions without need for temperature corrections. Pervasive spilite alteration preserves the original volcanic textures of the lavas. Thus, the variations of rock-matrix porosities and permeabilities in spilites are controlled by the variations in their inherited textures and by, their histories of vesicle formation via degassing of magmatic volatiles. The result for the spilitised upper crust is a zoned flow pattern that preferentially focuses fluids through the highly permeable networks of interpillow hyaloclastite, then through pillow cores, pillow rims, massive flows and finally dykes.

Despite mineralogical differences, spilite, fresh basalt and basalt altered clays and zeolites at low temperatures show overlapping values of porosity and permeability. This suggests that our new data on the various types of spilitised lavas and our upscaled values for entire lava stacks in the Semail ophiolite are directly transferable to *in-situ* mafic crust. Of particular interest is the effect of incorporating our unique measurements of extremely permeable interpillow hyaloclastites into the upscaled values. The resulting high permeabilities of the pillow stacks come close to resolving the long-standing disparity of  $> 3$  orders of magnitude between the permeabilities measured in *ex-situ* rock-matrix samples versus sub-seafloor *in-situ* hydraulic tests. According to our evidence from the Oman ophiolite, the highest *in-situ* values,  $\sim 10^{-14}$  m<sup>2</sup>, cannot be explained by networks of extensional fractures, because these are evidently too sparse and unconnected in distal zones. Inspired by the axial Geotimes lavas of Oman, the presence of massive hyaloclastites or large volcanic breccias are a more likely explanation for the high *in-situ* results. At modern mid-oceanic ridges, intra-pillow cooling joints may additionally play a significant role, whereas in the Geotimes lavas, cooling joints are relatively uncommon. Despite this possible difference between ophiolite and MOR settings, the strong influence of interpillow

hyaloclastites on pillow stack permeability re-enforces the message that these zones are the most critical fluid conduits in fault-distal blocks of lavas.

Undoubtedly, fault-damage zones are fracture-controlled flow channels that transport recharging seawater and discharging hydrothermal fluids. However, without fluid infiltration through the rock-matrix in the vast fault-distal rock masses of the upper crust, the metals, chemical components and heat in the crust would not be leached and transported to seafloor. The role of pervasive spilite and epidosite in the formation of VMS deposits (Jowitt et al., 2012; Patten et al., 2016, Richter & Diamond, 2019) attests to this fundamental role of porous-medium rather than fracture-network flow. In this context, interpillow hyaloclastite networks, which compose fully ~17 vol.% of pillow lava stacks, are likely to have more impact than cooling joints or fracture networks, owing to the potential of hyaloclastites to facilitate metal leaching in their high surface-area pore structures.

The results and deductions of this study are most directly applicable to the greenschist-facies spilite and epidosite lavas commonly present in Archean to Cretaceous ophiolites, but they also have important applications to fresh basalts and low temperature altered lavas present at *in-situ* mid-oceanic ridges. Our model of kilometre-scale distal zones as porous medium-type aquifers with permeabilities of  $\sim 10^{-16}$  m<sup>2</sup>, enhanced at regular intervals by fault-damage zones of  $\sim 10^{-11}$  m<sup>2</sup>, matches the  $10^{-16}$  to  $\sim 10^{-11}$  m<sup>2</sup> range of permeabilities independently invoked by previous numerical simulations that replicate fluid and heat discharge from the crust (Fisher, 1998 and references therein; Hasenclever et al., 2014). By incorporating our model of the upper crustal permeability architecture, characterized by kilometre-wide distal-zones separated by ~100–150 m wide fault-damage zones, the next generation of numerical simulators may expand our understanding of hydrothermal circulation that harnesses the chemical and thermal potential of the rock-matrix and that focuses upflow of fluids to form metal-rich and life-supporting vent structures on the seafloor.

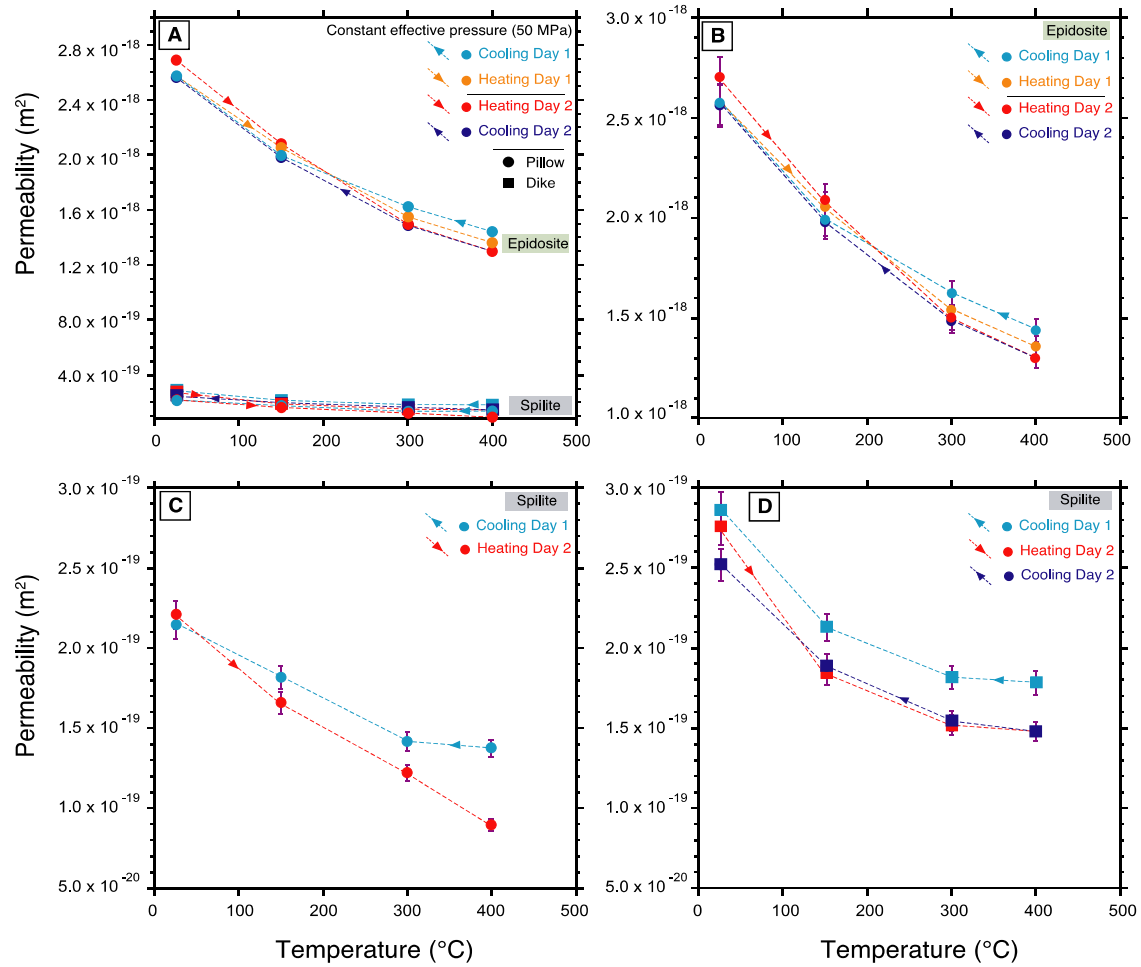
**References**

- Fisher, A.T., 1998. Permeability within basaltic ocean crust. *Reviews of Geophysics* 36, 143–182.  
<https://doi.org/10.1029/97RG02916>.
- Hasenclever, J., Theissen-Krah, S., Rüpke, L.H., Morgan, J.P., Iyer, K., Petersen, S., Devey, C.W., 2014. Hybrid shallow on-axis and deep off-axis hydrothermal circulation at fast-spreading ridges. *Nature* 508, 508–512. <https://doi.org/10.1038/nature13174>.
- Jowitt, S.M., Jenkin, G.R.T., Coogan, L.A., Naden, J., 2012. Quantifying the release of base metals from source rocks for volcanogenic massive sulfide deposits: Effects of protolith composition and alteration mineralogy. *J. Geochem. Explor.* 118, 47–59.  
<https://doi.org/10.1016/j.gexplo.2012.04.005>.
- Patten, C.G.C., Pitcairn, I.K., Teagle, D.A.H., Harris, M., 2016. Sulphide mineral evolution and metal mobility during alteration of the oceanic crust: Insights from ODP Hole 1256D. *Geochim. Cosmochim. Acta* 193, 132–159. <https://doi.org/10.1016/j.gca.2016.08.009>.
- Richter, L., Diamond, L.W. 2019. Identifying deep hydrothermal fluids that leach metals from the oceanic crust and generate seafloor VMS deposits. SGA Biennial Meeting: Proceedings of the 15<sup>th</sup> SGA Biennial Meeting, The Society for Geology Applied to Mineral Deposits (SGA), Scotland (2019), pp. 76–79.



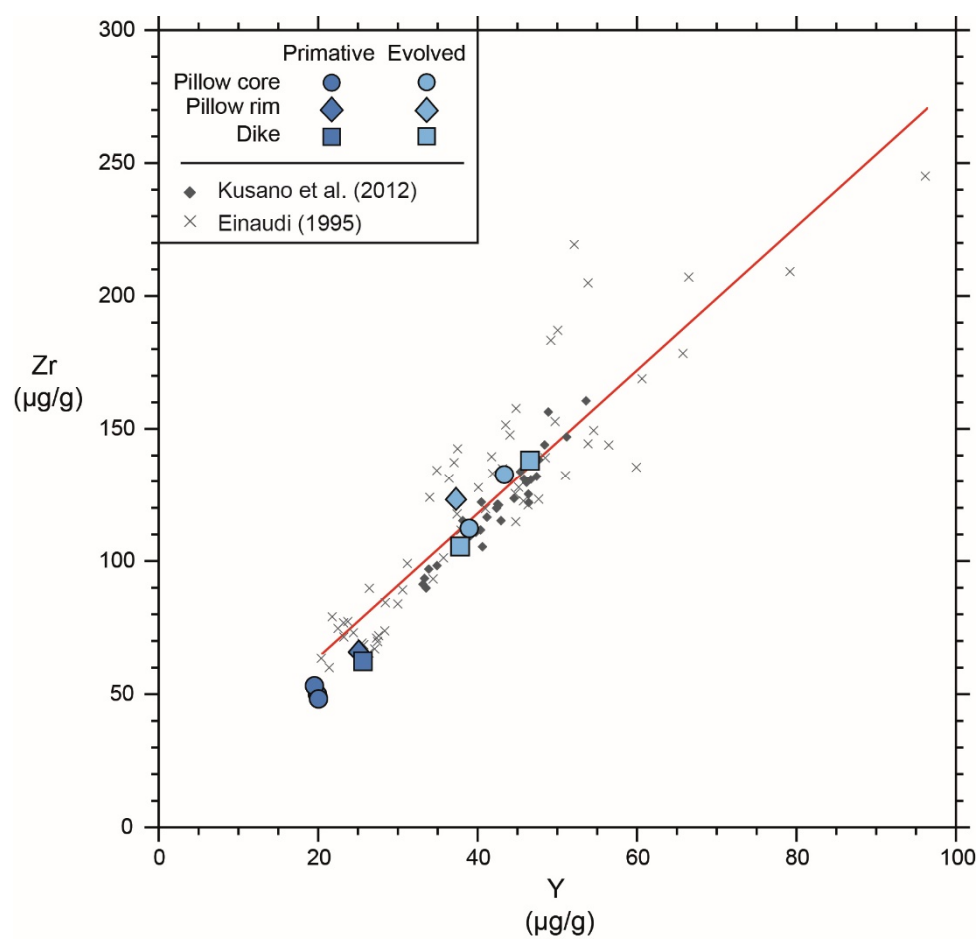
## Appendix

Figure A2.1



Changes in permeability during repeated cooling–heating cycles at 50 MPa effective pressure. Analytical uncertainties shown in purple error bars (values in Table 2.4). The order of cooling and heating sequences follow the legend of each plot from top to bottom; arrowheads mark directions of temperature change. Pressure was reduced overnight between some cycles (see text for explanation). Scales in all plots are linear, not logarithmic. Scale range in (a) is different from (b); scale ranges are the same in (c) and (d). (a) Compilation of data from three samples: epidotised pillow lava SG15-56, spilitised pillow lava LD10-104-3 and spilitised dyke AB17-32C-spl. (b) Permeabilities of epidotised pillow lava SG15-56 along two cooling–heating cycles. (c) Permeabilities of the spilitised pillow lava LD10-104-3 along cooling–heating cycles. (d) Permeabilities of the spilitised dyke AB17-32C-spl along two cooling–heating cycles.

Figure A3.1



Zr/Y ratios of a selection of lavas and dykes fit in two distinct groups on the magmatic fractionation trend line from Geotimes lava literature data. Red line is the fit through literature data.

**Table A2.1**

Bulk thermoelastic expansion of spilite and epidosite minerals at 50 MPa.

Minerals	Molar volume <sup>a</sup> at 25 °C (cm <sup>3</sup> /mol)	Molar volume <sup>a</sup> at 450 °C (cm <sup>3</sup> /mol)	Absolute increase in molar volume between 25 and 450 °C (cm <sup>3</sup> /mol)	Relative increase in molar volume between 25 and 450 °C (%)
Epidote	139.04	140.67	1.63	1.17
Quartz	22.88	23.22	0.34	1.48
Hematite	30.27	30.69	0.42	1.39
Titanite	55.62	56.17	0.54	0.97
Augite	73.28	75.47	2.19	2.99
Clinochlore	210.78	212.72	1.94	0.92
Albite	106.96	108.07	1.11	1.04

<sup>a</sup> Calculated from data in Holland and Powell (2011)



**Table A4.1.** All fractures data mapped at Hilti, Aswad, Rusays and Ajeeb Distal and Damage Zone locations.

Location	Latitude	Longitude	Geo. Group number <sup>1</sup>	Dip (°)	Dip Azimuth (°)	Strike (°)	Seafloor dip (°) <sup>2</sup>	Seafloor Dip Azimuth (°) <sup>3</sup>	Seafloor strike (°) <sup>4</sup>	Total fracture length (m) <sup>5</sup>	Length inside swath (m) <sup>6</sup>	Aperture (mm) <sup>7</sup>	Mineralogy	Additional observations <sup>8</sup>
Hilti	24.112598	56.523754	1	64	35	125	85.4	210.9	300.9	3.5	3.50	40.00	qz + ep	C
	24.112598	56.523754	1	64	35	125	85.4	210.9	300.9	3.5	3.50	40.00	qz + ep	C
	24.112598	56.523754	1	64	35	125	85.4	210.9	300.9	1	1.00	2.00	preh	C
	24.112598	56.523754	1	64	35	125	85.4	210.9	300.9	1	1.00	2.00	preh	C
	24.112921	56.522922	1	82	46	136	80.5	46.3	136.3	20	10.04	3.00	qz + ep	FG
	24.111048	56.522636	1	88	255	345	82.5	77.1	167.1	4	4.00	2.00	preh + LC	C
	24.110964	56.522674	1	78	82	172	81.8	257.3	347.3	2	2.00	3.00	preh + LC	C
	24.110359	56.523544	1	74	251	341	68.2	79.8	169.8	4	4.00	2.00	preh + LC	C
	24.110317	56.523518	1	88	62	152	80.8	63.5	153.5	3.5	3.50	1.00	preh + LC	PS; C
	24.110317	56.523518	1	88	62	152	80.8	63.5	153.5	3.5	3.50	1.00	preh + LC	PS; C
	24.110317	56.523518	1	88	62	152	80.8	63.5	153.5	3.5	3.50	1.00	preh + LC	PS; C
	24.110317	56.523518	1	88	62	152	80.8	63.5	153.5	3.5	3.50	1.00	preh + LC	PS; C
	24.110317	56.523518	1	88	62	152	80.8	63.5	153.5	3.5	3.50	1.00	preh + LC	PS; C
	24.110317	56.523518	1	88	62	152	80.8	63.5	153.5	3.5	3.50	1.00	preh + LC	PS; C
	24.110317	56.523518	1	88	62	152	80.8	63.5	153.5	3.5	3.50	1.00	preh + LC	PS; C
	24.110317	56.523518	1	88	62	152	80.8	63.5	153.5	3.5	3.50	1.00	preh + LC	PS; C
	24.110317	56.523518	1	88	62	152	80.8	63.5	153.5	3.5	3.50	1.00	preh + LC	PS; C
	24.110317	56.523518	1	88	62	152	80.8	63.5	153.5	3.5	3.50	1.00	preh + LC	PS; C
	24.110317	56.523518	1	88	62	152	80.8	63.5	153.5	3.5	3.50	1.00	preh + LC	PS; C
	24.110203	56.523659	1	89	250	340	81.3	72.1	162.1	3	3.00	4.00	preh + LC	C
	24.111715	56.525608	1	50	50	140	68.2	218.5	308.5	0.4	0.40	2.00	preh + LC	PS; C
	24.111715	56.525608	1	50	50	140	68.2	218.5	308.5	0.4	0.40	2.00	preh + LC	PS; C
	24.111715	56.525608	1	50	50	140	68.2	218.5	308.5	0.4	0.40	2.00	preh + LC	PS; C
	24.111715	56.525608	1	50	50	140	68.2	218.5	308.5	0.4	0.40	2.00	preh + LC	PS; C

# Appendix

Location	Latitude	Longitude	Geo. Group number <sup>1</sup>	Dip (°)	Dip Azimuth (°)	Strike (°)	Seafloor dip (°) <sup>2</sup>	Seafloor Dip Azimuth (°) <sup>3</sup>	Seafloor strike (°) <sup>4</sup>	Total fracture length (m) <sup>5</sup>	Length inside swath (m) <sup>6</sup>	Aperture (mm) <sup>7</sup>	Mineralogy	Additional observations <sup>8</sup>
	24.111715	56.525608	1	50	50	140	68.2	218.5	308.5	0.4	0.40	2.00	preh + LC	PS; C
	24.111715	56.525608	1	50	50	140	68.2	218.5	308.5	0.4	0.40	2.00	preh + LC	PS; C
	24.111715	56.525608	1	50	50	140	68.2	218.5	308.5	0.4	0.40	2.00	preh + LC	PS; C
	24.111715	56.525608	1	50	50	140	68.2	218.5	308.5	0.4	0.40	2.00	preh + LC	PS; C
	24.111715	56.525608	1	50	50	140	68.2	218.5	308.5	0.4	0.40	2.00	preh + LC	PS; C
	24.111715	56.525608	1	50	50	140	68.2	218.5	308.5	0.4	0.40	2.00	preh + LC	PS; C
	24.111715	56.525608	1	50	50	140	68.2	218.5	308.5	0.4	0.40	2.00	preh + LC	PS; C
	24.112059	56.524330	1	53	30	120	75.9	203.9	293.9	2	2.00	1.00	preh	C
	24.111891	56.524666	1	54	15	105	79.1	191.9	281.9	2	2.00	3.00	qz ± LC	FG
	24.112381	56.524000	1	85	55	145	80.8	55.8	145.8	2.6	2.60	4.12	preh + LC	
	24.112047	56.522942	2	78	130	220	61.7	302.4	32.4	1.9	1.90	3.00	chl	PS; FG
	24.112047	56.522942	2	78	130	220	61.7	302.4	32.4	1.9	1.90	3.00	chl	PS; FG
	24.112047	56.522942	2	78	130	220	61.7	302.4	32.4	1.9	1.90	3.00	chl	PS; FG
Aswad	24.836218	56.307015	1	48	22	112	72.9	192	282	1.5	1.50	1.00	ep	
	24.837128	56.307968	1	62	65	155	69.3	231.5	321.5	5	5.00	2.00	ep	
	24.837128	56.307968	1	62	65	155	69.3	231.5	321.5	5	5.00	2.00	ep	
	24.837128	56.307968	1	62	65	155	69.3	231.5	321.5	5	5.00	2.00	ep	
	24.837128	56.307972	1	63	51	141	76.5	220.8	310.8	2.5	2.50	3.50	ep	
	24.835350	56.306278	2	79	278	188	87.1	279.9	9.9	2.5	2.50	2.50	ep	
	24.835350	56.306278	2	79	278	188	87.1	279.9	9.9	2.5	2.50	2.50	ep	
	24.835350	56.306278	2	79	278	188	87.1	279.9	9.9	2.5	2.50	2.50	ep	
	24.835350	56.306278	2	79	278	188	87.1	279.9	9.9	2.5	2.50	2.50	ep	
Rusays	24.559469	56.452614	1	78	249	159	72.2	248.8	338.8	120	75.22	10.00	ep + qz	
	24.558062	56.439159	1	89	79	349	59.1	259.7	349.7	2.5	2.50	20.00	ep + qz	LC

# Appendix

Location	Latitude	Longitude	Geo. Group number <sup>1</sup>	Dip (°)	Dip Azimuth (°)	Strike (°)	Seafloor dip (°) <sup>2</sup>	Seafloor Dip Azimuth (°) <sup>3</sup>	Seafloor strike (°) <sup>4</sup>	Total fracture length (m) <sup>5</sup>	Length inside swath (m) <sup>6</sup>	Aperture (mm) <sup>7</sup>	Mineralogy	Additional observations <sup>8</sup>
	24.560463	56.450504	1	58	73	343	28	251.4	341.4	13	13.00	50.00	ep + qz	B
	24.560347	56.449341	1	77	232	142	75.3	231.8	321.8	84	10.03	25.00	ep + qz + py	
	24.558994	56.451782	1	84	274	184	67.7	275.5	5.5	2	2.00	2.50	ep + qz	
	24.559286	56.452579	1	88	58	328	59.5	235.2	325.2	10	10.00	50.00	ep + qz	B
	24.559290	56.447933	1	72	248	158	78.2	248.2	338.2	340	13.84	2.00	ep + qz	
	24.557123	56.451595	1	69	226	136	84.4	227.9	317.9	1	1.00	2.00	ep	FG
	24.560257	56.451115	1	66	245	155	84.4	245.8	335.8	54	18.10	7.00	ep + qz	
	24.560324	56.450459	1	56	252	162	86	72.5	162.5	25.5	12.80	10.00	ep + qz	
	24.558794	56.440727	1	63	240	150	87.9	241.7	331.7	1.5	1.50	7.50	ep	
	24.559364	56.447750	1	51	208	118	73.7	38.7	128.7	15	10.02	15.00	ep + qz	
	24.561037	56.448357	1	60	241	151	89.3	62.9	152.9	4	4.00	2.00	ep	
	24.561037	56.448357	1	60	241	151	89.3	62.9	152.9	4	4.00	2.00	ep	
	24.561037	56.448357	1	60	241	151	89.3	62.9	152.9	4	4.00	2.00	ep	
	24.561037	56.448357	1	60	241	151	89.3	62.9	152.9	4	4.00	2.00	ep	
	24.561037	56.448357	1	60	241	151	89.3	62.9	152.9	4	4.00	2.00	ep	
	24.561037	56.448357	1	60	241	151	89.3	62.9	152.9	4	4.00	2.00	ep	
	24.561037	56.448357	1	60	241	151	89.3	62.9	152.9	4	4.00	2.00	ep	
	24.561037	56.448357	1	60	241	151	89.3	62.9	152.9	4	4.00	2.00	ep	
	24.561037	56.448357	1	60	241	151	89.3	62.9	152.9	4	4.00	2.00	ep	
	24.561037	56.448357	1	60	241	151	89.3	62.9	152.9	4	4.00	2.00	ep	
	24.557241	56.451057	1	56	226	136	83	51.1	141.1	1	1.00	2.00	ep + qz	C
	24.556660	56.451042	1	69	287	197	85.1	284.8	14.8	5	5.00	2.00	ep + qz	
	24.557327	56.451473	1	73	264	174	77.3	263.8	353.8	10	10.00	10.00	ep + qz	C
	24.559399	56.447762	1	86	11	281	73.8	186	276	5	5.00	7.50	ep + qz	

# Appendix

Location	Latitude	Longitude	Geo. Group number <sup>1</sup>	Dip (°)	Dip Azimuth (°)	Strike (°)	Seafloor dip (°) <sup>2</sup>	Seafloor Dip Azimuth (°) <sup>3</sup>	Seafloor strike (°) <sup>4</sup>	Total fracture length (m) <sup>5</sup>	Length inside swath (m) <sup>6</sup>	Aperture (mm) <sup>7</sup>	Mineralogy	Additional observations <sup>8</sup>
A. Dis. Z	24.774433	56.322739	1	84	65	335	68.9	289.8	19.8	8	8.00	15.00	ep + qz	
	24.775356	56.327801	1	82	231	141	72.6	278.6	8.6	4	4.00	45.00	ep + qz	MG
	24.771902	56.327026	1	86	50	320	66	305.9	35.9	66	14.15	25.00	ep + qz	
	24.768301	56.332302	1	75	17	287	69.3	297.4	27.4	4	4.00	115.00	ep	B
	24.774727	56.322269	1	68	241	151	60.3	317.3	47.3	3	3.00	40.00	ep	LQH
	24.774088	56.323982	1	89	291	201	55	304.6	34.6	1	1.00	25.00	ep + qz	
	24.773884	56.323978	1	79	24	294	61.4	272.8	2.8	2	2.00	40.00	ep	LQH
	24.769081	56.327839	2	89	259	169	83.7	192.9	282.9	3	3.00	25.00	ep + qz	
	24.767803	56.328087	2	89	69	339	84.9	200.8	290.8	2	2.00	15.00	ep	
	24.774290	56.324615	2	79	238	148	89.4	6.2	96.2	4	4.00	10.00	ep	FG
	24.774452	56.327724	2	79	8	278	87	16.6	106.6	0.6	0.60	30.00	pump	
	24.775770	56.328346	2	74	266	176	84.2	17.7	107.7	3	3.00	20.00	ep	FG
	24.774403	56.327671	2	85	17	287	88	201	291	3	3.00	55.00	ep + pump	MG
	24.774130	56.328114	2	65	47	317	87.9	21.6	111.6	1	1.00	10.00	ep + qz + py + pump	MG
	24.774088	56.323994	2	89	237	147	73.6	204.4	294.4	3	3.00	65.00	ep	B
	24.771425	56.327095	2	75	57	327	89.3	167.4	257.4	4	4.00	3.50	ep	
	24.773817	56.324654	2	70	227	137	89.7	204.9	294.9	0.3	0.30	30.00	ep	
	24.773661	56.328213	2	89	226	136	62.3	7.6	97.6	1	1.00	10.00	ep + qz	LQH
	24.774298	56.322086	2	79	240	150	83.3	23.5	113.5	2	2.00	7.50	ep + qz	
	24.775848	56.328304	3	87	280	190	73.8	240.9	330.9	4	4.00	35.00	ep + qz	LC
	24.775381	56.327881	3	86	265	175	88	53	143	2	2.00	20.00	ep + qz	
	24.773760	56.325455	3	83	228	138	81.3	227.5	317.5	5	5.00	35.00	ep + qz	
	24.769985	56.327587	3	88	17	287	78.6	67.2	157.2	1.5	1.50	5.00	ep	FG
	24.769930	56.327633	3	82	23	293	75.8	257	347	3	3.00	30.00	ep + qz	C

# Appendix

Location	Latitude	Longitude	Geo. Group number <sup>1</sup>	Dip (°)	Dip Azimuth (°)	Strike (°)	Seafloor dip (°) <sup>2</sup>	Seafloor Dip Azimuth (°) <sup>3</sup>	Seafloor strike (°) <sup>4</sup>	Total fracture length (m) <sup>5</sup>	Length inside swath (m) <sup>6</sup>	Aperture (mm) <sup>7</sup>	Mineralogy	Additional observations <sup>8</sup>
	24.769978	56.327564	3	86	22	292	77.1	246.6	336.6	3	3.00	10.00	ep + qz	MG; C
	24.769665	56.327564	3	74	204	114	87.8	60.5	150.5	5	5.00	5.00	ep + qz	
	24.770971	56.331413	3	63	205	115	88.3	267.9	357.9	1.5	1.50	10.00	ep + qz	
	24.769678	56.326889	3	80	80	350	63.2	215.7	305.7	1	1.00	10.00	ep + qz	
	24.771162	56.323723	3	89	213	123	83.2	235.9	325.9	4	4.00	15.00	ep + qz	
	24.771357	56.323296	3	80	220	130	68.4	229.6	319.6	3	3.00	25.00	ep + qz	
	24.771149	56.323784	3	89	126	36	75.5	54.1	144.1	0.5	0.50	5.00	qz	
	24.771328	56.323128	3	89	217	127	87.4	225.7	315.7	20	10.79	30.00	ep + qz	
	24.770582	56.323261	3	89	39	309	88.5	62.3	152.3	1	1.00	20.00	ep + qz	
	24.773612	56.327495	3	80	232	142	77	263.8	353.8	70	13.02	50.00	ep	
	24.773417	56.327518	3	72	241	151	87.8	49.8	139.8	5	5.00	20.00	ep	
	24.774527	56.322739	3	70	32	302	70.2	31.4	121.4	5	5.00	20.00	ep + qz	
	24.773851	56.323200	3	88	298	208	60.6	37.5	127.5	1.5	1.50	6.00	ep + qz	
	24.774340	56.323204	3	83	136	46	65	254.4	344.4	4	4.00	6.00	ep + qz	
	24.775761	56.328274	3	72	350	260	87.5	33.7	123.7	3	3.00	55.00	ep	B; LC
	24.774227	56.327198	3	83	248	158	82	43.7	133.7	3	3.00	20.00	ep	
	24.774006	56.323997	3	89	50	320	89.1	37.4	127.4	1.7	1.70	25.00	ep + qz	
	24.769945	56.327637	3	85	26	296	88.3	218.5	308.5	2	2.00	5.00	ep + qz	C
	24.771103	56.332207	3	75	180	90	86.5	54.6	144.6	1.5	1.50	7.50	ep	
	24.770979	56.331432	3	72	191	101	82.3	65.8	155.8	2	2.00	15.00	ep + qz	
	24.770542	56.332272	3	78	125	35	85	248.3	338.3	1	1.00	10.00	ep + qz	
	24.768278	56.324139	3	89	202	112	84	228.6	318.6	15	15.00	30.00	ep + qz	
	24.774351	56.327614	3	74	210	120	63.4	19.9	109.9	1	1.00	10.00	chl	
	24.773291	56.327724	3	81	97	7	72.6	37	127	10	10.00	10.00	ep + qz	
	24.770506	56.323265	3	81	49	319	77	224.5	314.5	2.5	2.50	7.50	ep + qz	

# Appendix

Location	Latitude	Longitude	Geo. Group number <sup>1</sup>	Dip (°)	Dip Azimuth (°)	Strike (°)	Seafloor dip (°) <sup>2</sup>	Seafloor Dip Azimuth (°) <sup>3</sup>	Seafloor strike (°) <sup>4</sup>	Total fracture length (m) <sup>5</sup>	Length inside swath (m) <sup>6</sup>	Aperture (mm) <sup>7</sup>	Mineralogy	Additional observations <sup>8</sup>
<b>A. Dam. Z</b>	24.772797	56.327778	1	82	296	206	75.4	295.7	25.7	3	3.00	10.00	ep	FG
	24.773115	56.327320	1	71	143	53	49.1	327.2	57.2	5	5.00	25.00	ep + qz	LQH
	24.773285	56.324287	1	86	318	228	71.4	318.6	48.6	2	2.00	20.00	ep + qz	
	24.773336	56.324280	1	66	288	198	87.9	109.7	199.7	1.5	1.50	15.00	ep + qz	
	24.773191	56.322414	1	76	111	21	54	287.7	17.7	7	7.00	10.00	ep + qz	MG
	24.772919	56.327442	2	66	30	300	70.7	200.9	290.9	5	5.00	30.00	ep	FG
	24.773405	56.322433	2	67	351	261	84.2	167	257	3	3.00	1.00	ep + qz	PS
	24.773405	56.322433	2	67	351	261	84.2	167	257	3	3.00	1.00	ep + qz	PS
	24.773405	56.322433	2	67	351	261	84.2	167	257	3	3.00	1.00	ep + qz	PS
	24.773405	56.322433	2	67	351	261	84.2	167	257	3	3.00	1.00	ep + qz	PS
	24.773405	56.322433	2	67	351	261	84.2	167	257	3	3.00	1.00	ep + qz	PS
	24.773220	56.322365	2	86	11	281	83.9	11.4	101.4	2	2.00	10.00	ep + qz	
	24.773645	56.322021	2	75	190	100	65.8	17.6	107.6	3	3.00	50.00	ep	B; LQH
	24.772358	56.325081	2	62	349	259	79.9	163.9	253.9	2	2.00	10.00	ep + qz	
	24.772270	56.324333	2	73	24	294	79.3	198.5	288.5	7	7.00	30.00	ep	FG
	24.772467	56.324333	2	78	339	249	82.4	338.5	68.5	1.5	1.50	20.00	ep + qz	
	24.772799	56.324299	2	79	25	295	84.5	201.7	291.7	6	6.00	30.00	ep + qz	B
	24.773264	56.324856	2	70	16	286	79.4	190.2	280.2	1.5	1.50	7.50	ep + qz	
	24.773264	56.324856	2	70	16	286	79.4	190.2	280.2	1.5	1.50	7.50	ep	
	24.772808	56.323204	2	82	355	265	82.5	354.9	84.9	1	1.00	8.00	ep + qz	
	24.772690	56.326962	2	80	2	272	86.5	0.9	90.9	1	1.00		ep + qz	
	24.773359	56.322437	2	81	17	287	89.3	195.2	285.2	2	2.00	3.00	ep + qz	PS; C
	24.773359	56.322437	2	81	17	287	89.3	195.2	285.2	2	2.00	3.00	ep + qz	PS; C
	24.773359	56.322437	2	81	17	287	89.3	195.2	285.2	2	2.00	3.00	ep + qz	PS; C

# Appendix

Location	Latitude	Longitude	Geo. Group number <sup>1</sup>	Dip (°)	Dip Azimuth (°)	Strike (°)	Seafloor dip (°) <sup>2</sup>	Seafloor Dip Azimuth (°) <sup>3</sup>	Seafloor strike (°) <sup>4</sup>	Total fracture length (m) <sup>5</sup>	Length inside swath (m) <sup>6</sup>	Aperture (mm) <sup>7</sup>	Mineralogy	Additional observations <sup>8</sup>
	24.773359	56.322437	2	81	17	287	89.3	195.2	285.2	2	2.00	3.00	ep + qz	PS; C
	24.773359	56.322437	2	81	17	287	89.3	195.2	285.2	2	2.00	3.00	ep + qz	PS; C
	24.773359	56.322437	2	81	17	287	89.3	195.2	285.2	2	2.00	3.00	ep + qz	PS; C
	24.773359	56.322437	2	81	17	287	89.3	195.2	285.2	2	2.00	3.00	ep + qz	PS; C
	24.773359	56.322437	2	81	17	287	89.3	195.2	285.2	2	2.00	3.00	ep + qz	PS; C
	24.773359	56.322437	2	81	17	287	89.3	195.2	285.2	2	2.00	3.00	ep + qz	PS; C
	24.773359	56.322437	2	81	17	287	89.3	195.2	285.2	2	2.00	3.00	ep + qz	PS; C
	24.773359	56.322437	2	81	17	287	89.3	195.2	285.2	2	2.00	3.00	ep + qz	PS; C
	24.773359	56.322437	2	81	17	287	89.3	195.2	285.2	2	2.00	3.00	ep + qz	PS; C
	24.773359	56.322437	2	81	17	287	89.3	195.2	285.2	2	2.00	3.00	ep + qz	PS; C
	24.773359	56.322437	2	81	17	287	89.3	195.2	285.2	2	2.00	3.00	ep + qz	PS; C
	24.773359	56.322437	2	81	17	287	89.3	195.2	285.2	2	2.00	3.00	ep + qz	PS; C
	24.773359	56.322437	2	81	17	287	89.3	195.2	285.2	2	2.00	3.00	ep + qz	PS; C
	24.773359	56.322437	2	81	17	287	89.3	195.2	285.2	2	2.00	3.00	ep + qz	PS; C
	24.773359	56.322437	2	81	17	287	89.3	195.2	285.2	2	2.00	3.00	ep + qz	PS; C
	24.773359	56.322437	2	81	17	287	89.3	195.2	285.2	2	2.00	3.00	ep + qz	PS; C
	24.773359	56.322437	2	81	17	287	89.3	195.2	285.2	2	2.00	3.00	ep + qz	PS; C
	24.773359	56.322437	2	81	17	287	89.3	195.2	285.2	2	2.00	3.00	ep + qz	PS; C
	24.773359	56.322437	2	81	17	287	89.3	195.2	285.2	2	2.00	3.00	ep + qz	PS; C
	24.773359	56.322437	2	81	17	287	89.3	195.2	285.2	2	2.00	3.00	ep + qz	PS; C
	24.773359	56.322437	2	81	17	287	89.3	195.2	285.2	2	2.00	3.00	ep + qz	PS; C
	24.773359	56.322437	2	81	17	287	89.3	195.2	285.2	2	2.00	3.00	ep + qz	PS; C
	24.773359	56.322437	2	81	17	287	89.3	195.2	285.2	2	2.00	3.00	ep + qz	PS; C
	24.773359	56.322437	2	81	17	287	89.3	195.2	285.2	2	2.00	3.00	ep + qz	PS; C
	24.773359	56.322437	2	81	17	287	89.3	195.2	285.2	2	2.00	3.00	ep + qz	PS; C
	24.773359	56.322437	2	81	17	287	89.3	195.2	285.2	2	2.00	3.00	ep + qz	PS; C
	24.773359	56.322437	2	81	17	287	89.3	195.2	285.2	2	2.00	3.00	ep + qz	PS; C
	24.773359	56.322437	2	81	17	287	89.3	195.2	285.2	2	2.00	3.00	ep + qz	PS; C
	24.773359	56.322437	2	81	17	287	89.3	195.2	285.2	2	2.00	3.00	ep + qz	PS; C
	24.773359	56.322437	2	81	17	287	89.3	195.2	285.2	2	2.00	3.00	ep + qz	PS; C
	24.773359	56.322437	2	81	17	287	89.3	195.2	285.2	2	2.00	3.00	ep + qz	PS; C
	24.773359	56.322437	2	81	17	287	89.3	195.2	285.2	2	2.00	3.00	ep + qz	PS; C
	24.773359	56.322437	2	81	17	287	89.3	195.2	285.2	2	2.00	3.00	ep + qz	PS; C
	24.773359	56.322437	2	81	17	287	89.3	195.2	285.2	2	2.00	3.00	ep + qz	PS; C
	24.773359	56.322437	2	81	17	287	89.3	195.2	285.2	2	2.00	3.00	ep + qz	PS; C
	24.773359	56.322437	2	81	17	287	89.3	195.2	285.2	2	2.00	3.00	ep + qz	PS; C
	24.773359	56.322437	2	81	17	287	89.3	195.2	285.2	2	2.00	3.00	ep + qz	PS; C
	24.773359	56.322437	2	81	17	287	89.3	195.2	285.2	2	2.00	3.00	ep + qz	PS; C
	24.773359	56.322437	2	81	17	287	89.3	195.2	285.2	2	2.00	3.00	ep + qz	PS; C
	24.773359	56.322437	2	81	17	287	89.3	195.2	285.2	2	2.00	3.00	ep + qz	PS; C
	24.773359	56.322437	2	81	17	287	89.3	195.2	285.2	2	2.00	3.00	ep + qz	PS; C
	24.773359	56.322437	2	81	17	287	89.3	195.2	285.2	2	2.00	3.00	ep + qz	PS; C
	24.773359	56.322437	2	81	17	287	89.3	195.2	285.2	2	2.00	3.00	ep + qz	PS; C
	24.773359	56.322437	2	81	17	287	89.3	195.2	285.2	2	2.00	3.00	ep + qz	PS; C
	24.773359	56.322437	2	81	17	287	89.3	195.2	285.2	2	2.00	3.00	ep + qz	PS; C
	24.773359	56.322437	2	81	17	287	89.3	195.2	285.2	2	2.00	3.00	ep + qz	PS; C
	24.773359	56.322437	2	81	17	287	89.3	195.2	285.2	2	2.00	3.00	ep + qz	PS; C
	24.773359	56.322437	2	81	17	287	89.3	195.2	285.2	2	2.00	3.00	ep + qz	PS; C
	24.773359	56.322437	2	81	17	287	89.3	195.2	285.2	2	2.00	3.00	ep + qz	PS; C
	24.773359	56.322437	2	81	17	287	89.3	195.2	285.2	2	2.00	3.00	ep + qz	PS; C
	24.773359	56.322437	2	81	17	287	89.3	195.2	285.2	2	2.00	3.00	ep + qz	PS; C
	24.773359	56.322437	2	81	17	287	89.3	195.2	285.2	2	2.00	3.00	ep + qz	PS; C
	24.773359	56.322437	2	81	17	287	89.3	195.2	285.2	2	2.00	3.00	ep + qz	PS; C
	24.773359	56.322437	2	81	17	287	89.3	195.2	285.2	2	2.00	3.00	ep + qz	PS; C
	24.773359	56.322437	2	81	17	287	89.3	195.2	285.2	2	2.00	3.00	ep + qz	PS; C
	24.773359	56.322437	2	81	17	287	89.3	195.2	285.2	2	2.00	3.00	ep + qz	PS; C
	24.773359	56.322437	2	81	17	287	89.3	195.2	285.2	2	2.00	3.00	ep + qz	PS; C
	24.773359	56.322437	2											

# Appendix

Location	Latitude	Longitude	Geo. Group number <sup>1</sup>	Dip (°)	Dip Azimuth (°)	Strike (°)	Seafloor dip (°) <sup>2</sup>	Seafloor Dip Azimuth (°) <sup>3</sup>	Seafloor strike (°) <sup>4</sup>	Total fracture length (m) <sup>5</sup>	Length inside swath (m) <sup>6</sup>	Aperture (mm) <sup>7</sup>	Mineralogy	Additional observations <sup>8</sup>
	24.772930	56.323910	2	76	31	301	79.5	206	296	0.5	0.50	25.00	ep	
	24.772318	56.326363	2	82	196	106	74.5	20.6	110.6	3.5	3.50	45.00	ep + qz	
	24.773190	56.322411	2	88	17	287	84.2	17.7	107.7	3	3.00	30.00	ep + qz	
	24.773397	56.322453	2	71	24	294	77.5	197.7	287.7	6	6.00	200.00	ep + qz	LQH
	24.772896	56.322739	2	89	5	275	79	6.7	96.7	2.5	2.50	8.00	ep + qz	
	24.773256	56.322739	2	88	19	289	84.9	19.6	109.6	25	10.56	50.00	ep + qz	
	24.772871	56.323902	2	75	13	283	85.1	189.3	279.3	0.5	0.50	25.00	ep	
	24.772848	56.323906	2	88	13	283	82.7	14	104	2	2.00	20.00	ep + qz	
	24.772888	56.323910	2	76	19	289	83.9	195.1	285.1	1	1.00	40.00	ep	
	24.773056	56.325817	2	81	161	71	62.4	345.6	75.6	4	4.00	25.00	ep	LQH
	24.773012	56.327339	3	56	31	301	61.3	197.1	287.1	15	10.56	20.00	ep	PS
	24.773012	56.327339	3	56	31	301	61.3	197.1	287.1	10	10.00	20.00	ep	PS
	24.773012	56.327339	3	56	31	301	61.3	197.1	287.1	10	10.00	20.00	ep	PS
	24.773012	56.327339	3	56	31	301	61.3	197.1	287.1	10	10.00	20.00	ep	PS
	24.773172	56.327351	3	82	230	140	87.6	52	142	4	4.00	20.00	ep + qz	
	24.772926	56.327451	3	50	48	318	49.5	208.2	298.2	3.5	3.50	10.00	ep	FG
	24.772757	56.324253	3	81	211	121	79.4	35	125	0.8	0.80	20.00	ep + qz	
	24.773548	56.324718	3	86	69	339	74.3	245.5	335.5	1.5	1.50	100.00	ep + qz	
	24.773138	56.324871	3	76	227	137	81	51.6	141.6	7	7.00	30.00	ep + qz	
	24.773018	56.323204	3	82	214	124	81.5	37.4	127.4	10	10.00	10.00	ep + qz	
	24.773149	56.323204	3	80	207	117	76.9	31.7	121.7	4	4.00	40.00	ep + qz	
	24.772972	56.326942	3	88	222	132	89.9	222.4	312.4	3	3.00	10.00	ep + qz	
	24.772730	56.326977	3	79	256	166	86.2	257.1	347.1	4	4.00	20.00	ep + qz	
	24.773413	56.325314	3	87	42	312	85.3	220.4	310.4	4	4.00	80.00	ep	



# Appendix

Location	Latitude	Longitude	Geo. Group number <sup>1</sup>	Dip (°)	Dip Azimuth (°)	Strike (°)	Seafloor dip (°) <sup>2</sup>	Seafloor Dip Azimuth (°) <sup>3</sup>	Seafloor strike (°) <sup>4</sup>	Total fracture length (m) <sup>5</sup>	Length inside swath (m) <sup>6</sup>	Aperture (mm) <sup>7</sup>	Mineralogy	Additional observations <sup>8</sup>
	24.773336	56.323978	3	78	260	170	86	261.2	351.2	6.1	6.10	55.00	ep + qz	
	24.773525	56.323986	3	86	80	350	70.7	256.4	346.4	8.2	8.20	85.00	ep + qz	B
	24.773270	56.323978	3	69	79	349	55	249.1	339.1	2.7	2.70	60.00	ep + qz	B
	24.772133	56.327171	3	65	92	2	47.2	261.9	351.9	1	1.00	7.50	ep + qz	FG
	24.772179	56.327923	3	77	203	113	72.6	29.2	119.2	4	4.00	5.00	ep + qz	C
	24.772533	56.328358	3	65	36	306	67.5	205.8	295.8	1.5	1.50	35.00	ep	FG
	24.772615	56.327297	3	69	211	121	68.4	40.1	130.1	4	4.00	7.50	ep + qz	
	24.772886	56.324276	3	58	50	320	55.8	214.8	304.8	1	1.00	40.00	ep + qz	
	24.772852	56.324249	3	80	219	129	81.6	42.8	132.8	2.5	2.50	30.00	ep	FG
	24.773067	56.324337	3	86	73	343	72.9	249.4	339.4	2	2.00	2.00	ep + qz	
	24.773478	56.322369	3	87	228	138	88.5	228.3	318.3	3	3.00	1.00	ep + qz	PS
	24.773478	56.322369	3	87	228	138	88.5	228.3	318.3	3	3.00	1.00	ep + qz	PS
	24.773478	56.322369	3	87	228	138	88.5	228.3	318.3	3	3.00	1.00	ep + qz	PS
	24.773478	56.322369	3	87	228	138	88.5	228.3	318.3	3	3.00	1.00	ep + qz	PS
	24.773478	56.322369	3	87	228	138	88.5	228.3	318.3	3	3.00	1.00	ep + qz	PS
	24.773478	56.322369	3	87	228	138	88.5	228.3	318.3	3	3.00	1.00	ep + qz	PS
	24.773478	56.322369	3	87	228	138	88.5	228.3	318.3	3	3.00	1.00	ep + qz	PS
	24.772928	56.324947	3	85	43	313	83.1	220.6	310.6	2	2.00	20.00	ep + qz	
	24.773445	56.324833	3	67	49	319	64.2	218.5	308.5	8	8.00	20.00	ep + qz	
	24.772974	56.324921	3	85	55	325	78.4	231.7	321.7	2	2.00	100.00	ep + qz	B
	24.773605	56.322735	3	71	41	311	71	213	303	18	13.20	10.00	ep + qz	
	24.773243	56.326984	3	71	221	131	74.1	48.3	138.3	4	4.00	25.00	ep + qz	LQH
	24.772539	56.327290	3	57	81	351	43.2	245.2	335.2	1	1.00	3.00	ep	FG
	24.772781	56.327751	3	83	225	135	86.7	47.1	137.1	5	5.00	5.00	ep	

# Appendix

Location	Latitude	Longitude	Geo. Group number <sup>1</sup>	Dip (°)	Dip Azimuth (°)	Strike (°)	Seafloor dip (°) <sup>2</sup>	Seafloor Dip Azimuth (°) <sup>3</sup>	Seafloor strike (°) <sup>4</sup>	Total fracture length (m) <sup>5</sup>	Length inside swath (m) <sup>6</sup>	Aperture (mm) <sup>7</sup>	Mineralogy	Additional observations <sup>8</sup>
	24.773132	56.322437	3	88	213	123	86.6	34.1	124.1	10	10.00	100.00	ep + qz	
	24.773561	56.324718	3	87	227	137	88.9	227.4	317.4	23	20.43	10.00	ep + qz	
	24.773045	56.323910	3	72	46	316	70	218	308	2	2.00	55.00	ep	
	24.771767	56.329990	3	79	36	306	80.3	211.7	301.7	2.5	2.50	10.00	ep + qz	
	24.772387	56.327248	3	70	59	329	63.1	229.3	319.3	3	3.00	5.00	ep + qz	
	24.772928	56.327343	3	68	51	321	64.4	220.8	310.8	2	2.00	6.00	ep	FG
	24.772739	56.324287	3	72	55	325	66.5	226.4	316.4	3	3.00	5.00	ep	
	24.772839	56.324257	3	79	252	162	87.5	253.4	343.4	2.5	2.50	20.00	ep + qz	
	24.772852	56.324242	3	75	222	132	78.2	47.5	137.5	3.5	3.50	40.00	ep + qz	MG
	24.773235	56.324287	3	74	215	125	74.5	41.6	131.6	1.5	1.50	15.00	ep + qz	
	24.773289	56.324287	3	68	94	4	49.6	265.4	355.4	6	6.00	50.00	ep + qz	B
	24.773602	56.324287	3	74	90	360	56.4	263	353	1	1.00	10.00	ep + qz	
	24.773136	56.327351	3	75	261	171	88.6	263	353	5	5.00	12.50	ep	
	24.773035	56.324913	3	83	255	165	82.7	255	345	1	1.00	7.50	ep + qz	
	24.773544	56.324718	3	74	74	344	61.3	246	336	0.5	0.50	5.00	ep + qz	
	24.772381	56.327236	3	61	63	333	53.4	228.7	318.7	3	3.00	7.50	ep + qz	
	24.772381	56.327236	3	61	63	333	53.4	228.7	318.7	3	3.00	5.00	ep + qz	
	24.772753	56.324295	3	72	65	335	62.7	236.1	326.1	3	3.00	10.00	ep + qz	B
	24.772781	56.327347	3	75	41	311	74.7	214.7	304.7	6	6.00	20.00	ep	FG
	24.773148	56.327343	3	60	65	335	51.7	230.2	320.2	0.8	0.80	10.00	ep	
	24.772764	56.324314	3	63	238	148	73	66.5	156.5	4	4.00	30.00	ep + qz	
	24.772758	56.324280	3	71	54	324	65.9	225	315	1.5	1.50	7.50	ep	
	24.773523	56.324268	3	69	74	344	56.7	243.8	333.8	5	5.00	30.00	ep + qz	
	24.773754	56.322250	3	86	227	137	89.8	227.8	317.8	2	2.00	1.00	ep + qz	PS

# Appendix

Location	Latitude	Longitude	Geo. Group number <sup>1</sup>	Dip (°)	Dip Azimuth (°)	Strike (°)	Seafloor dip (°) <sup>2</sup>	Seafloor Dip Azimuth (°) <sup>3</sup>	Seafloor strike (°) <sup>4</sup>	Total fracture length (m) <sup>5</sup>	Length inside swath (m) <sup>6</sup>	Aperture (mm) <sup>7</sup>	Mineralogy	Additional observations <sup>8</sup>
	24.773754	56.322250	3	86	227	137	89.8	227.8	317.8	2	2.00	1.00	ep + qz	PS
	24.773754	56.322250	3	86	227	137	89.8	227.8	317.8	2	2.00	1.00	ep + qz	PS
	24.773754	56.322250	3	86	227	137	89.8	227.8	317.8	2	2.00	1.00	ep + qz	PS
	24.773754	56.322250	3	86	227	137	89.8	227.8	317.8	2	2.00	1.00	ep + qz	PS
	24.772722	56.327831	3	74	70	340	62.7	241.9	331.9	20	20.00	20.00	ep + qz	FG; LQH
	24.773397	56.322453	3	79	225	135	83	48.6	138.6	7	7.00	100.00	ep + qz	LQH
	24.773220	56.322395	3	85	80	350	69.8	256.1	346.1	1	1.00	5.00	ep + qz	
	24.773418	56.324825	3	76	257	167	88.8	259	349	7	7.00	10.00	ep + qz	
	24.773209	56.325745	3	75	49	319	71.5	222.1	312.1	5	5.00	30.00	ep + qz	
	24.773127	56.324871	3	73	224	134	77.1	50.1	140.1	7	7.00	50.00	ep + qz	
	24.772837	56.323883	3	82	215	125	81.9	38.3	128.3	1.5	1.50	30.00	ep	
	24.772900	56.323910	3	70	59	329	63.1	229.3	319.3	4.8	4.80	30.00	ep	
	24.772192	56.327766	3	83	44	314	80.8	220.7	310.7	5	5.00	10.00	ep + qz	LQH
	24.773018	56.327332	3	88	82	352	72	259	349	7	7.00	15.00	ep	
	24.773170	56.327351	3	67	77	347	53.8	246.1	336.1	3	3.00	10.00	ep + qz	
	24.771896	56.328953	3	75	204	114	71.1	31	121	2	2.00	15.00	ep + qz	
	24.772493	56.327217	3	67	70	340	56.3	238.8	328.8	2	2.00	20.00	ep	FG
	24.773195	56.322742	3	62	226	136	67.8	56.6	146.6	4	4.00	40.00	ep + qz	
	24.772518	56.326904	3	84	217	127	84.5	39.4	129.4	3	3.00	20.00	ep + qz	LQH
	24.772854	56.324978	3	77	217	127	78	42.2	132.2	4	4.00	10.00	ep + qz	
	24.773062	56.323208	3	84	68	338	72.8	243.8	333.8	2	2.00	50.00	ep + qz	
	24.773104	56.324875	3	72	222	132	75.4	48.7	138.7	1	1.00	40.00	ep + qz	
	24.772173	56.327812	3	89	42	312	87.1	221.2	311.2	3	3.00	5.00	ep + qz	C

<sup>1</sup>Geometric Group that fractures are in; <sup>2,3,4</sup>Restored for each location according to values in Table 4.1; <sup>5</sup>Length of fractures extending outside of swath; <sup>6</sup>Length of fractures inside swath, corrections applied from in text Section X; <sup>7</sup>Aperture (mm) refers to modal aperture in most cases and an average of minimum and maximum recorded values where no mode was recorded; <sup>8</sup>Additional observations include textures i.e. C = comb texture; FG = fine grained; B = breccia; MG = multiple hydrothermal filling generations. Late features i.e. LGH = late quartz-hematite overprint; LC = late calcite overprint. Finally, PS = a parallel set of adjacent fractures. Additional location notes: A. Dis. Z = Ajeeb Distal Zone; A. Dam. Z = Ajeeb Damage Zone.



## Declaration of consent

on the basis of Article 18 of the PromR Phil.-nat. 19

Name/First Name: Brett, Alannah C.

Registration Number: 14-140-453

Study program: PhD Earth Sciences

Bachelor ☐ Master ☐ Dissertation ☒

Title of the thesis: Hydrothermal flow paths in the upper oceanic crust: magnitude and distribution of porosity and permeability in altered, fractured basalts, Oman ophiolite

Supervisor: Prof. Larryn W. Diamond

I declare herewith that this thesis is my own work and that I have not used any sources other than those stated. I have indicated the adoption of quotations as well as thoughts taken from other authors as such in the thesis. I am aware that the Senate pursuant to Article 36 paragraph 1 literar of the University Act of September 5th, 1996 and Article 69 of the University Statute of June 7th, 2011 is authorized to revoke the doctoral degree awarded on the basis of this thesis.

For the purposes of evaluation and verification of compliance with the declaration of originality and the regulations governing plagiarism, I hereby grant the University of Bern the right to process my personal data and to perform the acts of use this requires, in particular, to reproduce the written thesis and to store it permanently in a database, and to use said database, or to make said database available, to enable comparison with theses submitted by others.

Bern / 15.03.2021



Place/Date

Signature



## Curriculum Vitae

**Alannah C. Brett**

### Personal Information

Date of birth: 21.05.1993  
Place of birth: Stanthorpe, Australia  
Nationality: Dual: British & Australian  
Residence: Bern, Switzerland

### Education

2017–2021 **Ph.D.**, Geology, University of Bern, Bern, Switzerland  
*Hydrothermal flow paths in the upper oceanic crust: magnitude and distribution of porosity and permeability in altered, fractured lavas, Oman ophiolite*

2015–2017 **M.Sc.**, Geology, University of Bern, Bern, Switzerland  
*Porosity and permeability changes associated with epidosite alteration of the upper oceanic crust, Semail ophiolite, Oman*

2012–2014 **B.Sc.**, Geology, University of Auckland, New Zealand